UNIVERSITÀ DEGLI STUDI DI PADOVA
Facoltà di Scienze MM.FF.NN.
Dipartimento di Fisica "G. Galilei"

Dottorato di Ricerca in Fisica
Ciclo XX

Novel Reflective Elements and Indirect Dark Matter Searches for MAGIC II and Future IACTs.

Coordinatore: Prof. Attilio Stella
Supervisore : Prof. Antonio Saggion
Correlatore : Dott. Mosè Mariotti

Dottorando: Michele Doro

Anno Accademico 2008–2009

To Florian Goebel.

Si muero, sobrevíveme con tanta fuerza pura que despiertas la furia del pálido y del frío, de sur a sur levanta tus ojos indelebles, de sol a sol que suene tu boca de guitarra.

No quiero que vacilen tu risa ni tus pasos, no quiero que se muera mi herencia de alegría, no llames a mi pecho, estoy ausente. Vive en mi ausencia como en una casa.

Es una casa tan grande la ausencia que pasarás en ella a través de los muros y colgarás los cuadros en el aire.

Es una casa tan transparente la ausencia que yo sin vida te veré vivir y si sufres, mi amor, me moriré otra vez.

Soneto XCIV "Cien sonetos de amor". Pablo Neruda

Abstract

Questo lavoro di Tesi riporta le attività svolte durante tre anni di Scuola di Dottorato presso Università degli Studi di Padova, Dipartimento di Fisica Galilei, in associazione con INFN Padova, sotto la supervisione di A. Saggion e M. Mariotti, per gli esperimenti MAGIC e CTA. Nel lavoro di dottorato ho svolto la mia ricerca seguendo due attività principali: una tecnologica relativa allo sviluppo e la produzione di unità riflettenti per il secondo telescopio MAGIC, ed una parte maggiormente scientifica concentrata sulla rivelazione indiretta di materia oscura con il telescopio MAGIC. Per entrambe le tematiche, ho svolto studi volti a capire le problematiche che questi settori avranno nei telescopi di futura generazione, come CTA.

L'attività tecnologica è cominciata con lo sviluppo di tecniche per la realizzazione di superfici riflettenti di grandi dimensioni con lo scopo di coprire la supericie del riflettore del secondo telescopio MAGIC, gà in fase di costruzione nel 2004. Sono stati sviluppati speciali pannelli a *sandwich* di pelli di alluminio e strutture a nido d'ape, incollati a caldo con resine epossidiche e strutturali e lavorati con fresatura a punta di diamante. In questa tesi, si riporta la descrizione tecnica completa dello specchio, incluse le tecniche di produzione e i materiali utilizzati. Ogni specchio ha raggio di curvatura diverso a seconda della sua posizione sul telescopio, il cui profilo é globalmente parabolico. La procedura di ottimizzazione dei raggi di curvatura dei singoli specchi e del loro posizionamento nel telescopio vengono descritti, assieme ad una breve discussione sull'ottica stessa di un telescopio parabolico di 17 m di diametro — quale è MAGIC — e delle sue aberrazioni. A seguito dell'assemblaggio e della fresatura a diamante, è seguita una fase di misurazione di qualità ottiche, che viene qui riportata. E' stata inoltre sviluppata una collaborazione per lo sviluppo di tecniche innovative e a basso costo, per la produzione di grandi superfici riflettenti, come la formatura a freddo di *sandwich* in vetro/alluminio, in collaborazione con INAF. Queste attività sono state di interesse per l'esperimento MAGIC ma ancor di piú nella prospettiva di esperimenti di prossima generazione come CTA (Cherenkov Telescope Array) dove saranno necessarie vaste superfici riflettenti ad un costo ragionevole. Alcune misure di qualitá su questi specchi sono qui riportate. Infine viene descritta la organizzazione delle attività di installazione degli specchi di vetro e di quelli di alluminio sul telescopio MAGIC II, da me personalmente seguita.

L'attività piú strettamente scientifica è stata svolta nella rivelazione indiretta di materia oscura con il telescopio MAGIC. La ricerca si basa sulla possibilità di poter rivelare segnali indiretti sotto forma di raggi gamma, provenienti da annichilazione o decadimento di particelle di materia oscura. Essa va ricercata nelle regioni dell'universo in cui e' maggiormente addensata, quali galassie satelliti della Via Lattea o buchi neri di massa intermedia. In questa tesi si riporta una breve introduzione sulla materia oscura, sulle evidenze sperimentali e sui principali modelli che la descrivono. In seguito, si riporta uno studio effettuato tra le sorgenti non indentificate di EGRET (un satellite per lo studio di radiazione gamma), volto a definire quali tra esse potessero essere candidati per osservazione di materia oscura. Si descrivono i risultati di osservazione di una sorgente (3EG 1835) con il telescopio MAGIC nel 2005, la riduzione dei dati e la stima dei limiti superiori di emissioni, che parzialmente riducono lo spazio dei parametri della materia oscura. Di seguito, si riportano i risultati della osservazione di una seconda sorgente di materia oscura con il telescopio MAGIC, la galassia nana satellite Willman 1, considerata una delle piú promettenti sorgenti. Anche in questo caso si riportano solo limiti superiori di flusso, che permettono tuttavia di fare alcune interessanti discussioni sui limiti sperimentali di questa tecnica. Infine, si riportano le prospettive di osservazione per due telescopi a venire: MAGIC II, che sará presto messo in opera e CTA.

Abstract

This thesis reports the activities performed during three years of PhD studentship at the University of Padova, Department of Physics G. Galilei in the years 2005–08, under the supervision of M. Mariotti and A. Saggion, for the MAGIC telescope experiment and the CTA consortium. During the PhD, my research activity focused on two principal occupations: *a) construction and installation of the mirrors for the MAGIC II reflector*, and *b) dark matter searches with MAGIC*. In both fields, the research activity was also extended for the Cherenkov Telescope Array (CTA), which represents the future of the observational technique.

The technological activity started with the development of a technique that permitted the realization of large reflective surface with the aim of covering the reflective surface of the second MAGIC telescope, already under construction in 2004. Special panels were developed, in the form of all–aluminum sandwiches of thin aluminum sheets and a hexcell honeycomb layer, glued together with epoxy structural weld in autoclave and milled with a novel diamond–milling technique. In this thesis, the complete technical description of the mirror is reported, together with the production techniques and the materials used. Each mirror has a different radius of curvature according to its position on the reflector, which has an overall parabolic profile. The procedures of optimization of the mirrors' radius of curvature and of the telescope's one are described, together with a short discussion of the optics of a parabolic reflector of 17 m diameter — like that of MAGIC — and of its aberrations. After the assembly of the mirrors and their milling, several optical measurements took place, which are hereafter described. Following a collaboration with INAF, studies were made for the realization of large reflective surfaces made of cold-slumped glass-aluminum sandwich. Those activities have been of interest also for the next generation of telescopes like CTA, where vast reflective surfaces will be necessary. Some quality measurements on those mirrors are reported. Finally, the installation of both aluminum and glass mirrors on MAGIC II is reported.

The scientific activity was based the study of indirect detection of dark matter with MAGIC. The research is based on the possibility for MAGIC to detect gamma–rays as a result of annihilation or decay of dark matter particles. Gamma–ray signal are searched for in places where dark matter is concentrated, like satellite galaxies of the Milky Way or intermediate mass black holes. In this thesis, a brief introduction on dark matter is reported, together with the principal experimental evidences and the principal theoretical models. A study of the unidentified EGRET sources (EGRET was a satellite experiment for gamma–ray detection) is reported, with the aim of defining who among them could fulfill the requirement of being candidate for dark matter observation. The results of the observation, data analysis and estimates of the upper limits of flux for a source 3EG 1835, observed with the MAGIC telescope in 2005, are reported. The results partially limits the dark matter parameter space. Following, the results of the observation of the satellite galaxy Willman 1 in 2008 with the MAGIC telescope are reported. Also in this case, only upper limits were produced, but they allow to make an interesting discussion on the current status of indirect dark matter searches. Finally, accurate prospects of detection are reported for MAGIC II, about to come, and CTA.

Contents

Preface

MAGIC is currently the largest telescope of the Imaging Atmospheric Cherenkov Telescope (IACT) class. These detectors take advantage of the electromagnetic shower of particles left in the earth atmosphere by cosmic gamma–rays coming from far distant objects in the universe, where intense and violent non–thermal phenomena take place. Gamma–rays are always associated to highly energetic parent particles which drive their production. They are called cosmic rays, and are charged particles with energies as large as 10^{21} eV and whose origin is hitherto almost unknown. Despite the recent birth, the study of gamma–rays from ground–based detector has revealed to have reached a mature stage, with important scientific results and large discovery potential. Gamma–astronomy is sometimes considered the only science which could solve questions in fundamental physics like the violation of Lorentz invariance, or the identification of dark matter and the new related physics behind the Standard Model of Particles. The scientific output of MAGIC is already quite large with three articles published on the Science magazine, more than 40 articles published on physics journals and a larger number of technical articles. MAGIC has the lowest energy threshold of all current IACTs and a sensitivity slightly smaller, which comes from being operated with one single telescope rather than an usual array configuration. To improve the performance, a second clone telescope, dubbed MAGIC II, was recently built and is under commissioning at the MAGIC site. The combination of the two telescopes, MAGIC I and MAGIC II, operating in stereoscopic mode, will permit to increase sensitivity, resolution and to possibly decrease the energy threshold. An intriguing future is around the corner for the MAGIC collaboration.

The telescopes are operated by a collaboration of around 150 physicists in more than 20 institutes, spread in several European countries, and headed by Germany, Italy and Spain. Within this collaboration, my research activity was focused on two main targets: *a) construction and installation of the mirrors for the MAGIC II reflector*, and *b) dark matter searches with MAGIC*, which are discussed in this preface to guide the reader through the thesis.

In the last year, I have also started several activities based on these two research grounds for the future generation of Cherenkov telescopes, becoming co–coordinator of the activities of the working–group for mirrors for the Cherenkov Telescope Array (CTA). CTA is a project for an array of 30–100 IACTs, operated simultaneously, with two–three different reflector sizes, to cover the energy band from a few GeV up to 100 TeV, which will start operation probably around 2015. More details about the project will be given in this work. The mirror working group is responsible for developing technologies for CTA reflective surface, which could cover up to $10,000$ m^2 area. Furthermore, I have recently investigated the prospects of detecting dark matter from two selected targets with CTA, given its expected properties, and defining which is the scenario for future experiments and which detector parameters are more critical for possible detection.

In the following, I will go more carefully into detail on the activities. Later on, the structure of this thesis work will be provided.

1) Technical activities on the MAGIC II telescope

The MAGIC II telescope reflector is a paraboloid surface with a 17 m diameter and around 17 m focal length. The reflective surface is tessellated with 247 mirrors of around 1 m^2 area each, of two different types: 143 aluminum sandwich mirrors, with diamond–milled surface, and 104 glass/aluminum sandwich mirrors made by cold–slumping. Each mirror has a square shape, a spherical profile, and a different radius of curvature optimized to fit into a defined position in the parabolic shape. The main mirror requirements for the telescope operation are: resistance to operation in open air, reflectivity larger than 80% in the Cherenkov band, reduced reflectivity loss with time, light–weight and reduced cost.

The work for the mirrors of MAGIC II constituted the major activity of my PhD, in particular for the aluminum mirrors, for whom I followed production, test and installation. In particular, my activities focused on:

i) *Ray–tracing simulation.* There was a general idea of going to larger mirrors for MAGIC II with respect to MAGIC I. While the telescope structure and paraboloid profile remained the same, it was considered to put mirrors of 1 m^2 area. To investigate the optical properties of such reflector, a ray–tracing simulation was performed. As a main result, it was demonstrated that 1 m^2 mirrors provide an acceptable solution for MAGIC II. The study is discussed in Chapter 3.

ii) *Design.* The major design ideas were proposed by A. Pepato at INFN–Padova. The design is basically a rescaling of MAGIC I mirrors, with particular attention paid to their sealing and their stiffness (This and the following points of this list are treated in Chapter 4).

iii) *Prototyping.* The first prototypes were produced at Laboratori Nazionali di Legnaro (LNL–Padova) by the Padova group. The optical qualification had good results and the massive production was therefore started.

iv) *Market research.* A research on the market was performed to find a suitable company for assembling the raw–blanks. The company Compositex Srl in Vicenza (Italy) was found to best fulfill our requirements. The company was asked to produce the tooling and about 150 raw–blanks in 2007–08 for MAGIC II.

v) *Massive production.* The complete work around the mirrors wass performed by different companies in Europe: Compositex assembled the raw–blanks, the company LT–Ultra diamond–milled the surface in Germany, which was later on quartz–coated at IFAM institute in Bremen, also in Germany. Continuous contacts with the companies, travels and on–the–pipeline tests were made to check the overall quality in the production.

vi) *Tests.* The major part of the research activity was based on the optical qualification and tests on the mirror samples. Focussing power, differential reflectivity, insulation, overall quality were defined for each mirror to be mounted on the telescope. In this I was helped by many collaborators and in particular by E. Giro.

vii) *Installation.* I personally performed the optimization of the mirror positioning the telescope, which is particularly important to maximize the telescope's optical performance. The full reflector was installed in two periods, November 2007 and August 2008. I personally organized the installation.

The design, production and preliminary tests of glass mirrors were performed at INAF–Milano in collaboration with the Medialario company. I performed a number of quality tests on these mirrors together with E. Giro and also followed their installation. These activities are also reported in Chapter 4.

2) Dark matter searches

There are currently solid experimental evidences that dark matter accounts for around 24% of the entire energy budget in the universe, around 5 times the total baryonic content. It is also strongly motivated that dark matter is in the form of weakly interacting massive particles (WIMPs), i.e. particles with no–strong or electromagnetic interaction, possibly weakly interacting and massive. These particles should have been produced in the early universe in a non thermal way and decoupled from ordinary matter when already non–relativistic ("cold"). This scenario well explains the structure formation as a result of collapse of baryons onto primordial overdensities of dark matter. The best candidate for being WIMP is the *neutralino*, a particle which arises in supersymmetric theories which extends the standard model of particles (see Chapter 6).

Given the neutralino expected mass of 100–1000 GeV, it could be indirectly observed by IACTs from the gamma–ray emission following annihilation reactions. The gamma–ray spectrum is usually a continuum with a rather steep cutoff at the neutralino mass, which constitutes a smoking–gun signature of dark matter. As the cutoff happens exactly to be at the dark matter particle mass, its observation would constitute a smoking–gun indication not only of the dark matter, but of the specific type of particle. It is remarkable that other experimental techniques like direct detection or direct production of dark matter cannot be that sensitive to the candidate species. More details are found in Chapter 7.

With MAGIC, two scientific cases were studied: that of low luminosity satellite galaxies and that of intermediate mass black holes. The former are small galaxies wandering in the Milky Way surroundings and gravitationally bound to it. They have low surface brightness but large stellar velocities which is explained by the presence of huge overdensity of dark matter located at their position. A precise estimation of the gamma–ray flux from dark matter annihilation is complicated by the rather imprecise knowledge of the morphology of the emission region, which introduce uncertainties of orders of magnitude in the flux. In this work, the observation of Willman 1 with MAGIC telescope is presented and discussed. The subject is explored in Chapter 10. A second class of emitters could be the intermediate mass black holes. These objects arise from theoretical and experimental evidences. Due to their history and evolution, they could be in the form of spiky overdensities of dark matter, wandering in the Milky Way halo. Their brightness in gamma–ray is expected to be very large. On the other hand, their location is unknown. In this thesis, I performed a search for possible candidates in the EGRET catalog of unknown sources. The observation of the most intense one (3EG 1835) is presented here and discussed in Chapter 8.

3) Activities for CTA

The Cherenkov Telescope Array (CTA) is expected to improve significantly the performance of the Cherenkov technique and reach its detection limits. The complete installation of the array is expected to be finalized around 2015. At present, the CTA consortium is under creation, and parallel activities are maintained on several technological aspects. It is planned to build telescope prototypes in a few years from now. The preliminary activities as co–coordinator of the mirror working group are described in Chapter 5, which are based on reviewing current

technologies, and preparing test facilities. In addition, an improved version of MAGIC II aluminum mirrors is under study for CTA.

For the same project, the prospects for observation of dark matter were explored in Chapter 9. The increased sensitivity with respect to the current generation of Cherenkov telescope would allow for an enhanced chance of detection, whereas the scenario is not completely optimistic. The study is applied to two target candidates, Draco and Willman 1, which are well–known low luminosity galaxies. Once defined the particle physics scenario through benchmark models of neutralinos, the prospects of detection are referred to. In particular, the study is performed to enlighten the technical aspects of IACTs which greatly influence the detection.

Outline of the work

This work is divided into an introduction, one part describing the activity on mirrors for MAGIC II and CTA, and the second part on the dark matter searches. The references are reported at the end of each chapter for improved readability. To conclude, a series of appendices is given.

Introduction

In Chapter 1, an introduction on gamma–ray astronomy is given. The following fundamental questions are discussed: where do the ultra–high–energy cosmic–rays come from? How are they accelerated? Places of acceleration in the universe are discussed as sources of high energy cosmic–rays and gamma–rays. A discussion of the fundamental physics studies that can be made with IACTs is finally reported.

Part I. Technical activities on the MAGIC telescope.

In Chapter 2, the MAGIC telescopes are introduced. The basic design considerations are discussed together with the overall telescope performance, introducing the most relevant features which are used throughout the thesis. In Chapter 3 the optics of the MAGIC telescopes are discussed. The aberrations of the parabolic shape are discussed and the ray–tracing simulations are presented. The decision of using large mirrors is discussed in detail. The final configuration of the mirrors on the MAGIC II reflector is reported. In Chapter 4, the complete description of design, production and tests on aluminum mirrors for MAGIC II is reported. A brief introduction of MAGIC I mirror and MAGIC II glass mirrors is also given. In Chapter 9, the activities for the CTA mirror working group are reported. The quality criteria for CTA mirrors are discussed, the ongoing activity for larger aluminum mirrors are presented and the planned construction of a measuring facility in Legnaro is also discussed. Company partners constituted an important gear for the production of MAGIC mirrors. Also many different institutes and institutions have contributed to the realization of MAGIC mirrors. At page 111, a list of references for companies and institutions is reported, together with a short presentation of their activities and if possible the reference person in case contacts are desired.

Part II. Dark matter searches.

In Chapter 6, the dark matter paradigm is introduced. Experimental evidence is presented and discussed together with the principal theories and candidates. In Chapter 7, a more

insight view on dark matter is given. In the first part, it is investigated *how* to detect dark matter, through its annihilations/decay product, or through nuclear recoils, or via direct production at accelerators. In the second part, the regions in the universe where dark matter is expected are presented. In Chapter 8 the observation of intermediate mass black holes is introduced and the analysis of 3EG 1835 is discussed. The way in which MAGIC data are analyzed is also presented in this chapter. In Chapter 9 the prospects of detection of two exemplar target sources for MAGIC II and CTA are discussed. In particular, the experimental features that affect DM detection are discussed. For the first time, internal bremsstrahlung is included in the spectra calculation. The chapter allows to introduce the way in which DM signals are normally analyzed with IACTs. In Chapter 10, the observation of the satellite galaxy Willman 1 with the MAGIC telescope is given.

Appendixes

In Appendix A the basic mechanisms of particle accelerations and transport are presented. In Appendix B the physics of development of atmospheric showers is presented. In Appendix C a short introduction on optical aberrations of a spherical and parabolic reflector are studied. Finally, in Appendix D the procedure for the calculation of flux upper limit for a general spectrum, as in the case of dark matter is described.

Accompanying papers and co–authorship statement

This thesis is a compendium of manuscripts written by myself on various occasions reporting different research activities. The content of this thesis can be therefore traced by the single manuscripts, whose content was rearranged and embedded in the thesis structure. In the following, a list of accompanying papers is provided, which are also reported at the header of the each chapter.

I would like to mention that most of the activities were performed together or with the help of many collaborators, which I want to acknowledge here.

Papers on journals.

I. **NIM A, 595 (2008)** M. Doro et al., *The reflective surface of the MAGIC telescope*, Nuclear Instruments and Methods A, Vol. 595, 2008, pages 200-203.
In 2007, I presented the main design considerations of MAGIC mirrors at the 6th International Workshop on Ring Imaging Cherenkov Counters (RICH 2007), Stazione Marittima, Trieste, Italy. The proceeding was reviewed and published in Nuclear Instruments and Methods A. The content of the paper was used to introduce MAGIC I mirrors in Chapter 4. E. Lorenz reviewed and commented the article.

II. **JCAP 01:016 (2009)** T. Bringmann, M. Doro, M. Fornasa, *Dark Matter Signals from Draco and Willman 1: Prospects for MAGIC II and CTA*, JCAP01(2009)016.
The article takes two targets for observation of dark matter from dwarf galaxies and calculates the prospects of observation for MAGIC II and CTA, with particular attention to the telescope's technical characteristics that affect the observation. The article is presented in Chapter 9. The work was done with T. Bringmann and M. Fornasa.

III. **MAGIC paper on Willman 1.** MAGIC collaboration. Corresponding authors: M. Doro and M.A. Sanchéz–Conde, *MAGIC upper limits on the VHE gamma-ray emission from the satellite galaxy Willman 1*, arXiv:0810.3561 (astro-ph), submitted to Astroph. Journal
The article describes the scientific case, the data analysis and the result of the observation of Willman 1 with the MAGIC telescope that took place in summer of 2008. The article is under review now. The results are presented in Chapter 10. The data analysis was also performed by D. Nieto, S. Lombardi and F. Zandanel and the article was written with M.A. Sanchéz–Conde.

IV. **MAGIC mirrors on JINST.** Author list to be defined, *The Reflectors of the Imaging Atmospheric Cherenkov Telescopes MAGIC I and MAGIC II*, under completion at the moment of writing this thesis, to be submitted to Journal of Instru-

mentation.
This work presents in detail the design specification for the MAGIC I reflector, the initial choice of materials and studies for the aluminum mirrors of MAGIC I, the design and tests on MAGIC aluminum mirrors and the optical performance of the telescope. Different authors contributed directly to this paper, which reports the work of many collaborators inside MAGIC. I personally followed the section of MAGIC II mirrors. I will also be the corresponding author for the paper. The content of the paper was used for the introduction in Chapter 3, and extensively for the MAGIC II mirrors description, in Chapter 4.

Main Conference proceedings.

i) **Procs. of Scineghe conference.** M. Doro and others, *Indirect dark matter searches with the MAGIC telescope*, Prepared for the 5th Workshop on Science with the New Generation High Energy Gamma-ray Experiments (SciNe-GHE07): The Light of the Dark: Solving the Mysteries of the Universe, Frascati, Rome, Italy, 18-20 Jun 2007. The content of this proceeding is used in Chapter 6.

ii) **Procs. of the ICATPP conference.** M. Doro and E. Lorenz, *Technical Solutions for the MAGIC Telescope*, Procs. of 10th ICATPP Conference on Astroparticle, Particle, Space Physics, Detectors and Applications. Villa Olmo, Como, Italy, 8–12 October, 2007.
In this conference proceeding, the basic telescope design and performance was presented together with the principal "firsts", i.e. the technological innovations adopted by MAGIC. Most of the discussion in this proceeding is reported in Chapter 2.

iii) **Procs. of ICRC conference.** M. Doro and others *Indirect Dark Matter Search at Intermediate Mass Black Holes with the MAGIC Telescope*, Procs. of the 30th International Cosmic Ray Conference, Merída, Mexico, 2008, Vol. 4 (HE part 1), pages 721–724. The content of this proceeding is used in Chapter 8.

Other manuscripts

a) **MAGIC 3EG 1835 Internal Note.** M Doro, F. Zandanel, M. Gaug *Upper limits on the very high energy gamma–ray emission from 3EG J1835*, MAGIC Internal Note (unpublished), 2005.
In this note, we present the analysis of 3EG J1835, the brightest of the unidentified EGRET sources, chosen as candidate target as being intermediate mass black hole for MAGIC. The analysis was done with F. Zandanel and M. Gaug. The results of this study are used in Chapter 8.

b) **MAGIC Mirror Internal Note.** M Doro, *Studies on the mirror configuration of the MAGIC-II reflector*, MAGIC Internal Note MAGIC-TDAS 060704, 2006.
In this note, which is available for MAGIC members only, I studied with a ray–tracing method the mirror configuration on the MAGIC II reflector. For this work, I was helped by A. Moralejo and J. Zapatero. The results of this study are used in Chapter 3.

c) **Building blocks for CTA.** E. Lorenz, M. Doro, *Building Blocks for CTA: existing solutions and new designs. Mount and Mirrors. (to be included in CTA*

Letter of Intent), Available at http://www.cta-observatory.org/ctawpcwiki/ index.php/WP_MIR (password–protected), 2008.
This document presents some general design considerations for future telescopes for the CTA observatory. It also reports two specific design considerations for a small size telescope (5 m diameter) and a large size telescope (24 m diameter). The contents were mainly written by E. Lorenz.

d) **Mirror specification for CTA.** A. Foerster, M. Doro, *Technical Information for the Development of Mirror Prototypes for the CTA Observatory*, Available at http://www.cta-observatory.org/ctawpcwiki/ index.php/WP_MIR (password–protected), 2008.
This document is a comprehensive list of requisites in order to give the mirror developer a specific idea of the needs of CTA.

Acknowledgments

The installation of the entire reflector of MAGIC II has been a sound success. It was done very rapidly and in a very jovial situation. It constituted one of the happiest moment in my life. On the other hand, that was the final step of 4-year activities within the Padova group and the MAGIC collaboration. There had been moments of tension and moments of happiness. It was only through the determination and the collaboration of many colleagues that the mirrors were mounted in time! I take the opportunity here to remember those people.

For all the activities on MAGIC II mirrors, I am particularly grateful to Enrico Giro. We worked together for more than two years, in a beautiful mood, sharing efforts and happiness. He is one of the hardest workers I know, never tired, always happy. I owe him a lot! I would also like to thank D. Bastieri, F. Dazzi, M. Mariotti, D. Pascoli L. Peruzzo, T. Saggion and M. Rebeschini from the Padova group. Another person that contributed very much with suggestions and fruitful discussions is Eckart Lorenz. I have had the privilege to learn many things directly from him, about mirrors, about physics, and about experiments. His wiseness and his experience are like a lighthouse which leads from the distance.

And of course, how not to remember the "mirror installation crew" for those magic/MAGIC days at La Palma: M. Scarcioffolo (the "young"), M. Rebeschini (the "wise") from the Padova group, E. Giro (the "boss"), A. Frigo (the "climber"), L. Lessio (Gigi,"close the window"–man) and C. Gonzales (the "spaniard") from INAF, C. Schultz and H. Hellermann (the "GGs") from MPI, and last but definitely not least U. Horisberger and C. Haller (the "swiss clocks") from ETH.

Thanks to all of you!

Our hands at the MAGIC telescope. Courtesy H. Hostettler

For the dark matter studies, I am particularly grateful to G. Bertone, A. Biland, M. Persic, L. Pieri and M. Rissi for many discussions. I want to thank T. Bringmann and M. Fornasa for having accepted my proposal of writing an article together and for the nice time spent

together. I also want to thank D. Mazin for having reviewed the JCAP article. Not least, I think that in the last two years we have created a very nice dark matter working group in MAGIC. Working with S. Lombardi, D. Nieto, M.A. Sanchez–Conde and F.Zandanel has been a great pleasure for me.

Finally, I want to remember and thank Florian Goebel. Florian followed my activities since the very first time I went to MPI for tests on the prototype mirrors. We soon became friends. Every time we met, somewhere, it was fun to spend some time together. He also spoke fluent Italian and practiced all the time with me and the other Italians. He loved to speak foreign languages — I think this was his way to welcome a stranger. He was open–minded, we often discussed about travels and music.

About the work, he really followed me and my activities in the last two years before the installation of the mirrors. I owe him a lot. I was reporting the results to him, discussing the results, planning activities, asking help for organizations, shipments, etc. Whenever I had any doubt or needed suggestions or simply I needed to vent after some annoying facts, Florian was there to calm me down and give me some advice. I admit that particularly during the last year before installation, I worked hard just to help him to complete his duties (he was responsible for MAGIC II installation), to make him happy and to have finally his approval. He was a great person, worker and friend, and a bright example to me: he was one of the most tenacious men I had ever met and at the same time, he had pure and sincere passion in his heart, for physics and life in general.

Tenacity and passion. This is what you taught me. It is for you that MAGIC II is there, and the work we did together, will be always accompanying me. I love you Florian!

Florian yelling "Ehi guys! Go back to work!"

1

Gamma–ray astronomy and astrophysics

The earth atmosphere is constantly hit by energetic particles, collectively called cosmic–rays, with energies up to 10^{21} eV. While the cosmic–rays composition is known with precision, only hypothesis were proposed about their origin. Being charged, they are deflected by cosmic magnetic fields and arrive almost isotropically to the earth, losing the information on their place of production. On the other hand, gamma–rays are always produced where high energy cosmic–rays are accelerates. Gamma–rays travel undeflected and therefore are unique probes for cosmic–ray studies. In this chapter, we introduce the cosmic–ray paradigm. We describe the basic experimental results and the principal experimental detection techniques. Cosmic–rays are usually divided into galactic and extragalactic and thus gamma–rays. A description of the candidate emitters for these two classes is reported, together with the catalogs of gamma–ray known sources in the TeV domain. Gamma–ray astronomy is also suited for investigation of fundamental physics question. This is shortly discussed at the close of the chapter.

1.1 Cosmic–ray and gamma–rays

Astronomical observation started around four thousands years ago with the naked eye observation of luminous far distant objects that filled the dark night sky, practically only stars and planets. More and more detailed catalogs of luminous objects were compiled and for long time it was thought that the there was nothing else to look for in the sky. Only during the last century, was it discovered that the universe communicates with us in different ways than with the sole visible light. At the beginning of the century, the galactic plane was observed to emit radio–waves. Radio–waves have wavelengths ranging from meters to several kilometers and energies between 10^{-9} eV and 10^{-6} eV[1]. The radio emission is usually determined by inverse Compton and synchrotron emission from charged particles and particularly from free electrons at GeV[2] energies that are common in many astrophysical environments (see Appendix A). In the second half of the century, an unexpected emission at X–rays was seen in the galaxy by the team of Rossi [31]. The X–ray emission is usually associated to massive objects where the gravitational drag heats up the local ambient gas. As a result, synchrotron emission from energetic electrons (in the TeV regime) and possibly from Ultra High Energety (UHE) pro-

[1] $1\text{ eV} = 1,6 \times 10^{-19}\text{ J} = 1,6 \times 10^{-12}\text{ erg}$

[2] $1\text{ keV} = 10^3\text{ eV}, 1\text{ MeV} = 10^6\text{ eV}, 1\text{ GeV} = 10^9\text{ eV}, 1\text{ TeV} = 10^{12}\text{ eV}, 1\text{ PeV} = 10^{15}\text{ eV}, 1\text{ EeV} = 10^{18}\text{ eV}$

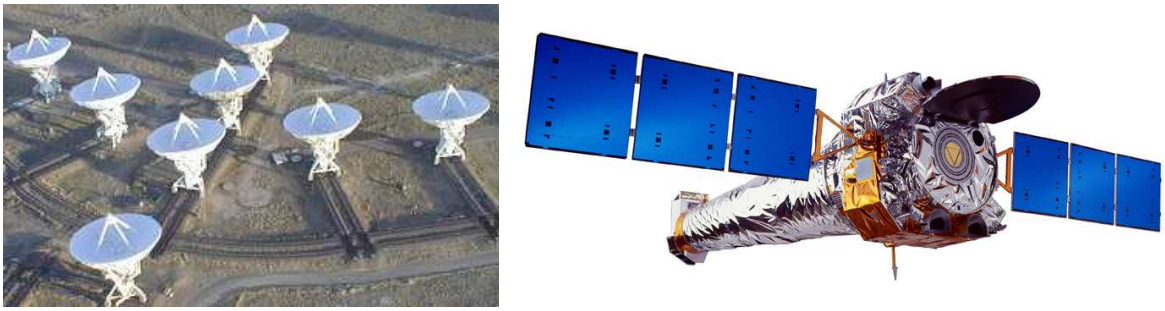

(a) The Very Large Array radio telescopes

(b) The Chandra X–ray satellite

Figure 1.1: (a) The Very Large Array (New Mexico) consists of 27 radio antennas. Each antenna is 25 m in diameter (http://www.vla.nrao.edu/). (b) The NASA Chandra X–ray observatory (http://chandra.harvard.edu/).

tons (beyond the PeV), produce X–rays. It is interesting to underline that this emission is often orders of magnitude more intense than the emission at other wavelengths, and therefore strongly determines the energy balance of the object. The typical energy range of X–rays is the keV–band. γ–rays above the MeV–band were observed even later. Calorimeters experiments mounted onboard satellites flying outside the earth atmosphere first measured MeV and GeV γ–rays in the 70's, with experiments like SAS-2 and COS-B. γ–rays were the last energy window left open in the electromagnetic spectrum. Their existence is connected to intense non–thermal emission from very violent and active regions.

Radio observations are performed at ground–based antennas (see Figure1.1(a)). The atmosphere is in fact transparent to such wavelengths. Large parabolas are operated in array mode and interferometric studies are applied to increase the angular resolution. X–ray astronomy is made at satellite. Nanometric precision cylindrical mirrors operated with grazing incidence and coupled to gratings are focused on spectrometers. A picture of a famous X–ray experiment is shown in Figure 1.1(b). Both techniques reached a mature stage already at the end of the last century, and catalogs with thousand of radio and X–ray emitters are available. The reason is related to the development of the technique of reflecting radio and X–ray photons, which is always accompanied by the capacity of collecting and amplifying signals. This is not the case for γ–rays. There is no physical mechanism to reflect γ–rays due to the nuclear interactions they manifest with matter. γ–rays can therefore only be observed *indirectly* and subsequently *reconstructed*.

The angular resolution for different experimental detection techniques varies by many orders of magnitude. Optical telescopes reach precisions of the order of the arcsec. The sub–arcsec precision can be reached with X–ray satellite experiments, while radio observation can have $\mu-$arcsec precision when operated interferometrically. Typical precision for γ–ray astronomy are instead of the order of 15 arcmin. To compare the different angular resolution, an image of the Crab Nebula (see below in the text) is shown in Figure 1.9(b). While in other wavelengths the source shows many features, it is almost observed as point–like in γ–rays (dashed circle). γ–ray astronomy cannot therefore resolve the morphology of the emission region to a great extent for most astrophysical objects.

Cosmic rays spectrum and composition

So far, we have discussed about electromagnetic emission. On the other hand, the earth is constantly hit by a high flux of particles, collectively defined as *cosmic–rays* (CRs). CRs

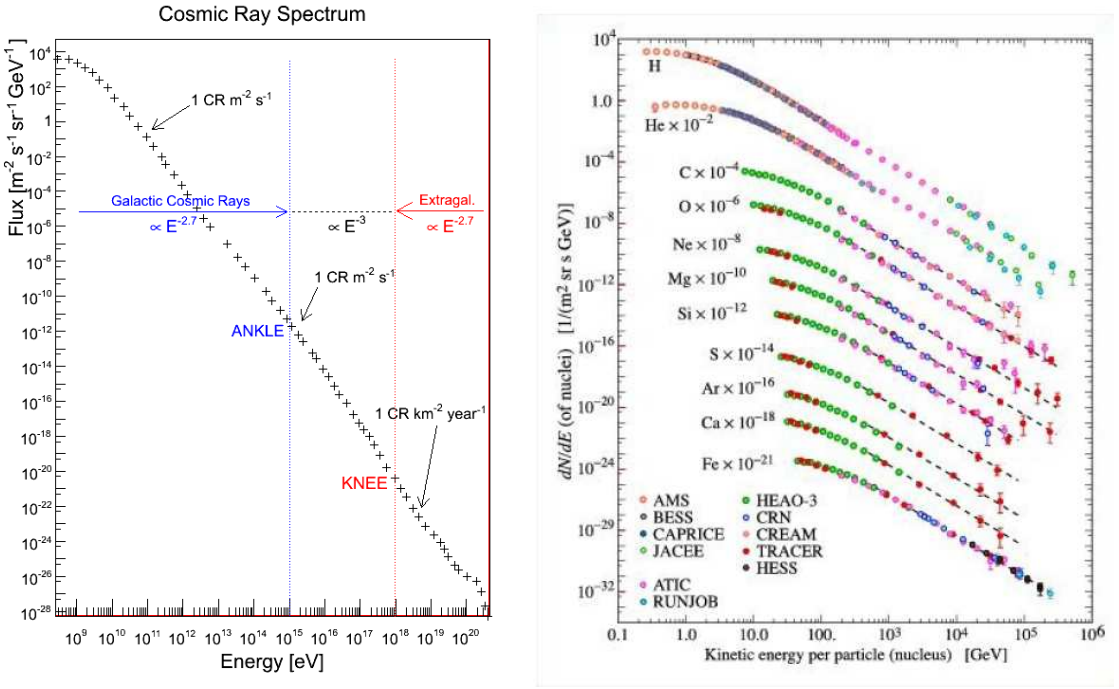

(a) Cosmic–ray spectrum

(b) Cosmic–ray composition

Figure 1.2: The differential energy spectrum and particle composition of cosmic–rays.

comprehend atoms and leptons, but they are mostly constituted by protons and helium, with smaller amount of heavier nuclei (see Figure 1.2b), electrons, and an unprecised amount of neutrinos. CRs are much more frequent than γ–rays, which represent only a tiny fraction of the incoming flux: very roughly 1 γ–ray is observed every 1000 CRs.

The CR spectrum is shown in Figure 1.2a. They cover an incredibly large range of energies, ranging from 10^9 to 10^{21} eV. Below 100 GeV the interaction with the Sun wind is efficient and they are absorbed. Furthermore, their flux covers more than 32 (!) orders of magnitude. While at 100 GeV, they are seen once per meter square per second, at 10^{16} eV they are seen only once per year and at 10^{20} eV only once per century. This immediately suggest that one single experimental technique cannot be sensitive in the entire CR spectrum. The differential energy spectrum can be fitted with a power–law $I(E) \sim E^{-\alpha}$. The spectral index is constant in subregions, separated by two special positions: the so–called *knee* at 10^{15} eV (1 PeV) where the spectral index changes from $\alpha = -2.7$ to around $\alpha = 3$, and the so–called *ankle* at 10^{18} eV (1 EeV), where the spectral slope hardens back to $\alpha = -2.7$. The change in slope is ascribed to a different origin: CRs below the knee are thought to be accelerated inside the galaxy, while beyond the ankle they should have an extragalactic provenance. The reasons will be discussed below.

The connection with gamma–rays

The emission of γ–rays is always associated to the presence of accelerated particles above the very–high–energy (VHE) regime, i.e. above the TeV. Among the basic mechanisms of production of γ–rays, reported and discussed separately in Appendix A, one can find:

a) synchrotron emission from TeV electrons or super–PeV protons in interaction with local strong magnetic fields,

b) inverse Compton scattering of GeV–TeV electrons on soft photon fields,

c) *bremsstrahlung* of electrons and protons intersecting a high dense region of plasma or gas,

d) electron–positron annihilation

e) decay of energetic neutral pions.

Normally, several of these mechanisms interplay to shape the γ–ray outflow from a given source. In addition, the presence of gas, plasma and radiation fields in the vicinity of the emitters can strongly shape the observed emission. A more detailed description of the acceleration mechanisms for each class of emitters will be presented. As in the case of CRs, γ–rays have typical astrophysical spectra with rapidly falling fluxes. Therefore, single experiments cannot be sensitive in the entire γ–ray energy range and realistically only around 2–3 orders of magnitudes can be covered by one observational technique.

CRs below 10^{18} eV show a large degree of isotropy as a result of scattering off interstellar and intergalactic magnetic fields, which they cross during their travel to the earth. This constituts a major disadvantage in the study of CRs, because one cannot trace back their provenance, and disentangle their emission features from the transport mechanisms. This is the reason why recently γ–rays has become one of the most promising scientific research fields: γ–rays are in fact perfect probe to study the sites of CR acceleration, because they travel undeflected and point directly back to their origin.

Open Questions

Despite the pretty high precision in the measurement CR fluxes and composition, there are several basic questions about CRs which are left open:

1. How are galactic and extragalactic CRs accelerated?
2. Does the acceleration involve mainly hadrons or leptons?
3. Where does this acceleration takes place?
4. What happens in the transport of CRs at extragalactic distances?
5. How the presence of such energetic particles determines the history and evolution of cosmic structures?

There are many theories that try to answer those questions, but none of them has been proved yet. An important recent result is the observation of a spatial correlation between Extremely High Energies (EHE, $> 10^{18}$ eV) CRs and active galactic nuclei [2], which will be discussed below. But below this energy, the origin of the main part of the CRs spectrum is still unveiled.

1.1.1 Galactic cosmic–rays and gamma–rays

Up to the knee and possibly in the region between the knee and the ankle of the CR spectrum of Figure 1.2a, CRs are thought to be accelerated within the Milky Way (MW) disk. There are several reasons supporting this assumption: first, there is a known mechanism that can guarantee energies up to the knee, namely the *diffusive shock acceleration* (DSA) [30], based on the Fermi mechanism of shock acceleration (see Appendix A); second, galactic CRs (GCRs)

at energies larger than the ankle would not be as isotropic as observed, given the galactic magnetic fields strength. The magnetic field also determines the escape time of GCRs in $\sim 10^7$ years (for the calculation, see [35]). This means that the observed GCRs spectrum is composed by accumulated events over this period. A third evidence is that all expected acceleration mechanisms provide harder spectra than those observed, while this could also be explained by interaction with ambient gas [4].

The GCRs are formed by mainly electrons, protons and light nuclei, while the observed antiprotons and positrons are secondary particles, i.e. originated in secondary processes like spallation of primary GCRs with ambient gas and plasma. The observation of secondary particles is a clear evidence of GCRs transport over large scales. The radiation is sometimes so energetic that its contribution is comparable to that of the galactic magnetic fields, meaning that GCRs are playing/have played an important role in intragalactic dynamics and possibly star chemistry. Besides that, there is no substantial body of evidence on which are the acceleration mechanisms and where GCRs are accelerated. It is commonly believed that it comes from the superposition of many contributions from different emitters, but the local GCRs spectrum could even be fitted with the sum of a contribution of one local source at 100 pc and a diffuse galactic emission [6]. The best candidates for being sources of GCRs are the supernova events, which will be discussed below. The DSA mechanism predicts that the *acceleration efficiency* (the fraction of mechanical energy released at the supernova explosion and transferred to non–thermal particles) can be as high as 10% or more. Given the rate of supernova explosion in the MW (around 1/year), this alone can guarantee the GCRs budget observed at ground. However, DSA can explain CRs energies up to 10^{14} eV and only hardly up to the ankle. Only recently, Bell and Lucek [26] discovered a way to fulfill this gap through a mechanism of magnetic field amplification. A confirmation of DSA from observation of GCRs is complex because their isotropic origin makes it difficult to disentangle emission processes from transport.

γ–ray astronomy is particularly suited for galactic studies: from one hand they trace back the emission, on the other hand, their signal carries information on the composition of the interstellar medium that separates the emission region and the earth. For this reason, γ–rays should not only be searched for directly in the source, but also be investigated in the proximity of the individual emitters, in order to disentangle interactions with external ambient fields besides internal processes. They constitute a unique way of understanding if the observed GCRs density is only local or homogeneous in the entire disk.

1.1.2 Extragalactic cosmic–rays and gamma–rays

The CR spectrum extends above 10^{20} eV[3]. It is still unclear which are the details of the mechanisms that can accelerate particles to such large energies. Normally, either either extremely powerful direct acceleration or prolonged acceleration times are required. The acceleration must also compete with the natural radiative processes which particles are subject to. The proposed mechanisms are: a) direct particle acceleration at jets of active galactic nuclei, b) secondary acceleration of particles at termination shock of expanding materials, c) ultrarelativistic jets heating up dense plasma regions, d) interaction with ultra–strong magnetic fields. When discussing the targets of observation, we will go more into detail of these mechanisms.

The solution of the problem of CR acceleration is basically connected to the capacity of discriminating between direct acceleration, secondary acceleration and transport of such particles, i.e. understanding both the morphology of the target region and of the intergalactic region crossed by CRs. We observed that γ–rays provide a unique insight.

[3]This is the kinetic energy of a tennis ball flying at 100 km/h!

In particular, the ground–based γ–ray has the advantage to be sensitive in the TeV region, where the emission mechanism shows distinctive features for example between hadronic and leptonic emission. Current instruments provided already several results, but none capable of a striking identification of the acceleration mechanism. A final answer will be given possibly only by future experiments with increased sensitivity and increased angular resolution that will perform morphological studies. In addition, increased sensitivity and energy resolution will allow for more significant observation of spectral features.

1.2 Experimental techniques

Gamma–astronomy is the last open window on the exploration of the electromagnetic emission of the universe. However, the window is wide: the low–energy limits can be placed around the mass of the electron ($\simeq 0.5 \times 10^6$ eV), where the nuclear and electron–positron annihilation lines start to be observable. The high–energy limit is based on the observation of CRs beyond 10^{20} eV, but potentially there can be no upper limit. Sub–bands must be defined to handle the discipline of γ–ray astronomy, only marginally corresponding to different acceleration mechanisms and observable with different detectors. A possible classification is shown in Table 1.1.

	Range	Type	Detection mec.	Experiments
LE	< 30 MeV	Balloon	Compton Effect	
HE	30 MeV–30 GeV	Satellite	Calorimeter	EGRET, Fermi
VHE	100 GeV–30 TeV	Ground	Atm.–Cherenkov	Whipple, HEGRA (past)
				MAGIC, HESS, Veritas
UHE	30 TeV–30 PeV	Ground	Water–Cherenkov	Milagro
EHE	> 30 PeV	Ground	Atm. Fluorescence	Hires, Auger

Table 1.1: Classification of γ–ray astronomy. The energy range, the main type of detector and the principal physical detection mechanism are reported, together with the principal experiments.

Some of these experimental techniques will be discussed in § 1.2.2, with particular attention on the IACT technique. On the other hand, the research activity on CRs is also quite advances, with several detectors spread all over the world. Sometimes, detectors for CRs are also senstitive to EHE CRs.

1.2.1 Particles detector experiments.

Fluorescence experiments.

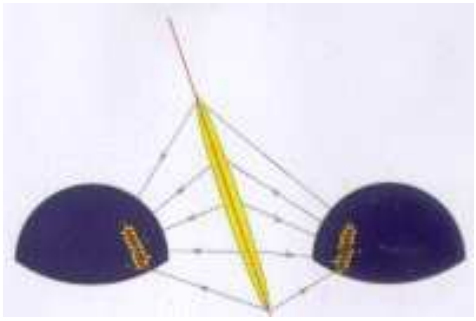

In cases of UHE and EHE primary CRs or possibly γ–rays, the charged component of the shower can cross a large fraction of the atmosphere. At their passage, charged particles can ionize and excite the atmospheric molecules (mainly nitrogen and oxygen), which in turn deexcite in fluorescence light. This light is concentrated in the UV and optical band and can be produced over a track of many kilometers in length. By focusing the light with the use of several small reflectors displaced at a certain distance one another, and measuring the intensity and the time separation, one is able to reconstruct the energy of

the primary CR energy and its direction. The telescopes must be located at a few Kilometers of distance and operated simultaneously. Usually they are located at very high altitudes where the absorption is less pronounced.

An example of this experiment is the HiRes detector, located in the Utah desert, composed of two groups of telescopes at 12.6 km distance (http://hires.physics.utah.edu/). HiRes has made the first statistically significant observation of the Griessen–Zatsepin–Kuzmin suppression (GZK)[4]. The break energy was measured at 5.6×10^{19} eV, with a significance of 5.3σ. No spatial association with any target was found [27].

Direct particle detection experiments

Particle detector experiments directly detect the charged component of the atmospheric shower by measuring the arrival time of the shower front at several water tanks distributed over a large area. The direction of the primary CR can be calculated to about one degree accuracy.

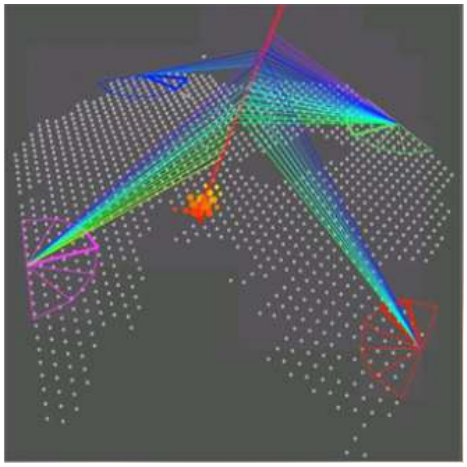

Figure 1.3: The detection technique of Auger. Four detectors measure the fluorescence and at the same time several tanks are directly hit by CRs.

A well–famous representative of this technique is the Auger experiment (http://www.auger.org/). Auger is composed of 1600 water tanks distributed over $3,000$ km^2 in Argentina and also hosts 4 detectors for atmospheric fluorescence detection. It is the biggest of all direct particle detection experiments. Recently, the Auger experiment has become known for its detection of EHE CRs spatially associated with active galactic nuclei [2]. Active galactic nuclei are believed to the place where most of the extragalactic CRs are accelerated. They will be discussed below. This fact is of utmost importance because it is the first experimental evidence that acceleration of CRs is not isotropic but associated to some emitters and that the active galactic nuclei are effectively accelerators of particles. Auger also measured with higher precision than preceding experiments the GZK effect [3].

1.2.2 Gamma–ray experiments

HE domain. Satellite–borne experiments

Satellite and balloon borne detector consists of a standard calorimeter adapted for the HE band with a segmented tracking system. The detection mechanism is pair production in the tracker and consequent γ–ray production into a calorimeter. The energetic range is basically defined by the width of the calorimeter and the telescope area, because γ–ray at high energies have both small fluxes and cannot be contained by a too short detector. A famous representative experiment based on this technique was the EGRET experiment, onboard the CGRO satellite, which operated until the year 2000. The recently launched Fermi–LAT satellite, marking the footsteps of EGRET, is expected to provide new insight on the HE γ–ray astronomy over the next few years. These detectors are characterized by very large field

[4]In 1966, Griessen, Zatsepin and Kuzmin predicted that EHE protons dominating the extragalactic CR flux would interact with the photons in the cosmic microwave background (CMB). Given the CMB temperature, they estimated the GZK–threshold at 6×10^{19} eV and above this value a suppression in the CR flux. This effect would limit the observation of EHE CR source to a distance smaller than 50 Mpc.

of view (Fermi covers the entire sky in 3 hours) but quite small angular resolution (depending on the energy, but of the order of 1 deg). Due to the rapidly falling flux of γ–rays, they are only marginally sensitivite above few tens of GeV for point–like emissions, while the diffuse emission, that can be integrated for thousand of minutes, can be observed up to few hundreds of GeV (in the case of Fermi).

UHE domain. Water Cherenkov experiments.

The Water Cherenkov experiments take advantage of the Cherenkov light produced by atmospheric shower's electrons and positrons in clear water. The water tanks must be located at high altitude to observe a large fraction of atmospheric products which are rapidly absorbed. The tanks are surveyed with several photomultipliers which collect the light signal. A water Cherenkov experiment is usually composed of several tanks distributed over a large area. The field of view is therefore very large, and cover almost the complete above sky, while the angular resolution is rather small.

A representative of this technique is the Milagro experiment (www.lanl.gov/milagro/), situated in the Jemez Mountains near Los Alamos, New Mexico, which operated until the year 2008. Milagro measured the γ–rays at average energies of 15 TeV. Recently, an anisotropy was found in their data, revealing the existence of hot spots [1], on angular scales of around 10° of unknown origin. One of the regions has a different energy spectrum to that of the isotropic γ–ray flux and it is consistent with harder spectrum protons. The nature of the hot–spots is still to be unveiled but is currently not confirmed by VHE IACT data.

There is a proposed follow up experiment called the High Altitude Water Cherenkov Experiment (HAWC) to be located at the Sierra Negra volcano, Mexico. HAWC should be 15 times more sensitive than Milagro (http://hawc.umd.edu/).

VHE domain. Ground–based atmospheric Cherenkov technique

Ground–based imaging atmospheric γ–ray astronomy is concerned with γ–rays of energies from around 100 GeV up to several TeV. The atmosphere is not transparent to γ–rays, which interact with atmospheric atoms and develop a shower of particles which grows for few radiation lengths, before being completely absorbed. The theory of atmospheric showers is reported separately in appendix B. For the sake of the following discussion, it is only to mention that atmospheric showers initiated by γ–rays are mostly constituted by electrons and positrons which travel at velocities larger than the velocity of light c/n and therefore also emit Cherenkov radiation. While these charged particles, are usually completely absorbed in the atmosphere and do not reach the ground, Cherenkov photons can propagate. There is only some absorption in the UV band, but most of the light can reach the ground. The scheme of the Cherenkov emission and its detection is shown in Figure 1.4.

There one can see that the light is emitted at around 10 km altitude. If a telescope is located inside the Cherenkov light pool, the photons are reflected onto the focal plane and in a shape which resembles an ellipse. The ellipse contains information about the primary γ–ray that initiated the shower: the ellipse size is related to the the γ–ray energy and its position in the camera is related to the shower direction. The technique of observation is called imaging because of the study of the image of the shower at the focal plane. This is a powerful tool. For example, shower initiated by CRs also produced Cherenkov photons which reach the ground and are reflected in the focal plane. But the images of such showers is rather different compared to pure γ–ray showers and this background can be suppressed up to 99% or more just on the basis of image reconstruction.

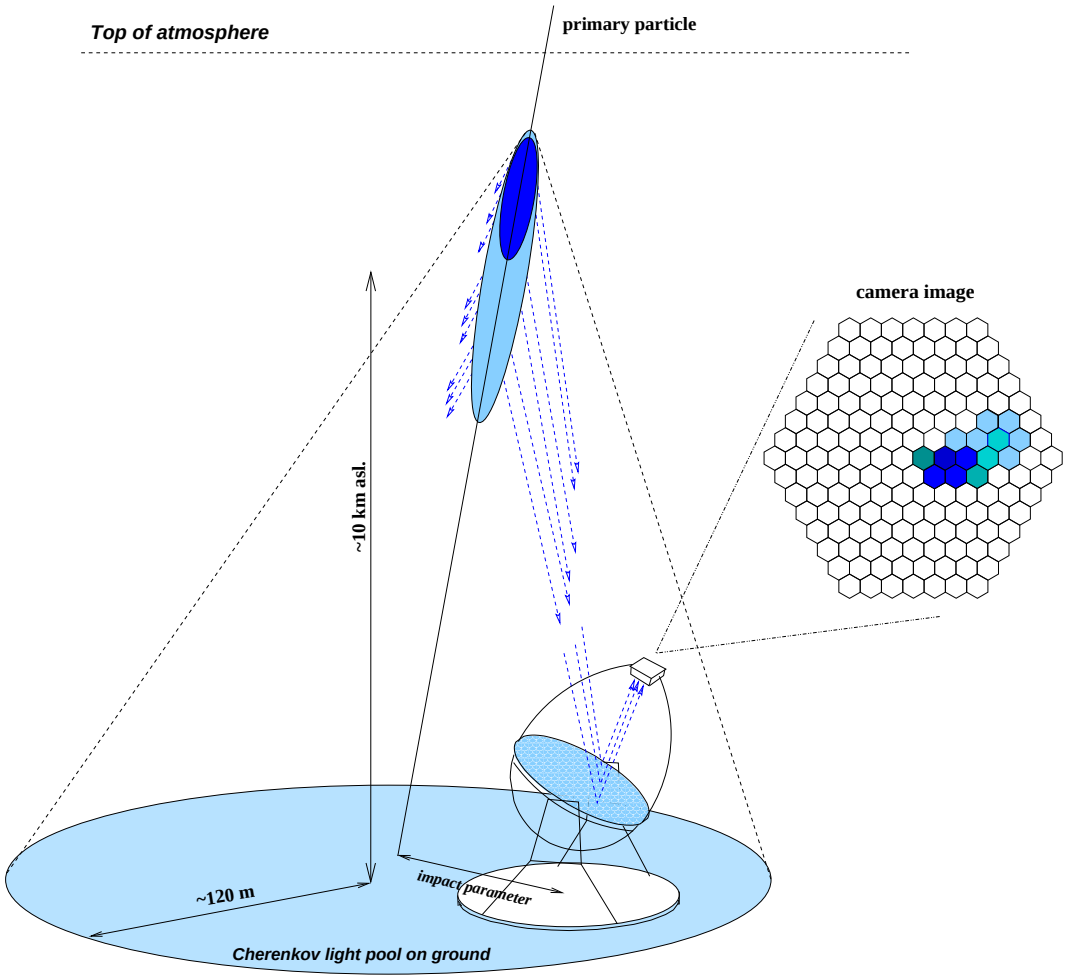

Figure 1.4: Schematics of the IACT detection of atmospheric showers. When the primary particle interact in the top atmosphere, a particle showers is formed, characterized by a tail (dark blue) and an head (light blue). From the showers, the Cherenkov photons (blue lines) propagate to the ground at increasing angle with increasing shower development. The photons are reflected into the focal plane at a distance from the center of the camera which reflects the shower's impact parameter, i.e. the distance from the telescope axis. The camera is pixelized and the image can be reconstructed. Courtesy of M. López [38].

The image in the camera like in Figure 1.4 is studied by a set of parameters which were first defined by Hillas [32] and shown in Figure 1.5. They represent the basis on which the shower reconstruction is performed. The main Hillas parameters are:

size	The sum of the number of photons in the image.
alpha	The angle between the major ellipse axis and a line going from the center of the ellipse to the center of the camera.
dist	The distance from the center of the ellipse to the camera center.
length	The major semi-axis of the ellipse
width	The minor semi-axis of the ellipse

The IACT technique is characterized by an overwhelming amount of background, which must be carefully treated to extract statistically significant signals. There are two types of

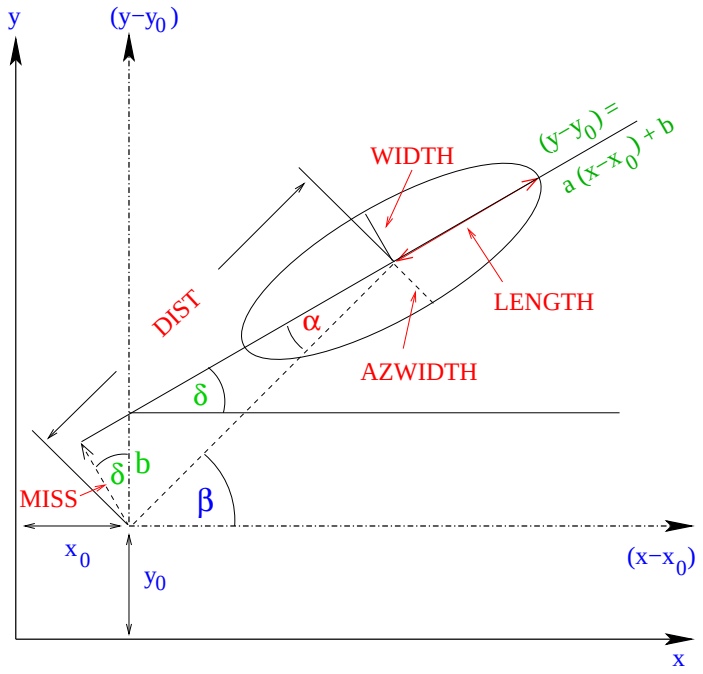

Figure 1.5: The characterization of the camera image based on the Hillas parameters [32].

background, a first one, of cosmic origin, constituted by primary CRs or secondary particles in the atmosphere that can mimic the signal of γ–rays, and a second one, connected to the telescope functioning and its location.

The principal contribution to the background comes from:

i) *Hadronic Shower* When a CR hit the top atmosphere, among other particle, neutral pions are produced. They immediately decay into a pair of γ–rays ($\pi_0 \rightarrow \gamma\gamma$) which trigger a secondary electromagnetic shower. Those sub–electromagnetic showers constitute the more frequent background. About 1000 hadronic showers are found every γ–ray shower. They are mainly rejected by an image analysis based on the Hillas parameters, because their image is quite irregular compared to pure γ–ray showers. The so–called gamma/hadron separation efficiency can be larger than 99%. However, the hadronic background cannot be completely removed.

ii) *Electron initiated Showers* Cosmic electrons or secondary electrons in the atmosphere also initiate electromagnetic showers. This background is even more subtle compared to hadronic background because an electron–initiated shower is pretty indistinguishable from a pure γ–ray one. Fortunately, the electron flux is smaller than γ–ray, at least for energies larger than 100 GeV. The only way to estimate them is via Monte Carlo simulation.

iii) *Muonic Component* The muons produced in hadronic showers are extremely penetrating and can easily reach the ground. They directly produce Cherenkov light at moderate altitude which can mimic that of low–energy electromagnetic shower. Muons are almost completely rejected with the use of stereoscopic observation and partly by image analysis.

There are other sources of background of different origin:

- *Electronic Noise* All the devices and the readout chain have an intrinsic electronic noise that could not be eliminated. The photon sensors in the focal plane instrumentation produce the so–called *dark noise* which is the output current when the device is not illuminated. Dark noise has continuous and pulsed components which can vary in time. Other sources of noise are the Vertical Cavity Surface Emitting Lasers (VCSELs) which convert the currents into a light signal, the receiver circuit and the FADCs. The continuous component is eliminated by an AC coupling of the signal but the pulsed one can be confused with the signal. These background are treated with the use of special data runs, called *pedestal runs*. is a run of data
- *Environmental noise* Has several contributions: *a) Night Sky Background Light* (NSB). All possible sources of diffuse light of the night sky contribute to this term. During normal observation there are stars in the field of view of the telescope which can illuminate one or few pixels, thus producing a higher pedestal RMS in the corresponding pixel which affects the pixel signal to noise ratio. *b) Light pollution* Light coming from town or human activity can be reflected by clouds or snow and increase the average illumination of the camera

1.3 Milestones in cosmic–ray and gamma–ray astronomy

The history of CRs and γ–rays can be traced back to a few relevant events.

1912 **Discovery of cosmic rays.** In a balloon–borne experiment, V. Hess discovered an ionizing radiation that increases with altitude, and therefore "enters the atmosphere from above".

1932 **Definition of cosmic rays.** Millikan and Compton coined the term "cosmic–rays" to define the unknown radiation.
Air showers. Rossi and Auger discovered through coincidence measurements the existence of extensive air showers in the atmosphere after collision of energetic primary cosmic–rays.

1949 **Fermi mechanisms.** Fermi proposed the mechanism that takes his name to explain the acceleration of high energy cosmic–rays in shocks.

1950's **First accelerators.** With the construction of the first accelerators, cosmic ray physics and high energy particle physics start to decouple, and former physicists focus on astrophysical questions.

1958 **Gamma–ray astronomy.** For the first time the term "gamma–ray astronomy" was used by Morrison, who first pointed out how γ–rays were the only carriers and that at the same time were carrying information of nuclear or high–energy processes (unlike optical photons) and were relatable to the emission source because undeflected (unlike CRs). This seminal and simple idea had important consequences in changing astronomers' minds on the importance of γ–ray–astronomy.

1960's **First atmospheric Cherenkov telescope.** The Crimean group of the Levedev institute developed the first atmospheric Cherenkov detector. They did not detect any signal but laid the basis of the technique.

1962 **First detection of astrophysical X–ray source.** Discover of Sco X–1, the first extra–solar source of X–rays [31]

1965 **First HE γ–rays** The first evidence of cosmic γ–rays came from the Explorer XI telescope which detected a small signal above the Earth's atmosphere.

1972 **SAS-2** The short–lived SAS-2 spark–chamber satellite–borne detector, in only 6 months of operation, detected the diffuse galactic γ–ray emission and mapped the galactic disk.

1970's **COS-B** The European COS-B gave a solid basis for HE γ–ray astronomy by mapping the diffuse γ–ray emission for 6 years.

1989 **Crab Nebula** The Whipple IACT detects a signal from the PWN Crab Nebula. This is the first time a γ–ray signal is observed from a very source. These events opened the γ–ray astronomy era.

1998 **Neutrino oscillations.** SuperKamiokande detected the first convincing evidence for neutrino oscillations

1999 **HE γ–ray catalog.** The EGRET experiment published a catalog of 270 sources, out of which more than a hundred were unidentified.

2008 **Origin of cosmic–rays.** The Auger detector found a correlations between EHE cosmic–rays and AGN.

1.4 Galactic Objects

In the following two sections, an attempt to describe the galactic and extragalactic population of VHE γ–ray emitters is reported. To compile the catalogs of objects and to complete the physics framework, mainly the following reviews were consulted [4, 33, 5, 28, 35, 43]. A precise catalog of VHE γ–ray emitters cannot be drafted yet: some targets are not associated to any known objects, some have multiple associations at other wavelengths, for some the nature is still unknown, and finally new sources are constantly being added.

The galactic plane of our Milky Way (MW), and in particular the galactic center (GC) are very crowded regions where many astrophysical emitters are spatially close, and embedded into a dense region of gas and radiation that strongly shape the emission of radiation and determine its transport. As far as the γ–ray galactic sky is concerned, a significant improvement came after HESS performed a scan of the region around the GC [9], which led to the discovery of several point–like objects — many of them still unidentified — and a diffuse galactic γ–ray emission, the comprehension of which is still one of the main goals of γ–ray astronomy. Figure 1.6 report the HESS scan together with a simulation of the same sky as possibly observed by future IACT experiments. In Tables 1.3 and 1.4 the up–to–date list of galactic sources is reported.

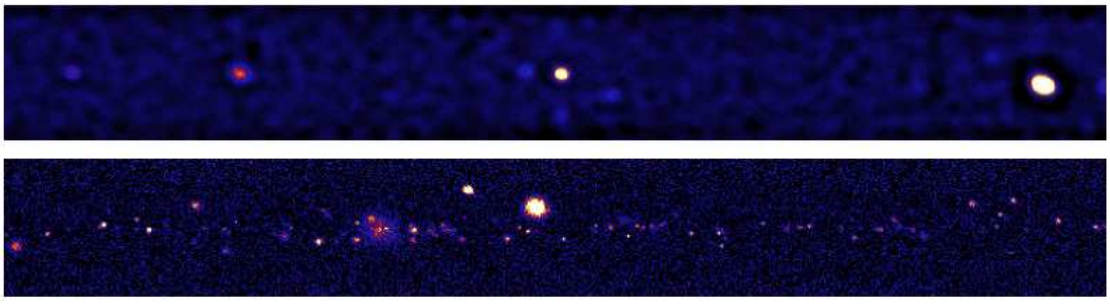

Figure 1.6: (*Top*) A sky map of the galactic plane scan from HESS [9]. Several point–like sources are observed on top of an extended diffuse γ–ray emission. (*Bottom*) A simulation on the possible outcome of a galactic scan with future IACTs. Figure from Ref. [28]

TeV–name	Common names	Ra (hh mm)	Dec (dd mm)	Type	Dist. (kpc)	Flux (^{a})	Γ (^{b})
TeV0852-463	RX 0852-4622	08 52	–46 20	Shell	10.2	21	2.1
TeV1442-625	RCW86	14 42	–62 29	Shell	1	2.7	2.5
TeV1714-398	RX 1713.7-3946	17 13	–39 45	Shell	1	17-19	-
TeV1714-382	CTB37B	17 14	+38 12	SNR	10.2	-	-
TeV1714-385	CTB37A	17 14	+38 12	SNR	10.3	-	-
TeV1802-233	W28	18 00	–24 00	Shell	2	1.9	2.5
TeV2323+588	Cassiopeia A	23 23	+58 49	SNR	3.4	0.7	2.5
TeV0616+225	IC443,m0616+225	06 16	+22 31	SNR/PWN	1.5	0.6	3.1
TeV1747-282	G0.9+0.1	17 47	–28 09	SNR/PWN	8.5	0.8	2.4
TeV1833-105	G21.5-0.9	18 33	–10 33	SNR/PWN	4	0.5	2.1
TeV1846-027	Kes 75	18 46	–02 59	SNR/PWN	6–19	0.6	2.3
TeV0535+220	Crab Nebula,M1	05 35	+22 01	PWN	2	22–37	2.4– 2.8
TeV0835-463	Vela X	08 35	–45 34	PWN	0.29	9	1.5–3.4
TeV1418-610	Kookab.Rabbit,G313.3+0.1	14 18	–60 58	PWN	5.6	2.6	2.2
TeV1420-607	Kookab.Pulsar,P1420-6048	14 20	–60 45	PWN	0.27	3.5	2.2
TeV1514-592	MSH	15 14	–59 09	PWN	5.21	5.7	2.3
TeV1641-465	G338.3-0.0	16 40	–46 31	PWN	8.6	3.0	2.4
TeV1718-385	h1718-385	17 18	–38 33	PWN	4.2	0.3	0.7
TeV1811-193	PSR 1809-1917	18 10	–19 18	PWN	3.7	4.6	2.2
TeV1826-138	PSR 1826-1334	18 26	–13 44	PWN	3.9	20	2.4
TeV1913+102	PSR 1913+1011	19 12	+10 10	PWN	4.6	-	-
	P1259-63	13 02	+63 49	PUL	-	1.3	2.7
	Crab Pulsar	05 31	+21 58	PUL	2	-	-
	LSI+61 303	02 40	+61 15	XRB	2	2.7	2.6
	LS 5039	18 26	–14 49	XRB	3.1	1.9	2.1
	Cygnus X-1	19 58	+35 12	XRB	2.2	2.3	3.2
	Westerlund2	10 23	+57 45	OC	7.9	4.5	2.5

Table 1.3: Tentative catalog of identified galactic objects. (^{a}) The flux given in units of 10^{-12} photons cm^{-1} s^{-1} TeV^{-1} at 1 TeV, (^{b}) The spectral index of a power–law $E^{-\Gamma}$ fit of the γ–ray spectrum. − Not found.

Galactic objects are of basic interest in γ–ray astronomy for several reasons:

- Due to their vicinity, they are often observed as extended objects in a vast range of wavelengths, and thus provide a unique opportunity to carry out studies on the morphology of the emission region

- Due to their vicinity, the γ–ray emission does not suffer from absorption of cosmological background light, as the cosmic microwave background or the infrared diffuse light. On the other hand, they could be absorbed locally in the vicinity of the emission region and thus give a clear indication on the distribution of matter and gas around the source

- They are the prime candidates for being accelerators of cosmic rays. For example, the supernovae alone could explain all the cosmic ray density detected on Earth.

A basic distinction between emission from extended regions and from point–like sources is hereafter applied. Acceleration mechanisms are usually different for the two classes and the acceleration in extended regions is normally shaped by the local environmental conditions around the emitting region, i.e. presence of globular clusters. Emission from compact objects is normally associated to jet emission and relativistic outflows.

Type	Associations	Ra (hh mm)	Dec (dd mm)	Flux (^{a})	Γ (^{b})
SNR?	G40.5-0.5/MGRO1908+06/HESS1908+063	19 08	+06 30	8.8	2.3
	HESS1640–465	16 40	–46 31	3.0	2.4
PWN?	P1617-5055/HESS1616-508	16 16	-50 53	6.7	2.4
	G75.2+0.1/MGRO2019+37	20 19	+37 00	8.7	2.3
UID	Monoceros/E0634–0521/HESS0632+058	06 33	+05 21	0.9	2.5
	HESS1303–631	13 03	–63 11	4.3	2.4
	HESS1427–608	14 28	–60 51	1.3	2.2
	HESS1614–518	16 41	–51 49	8.1	2.5
	HESS1626–490	16 26	–49 05	4.9	2.2
	I16320–4751?/HESS1632–478	16 32	–47 49	5.3	2.1
	I16358–4726?/G337.2+0.1?/HESS1634–472	16 34	–47 16	2.0	2.4
	P1702–4128?/HESS1702–420	17 02	–42 04	9.1	2.1
	HESS1708–410	17 08	–41 04	2.7	2.5
	HESS1731–347	16 32	–34 43	6.1	2.3
	HESS1745–290	17 45	–29 00	2.5	2.2
	E1744–3011/HESS1745–303	17 45	–30 22	2.5	1.8
	G8.7–0.1/P1803–2137?/HESS1804–216	18 04	–21 42	5.7	2.7
	G23.3–0.3/W41?/HESS1834–087	18 34	–08 45	2.6	2.5
	G25.5+0.0/HESS1837–069	18 37	–06 56	5.0	2.3
	HESS1841–055	18 41	–05 33	12.8	2.4
	HESS1857+026	18 57	+02 40	6.1	2.4
	HESS1858+020	18 58	+02 05	0.6	2.2
	Cyg OB2?/TeV2032+4130/MGRO2031+41	20 32	+41 30	0.6	1.9

Table 1.4: Catalog of unknown galactic VHE γ–ray emitters. (^{a}) The flux given in units of 10^{-12} photons cm^{-2} s^{-1} TeV^{-1} at 1 TeV, (^{b}) The spectral index of a power–law $E^{-\Gamma}$ fit of the γ–ray spectrum.

1.4.1 Galactic emission from extended regions

Supernova Remnants

At the end of fusion processes in stars with masses larger than 5–8 $M_\odot$, dramatic collapse events occur. After having burnt the lighter elements, the massive star shows a degenerate iron core. There is no further nuclear process that can release energy and the iron is destroyed by photo–disintegration into neutrons and helium: $\gamma + {}^{56}\mathrm{Fe} \rightarrow {}^{4}\mathrm{He} + \mathrm{n}$. This process takes away also thermal energy and weakens the internal pressure support. The star starts to collapse. Free electrons combine with protons in inverse beta–decays: $e^- + p \rightarrow n + \nu_e$, until all the matter from the star is converted into neutrons. The collapse continues until the core density reaches the nuclear density. No further compression is possible and all the infalling material is bounced back outwards. According to the primary star mass, the neutron protostar becomes a spinning neutron star (pulsar) or collapses into a black hole. The other half of the mass is ejected outwards and starts to form a propagating nebula called a Super Nova Remnant (SNR). About 99% of the initial gravitational energy is released into neutrinos, 1% into kinetic energy of the remnants particles and only 0.01% of the energy goes into radiation.

The supernova event prompts a brief burst of radiation that may temporarily outshine the entire host galaxy, before fading out over several weeks or months. During this interval, a supernova can radiate as much energy as the Sun would emit over 10 billion years. This argument was historically taken to explain the origin of GCRs. The reasons are the following: using the local cosmic ray density $\rho_{CR} \sim 1$ eV cm^{-3} and the volume of the galactic disk $V_D = \pi d^2 h \sim 4 \times 10^{66}$ cm^3 (where $d = 15$ kpc is the disk radius and $h = 200$ pc is the dish thickness), and taking into account that the escape time for galactic cosmic rays is $t_{esc} \sim 6 \times 10^6$ years,

one can calculate the GCRs luminosity: $L_{CR} = V_D \rho_{CR}/t_{esc} = 5 \times 10^{40}$ erg/s. Considering now that 10 $M_\odot$ are ejected at a supernova event with $\beta = 10^{-2}$ and that the supernova rate is one every 30 years in the MW, the result is an output energy of $\sim 10^{42}$ erg/s. Thus, even an efficiency of 0.01% could account for the entire energy budget of GCRs. A second reason for believing that SNRs explain the GCR budget is that there is a very convincing theory on particle accelerations (the already mentioned diffusive shock acceleration mechanism) which can describe accelerations up to the knee of the CR spectrum, combined with a large reservoir of particles to be accelerated.

One of the best ways to study the acceleration mechanisms is to look at secondary photons accompanied to the accelerated CRs. While the evidence for acceleration of GeV–TeV electrons is compelling, many theories allow for the possibility of acceleration of protons. GeV electrons emit radio–waves through synchrotron emission, while X–ray photons are produced by TeV electrons. A hadronic acceleration is seen in γ–rays mainly through decays of neutral pions, but the resulting γ–ray spectra and fluxes are similar to predictions for leptonic acceleration, at least in a wide range of energies, so that the discrimination is normally complicated. A discrimination between leptonic and hadronic acceleration from SNR could be based on some experimental evidence:

i) The decay of pions is always accompanied by a the production of neutrinos. A potential detection of neutrinos associated with SNRs would determine a smoking gun signature of hadronic acceleration,

ii) The presence of electrons in propagating shocks can be observed through non–thermal radiation in the X–ray band and at the same time in the VHE regime because of the self Compton scattering. Combining data in the two bands can constrain electron density, maximum electron energy and local magnetic field strength at the shocks,

iii) In case of hadronic accelerations at the shocks of SNRs, the γ–ray spectrum is less approximated by a pure power–law than in the case of leptonic acceleration, and the effect is maximum in the 50–100 TeV domain.

iv) Normally, the energy flux in γ–rays should exceed that in X–rays in case of hadronic acceleration.

Compelling evidence for acceleration of GeV– and TeV–electrons has been found for SN 1006 [41], where radio and X–rays are observed from a spherical region around the target with $\sim$ 20 pc radius. Due to the strong absorption of electrons, they cannot be transported over large distances and consequently the synchrotron radiation can only be found locally. Electrons in SN 1006 must be accelerated up to 100 TeV. Important evidence for the correlation between TeV γ–rays and X–rays come from two SNRs: RX J1713.7-3946 and RX J0852.0-4622. Both show a correlation down to $\sim 0.1^\circ$ which suggest a common origin for their photons. While this evidence seems to favor the leptonic acceleration, hadronic acceleration has still not been ruled out. The reasons depend very much on the local presence of gas densities and magnetic field which can boost or suppress one of the two contributions.

There are 7 sources firmly associated to SNRs and additional 4 whose association is still under debate (see Table 1.3). RX J1713.7-3946 is the prototype of supernova remnant because of its interesting morphology. It was observed by HESS in 2004 [14]. The spectrum and skymaps of the source are shown in Figure 1.7.

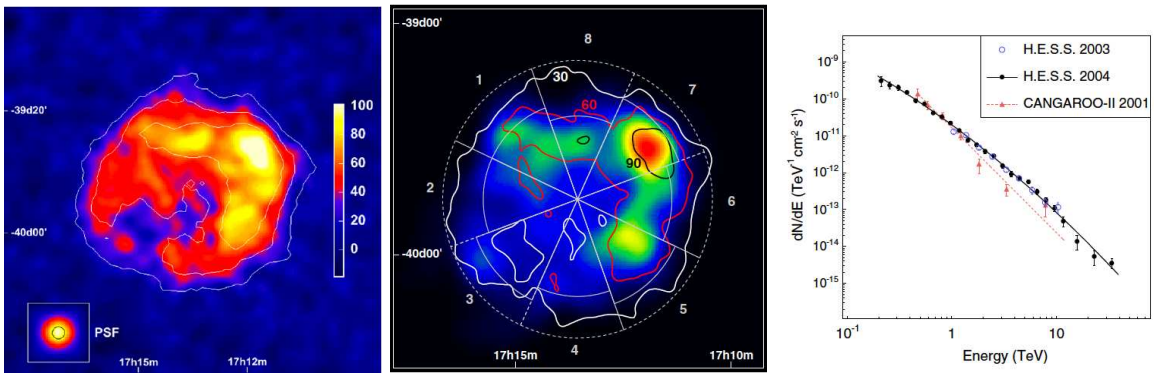

Figure 1.7: (*left*) Skymap of the γ–ray emission from RXJ1713 as seen by HESS [14]. The black contours indicate the X–ray emission at 1–3 keV. (*center*) The same skymap in X–ray. The correlation with γ–ray is striking evident. (*right*) The differential energy spectrum of emission, fitting a power–law with exponential cut–off.

RX J0852.0-4622 (also called Vela Junior) is also interesting because of its morphology. Differently from RX J1713.7-3946, it has a ring-like structure composed of a thin shell. Nonetheless, energy spectrum and flux are similar to RX J1713.7-3946, revealing a common origin. Cassiopea A is interesting because it is the brightest galactic radio source and is a very bright X–ray emitter. The hard γ–ray spectrum reported by MAGIC favors a hadronic origin of the γ–ray for this source [19]. Future multiwavelength campaigns could unveil the origin of accelerated particles. For IC 443, also observed by MAGIC [17], the statistics of observation is limited and a clear association is complicated. Nevertheless, due to the close presence of giant molecular clouds, the source is very interesting in order to unveil acceleration mechanisms.

A substantial improvement for the detection of SNRs requires a telescope with increased angular resolution in order to perform morphological studies and sensitivity up to 100 TeV in order to explore the differences between leptonic and hadronic acceleration. To accomplish this requirement, the sensitivity of future experiments must therefore grow substantially in order to allow a good coverage of an extended source in the focal plane.

OB–associations and superbubbles

Supernova events are more frequent for massive stars of type O and B, which are usually found in loose systems of 10–100 stars, called *OB–associations*, formed by stars of common origin and history. The region comprising an OB–association is filled with SNRs and stellar winds, and therefore, is a perfect place for CRs acceleration because one has both the acceleration engine and the particle reservoir. The regions are also defined as *superbubbles*. Superbubbles are thought to explain or at least contribute significantly to the GCRs density observed.

The study of these objects is made more difficult by the poor knowledge of their history and evolution, which is more complicate that for simple SNRs, due to their interactions. For example, superbubbles can maintain efficient acceleration for more than 10^5 years before entering the Sedov phase, almost two orders of magnitude larger than for single SNRs. In addition, superbubbles are extended up to 10 deg with complex geometry, and therefore an observation with limited FOV telescopes is made more difficult. Only a detailed extended γ–ray survey coupled with multiwavelength observations can disentangle the emission.

A famous superbubble is known in the Cygnus region. Others are found in the Large Magellanic Cloud and in the 30 Dor C, but no observation in VHE γ–ray has been performed yet.

Diffuse galactic emission

EGRET, the Energetic Gamma-Ray Experiment Telescope onboard the CGRO satellite, detected γ–rays in the 20 MeV–30 GeV range. It had a very large field of view, approximately 80 deg in diameter, although the instrument angular resolution was rather poor and the sources were reported with a large error–box. On the contrary, EGRET was perfectly suited for the observation of the diffuse galactic γ–ray emission, which was seen to be pretty isotropic [34]. Important news are expected from the recently launched Fermi–LAT satellite (http://fermi.gsfc.nasa.gov/), formerly known as GLAST, which has a pretty larger sensitivity compared to EGRET. A sketch of the Fermi–LAT first released full–sky map after only 4 days of datataking is shown in Figure 1.8.

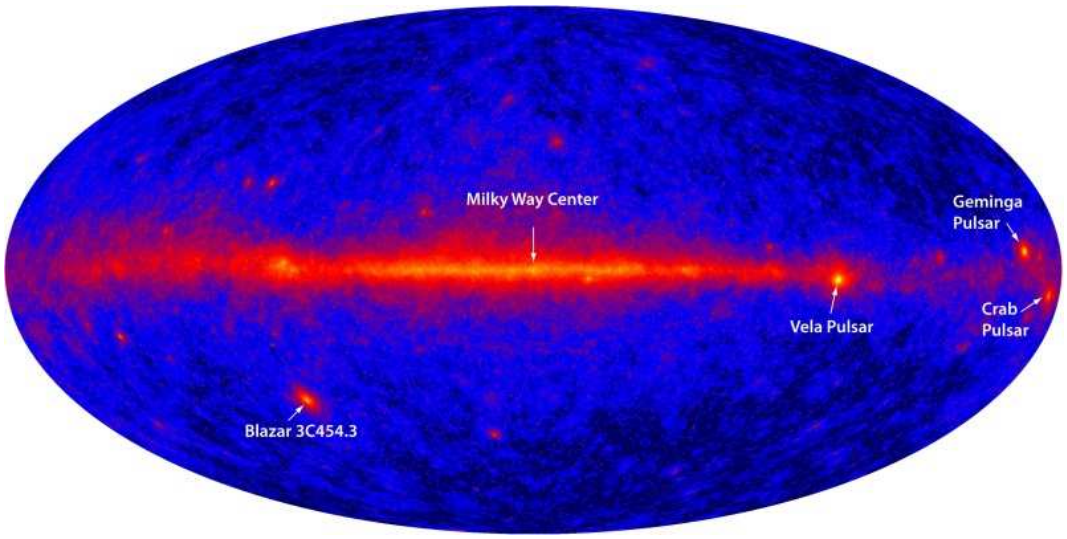

Figure 1.8: Fermi–LAT first map of the γ–ray sky with some labels for the principal point–like emitters. Image from http://fermi.gsfc.nasa.gov/.

Diffuse γ–ray emission is thought to come mainly from inverse Compton scattering of electrons onto seed photons pervading the galaxy, but can be also associated to hadronic acceleration through pion decay. Hadrons in fact, are isotropically distributed due to their interaction with magnetic fields. An increased angular resolution could probably disentangle the diffuse emission by localizing eventual anisotropies that could be associated to singular emitters. The origin of the galactic diffuse γ–ray emission can be reported to many astrophysical sources like SNRs and pulsar wind nebulae or larger compound systems such as superbubbles or molecular clouds. As already discussed, in the TeV–band, electrons are more confined to the place of production because of the strong absorption, and therefore, an eventual leptonic diffuse emission should reveal more anisotropies. It is interesting to note that the spectrum of the diffuse emission EGRET recovered (after subtraction of point–like sources) was harder ($\Gamma \sim 2.3$) compared to the γ–ray spectrum expected from the CRs ($\Gamma \sim 2.7$).

At TeV energies, IACTs with a very large FOV may help, but while the number of γ–rays and the background contribution increases linearly with the FOV, the sensitivity increases only with the square root of the number of events. An important contribution from ground–based experiments for diffuse γ–ray observation comes from water–Cherenkov detectors, that have a larger FOV than IACTs and are usually limited by statistics rather than by significance. The only IACT that tried to perform observation of diffuse emission was HESS that scanned the galactic plane around the GC [9].

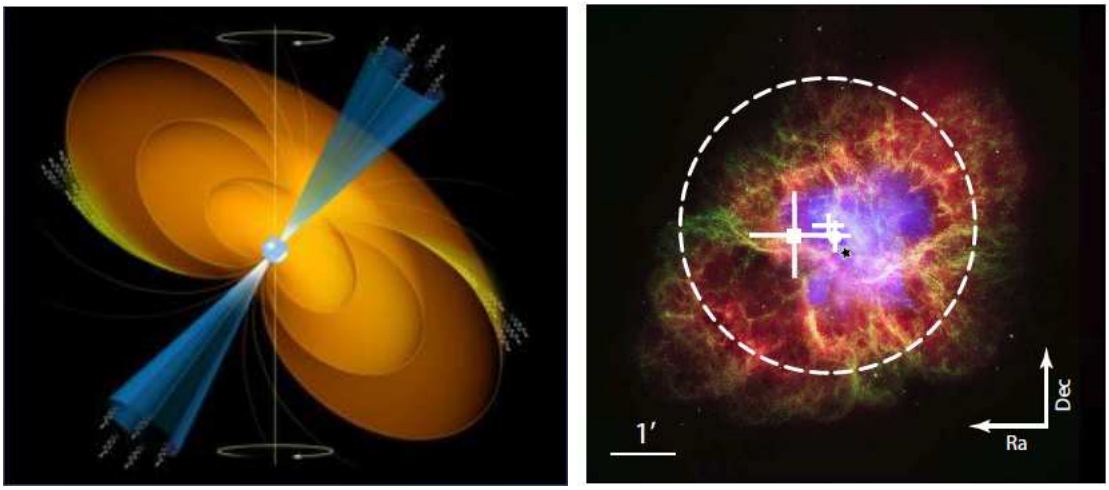

(a) Artistic view of a pulsar (b) The Crab Nebula

Figure 1.9: (a) Artistic view of a PWN. The pulsar rotation axis is shown together with the outcoming jets and the pulsar winds. The regions where γ–rays are produced is also shown. (b) An image of the Crab Nebula PWN in different energy bands. The position of the Crab pulsar is marked with a black star. The Chandra X-ray image is shown in light blue, the Hubble Space Telescope optical images are in green and dark blue, and the Spitzer Space Telescope's infrared image is in red [24].

1.4.2 Galactic emission from compact objects

Compact objects are able to accelerate CRs to extremely high energies through a dramatic process usually localized in a small region. A typical mechanism is trough jets of ultrarelativistic particles which are expelled at large distances from the source. Again, the jet mechanism allows to accelerate both leptons and hadrons.

Pulsar Wind Nebulae

In § 1.4.1, it was shown that at the end of the life of a massive star, most of the matter is in the form of neutrons. When the density is comparable to nuclear density, no more matter can accrete and the outmost part of the star is ejected away. The newly born neutron star starts to spin around very rapidly. The angular momentum of a star like the Sun is $L = I\,\omega$ where $I \propto M\,R^2$ and $\omega \sim 10^6$ rad s^{-1}. By knowing that the radius of a neutron star is about 10^{-5} times the radius of the progenitor (i.e. $\sim$ 10 km), and that around half of the mass is expelled, one obtains a rotation speed with a period of the order of the millisecond. Most of the pulsars are in fact millisecond–pulsars. The kinetic energy of such a fast rotating object has a derivate $\dot{E} = I\omega\dot{\omega}$ that for a millisecond–pulsar gives fluxes of about 10^{38} erg/s. Similarly, by scaling the magnetic flux of the progenitor to the size of the newly–born neutron star, one obtains a factor of 10^{10}. Magnetic fluxes of the order of 10^{12} G are threfore predicted for pulsars. These are the highest magnetic fields believed to exist in the universe.

The energy related to the rotation of this ultra–compact object is the fuel for acceleration of CRs. The pulsar expells a relativistic wind of particles and magnetic fields which determines the formation of a synchrotron nebula in the sorroundings of the source. The nebula is also called a pulsar wind nebula (PWN) or *plerion*. The magneto–hydrodynamics of the PWN is well–described by Kennel and Coroniti [36] applied to the case of the Crab Nebula. The acceleration takes place in at least three places in the proximity of the pulsar:

i) in the *magnetosphere*, electrons can be directly accelerated up to very high energies. As a result, a strong γ–ray emission is expected, which is rapidly absorbed because γ–rays efficiently interact with the local high magnetic field and consequently pair–produce. For this reason, this region is thought to be observable in γ–rays only below few tens of GeV. The millisecond–pulsars are more interesting because the magnetosphere magnetic field is rather small compared to other pulsars and the γ–ray absorption is less efficient,

ii) in the *unshocked ultrarelativistic wind* of electrons and positrons, the largest amount of energy is taken away from the pulsar in the form of Poynting flux and kinetic energy of particles. From this region, a strong TeV γ–ray emission is expected. Before the termination shock, electrons have a bulk ultrarelativistic motion that could perhaps be observed through a line–type emission in the γ–ray energy spectrum,

iii) in the *pulsar wind nebula*, which is a few parsec away from the pulsar, the DSA acceleration of particles takes place (Appendix A). This is the region where CRs are accelerated to the highest energies, up to 10^{15} TeV through a standing reverse shock which both accelerates electrons and randomizes their direction. The electrons later on eventually IC–scatter on local seed photons and VHE γ–ray emission is initiated. The associated γ–ray spectrum is usually very steep beyond 100 GeV and therefore, only high sensitive telescopes can detect emission from this region. The synchrotron radiation is emitted both in the X–ray and γ–ray domains, and multiwavelengths observations are therefore very promising to understand the feature of the local magnetic field.

It is interesting to observe that for the observed PWNs, the hosting pulsar itself is not located at the center of the wind nebula, neither in X–rays nor in γ–rays. This is probably related to the presence of a highly inhomogeneous medium that affects the propagation of the reverse shock. The X–ray emission is usually more confined than that of the γ–ray one because the X–ray emission is associated to more energetic electrons that lose more rapidly their energy.

The most notorious object belonging to this category is the Crab Nebula (see Figure 1.9(b), and box at page 21 for an historical introduction). The Crab Nebula is the remnant of a supernova explosion that occurred in the year 1054. It is located at a distance of 2 kpc. It is one of the best studied non–thermal celestial objects in almost all wavelengths of the electromagnetic spectrum from 10^{-5} eV (radio) to nearly 10^{14} eV (γ–rays). The engine of the nebula is the pulsar PSR B0531+21 (also called the Crab pulsar). In VHE γ–rays, the Crab Nebula was first detected by the Whipple telescope in 1989. It is the strongest source of steady VHE γ–ray emission in the Galaxy. It is thus used as the standard "calibration candle" for ground–based and satellite–borne γ–ray experiments. For example, this source will be used for counter–checks in the analysis of MAGIC data in Chapter 8. The MAGIC telescope is constantly observing the Crab, and its observation is reported in Ref. [24]. The γ–ray flux was measured between 60 GeV and 9 TeV. The energy spectrum can be described by a curved power law:

$$\frac{dF}{dE} = f_0 \left(\frac{E}{300\text{GeV}} \right)^{a+b\, log_{10}(E/300\text{GeV})} \tag{1.1}$$

with a flux normalization $f_0 = (6.0 \pm 0.2 stat) \times 10^{-10}$ cm^{-2} s^{-1} TeV^{-1}, $a = -2.31 \pm 0.06 stat$

and $b = -0.26 \pm 0.07 stat$. The peak in the spectral energy distribution is estimated at 77 ± 35 GeV. Within the observation time and the experimental resolution of the telescope, the γ–ray emission is steady and point–like. The emission center of gravity coincides with the position of the pulsar.

Other two well–known PWNs are Vela X and MSH 15–52. The spectral features of those objects are rather featured which make them very interesting. Disentangling the emission process is complicated by the unknown interaction of the accelerated particles with the dense intergalactic matter and radiation fields that surround those objects.

Recent observation of the pulsed emission from the Crab Pulsar by MAGIC

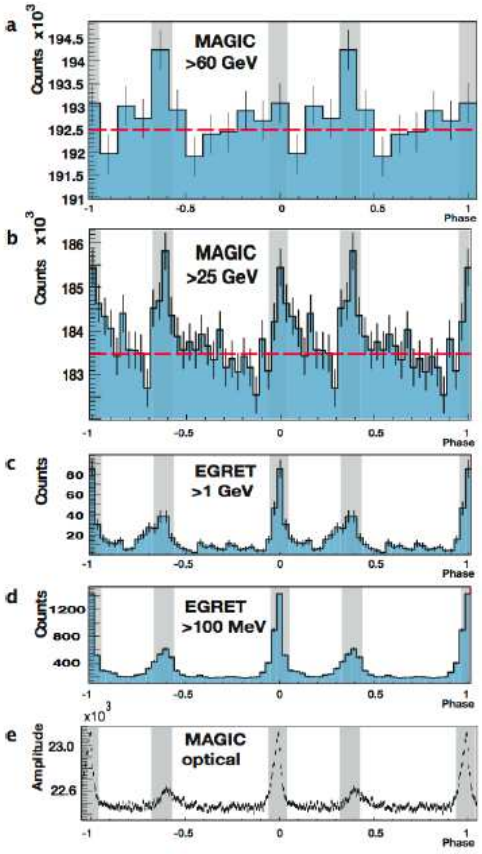

Figure 1.10: Pulsed emission in different energy bands. The shaded areas show the signal regions for the main pulse (P1) and the inter pulse (P2). From top to bottom: (a) Evidence of an emission above 60 GeV for P2 measured by MAGIC; (b): Emission above 25 GeV measured by MAGIC; (c) Emission above 1 GeV measured by EGRET; (d) Emission above 100 MeV measured by EGRET; (e) Optical emission measured by MAGIC with an optical pixel.

By developing a new electronic trigger, MAGIC lowered the energy threshold to 25 GeV. In this configuration, for the first time in the history of IACT astronomy, pulsed γ–rays from the Crab pulsar above 25 GeV were revealed [25], see Figure 1.10. They reveal a moderately high cutoff energy in the phase–averaged spectrum. This indicates that the emission occurs far out in the magnetosphere, hence possibly excluding the polar–cap scenario and favouring an outer–gap scenario. For the Crab pulsar, EGRET measured a power–law spectrum with spectral index $\simeq -2$ in the energy range $0.1 - -5$ GeV. At 25 GeV, MAGIC measured a flux that was several times lower than a straightforward extrapolation of the EGRET spectrum. This requires a spectral cutoff somewhere between 5 and 25 GeV. The spectral cutoff is explained as a combination of the maximum electron energy (a balance between acceleration and radiation losses) and the absorption of the emitted γ–rays in the magnetosphere.

The amazing history of the Crab Nebula

In the summer of 1054, Chinese astronomers observed the appearance in the sky of a very intense spot of unprecedented brightness above the southern horn in the constellation of the Taurus. They described the light as bright as Venus, comparable to the full moon. The light was so bright that the people saw it in the sky even during the day for almost a month. The star was as bright as 400,000,000 suns. It remained visible in the night sky for more than a year. According to Chinese accounts, the supernova was a tremendous celestial omen.

A pictograph of Crab Nebula at Chaco canyon, New Mexico, from the Asanazi tribe.

The Crab explosion was only marginally recorded in Europe (Ireland, Italy, Constantinoples, etc.) but with less scientific detail and less astrological interpretation.

Also the Native Americans Anasazi tribe in New Mexico recorded the observation of the Crab Nebula. Two pictographs have been found at observation points in canyons, depicting a crescent moon, a large star and a hand. One is shown in the figure. The image is an astronomical map: at the beginning of July, the moon and earth return to approximately the same positions they had when the Crab Nebula was observed in 1054. Standing in front of the pictograph, and waiting until the moon is in a position pointed to by the fingers of the hand, if one orientates a telescope to the position of the large star in the pictograph, the telescope points to the Crab Nebula.

After having faded out, the supernova was unvisible for more than 600 years until the invention of telescopes, which revealed fainter celestial details than the human eye can detect. In 1731, the English astronomer John Bevis observed the strings of gas and dust that form the Crab Nebula. Later in 1758, Charles Messier spotted the nebula, noting that it had no apparent motion. The nebula became “M1”, the first entry in his famous ”Catalogue of Nebulae and Star Clusters,” first published in 1774. Lord Rosse named the nebula the ”Crab” in 1844 because its tentacle-like structure resembled the legs of the crustacean.

References: physics.gac.edu/∼chuck/astro/archeo.html and www.astronomy.pomona.edu/archeo/outside/chaco/nebula.html and Polcaro V. F, Mattocchia A. “Supernovae astrophysics from Middle Age documents”, Procs. IAU Symposium, 230 (2005)

Binary systems

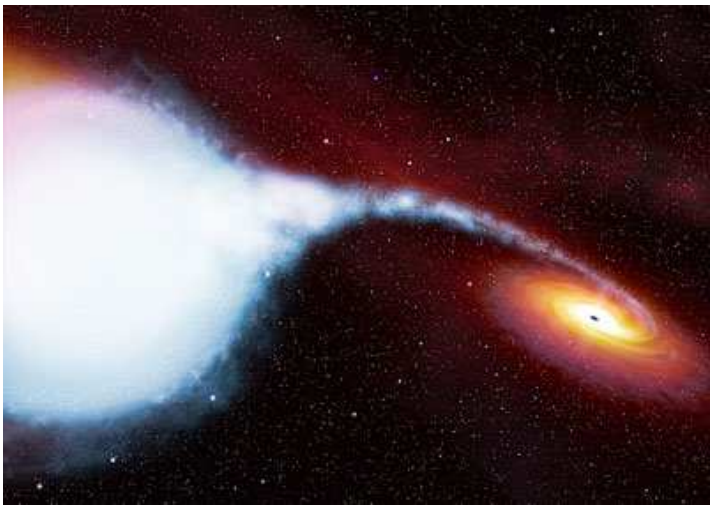

Figure 1.11: Artistic view of an X-ray binary system. The infall of material from the companion star to the compact object is dramatic.

When a star is in the vicinity of an object with a very high gravitational field like that of a neutron star, a pulsar or a black hole, may start to vortex around the compact object loosing an enormous amount of matter that collapses onto the dense object, as depicted in Figure 1.11. An associated X–ray emission directly comes from the stream of collapsing particles. There is already evidence that particles are also accelerated to very high energies. For example, as a result of the infall of materials onto the black hole, two jets pop out in the direction orthogonal to the rotation of the black hole where particles are directly accelerated in a similar way to what happens for active galactic nuclei. For this reason, those objects are also called *micro–quasars*. Particle acceleration can also happen at the termination shock of pulsar winds as for PWN. In all cases, the massive presence of target materials and photons is in favor of a copious γ–ray emission.

An important member of pulsar–powered binary systems is PSR B1259-63 / SS2883. The pulsar has a period of 48 ms and the star is a B2e. The source was observed by HESS [11] above 380 GeV. The spectral index is very hard $\Gamma \sim 2.7$, which seems to confirm the IC scattering as mechanism for acceleration, whereas hadronic emission is not ruled out. In 2006, another important target was observed with MAGIC, namely the binary systems LSI+61 303 [16]. A compact object is accreted by materials from a companion B0 star orbiting around for a period of $\simeq 29.5$ days. The spectrum is also characterized by a $\Gamma \sim 2.7$ power–law. The signal is not observed at periastron but in the phase interval $0.45 - 0.65$ and the estimated total energy emission is $\sim 7 \times 10^{33}$ erg s^{-1}. Another interesting object is LS 5039, observed with HESS [12]. The system is characterized by a very short rotation period of 3.9 days. The emission comes from half of the orbit about the periastron and is characterized by two very distinct contributions (one power–law spectrum and one very hard, exponentially cut spectrum) according to the origin in the phase diagram. This can be justified by the presence of a very different environment around the compact object, which influences absorption and accelerations processes, and/or by a variation of infalling material.

1.4.3 Galactic Center

The center of the Milky Way is crowded with many astrophysical sources where history and evolution have played an important role in shaping the γ–ray emission. A sketch of the γ–ray sky around the GC is shown in Figure 1.12, where both point–like and diffuse emission are reported, as observed by HESS [13].

The GC was observed by almost all the IACTs: Whipple [37], CANGAROO [42], HESS [8] and finally with MAGIC [15]. In particular, MAGIC and HESS results agree on a quite hard γ–ray spectrum with index $\Gamma \sim 2.25$ and a light–curve which does not show any variability on timescales from hours to years. The GC has several candidate emitters of γ–rays:

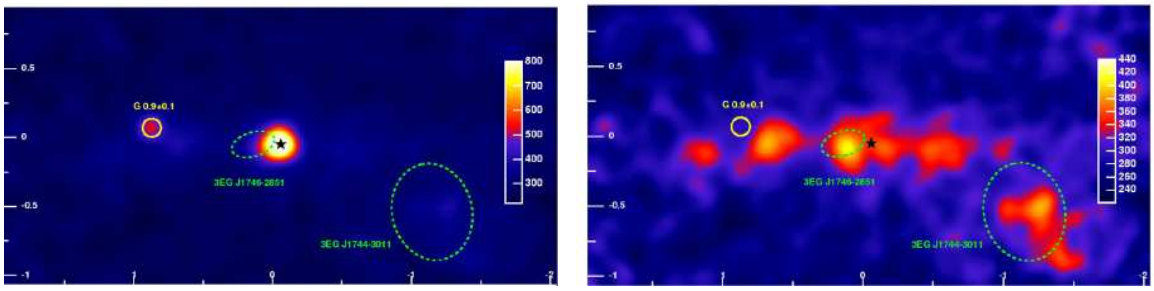

(a) GC skymap (b) GC skymap after point–like sources subtraction

Figure 1.12: Galactic Center

i) The super–massive black holes SgrA*. While the vicinity of this object should make it very bright in γ–rays, the very dense accreting torus around it could make it opaque. From SgrA* both electron and hadrons could be accelerated, and depending on the nature of the surrounding medium, they could be also displaced and accelerated again in a region faraway from the black hole itself. A firm sign of an emission from SgrA* could be the observation of a time variability in the light–curve.

ii) The young SNR SgrA East. At the shock wave, particles coming from the star or from the black hole itself can be accelerated to very high energies.

iii) In a similar way, acceleration can take place at the wind of the PWN G359.95-0.04, which is a closeby source.

iv) The presence of dense molecular clouds can act as a target for any shock wave and acceleration can thus take place here.

The observation of the GC requires an extremely good position accuracy, good sensitivity in order to observe any flux variations and multiwavelength observation with X–rays and optical telescopes in order to model the emission.

1.5 Extragalactic Objects

About 20 extragalactic VHE γ–ray emitters have been detected so far, but their number is expected to grow substantially in the next years with the observation of Fermi–LAT and with the future class of IACTs. The current map of extragalactic emitters is shown in Figure 1.13.

The universe is not completely transparent to γ–rays. Due to their interaction with soft photons of the near-IR and UV background, γ–rays disappear through pair–production. For this reason, it is believed that we cannot observe VHE γ–rays from objects at a distance larger than $z \sim 1$, for example. Only γ–rays at energies below 100 GeV have almost null cross sections for pair production and therefore, can travel larger distances. The distribution of soft photons, also called the extragalactic background light or EBL, is not known to a very high level of precision and only upper or lower limits are found. The absorption from the EBL shapes the original spectrum of emission in function of the energy, and therefore, the observation performed on the ground must be deconvoluted to find the original spectra. For this reason, γ–ray astronomy on distance sources can be a probe for the EBL and eventually an estimator of the distance for extragalactic objects.

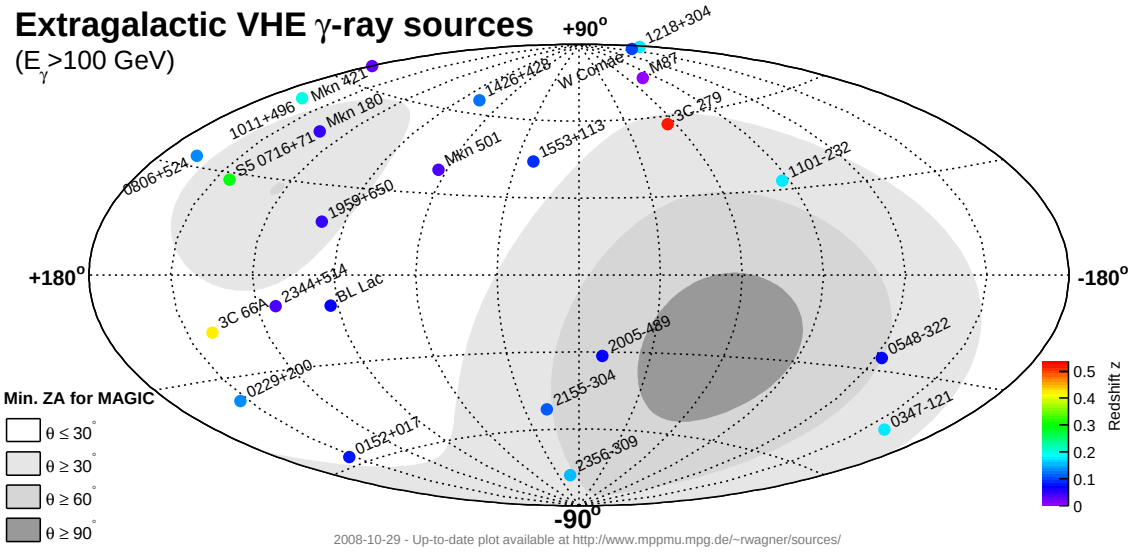

Figure 1.13: Extragalactic VHE γ–ray sources skymap. MAGIC zenith angle ranges are superimposed. Figures from http://wwwmagic.mppmu.mpg.de/ rwagner/sources/ (R. Wagner).

The class of extragalactic emitters is almost completely filled with blazars, while only one radiogalaxy has been firmly detected so far. A tentative catalog is shown in Table 1.5.

1.5.1 Blazars

Most galaxies are believed to host a supermassive black hole (SMBH) at their center, with mass of the order of $\sim 10^9$ $M_\odot$. The existence of such heavy objects is subject to theoretical discussion, as also discussed in Chapter 8. Some of them are observed to be "active" (hence the name active galactic nuclei or AGNs), i.e. emitting a huge amount of energy over the entire electromagnetic spectrum and expelling a copious flow of particles. This derives from the constant infall of large amount of materials from the surrounding region. The extremely intense gravitational attraction of the SMBH forms a dense accreting torus around it, as pictured in Figure 1.14.

From the torus, a continuous source of radiation is observed as a result of the heated infalling material, which emits in X–ray. The accreting torus somehow masks the nucleus if the AGN is seen from the side. In this case, a bright strong emission in radio–waves is observed and the source is classified as *radiogalaxy*. With a mechanism which is still unknown, the infall of material into the black hole determines the birth of two gigantic jets of expelled material and radiation, propagating in opposite directions perpendicular to the torus plane. These jets can be as large as many thousand times the extension of the entire galaxy, up the Mpc scale. If by chance the observer is aligned with the jets, the emission is strongly boosted because of the Doppler effect, so that the chance of observation of a distant object is increased. An AGN observed from this point of view is called a *blazar*. This is the most common class of AGNs observed, as shown in Table 1.5.

The AGNs catalog in other wavelengths is very crowded, and it is often difficult to provide a firm classification of the object. It is generally believed that all AGNs show similar properties and that the surrounding medium only affects the acceleration of CRs at a secondary order. They are of the most varying emitters in the sky: due to variation in the infall of materials, the flux can vary by up to two orders of magnitude in intensity. The observation of these "flares" are of utmost importance to study the source morphology and characteristics. For

Name	z	Ra	Dec	Flux	Γ
$M87$	0.004	12 30 54.4	+12 24 17	1	2.9
Mkn 421	0.031	11 04 27.6	+38 12 54	$12-97$	2.4–3.1
Mkn 501	0.034	16 53 52.1	+39 45 37	$0.5-100$	1.9–5
1ES 2344+514	0.044	23 47 06.0	+51 42 30	$1-5$	2.3–2.5
Mkn 180	0.046	11 36 26.4	+70 07 28	0.9	3.3
1ES1959+650	0.047	19 59 59.9	+65 08 55	$4-120$	1.8–10
PKS 0548–322	0.069	05 50 40.8	−32 16 18	~ 0.3	2.8
BL Lacertae	0.069	22 02 43.3	+42 16 40	~ 0.3	3.6
PKS 2005–489	0.071	20 09 29.3	−48 49 19	0.2	4
PKS 2155–304	0.116	21 58 52.7	−30 13 18	$2-3$	3.3–3.4
H 1426+428	0.129	14 28 32.7	+42 40 20	$1-2$	2.6–3.7
1ES 0229+200	0.140	02 32 53.2	+20 16 21	0.62	2.5
H2356–309	0.165	23 59 07.9	−30 37 41	~ 0.3	3.1
1ES 1218+304	0.182	12 21 22, 1	+30 10 37	1.3	3.0
1ES 1011–232	0.186	11 03 37.7	−23 29 31	0.4	2.9
1ES 0347–121	0.188	03 49 23.0	−11 58 38	0.45	3.1
1ES 1011+496	0.212	10 15 04.1	+49 26 01	~ 0.3	4.0
PG1553+113	0.36?	15 55 43.2	+11 11 21	$0.1-0.2$	4.0
3C279	0.536	12 56 11.1	−05 47 22	?	?

Table 1.5: Catalog of known VHE–emitter extra–galactic objects ordered by distance. The flux is given in units of 10^{-12} cm^{-2} s^{-1} TeV^{-1} at 1 TeV, Γ is the spectral index. $M87$ is the only radiogalaxy, all others are AGNs.

example, the duration of the flare is inversely correlated to the extension of the region where CRs are produced. The characteristics of flares are very different: flares do not necessarily occur simultaneously at all wavelengths, sometimes they last different times and the flare is not as intense at all wavelengths. For this reason, there is no current theory which can explain the entire data available. At present, the leptonic model for emission is favored, whereas the hadronic one is by no means ruled out. Nonetheless, while in the former case one can easily obtain high energy electrons accelerated in shock mechanisms and consequent X–ray and γ–ray radiation through synchrotron and IC scattering, in the latter case one needs to accelerate protons up to 10^{20} eV to have efficient γ–ray production mechanisms. Hadronic γ–ray emission could come from pure high–energy hadrons collisions, proton synchrotron emission or even photo–pion production. In any case, the poor knowledge of the magneto–hydro–dynamics of the blazar does not allow to disentangle the emission with current knowledge.

In Table 1.5 it is shown that the current blazars are known at an incredibly large range of distances, in particular after MAGIC observation of 3C279 at redshift $\simeq 0.5$ [23]. The two most representative blazars are Mkn 421 and Mkn 501, discovered by the Whipple collaboration in 1992 and 1996 respectively [39, 40]. The sources have been observed for 15 years at many wavelengths and show very variable emission on the timescale of minutes, as recently reported by MAGIC [20].

We have already mentioned many times the results obtained with the Auger experiment, which spatially associated EHE CRs with AGNs. This fact is under very active studies now, and has important consequences on the study of the acceleration mechanisms. Important news are expected in the future from the Auger experiment.

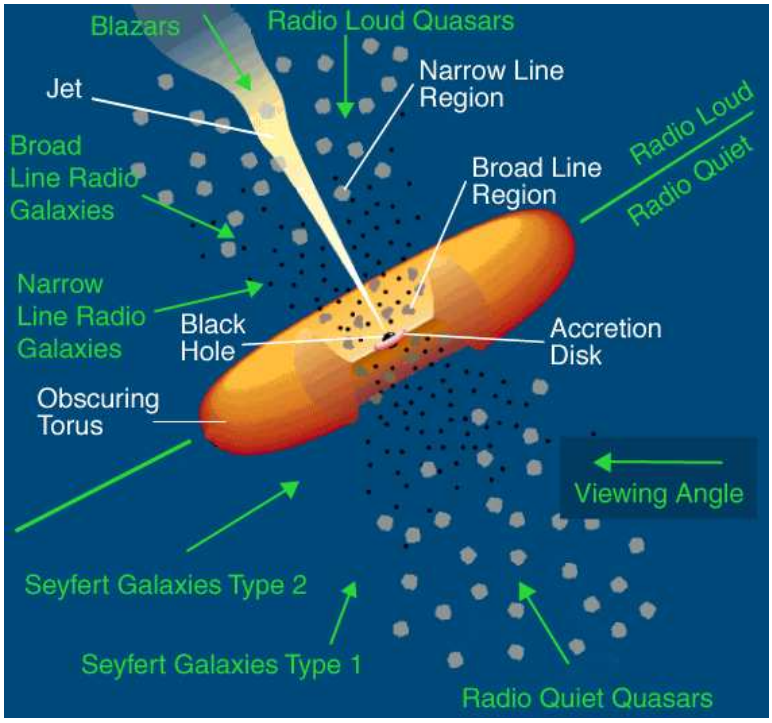

Figure 1.14: Classification of active galactic nuclei. It is constituted by an accreting torus composed of star and materials infalling into the central supermassive black hole. In the perpendicular plane two co-aligned jets emerge and extend up to a thousand times the extension of the galaxy itself. When observing an AGN from the side of the jets, the obscuring torus shadows the black hole and the galaxy is either radio quiet or radio loud. When the jet is co-aligned with the observer, the strong Doppler effect boosts the emission and the AGN is extremely VHE emitting.

1.5.2 Radiogalaxies

The prototype of radiogalaxy is M87, located in the Virgo cluster at the close distance of 16 Mpc. After the weak detection performed by HEGRA [7], the source was observed by all present IACTs. The low signal recently observed with MAGIC [21] confirms that the source shows a fast variability, which restricts the emission to the regions close to the SMBH, whereas the exact acceleration mechanism is still unknown. It is also very interesting the observation of its gigantic jets, extending 1 kpc, which are in many wavelengths.

1.5.3 Starburst galaxies

The high rate of supernova explosions (1/year in the Galaxy) that occurs in starburst galaxies guarantees both the mechanism of acceleration of particles at SNR shocks and a large amount of seed photons for IC scattering and consequent production of very high energy γ–rays. As usual, both hadronic and leptonic acceleration mechanisms are possible. The two prototype starburst galaxies, M82 and NGC 253, both observed in synchrotron radio emission, are not observed in γ–rays where only upper limits were provided [10]. A second class of star burning regions is formed by the ultraluminous infrared galaxies (ULIGs), of which Arp220 is a major member. ULIGs are among the most luminous places in the universe, nonetheless, in γ–rays only upper limits were reported by MAGIC in 2006 [18]

1.5.4 Gamma–ray Bursts

Gamma–ray Bursts (GRBs) are extremely powerful phenomena observed as a sudden outburst of radiation at all wavelengths. During a GRB an enormous amount of energy is released in seconds. A GRB can release from 10^{48} to 10^{53} erg s^{-1} and convert into energy a mass of 10^{-3} $M_\odot$ in a region as small as a neutron star or stellar black hole. This corresponds to the mass of one thousand earths! They are observed at an average rate of one per day. GRBs origin is now firmly extragalactic with measured redshifts ranging from 0.0085 up to 6.7, with

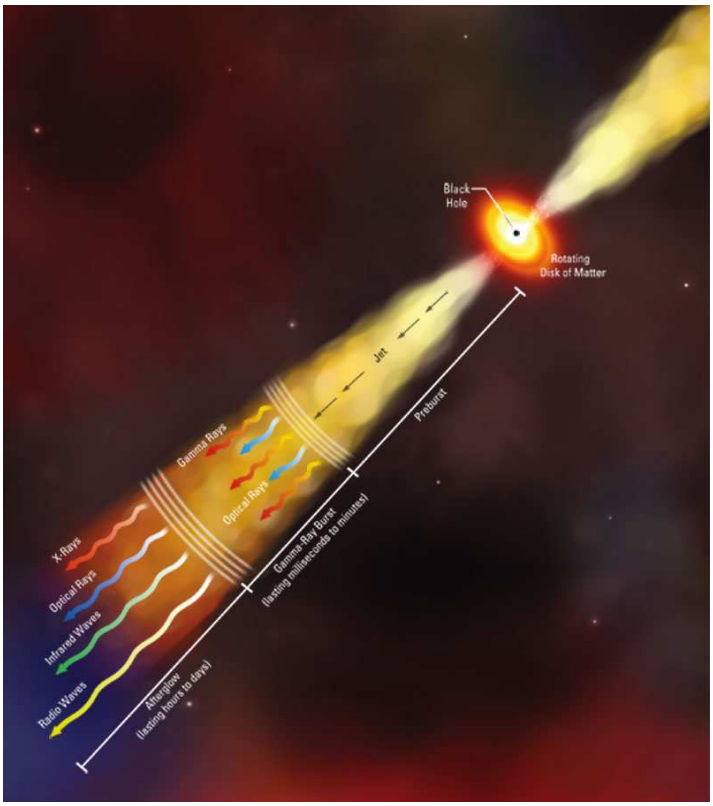

Figure 1.15: Artistic view of the jet structure of a GRB. The first part of the jet expel materials $10^7 - 10^9$ km away from the progenitor in a fraction of a second. Following a prompt emission they come at all wavelengths and last from milliseconds to several seconds. Later on, many afterglows can occur.

an average age of $z = 2.3 - 2.7$. Up to now, the origin of GRBs is still unknown and they are believed to be originated from two possible different progenitors: *a*) the sudden catastrophic collapse of rapidly rotating very massive stars ($M^* > 100$ $M_\odot$), *b*) the merge of two compact objects. The existence of two different origins is somehow confirmed by the existence of two different families of GRBs: a *long duration* (> 2s) one, possibly related to the first class of progenitors with lower energies, and a *short duration* (< 2s), related to the latter and of high energies and therefore more of interest for IACT (where the duration is referred to the prompt sub–MeV emission).

A GRB is typically characterized by a prompt emission mainly emitted in the γ–ray band followed by a so-called "afterglow" emission observed at all wavelengths from X–ray down to radio–band which lasts from hours up to weeks. The origin of the afterglow is related to the external shock mechanisms, i.e. to the interaction of the fireball with the surrounding interstellar medium. The prompt emission is usually so intense to almost overshine the entire sky in γ–ray and it is the result of the grow of huge ultrarelativistic jets where electrons, protons and photons are interacting. The way how the energy is distributed among these three components determines the exact mechanism of acceleration. The outflow of particles is converted into radiation through an internal shock mechanism when there is a variability in the injection rate of particles into the jets. When the electrons carry more than around 0.1% of the energy, the IC scattered photons dominate the γ–ray spectrum. On the other hand, the photons from pion decays dominate the spectrum at least at high energies. The seed photons for IC scattering come from synchrotron photons (SSC mechanism) which dominate at lower energies. If GRBs are emitting at VHE (> 1 GeV,) the EBL absorption could strongly limit the observability at these frequencies. For this reason, the search for GRBs in the VHE band needs very sensitive instruments and the occurrence of an event as close as possible to the Earth. While at TeV energies the difference between hadronic and leptonic emission is more

evident, in the sub–GeV regime the synchrotron radiation can mimic the hadronic origin. After the prompt emission, secondary bursts can happen during the afterglow phase. The observed emission now could be the result of many different contributions, and therefore the light–curve presents important features. Such a refill of energy can provide the seed photons for IC emission at higher energies well within the external shock scenario.

Recently, an interesting review was published [44, 45].

1.6 Fundamental physics

Violation of the Lorenz invariance

The quantum gravity paradigm infer that at an energy/length close to the Planck scale, the gravitational field becomes quantistic. The Planck scale is characterized by energies of $E_{QG} = \sqrt{\hbar\, c^5/G} = \hbar\, c/L_{QG} \simeq 10^{28}$ eV, where $\hbar$ is Dirac's constant, c is the velocity of light, G is Newton's constant and $L_{QG} = 1.6^{-35}$ m is the Planck's length.

The quantization of the gravitational field has the fundamental effect that the space–time becomes a dispersive medium with dispersion relation in the form of $c^2\, p^2 = E^2\, (1 + \xi\, (E/E_{QG})^n + \mathcal{O}(E/E_{QG})^{n+1})$ where $n = 1, 2$ according to different models. A non–zero value of the dimensionless parameter ξ corresponds to a violation of the so–called Lorenz invariance.

The above dispersion relation has also the effect that the propagation of the photons is dependent on their energy. The velocity of the light is no longer constant and $v = dE/dp = c(1 - \xi(E/E_{QG})^n)$, and therefore photons with different energies produced at the same place, arrive at the Earth in a different moment $\Delta t \simeq \xi\, (L/c)\Delta E/E_{QG}$, where L is the distance of the source and ΔE is the energy difference of the two photons. In particular, higher energy photons arrive before those at lower energies. A natural place where to look for this effect is during flares of faraway AGNs. The large distance allow to increase the time discrepancy between photons and the flare allows to provide the time stamp of the produced photons (in the hypothesis that photons are produced simultaneously at different energies). With this method, MAGIC reported a lower limit to the quantum gravity scale after a flare occurred in Mkn 501 of the order of $M^1_{QG} > 2.1 \times 10^{17}$ GeV and $M^2_{QG} > 2.6 \times 10^{10}$ GeV [22] according to $n = 1, 2$ respectively.

Transport of photons

The observation of far distant γ–ray sources like the blazar 3C279 at redshift z = 0.536 [23] put serious constraints on the features of the EBL. Because of the absorption produced by the EBL, the propagation of a VHE γ–ray from a source at redshift z is governed by the optical depth $\tau(E, z)$. It increases with the redshift, since the probability of interaction with the EBL increases. Implicit in this consideration is the hypothesis that photons propagate in the standard way throughout cosmic distances. De Angelis et al [29] suppose instead that in the presence of cosmic magnetic fields, photons can oscillate into a new, very light, spin-zero Axion-Like particle (ALP). ALPs travel unimpeded throughout the Universe and can convert back to photons. Since ALPs do not undergo EBL absorption, the overall optical depth τ seems smaller. The interesting fact is that ALPs is not an ad hoc assumption invented to solve the problem. Instead, ALPs are generic predictions of many extensions of the Standard Model of elementary particle physics.

Dark matter

This part will be discussed extensively in PART II of this thesis work, at Page 115.

References

[1] A. A. Abdo et al. Discovery of Localized Regions of Excess 10-TeV Cosmic Rays. *Phys. Rev. Lett.*, 101:221101, 2008.

[2] J. Abraham et al. Correlation of the highest energy cosmic rays with nearby extragalactic objects. *Science*, 318:938–943, 2007.

[3] J. Abraham et al. Observation of the suppression of the flux of cosmic rays above 4×10^{19}eV. *Phys. Rev. Lett.*, 101:061101, 2008.

[4] F. Aharonian. *Very High Energy Cosmic Gamma Radiation - A Crucial Window on the Extreme Universe*. World Scientific, Singapore, 2004.

[5] F. Aharonian, J. Buckley, T. Kifune, and G. Sinnis. High energy astrophysics with ground-based gamma ray detectors. *Rept. Prog. Phys.*, 71:096901, 2008.

[6] F. Aharonian et al. High energy electrons and positrons in cosmic rays as an indicator of the existence of a nearby cosmic tevatron. *Astron. Astrophys.*, 294:L41, 1995.

[7] F. Aharonian et al. Is the giant radio galaxy M87 a TeV gamma-ray emitter? *Astron. Astrophys.*, 403:L1–L6, 2003.

[8] F. Aharonian et al. Very high energy gamma rays from the direction of Sagittarius A*. *Astron. Astrophys.*, 425:L13–L17, 2004.

[9] F. Aharonian et al. A new population of very high energy gamma-ray sources in the Milky Way. *Science*, 307:1938–194, 2005.

[10] F. Aharonian et al. A search for very high energy gamma-ray emission from the starburst galaxy NGC 253 with HESS. *Astron. Astrophys.*, 442:177–183, 2005.

[11] F. Aharonian et al. Discovery of the binary pulsar PSR B1259-63 in very-high- energy gamma rays around periastron with HESS. *Astron. Astrophys.*, 442:1–10, 2005.

[12] F. Aharonian et al. Discovery of very high energy gamma-rays associated with an X-ray binary. *Science*, 309:746–749, 2005.

[13] F. Aharonian et al. Discovery of very-high-energy gamma-rays from the galactic centre ridge. *Nature*, 439:695–698, 2006.

[14] F. Aharonian et al. Primary particle acceleration above 100 TeV in the shell-type supernova remnant RX J1713.7-3946 with deep HESS observations. *Astron. Astrophys.*, 464:235–243, 2007.

[15] J. Albert et al. Observation of gamma rays from the galactic center with the MAGIC telescope. *Astrophys. J.*, 638:L101–L104, 2006.

[16] J. Albert et al. Variable very high energy gamma-ray emission from the microquasar LS I +61 303. *Science*, 312:1771–1773, 2006.

[17] J. Albert et al. Discovery of VHE Gamma Radiation from IC 443 with the MAGIC Telescope. *Astrophys. J.*, 664:L87–L90, 2007.

[18] J. Albert et al. First bounds on the very high energy gamma-ray emission from Arp 220. *Astrophys. J.*, 658:245–248, 2007.

[19] J. Albert et al. Observation of VHE gamma-rays from Cassiopeia A with the MAGIC telescope. *Astron. Astrophys.*, 474:937–940, 2007.

[20] J. Albert et al. Variable VHE gamma-ray emission from Markarian 501. *Astrophys. J.*, 669:862, 2007.

[21] J. Albert et al. MAGIC Observations of a 13-Day Flare Complex in M87 in February 2008. Submitted to Astrop. J., 2008.

[22] J. Albert et al. Probing quantum gravity using photons from a flare of the active galactic nucleus Markarian 501 observed by the MAGIC telescope. *Phys. Lett.*, B668:253–257, 2008.

[23] J. Albert et al. Very-High-Energy gamma rays from a Distant Quasar: How Transparent Is the Universe? *Science*, 320:1752–, June 2008.

[24] J. Albert et al. VHE Gamma-Ray Observation of the Crab Nebula and its Pulsar with the MAGIC telescope. *Astrophys. J.*, 674:1037–1055, 2008.

[25] E. Aliu et al. Detection of pulsed gamma-ays above 25 GeV from the Crab pulsar. *Science*, 322:1221–1224, 2008.

[26] A. Bell and S. Lucek. Cosmic ray acceleration to very high energy through the non-linear amplification by cosmic rays of the seed magnetic field. *Monthly Notices of the Royal Astronomical Society*, 321:433, 2001.

[27] D. R. Bergman. Latest Results from HiRes. In *Procs. of the 20th Recontres de Blois, Blois, France, May 2008*, 2008.

[28] J. Buckley et al. The Status and future of ground-based TeV gamma-ray astronomy. A White Paper prepared for the Division of Astrophysics of the American Physical Society., 2008.

[29] A. De Angelis, O. Mansutti, M. Persic, and M. Roncadelli. Photon propagation and the VHE gamma-ray spectra of blazars: how transparent is really the Universe? *Il Nuovo Cimento*, 31:187, 2008.

[30] L. Drury. An introduction to the theory of diffusive shock acceleration of energetic particles in tenuous plasmas. *Rept. Prog. Phys.*, 46:973, 1983.

[31] R. Giacconi, H. Gursky, F. R. Paolini, and B. B. Rossi. Evidence for x Rays From Sources Outside the Solar System. *Physical Review Letters*, 9:439–443, Dec. 1962.

[32] A. M. Hillas. In *Proc. of the 19th ICRC*, La Jolla, January 1985.

[33] J. Hinton. Gamma-ray Astronomy. In *Proc. of the 30th ICRC*, Merída, Mexico, 2007.

[34] S. D. Hunter et al. EGRET observations of the diffuse gamma-ray emission from the galactic plane. *Astrophys. J.*, 481:205–240, 1997.

[35] M. Kachelriess. Lecture notes on high energy cosmic rays. Prepared for the 17th Jyvasllya Summer School, 2008.

[36] C. F. Kennel and F. V. Coroniti. Confinement of the Crab pulsar's wind by its supernova remnant. *Astrophys. J.*, 283:694, 1984.

[37] K. Kosack et al. TeV gamma-ray observations of the galactic center. *Astrophys. J.*, 608:L97–L100, 2004.

[38] M. Lopez Moya. Observaciones de la nebulosa y pulsar del cangrejo (in spanish), 2006.

[39] M. Punch et al. Detection of TeV photons from the active galaxy Markarian 421. *Nature*, 358:477–478, 1992.

[40] J. Quinn et al. Detection of gamma-rays with E ¿ 300-GeV from Markarian 501. *Astrophys. J.*, 456:L83–L86, 1996.

[41] R. Rothenflug et al. Geometry of the non-thermal emission in SN 1006 - Azimuthal variations of cosmic-ray acceleration. *Astron. Astrophys.*, 425:121–131, 2004.

[42] K. Tsuchiya et al. Detection of sub-TeV gamma-rays from the galactic center direction by CANGAROO-II. *Astrophys. J.*, 606:L115–L118, 2004.

[43] T. C. Weekes. TeV Gamma-ray Astronomy: The Story So Far. In *Proc. of the Heidelberg International Symposium*, Heidelberg, Germany, 2008.

[44] H. Ziaeepour. Gamma Ray Bursts Cook Book I: Formulation. 2008.

[45] H. Ziaeepour. Gamma Ray Bursts Cook Book II: Simulation. 2008.

PART ONE

THE MIRRORS OF THE MAGIC II TELESCOPE
and
ACTIVITIES FOR CTA

Picture by C. Haller

2 Technical description of the MAGIC telescopes

The atmospheric Cherenkov telescope MAGIC I for ground-based gamma-ray astronomy has been operating since late 2003 on the Canary island La Palma. A second telescope, dubbed MAGIC II is currently under completion on the same site. Both telescopes have a 17 m diameter reflector: the former composed of 964 light weight, square all-aluminum mirrors with a total area of 234 m^2, and the latter of 247 1 m^2 mirrors, of which 143 are all-aluminum mirrors and 104 are cold–slumped glass mirrors. The large reflective surfaces permit to lower the energy threshold to a value far beyond that of past generation of telescopes. The trigger system, based on ultra-fast decision logics (topological, time-coincidences, etc.) is designed to cope with very fast PMT signals (2 ns). Details of the first MAGIC telescope will be presented, technical problems and solutions will be discussed, and a report on three years of operations will be given. A brief discussion of the differences introduced in the second telescope will also be discussed.

This chapter has been adapted from: *Technical Solutions for the MAGIC Telescope*, 2007 [10].

2.1 Introduction

The MAGIC telescope system has been designed and is operated thanks to a collaboration of around 150 physicists from 22 institutes and 7 countries. The first telescope has been fully operational since fall 2003 and is currently in its fourth observations cycle. The second is under completion at the moment of writing this thesis. A picture of both telescopes is shown in Figure 2.1.

MAGIC belongs to the Imaging Atmospheric Cherenkov Telescope (IACT) class of detectors and is constituted by the world's largest mirror dishes (HESS I and VERITAS telescopes have 12 m dishes, while currently a 28 m diameter telescope, named HESS II is under construction). γ–rays (as well as the many orders of magnitude more frequent charged cosmic rays) after hitting the Earth atmosphere, initiate atmospheric particle showers with a typical shower maximum around 8–12 km asl. The charged shower particles, mostly electrons and positrons, emit Cherenkov light when their speed exceeds that of light in the atmosphere. The Cherenkov

Figure 2.1: The MAGIC stereoscopic system of telescopes. On the left, the first MAGIC telescope that has been operating since 2003 and now faces the fourth cycle of scientific observation. On the right, the second MAGIC telescope, currently under commissioning. While the structures of the two telescopes are very similar, all MAGIC II subsystems are substantially ameliorated to the advantage of the overall performance. Picture from R. Wagner.

light illuminates nearly uniformly a dish of ~ 120 m radius. For a more detailed description of atmospheric showers, refer to Appendix B. If a telescope is located inside this Cherenkov-light pool, the light hitting the mirror can then be reflected and focused onto a multi–pixel camera composed of a large number of photomultipliers. An image reconstruction algorithm allows the determination of some major parameters of the primary particles, such as energy and direction, as well as its likeliness to be a hadron or a γ–ray. As lower energy γ–rays produce a lower density of photons at ground, a larger telescope mirror area is required to decrease the energy threshold of the telescope. In the case of MAGIC, the 17 m reflector allows the reconstruction of primary gamma-rays above ~ 70 GeV (zenith angle dependent) with an integral sensitivity above 100 GeV of $\sim 10^{-11}$ph cm^{-2} s^{-1} in 50 hours of observation and with an effective area, which is of the order of 10^5 m^2. In the following, we start the discussion with MAGIC I telescope, MAGIC II being a clone of the former telescope. At the end of the chapter we will briefly review the most important design modifications for the second telescope.

A complete discussion of technical design and solutions of MAGIC is not the aim of this thesis. A detailed document of the initial design ideas can be found in the MAGIC design report [4]. The interested reader can find additional information at the following selection of references [3, 10, 9, 6, 19]. For a detailed discussion of MAGIC systematics and analysis, we also refer the reader to Ref. [2]).

2.2 Technical Solutions

MAGIC I is located on the Canary island of La Palma (28.75 N, 17.89 W) at 2225 m asl. The observation conditions on site are amongst the best in the world, even if occasional strong winds, winter snowfalls, *calima*[1] and high humidity demand a strong technical effort to prevent damaging and ageing. The MAGIC telescope is in fact, too large to be protected

[1]Calima is the name of the ultra–thin Saharan sand transported by the wind from Africa, which for some days a year fills the entire sky.

Figure 2.2: The first MAGIC telescope. The reflector dish has a 17 m diameter and the camera is placed at a distance of 17 m ($f/D = 1$). The reflector is tessellated and composed by 956 mirrors of 0.5×0.5 m^2 area. The camera weighs $\simeq 0.5$ tons and contains the 576 photomultipliers and the optical converter that transmit the signal through a 160 m optical fibre. The structure is a CFRP space–frame plus some aluminum parts for connections and bearings. The structure is mounted alt–azimuthally and rotates on a 18 m diameter rail. More details are in the text. Picture from R. Wagner.

by a dome as is typical for optical astronomical telescopes. An enlarged picture of the first MAGIC I telescope is shown in Figure 2.2.

The telescope construction incorporates a number of "firsts" used in IACTs:

i) It has the world's largest mirror dish [4]

ii) It is the first time that a lightweight structure frame has been constructed from carbon fiber reinforced plastics (CFRP) [4].

iii) First use of diamond–turned light weight all–aluminum sandwich mirrors [5, 9].

iv) First use of an active mirror control to counteract small deformations of the 17 m ϕ mirror during positioning and tracking [11, 6],

v) First use of low gain hemispherical PMTs with diffuse lacquer coating and special light catchers resulting in increased quantum efficiency and allowing prolonged operation during modest moon shine [19].

vi) First use of a 2 GHz FADC digitization of the fast PMT pulses.

In the following, an overview on the technical solutions adopted for each subsystem is reported and discussed.

2.2.1 The Mounting and Drive System

The reflector frame satisfies at the same time four main demands: *a*) it is very large, *b*) it is light–weight, *c*) it is very stiff and *d*) it allows for fast repositioning. The space frame is made from carbon fiber reinforced plastic (CFRP) tubes and has a weight of only 5.5 tons. CFRP is a very strong but light composite reinforced fiber, similar to Fibreglass™. The tubes are joined with aluminum knots as shown in Figure 2.3(c). The CFRP construction is about three times stiffer and has less than a third of the weight of an equivalent steel construction [4]. The structure of an alt-azimuth design is mounted on a circular rail of 19 m ∅. The telescope can be moved from $-80°$ to $105°$ in declination and $450°$ in azimuth. The camera at a distance of around 17 m from the reflector is carried by a single aluminum tubular arc. The weight of the camera is around half a ton, and the small bending, unavoidable during the telescope tracking, is corrected via a re-orientation of the mirror. Two motors control the motion in azimuth and one motor the zenith motion with a maximum power consumption of ~ 7 kW per motor, see Figure 2.3(a), 2.3(b). The angular positions are controlled by absolute shaft-encoders of 14-bit precision/360°. In addition, a starguider camera, shown in Figure 2.3(d), mounted at the centre of the reflector, monitors the positioning of the telescope by viewing both the camera of the telescope and the corresponding section of the sky star-field [16]. The lightweight structure allows for very fast repositioning of the telescope to any position in the sky within ~ 30 s. This challenging feature was designed to instantly react to Gamma-Ray Burst (GRB) alerts from dedicated satellites detecting GRBs in the KeV/MeV domain.

2.2.2 The Reflector and Details on its Construction

The 17 m diameter reflector (17 m focal distance) follows a parabolic profile which was chosen to maintain the temporal structure of the shower light flashes. The reflector of MAGIC I is tessellated and comprises 956 mirrors with a total area of 234 m^2. Each mirror is a square of 0.495 m side length and has a spherical profile whose radius of curvature is optimized for the position in the telescope to best approximate the paraboloid. MAGIC I mirrors are grouped onto panels of 4 or 3 elements and each panel can be moved by the Active Mirror Control system (AMC) [6]. The AMC was designed to correct small deformations of the mirror support dish during telescope positioning and tracking. The mirrors are an all-aluminum, light weight sandwich construction composed of an Al-skin and an Al-box and filled with a Hexcell honeycomb structure [9]. A heating wire mesh, embedded in the sandwich, can be switched on in cases of dew or ice deposits on the mirrors. The total power consumption for heating the entire reflector is 40 KW. The reflecting aluminum surface of the mirror elements is diamond turned using the so-called fly-cutter technique, which provides an average roughness of 4 nm and a mean reflectivity of 85%. The surface of the mirrors was coated with a thin layer of quartz (with some admixture of carbon) for protection against corrosion and acid rain. Very little degradation ($< 3\%$/year) of the reflectivity was observed after 4 years exposure to the atmosphere at La Palma. The overall adjusted reflector has, for an infinite point-like source, a point spread function (PSF) of the reflected spot of ~ 10 mm ϕ at the camera of the telescope.

A more complete description of the telescope optics and mirrors, which is a relevant part of my PhD activities, is left to a dedicated section (Chapters 3 and 4).

2.2.3 Camera and read-out

The camera of the MAGIC I telescope has a 3.6° field of view (FOV) and comprises 576 photomultipliers with 396 $1' \varnothing$ PMTs from Electron Tubes Ltd of type 9116 covering the

(a) Azimuth motor

(b) Zenith motor

(c) CFRP tubes

(d) SBIG camera

Figure 2.3: The mount and drive system. In figure (*a*) one can see the azimuthal motor, mounted on the circular rail. In figure (*b*), the zenith motor drives the elevation and is mounted on the Gothic aluminum arc. Figure (*c*) shows the joints between the CFRP tubes and the aluminum knots and figure (*d*) shows the open box of the SBIG camera, which controls the active mirror repositioning system.

inner section up to 1.2° radius, and 180 PMTs of type 9117 and 1.5′ ∅ for the outer part of the camera. A sketch of the camera and the two PMT types are shown in Figures 2.4. The PMTs of a hemispherical cathode were enhanced in quantum efficiency (QE) with a diffuse lacquer doped with P–Terphenyl shifting the short wave UV component of the Cherenkov light into the spectral range of larger sensitivity [19]. In order to minimize losses due to the dead space between the densely packed PMTs, hex-to-round light concentrators were used, which added a further increase of the QE by deflecting many photons such that their trajectory passed the semitransparent photocathode twice. The mean QE of the entire system (mirror, camera window, cone, effective PMT QE) between 300 and 600 nm was 15%. The 6 dynode PMTs were operated at a gain of $\sim 3 \cdot 10^4$ in order to allow also observations at modest moon shine [1]. Finally, the fast PMT signals are converted back into optical signals by means of large dynamic VCsels operating in the analog mode and routed via 160 m long optical fibers to the 80 m distant counting house. At the counting house the optical signals are converted back into electronic signals, split and routed to the trigger branch and to the fast digitization and recording system. The trigger is two-fold: in level–0 the PMT analog signals are converted into logical signals once the signals exceed a 5-8 overlapping photoelectrons threshold. Level–1 is dedicated to the time-coincidence topological reconstruction of the signal in the camera:

when a number of pixels (adjustable by software) are activated at the same time according to the next-neighbor logic (2NN–5NN), a level-1 trigger signal is generated. The typical trigger rate is about 150-250 Hz interleaved by frequent calibration events. Upon triggering the data received by the telescope camera are digitized by ultra-fast Flash-ADCs of 2 GHz sampling rate. It has been around a year since this system has replaced the original digitizing system with a sampling rate of only 300 MHz and allows a much better timing measurement and a considerable reduction of the night sky light background.

(a) MAGIC I camera (b) MAGIC I PMTs

Figure 2.4: The camera system of MAGIC I. In figure (*a*), the camera before shipment. Inner and outer pixels, shown in figure (b), are mounted. The light–catchers (Winston–cones) are also mounted in front of the pixels. In figure (*b*), the two types of Electron Tubes PMT are shown. The larger one ($1.5' \varnothing$) is mounted on the outermost part of the camera, the smaller pixels ($1' \varnothing$) are mounted in the central part.

2.3 Telescope operations and data flow.

MAGIC I is operated through sequential runs. Each run is composed of three different items: the *pedestal run*, the *calibration runs* and the proper *data run*.

The pedestal run is taken with a fixed trigger frequency of 1 kHz. This corresponds to a random trigger with null probability of recording atmospheric shower events. The pedestal run is important to define the electronic noise of the entire read-out system. In particular, it is recalled that MAGIC PMTs are read–out in AC–coupling, where the reference ground value is arbitrarily fixed to a positive value that allows to keep the AC–signal positive all the time, which is needed for the FADCs. There are two types of calibration runs (in principle there can also be many more). One "extensive" calibration run is taken at the beginning of the observation of a new source during each night. A special combination of calibration LEDs are fired at a frequency of 50 kHz onto the camera. A dedicated trigger for the calibration system allows to completely reject all cosmics so that only calibration signals are recorded. If the camera is well flat–fielded, one would expect that the signal of all PMTs from a homogeneous light is the same. On the other hand, the PMTs, and in particular the PMTs operated in low–gain mode as for MAGIC, suffer from fast ageing and intrinsic fluctuations, which requires continuous monitoring. With the calibration light, one is able to artificially flat–field the camera by multiplying each and every PMT signal for a corrective factor. This factor can be calculated in different ways. The best–known method is the F–factor method, which uses an intrinsic PMT parameter called F–factor indeed. More details on the calibration system

can be found in my Diploma Thesis work [8] and in particular in the PhD Thesis work of M. Gaug. [12]. A second calibration run is taken as "interleaved" into the normal data, and is meant to monitor the correction factor during time. A second aim of the calibration system is to absolutely calibrate the camera, i.e. to find the conversion factor between FADC units and photoelectrons (or photons) hitting the PMTs. This is done with the use of three methods: the already mentioned F–factor method with the use of filtered pixels which observe the single photoelectrons, and with the use of a PIN–diode which measures the direct light from the calibration pulser and confronts it with the signal from a radioactive source.

The data are taken with a three level trigger: the first trigger is a level–0 discriminating trigger which accepts only PMTs illuminated above a certain threshold. The level–1 trigger is instead topological. It checks whether a number N of *next–neighbour* pixels are hot, and in this case triggers the acquisition. The term "neighbour" means that the pixels should have an adjacent hot pixel, and the term "next" means that the one pixels should have at least two close–by pixels, i.e. that the hot pixels cannot stay in a line but rather on a circular shape. Currently we operate with $4NN$ trigger logic. The third trigger level is currently transparent. For MAGIC II, a fourth level will select signals from the two telescopes.

After the PMTs, as already mentioned, the signal is transmitted through an optical cable and converted back into charge. The trigger permiting, the signal is digitized by FADC at 2 GHz and written on tape. Data are sent over day by Gbit connections to some nodes in Europe.

2.4 Principal design improvement for MAGIC II

The structure of the MAGIC II telescope clone, namely the foundations, and the telescope chassis with the space frame structure, are basically a perfect repetition of MAGIC I. They were assembled and mounted in La Palma already in 2006–07. On the other hand, all the other subsystems were substantially improved. Even if the telescope is still under commissioning, this overall enhancement should substantially increase MAGIC II performance, compared to MAGIC I, and cure some of its design weaknesses.

In the following, I will rapidly go over the subsystems, to explain the major activities carried out and the new solutions with respect to MAGIC I:

The camera A major effort was made to improve the MAGIC camera photon detection system. First of all, on the market there were already photomultipliers with quite larger quantum efficiency compared to MAGIC I EMI-Thomson devices [14, 17]. After a market selection Hamamatsu PMTs were chosen. Their photon conversion efficiency is 32% at 350 nm without lacquer coating, as shown in Figure 2.5, compared with MAGIC I pixels. All the PMTs have the same size of 0.1°. The number of PMTs has increased from 577 to 1039 in total. Also the triggers have been increased and now comprise 559 PMTs in the central camera. The design of the PMT housing has also been completely renewed. The PMTs are grouped into clusters of 7. Each cluster can be easily removed in case of problems. Inside the cluster, the HV is produced, a sampling signal can be injected to test the electronics after the PMT. The PMT is read via Lemo cables and controlled with Ethernet communication. The new camera will bring an increased effective area, and an increased signal to noise ratio. The MAGIC II camera was designed and realized by F. Goebel (in the picture) at MPI. For the future, it is also foreseen the replacement of the entire camera with an avalanche photon detector (HPD) Hamamatsu R9792U-40 [13, 18, 15]. This device is composed of a GaAsP photocathode, where the photon is converted into a photoelectron, which is subsequently accelerated directly by

an intense voltage drop of 8 kV. The electron hits an avalanche photon detector (APD) where the signal is amplified with a total gain of around 5,000. The HPDs have a much higher quantum efficiency than PMT, better single–photon resolution and are almost free of after–pulses.

Figure 2.5: The MAGIC II camera, trigger and photomultipliers photocathode efficiency.

Electronics The signal from the PMTs is transmitted via optical cable to the counting house, where receiver boards convert the signal back into charge, as for MAGIC I. The signal, after some trigger logic, is digitized with Domino III chips, which sample the signal at 2 GHz. The L1 trigger board (topological trigger) was adapted from MAGIC I for an increased trigger area. For the moment, the topological next–neighbors logic has been implemented, whereas different logics could be adapted in the future [7]. The calibration is performed with an ultra–bright laser mounted on the main reflector and controlled remotely. A diffusing sphere is mounted in front of the laser to illuminate homogeneously the MAGIC II camera.

Mirrors The MAGIC II reflector is composed of two types of mirrors: 143 full–aluminum mirrors similar to MAGIC I mirrors but with a larger area of 1 m^2 and improved design and 104 cold–slumped glass–aluminum sandwich developed at INAF–Milano. The work on MAGIC II reflector and mirrors is the most relevant activity I performed during the PhD. This is therefore, dealt with in greater detail in the following two chapters 3 and 4.

References

[1] J. Albert et al. Very high energy gamma-ray observations during moonlight and twilight with the MAGIC telescope. Submitted to Astrop. J., 2007.

[2] J. Albert et al. VHE Gamma-Ray Observation of the Crab Nebula and its Pulsar with the MAGIC telescope. *Astrophys. J.*, 674:1037–1055, 2008.

[3] C. Baixeras et al. Commissioning and first tests of the magic telescope. *Nuclear Instruments and Methods in Physics Research Section A*, 518(1-2):188 – 192, 2004. Frontier Detectors for Frontier Physics: Proceedin.

[4] J. Barrio et al. MAGIC Design Report. Available at http://wwwmagic.mppmu.mpg.de/publications/proposals/, 1998.

[5] C. Bigongiari et al. The magic telescope reflecting surface. *Nuclear Instruments and Methods in Physics Research Section A*, 518(1-2):193 – 194, 2004. Frontier Detectors for Frontier Physics: Proceeding.

[6] A. Biland et al. The Active Mirror Control of the MAGIC Telescope. In *Proc. of 30th International Cosmic Ray Conference, Merída, Mexico*, 2007.

[7] F. Dazzi. Private communication., 2008.

[8] M. Doro. The commissioning and characterization of the calibration system of the magic telescope. Master's thesis, Universitá degli Studi di Padova – Institut de Física des Altes Energies de Barcelona, Padova, Italy, 2004. Diploma Thesis. Available at http://wwwmagic.mppmu.mpg.de/publications/theses.

[9] M. Doro et al. The reflective surface of the MAGIC telescope. *Nucl. Instr. and Meth. in Phys. Res. A*, 595:200–203, Sept. 2008.

[10] M. Doro and E. Lorenz. Technical solutions for the magic telescope. In *Proc. of 10th ICATPP Conference on Astroparticle, Particle, Space Physics, Detectors and Applications, Como, Italy*, 2007.

[11] M. Garczarczyk. First observations of the grb prompt and early afterglow emission phase at $\sim$ 100 gev energy regime with the 17 m $\varnothing$ magic imaging atmospheric cherenkov telescope. Master's thesis, Max-Planck-Institut fuer Physik, Muenchen, Germany, 2006. PhD Thesis. Available at http://wwwmagic.mppmu.mpg.de/publications/theses.

[12] M. Gaug. Calibration of the magic telescope and observation of gamma ray bursts. Master's thesis, Institut de Física des Altes Energies, Barcelona, Spain, 2006. Available at http://wwwmagic.mppmu.mpg.de/publications/theses.

[13] M. Hayashida et al. Development status of high-qe hpds with 18-mm gaasp photocathode for iacts. *Nuclear Instruments and Methods in Physics Research Section A*, 572(1):456 – 458, 2007. Frontier Detectors for Frontier Physics - Proceedings of the 10th Pisa Meeting on Advanced Detectors.

[14] R. Mirzoyan et al. Enhanced quantum efficiency bialkali photo multiplier tubes. *Nuclear Instruments and Methods in Physics Research Section A*, 572(1):449 – 453, 2007. Frontier Detectors for Frontier Physics - Proceedings of the 10th Pisa Meeting on Advanced Detectors.

[15] R. Mirzoyan et al. Sipm and add as advanced detectors for astro-particle physics. *Nuclear Instruments and Methods in Physics Research Section A*, 572(1):493 – 494, 2007. Frontier Detectors for Frontier Physics - Proceedings of the 10th Pisa Meeting on Advanced Detectors.

[16] R. Mirzoyan, M. Garczarczyk, J. Hose, and D. Paneque. A method to measure the mirror reflectivity of a prime focus telescope. *Astropart. Phys.*, 27:509–511, 2007.

[17] R. Mirzoyan, M. Laatiaoui, and M. Teshima. Very high quantum efficiency pmts with bialkali photo-cathode. *Nuclear Instruments and Methods in Physics Research Section A*, 567(1):230 – 232, 2006. Proceedings of the 4th International Conference on New Developments in Photodetection - BEAUNE 2005, Fourth International Conference on New Developments in Photodetection.

[18] J. Ninkovic et al. The avalanche drift diode–a backilluminated silicon photomultiplier. *Nuclear Instruments and Methods in Physics Research Section A*, 572(1):454 – 455, 2007. Frontier Detectors for Frontier Physics - Proceedings of the 10th Pisa Meeting on Advanced Detectors.

[19] D. Paneque, H. J. Gebauer, E. Lorenz, and R. Mirzoyan. A method to enhance the sensitivity of photomultipliers for air cherenkov telescopes by applying a lacquer that scatters light. *Nuclear Instruments and Methods in Physics Research Section A*, 518(1-2):619 – 621, 2004. Frontier Detectors for Frontier Physics: Proceedin.

3
Optics of the MAGIC Telescopes

Despite the similarity with optical astronomical telescopes, Cherenkov telescopes have a much simpler construction and much lower optical quality demands. The internal fluctuations in the development of atmospheric showers make a higher resolution useless. Furthermore, the reflector is a compromise between different — and sometimes — competing factors, in particular between performance and costs. In this chapter we motivate the choice of the parabolic shape for MAGIC reflectors and discuss the annexed aberrations. We also motivate the choice of larger mirrors for MAGIC II with respect to MAGIC II and briefly present MAGIC II reflector design.

This chapter is adapted from *Studies on the mirror configuration of the MAGIC-II reflector*, 2006 [6], and *The Reflectors of the Imaging Atmospheric Cherenkov Telescopes MAGIC I and MAGIC II*, 2009 [7].

3.1 General considerations

MAGIC is a new generation imaging air Cherenkov telescope (IACT) for ground-based, very high energy (VHE) gamma-astronomy. The main mirror of the MAGIC telescope is quite similar to that of large optical telescopes. Nevertheless, there are quite a few different constraints that very much influence some design parameters, in comparison to optical telescopes.

i) Although one tracks in both cases very distant stellar objects, the light emitting sources are very different. In cases of optical astronomical observations one observes stellar light, which originates basically at infinity and is parallel. In the case of VHE gamma-astronomy one detects Cherenkov light emitted by an extended air shower initiated by gammas in the atmosphere, i.e. from a "close by" (5-20 km) region with a diffuse transverse extension and a typical length of a few km. Due to the stochastic showering process the light emission region will have an inherent limitation in precision (improving normally with the energy). The Cherenkov light is emitted with a small angle off the shower particle tracks, therefore while the single photons do not point directly to the source like in optical astronomy, nevertheless, the entire bunch of photons has a symmetry which can be traced back to the source. Its position has to be determined by a complex shower image analysis. A more detailed description of atmospheric showers is given in Appendix B.

ii) In optical telescopes the mirror precision is of the order of arcsec, and can almost reach the diffraction limit in cases of adaptive optics. The best possible optical resolution is required. In IACTs the observation of a "near" extended object allows for a mirror of lower optical quality and of a segmented construction, which may be composed of many small and therefore, less costly mirror facets that can even be staggered. Converted to the point spread function (PSF) requirements these conditions show that IACT mirrors can have a factor $100 - 500$ worse PSF compared to that of optical telescopes. The PSF of the mirror facets typically is 0.02° and that of the overall mirrors 0.05°.

iii) The tracking precision must be equally precise for optical telescopes. The tracking and stability requirements for IACTs are much less demanding compared to those of optical telescopes. Modern IACTs achieve a pointing resolution from single showers of $0.01 - 0.1^\circ$ (energy dependent) and typical one order of magnitude better resolution for the center of gravity of a large sample of showers.

iv) The Cherenkov light flux from VHE showers is extremely low. Therefore, very large mirrors are desirable and the construction of the telescope should minimize the loss of photons in the optical system and their conversion into photoelectrons. The overall photon detection efficiency for state of the art IACTs is only 10–15% when averaged over the spectral range between 290 and 600 nm.

v) In order to record the shower image in Cherenkov light one needs a "wide field" camera of at least $3 - 5^\circ$ field of view (FOV). For observing significant sections of the sky one would in principle need an even wider field camera. Unfortunately, this is very difficult to achieve. The use of Schmitt optics or a secondary mirror[1] are both very costly, require much more precise optical elements and would result in an additional loss of photons. The optical image quality at the rim area of the $3 - 5^\circ$ FOV camera should not be degraded too much. This requires a rather large f/D (≤ 1) in cases of single mirror optics. As cameras can be quite heavy, a strong and heavy camera support is needed. The structure has to be anchored to the mirror support dish resulting often in a large local mirror deformation.

vi) In IACTs the light sensors must have an ultra-fast response, of the order of a nanosecond, to very much reduce the large NSB, as well as provide some information about the timing structure differences in showers originating from different types of incident particles, while in optical telescopes sensors can integrate source photons over rather long times but the spatial resolution must be high. State of the art IACTs have pixels ranging between $0.05 - 0.2^\circ$ diameter; therefore, a PSF of similar size (ideally a factor 2 better) is sufficient. This allows for a considerably cheaper mirror construction. For large diameter mirrors a coarse isochronous mirror profile (< 0.5 ns time spread for a parallel light beam) is nevertheless required.

vii) Due to its very large dimension, MAGIC, as other large IACTs, has no protective dome. It is constantly exposed to the atmosphere, to wind and rain, temperature and intense sunlight and suffers much more aging than optical telescopes. The

[1] Currently, there is an ongoing study to design an IACT with a secondary optics for the AGIS project (http://gamma1.astro.ucla.edu/agis/index.php/Main_Page). The AGIS project is an array of very wide FOV telescopes, possibly with secondary optics layout, for future installation of IACTs in the United States of America.

reflectivity of the mirror surface is particularly affected by the impact of constant exposure to the ambient.

In addition, one of the main physics goals of MAGIC, besides the observation of steady or slowly flaring gamma-sources, is the (nearly real time) observation of gamma-ray bursts (GRB) and their prompt afterglow and has much influenced the design of the telescope. This requires the telescope to be repositioned as fast as possible to the sky position provided by an alerting satellite (typically within 10 s after the start of the outburst). To achieve a positioning time to any position on the sky map within much less than a minute requires both a very lightweight but sturdy telescope and a fast acting drive system (see more details below). MAGIC uses therefore, a low weight mirror, as well as a low weight mirror support frame made from carbon fiber reinforced plastic (CFRP) tubes. The space frame weighs only 5.5 tons. Nevertheless, it deforms by a factor 3 less than a steel construction of the same size of 27 tons. Other positive effects of the CFRP tubular construction are minimal thermal expansion and a high damping of oscillations.

3.2 The Overall Parabolic Mirror Shape

In Appendix B, it is shown that the Cherenkov photons come as a disk of photons with a width of a few meters which covers an area of around 10 m^2. Therefore, most of the time the light–rays hit the reflector at a tilted angle. While for vertical incidence the best reflective surface, aberrations free for light coming at infinity is a parabola (see Eq. C.7), soon when the impinging light is tilted, the effect of astigmatism and coma aberration become very relevant and deform the reflection at the focal plane. On the other hand, the spherical reflector is affected by very strong spherical aberrations already at vertical incidence and the aberrations increase with the telescope diameter.

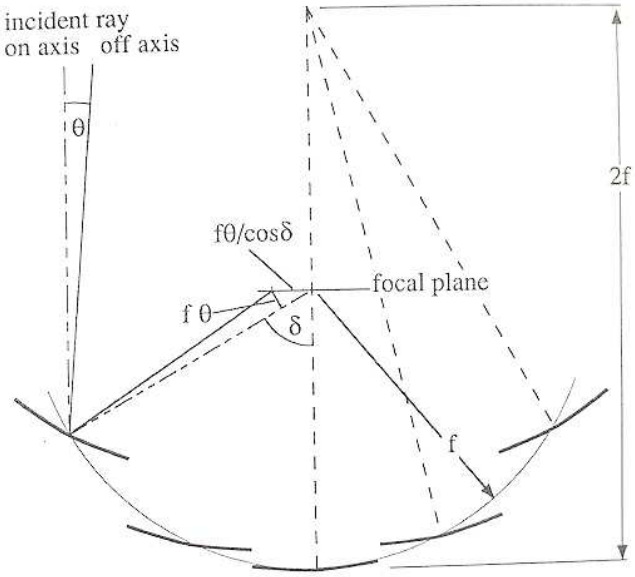

Figure 3.1: The Davies–Cotton mounting [5]. The spherical mirrors all of focal length f are arranged on a sphere of radius f and focused at $2f$ distance. This optics was originally developed for solar power concentrators and best performs for Cherenkov telescopes of $\varnothing \lesssim 10$ m. It is currently used by HESS and VERITAS. For larger surfaces, as for MAGIC, a parabolic profile is most recommended to maintain the temporal structure of the showers.

A brilliant solution was found by Davies and Cotton [5]. They developed a spherical reflector for solar power concentrators composed of mirror tiles arranged in a smart way, as shown in Figure 3.1. In this configuration, the mirror facets have as radius of curvature twice the radius of curvature of the overall reflector. Furthermore, they are mounted so that their

perpendicular points at a point twice the telescope focal length far from the reflector vertex. In this way, the center of the mirror, the center of the image in the focal plane and the point at twice the focal length form an isosceles triangle. The alignment is straightforward and the spherical aberration for vertical incidence is strongly reduced.

It was also demonstrated in the study of the optics for the Whipple telescope [9], that the Davies–Cotton layout is by far better than the parabolic profile even for off–axis light, at least for the Whipple reflector of 10 m diameter and 14.6 m focal plane. For this reason this design was used by almost all Cherenkov telescopes. Another study in the case of the HESS telescope is presented in Refs. [3, 4], while the HEGRA optics, with mirror facets of different curvature radii, was discussed in Ref. [1]. On the other hand, the mirror facets in the Davies–Cotton layout are arranged on a sphere and therefore, there is a time delay between light hitting the reflector at different positions, which was up to 6 ns in the Whipple case. For larger surfaces the delay is even larger. While this is of minor importance for the very optical image itself, it strongly competes with background discrimination, both from hadronic showers which develop differently in time, and from the night sky background light which is integrated over a larger time. In addition, the MAGIC collaboration recently showed that a precise reconstruction of the time evolution of the signal is a very useful estimator of the probability of an event to be a γ–ray or a hadron. The sensitivity can therefore, be increased almost by a factor 1.4 [2].

3.2.1 Preservation of the signal time–structure

The preservation of the time stamp of Cherenkov photons was probably the driving argument for the decision of the parabolic shape of MAGIC.

When the telescope dish becomes larger than $\simeq$ 10 m$\varnothing$, the time spread between light–rays hitting the reflector at the center and light–ray hitting the mirrors at the edges, becomes non–negligible. A spherical dish of 17 m diameter with an $f/D = 1$ would introduce a delay of tens of ns between photons at the mirror center and photons at the edge.

The reflector profile was therefore chosen to be parabolic, which is a good approximation with respect to an ellipsoidal shape[2]. It must be said that the increase time spread can be also mitigated with an increase of the telescope focal length, which also results in reduced optical aberrations. On the other hand, larger focal lengths directly imply technical problems for the displacement of the camera, and increased shadowing from the camera. A more detailed discussion will follow.

3.2.2 Optical aberrations

Optical aberrations greatly influence the quality of the reflected image and the capability of reconstruction of the primary particle parameters from its image at the focal plane. Nevertheless, while in cases of optical telescopes aberrations should be reduced as much as possible, as already discussed at the beginning of this chapter, in the case of IACTs the requirements can be relaxed. This is due to the location of the photon shower at 10 km altitude and its extension of a tenth of degree and most of all the fact that shower electrons and positrons undergo significant Coulomb scattering in their travel to the ground.

There is a vast literature on the theoretical treatment of optical aberrations. We have reported the basics of the aberration theory for a spherical and parabolic reflector in appendix C, on the basis of Mahajan [10]. The basic results for a parabolic reflector were that

[2]The paraboloid is in fact, the perfect surface that focuses parallel light coming from infinity

the surface is spherical aberration free, while the surviving aberrations, coma and astigmatism, can be described by the following wave–aberration formula, which we report here for readability:

$$W_{parabolic}(r,\theta,\beta) = \frac{1}{4f^2}\beta r^3 \cos\theta - \frac{1}{2f}\beta^2 r^2 \cos^2\theta \tag{3.1}$$

where r,θ is the coordinate of where the light hits the reflector, β is the light angle of incidence and f is the telescope focal length.

We also recall that the paraboloid is the perfect shape for focusing parallel light coming from infinity, or from the shower region at 10 km altitude. On the other hand, the effect of the coma aberration is quite determining for the image quality for tilted emission, which is the by–far most common case. The effect of coma has been simulated with a ray-tracing technique. A sketch of the aberration is shown in Figure 3.2.

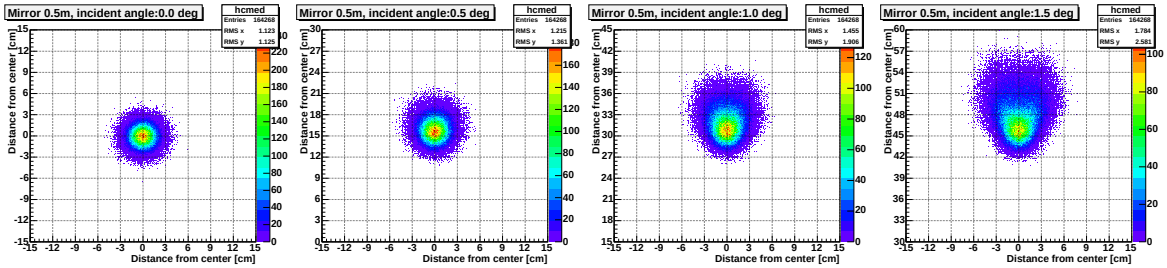

(a) $\theta = 0.0°$ incidence (b) $\theta = 0.5°$ incidence (c) $\theta = 1.0°$ incidence (d) $\theta = 1.5°$ incidence

Figure 3.2: The effect of coma aberrations for atmospheric showers observed at different impact parameters obtained with ray–tracing simulations of the MAGIC II reflector.

The coma aberration decreases almost linearly with the increase of the telescope $f-$number. On the other hand, as will be discussed below, there are competing problems, both technical and physical, that prevent from increasing the focal length of the telescope. The coma aberrations cannot therefore be avoided for larger telescopes. The effect of tilted incidence is usually neglected when discussing the optical quality of a Cherenkov reflector. Nonetheless, the image quality in most of the recorded events is much more determining. It should be recalled in fact, that the probability of having a photons shower aligned with the optical axis is far rarer than having showers at a certain distance from the optical axis, i.e. with non–null impact parameters. A discussion of what this implies for the MAGIC telescope is postponed to § 3.4, where MAGIC II reflector will be discussed. In the following, we limited to describe the effect of the principle aberration related to non–vertical light incidence.

Other aberrations

There are two sources of additional aberrations that come from the finite quality of the mirror surface, their being spherical instead of parabolic, and their possible misalignment.

Each mirror facet within the reflector does not have a parabolic profile but is simply spherical. The effect is that Cherenkov photons coming from the same shower are reflected at different points in the focal plane according to the mirror they were reflected by. The global effect is just a smearing of the image like for spherical aberrations. Two other facts determine a degradation of the reflected image: the finite precision in the optical quality of the reflective surface of the mirrors implies a non–point–like reflected spot at a focal distance, second, the finite precision in the orientation of the panel onto the camera of the telescope

also contributes to a smearing of the spot. It must be said that while the first effect cannot be corrected, the second contribution is constantly minimized by the active mirror control.

Problems concerning large telescope f/D ratio

From the above discussion, it has emerged that all aberrations are linearly reduced by increasing the focal length of the reflector or even better by increasing the f/d ratio. Nevertheless, an increase of the focal length has some drawbacks:

- an increase in the camera size is usually accompanied by an increase in its weight which creates serious technical problems in maintaining the camera position stable during operations, for example in order to avoid oscillations.
- an increase in the camera size also implies an increasing shadowing of the reflector with the net effect of loss of effective reflective area
- it is usually accompanied by an increase of costs

For these reasons, the f/D for MAGIC was kept at the minimum acceptable value, which was found to be $f/D = 1$, i.e., such that the camera is placed at 17 m distance from the reflector. Due to the effect of the coma aberrations, mostly the outer pixels in the camera contribute to image blurring. For this reason, there is no strong justification to use extremely small-size pixels, because some intrinsic image blurring is unavoidable. In the case of MAGIC I (and motivated by cost reduction) two pixel sizes were chosen, 396 inner pixels have a $\varnothing = 0.1^\circ$ and the remaining 280 outer pixels have instead $\varnothing = 0.2^\circ$. For MAGIC II all pixels in the camera have the same $\varnothing = 0.1^\circ$.

In addition, the parabolic shape is not even perfectly guaranteed by the fact that each mirror facet in the reflector has only a spherical profile rather than a parabolic one. In the case of MAGIC I a mirror facet has an area of around 0.25 m^2 while for MAGIC II the mirror facet areas are increased by a factor of four to 1 m^2. The outermost mirror facets in the reflector contribute most to the coma aberration. The deviation of the spherical shape compared to a paraboloid section in the outer facets of the mirror causes already some enlargement of the focal spot.

The question is: which is the best radius of curvature for a spherical facet to better approximate the parabola at a given position? For each position on the paraboloid in fact, not a unique local curvature can be defined. To solve this problem we follow a geometrical approach and make use of ray-tracing simulation, as explained in § 3.3.

3.3 Optimization of the radii of curvatures of mirrors

A paraboloid is the place of points that satisfies the relation $P(\alpha) = \alpha(x^2+y^2)\}$ and the points of the paraboloid have the coordinates $(x, y, \alpha r^2)$, where $\alpha = 1/(4f)$ and f is the focal length of the paraboloid; this means that the coordinates of the focus are $F = (0, 0, f) = (0, 0, 1/4\alpha)$. Excluding the center, all the other points of the paraboloid do not have a unique curvature. Out of the infinite possible radii of curvature, of common use is the so-called average radius of curvature, which is the average between the two principal radii of curvature: they are the maximum and the minimum of the local radii of curvature. In particular, the maximum radius is calculated using the intersection with a vertical plane (direction of the generator of the paraboloid or radial direction, hence the suffix r): $\rho_r = (1 + 4\alpha^2 r^2)^{3/2}/2\alpha$ and the minimum is taken along the plane perpendicular to the previous one: $\rho_p = (1+4\alpha^2 r^2)^{1/2}/2\alpha$.

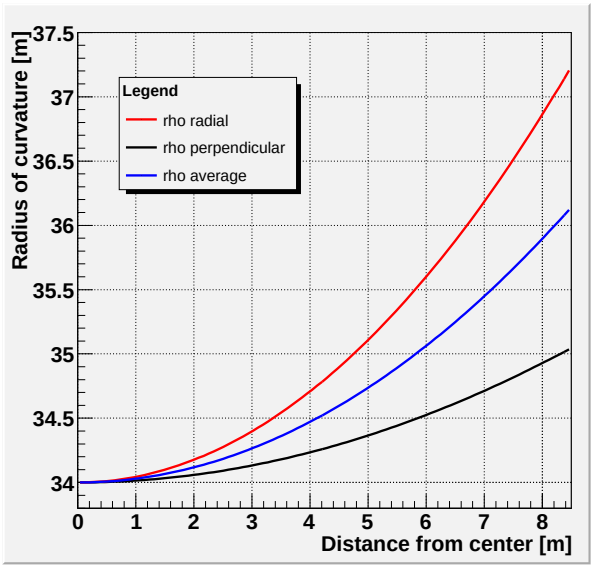

Figure 3.3: Principal and average radii of curvature of a paraboloid as a function of the distance from the optical axis for a paraboloid reflector of 17 m focal length as MAGIC and vertical incidence.

The following relation is valid: $\rho_r = (1 + 4\alpha^2 r^2) \cdot \rho_p$ and $\rho_2 < \rho_1$. The average of the two minimum and maximum radii of curvatures takes the definition of *average radius* and is obviously $\rho_a = (\rho_r + \rho_m)/2$.

The behavior of the above radii of curvature as a function of the distance from the center for the case of a paraboloid with focal length $f = 17$ m is shown in Figure 3.3. The difference between the two principal radii of curvature is maximal on the outer facet ring and is around 2 m. It is interesting to understand the different reflection obtained with different radii for vertical incidence. In the following, the reflection for the extreme cases of radial and perpendicular curvature is studied, together with the effect of the average radius. A ray–tracing program[3] was used. The reflection of single photons on the mirrors was studied on the focal plane. Around 10^4 photons per mirror (one every 2 cm) are reflected. The reflection is then artificially shifted on the focal plane in order to observe the contribution from the single mirror. Results are shown in Fig. 3.4. The x and y coordinates of the reflected spot are smeared with a two–dimensional Gaussian distribution of $\sigma = 3$ mm, which is about half of the real MAGIC dispersion, but is used here for clarity's sake.

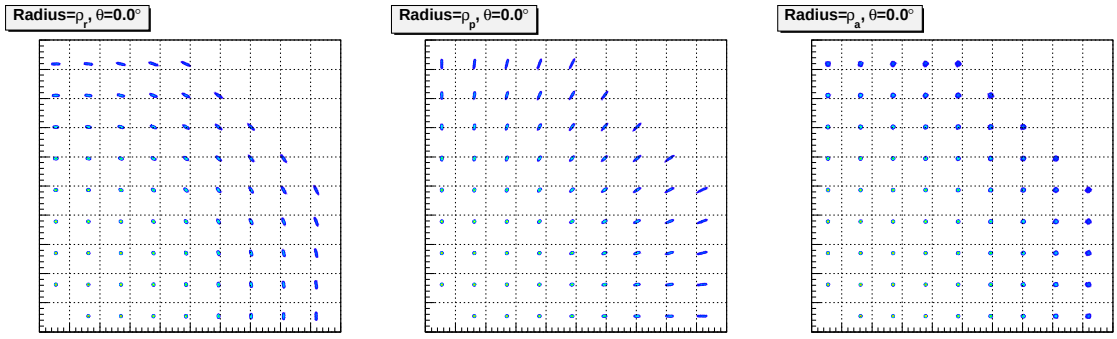

Figure 3.4: Reflection of the single mirrors in the focal plane for vertical incidence in the case of three different radii of curvature: ρ_r (left), ρ_p (centre), ρ_a (right).

[3]The original version of the macro was made by N.Tonello. The macro was adapted to simulate the MAGIC II reflector of all the mirrors of 1 m^2.

The explanation of the elongated shape of the reflected spot for ρ_r, ρ_p is natural: if the curvature is calculated along the radial (perpendicular) direction, this direction better resembles the parabola, such that photons reflected along this line are well-focused; photons impinging onto the mirror far from this ideal line are spread in the perpendicular (radial) direction. The effect is almost completely washed out when the average radius is used. In this case a compromise is taken and the reflected spot maintains a roundish shape. It should be noted that the average radius results in a nearly minimal time dispersion and was therefore chosen as curvature for the panels.

3.4 Impact of the use of larger mirrors on MAGIC II reflector

Small spherical mirror facets better resemble the paraboloid compared to larger spherical facets. This is quite obvious. On the other hand, the use of larger facets is motivated by a decrease of the number of items to be produced and installed, and in general by a decrease in costs. A compromise between size and quality must be therefore accepted. For MAGIC II, a configuration with larger mirrors, of 1 m^2 area, was tested with ray–tracing simulation. A discussion of the results of these tests is reproduced in the following section and taken from Ref. [6]. The reason for going to 1 m^2 area and not other sizes is related to the telescope frame. One can see in Figure 3.5 that the structure of the telescope is a grid of CFRP with a 1 m step. In the same figure some mirrors were already mounted. In the case of MAGIC I each position was occupied by one panel hosting four mirrors of 0.25×0.25 m^2 each, while for MAGIC II the size was upgraded therefore to 1 m^2.

Figure 3.5: MAGIC spaceframe structure

The simulation of the MAGIC reflector

The original idea was to simulate the reflective quality for three different layouts for the inner and outer half of mirrors in the MAGIC II reflector, see Figure 3.6:

I. All 1 m^2 mirrors for the entire reflector

II. Half innermost mirrors of 1 m^2 are and half outermost mirrors of MAGIC I size

III. A layout II, but the outermost mirrors made of aspherical 1 m^2 mirrors, i.e. mirrors with a different radius of curvature along the vertical and the horizontal axis.

Nevertheless, the results for layout I were satisfactory enough to overcome the necessity of investigating layout II and III. Furthermore, these two layouts would have required increased production problems and costs.

The simulation was performed with the use of the standard MAGIC Monte Carlo simulation chain. The `REFLECTOR` program is the second step of the MC chain, following `CORSIKA` that produces the Cherenkov light from the showers, and followed by `CAMERA`, which transform the photons in the focal plane of the reflector in events in the camera of the telescope [4]. Minor changes had been applied in the `REFLECTOR` in order to introduce the $1m^2$ mirrors, followed by a new software release. The simulation was carried out for the reflector layouts of MAGIC I (all the reflector composed by 964 mirrors of 0.5×0.5 m area) and MAGIC II (all the reflector composed by 249 mirrors of 1 m^2 area). For both configurations, two "operational" conditions were investigated:

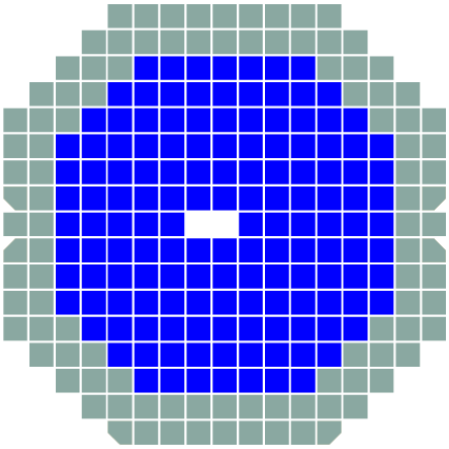

Figure 3.6: Mirror configuration of MAGIC II. The blue and gray parts comprise half of the reflector each.

- condition of *perfect* reflector,
- condition of *real* reflector

In the former case, the simulation takes into account a perfect spherical shape for the mirrors and a perfect alignment of the facets in the reflector. A more realistic scenario is that considered in the latter case, called "real". Inside the `REFLECTOR` code, this condition is introduced by putting two parameters: *a*) a parameter called `point_spread` is the *"point spread function, sigma in x and y on camera [cm]"*. This means that artificially the photon impinging the camera at a given position x, y is artificially moved in a direction according to a 2-dim Gaussian of sigma 0.5 cm. This value was decided after some considerations on the real reflected spot in the MAGIC camera[5]; *b*) a second parameter that gives information on the axis deviation for each mirror. For each mirror a pair of numbers is defined, giving *"the deviations in x and y of the spot of a single mirror on the camera plane. The numbers are taken at random from a Gaussian distribution n with sigma = 0.5 cm"*.

Composition of the reflected spot

The image on the camera due to a beam of parallel light coming from infinite is smeared due to aberrations. However, the contributions from the inner and outer halves of the reflector is different on the global reflected spot profile. This is shown in figure 3.7.

From figure 3.7 one can see how the outermost half contributes differently in cases of vertical and tilted incidence. In the case of vertical incidence, the contribution due to inner and outer halves is almost the same: the width of the two distributions does not differ too much. This is not the case in the rightmost plot. Here one can clearly see how the outer rings produce a shift of the image towards a larger radius, according to the theory of coma aberration. One can already see how this aberration dominates the point spread function for tilted incidence (see also figure 3.2).

[4]While `CORSIKA` is a standard Monte Carlo software for particle physics, `REFLECTOR` and `CAMERA` were developed inside the MAGIC collaboration. A complete description of the software can be found at the webpage http://wwwmagic.mppmu.mpg.de/documents/tdas_notes.html under private request. The relevant internal notes are MAGIC-TDAS 00-13 (H.Kornmayer), MAGIC-TDAS 01-04 (O.Blanch), MAGIC-TDAS 03-06 (O.Blanch) MAGIC-TDAS 04-07 (O.Blanch)

[5]The smearing introduced artificially with `REFLECTOR` contributes for about 0.7 cm PSF. Usually at the `CAMERA` level another 1.4 cm PSF is added to reproduce the real working condition PSF of MAGIC

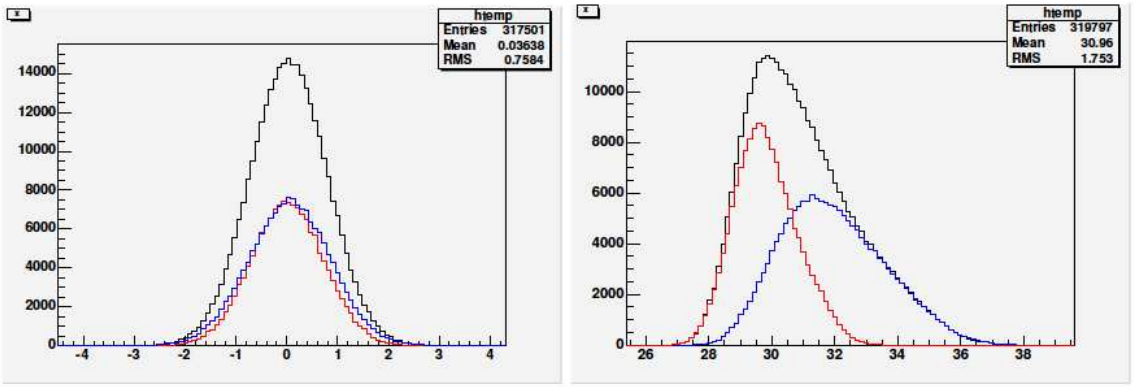

Figure 3.7: Contribution to the reflected spot by the inner half of the reflector (red line) and the outer half (blue line). In the left plot, the incidence is vertical. In the right one, the incidence is 1 deg. The $x-$axis is the position with respect to the center of the camera [cm]. In the case of the tilted incidence of the right plot the entire spot is shifted from the center.

Images of the reflected spot in the camera

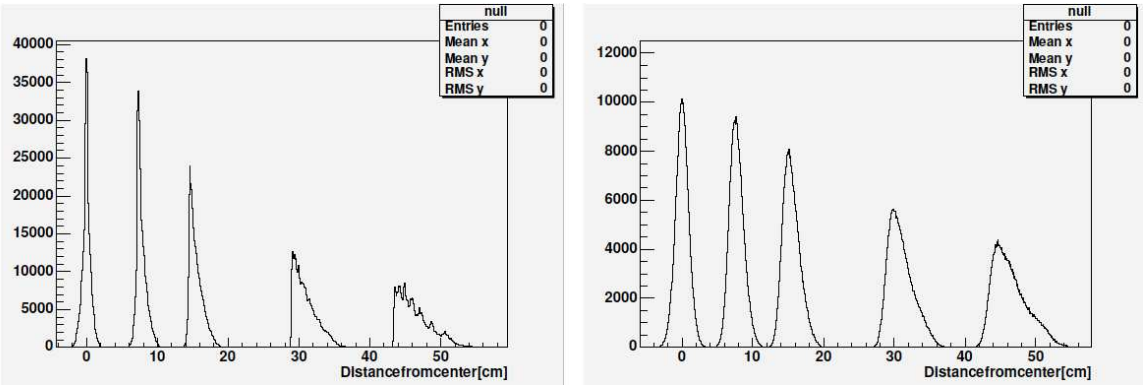

Figure 3.8: The profile of the spot at the focal plane for a different inclination of the light. *left* Perfect reflector with 1 m^2 mirrors, *(right)* Real reflector.

The behavior of the reflected spot at the varying incident angle, for the two layouts and for the case of a perfect and real reflector is given in Figure 3.8, basically intended to have a graphical impression of the way the spot profile changes at different incident angles. However, some effects can be here underlined:

- In the case of the perfect reflector, the spot profile presents some irregular peaks. These are due to the outermost part of each mirror, which is the part that is mostly different from the parabolic shape. In fact, one can see how the number of the peaks is clearly equal to the number of the rings of mirror of that size. This effect is washed out in the real reflector by the finite quality aberrations.
- The appearance of the spot in the case of the real and perfect reflector is strongly different. The enlargement is substantial. The spot characteristics are strongly modified by taking into account the optical quality of the mirror and the non-perfect alignment.

In figure 3.9 a comparison of the vertical and tilted incidence in the case of the real and perfect reflector is provided. Note that the vertical scale is different between the two figures,

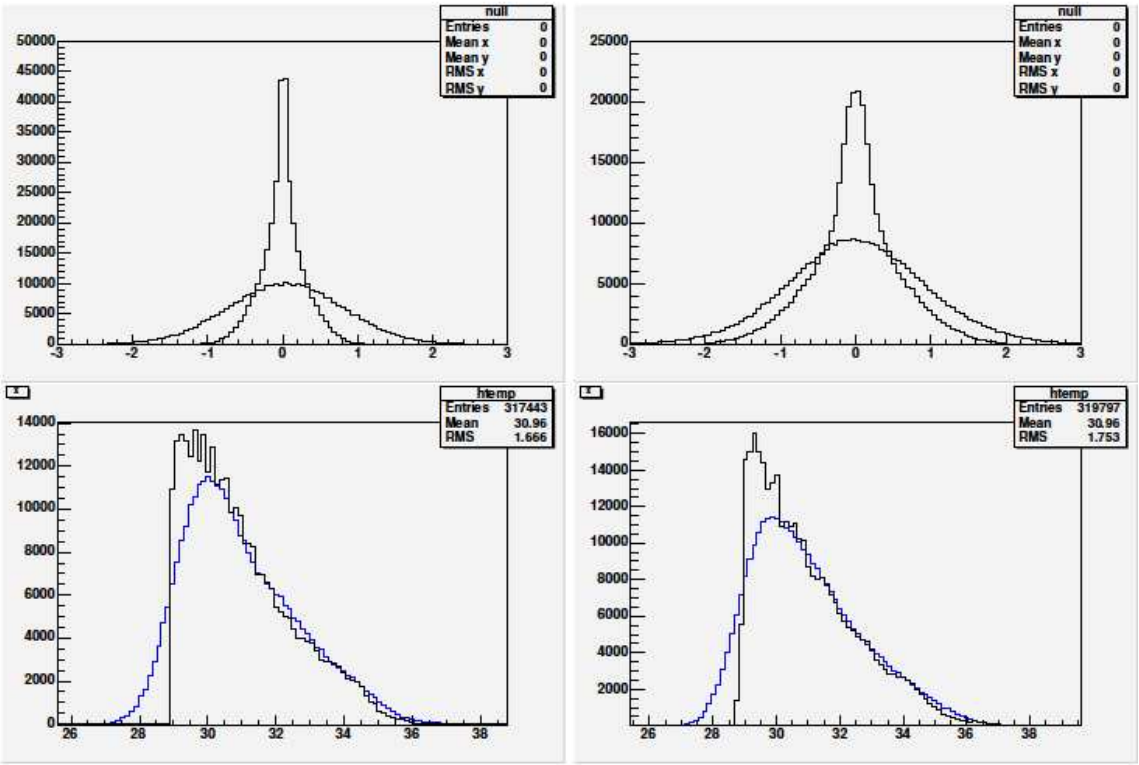

Figure 3.9: Performance of real reflector at different incidence angles. (left) 0.5 m mirrors. (right) 1 m mirrors. Topmost plots show the vertical incidence and downmost plot show an incidence angle of 1 deg.

while the integral is almost the same, so in the case of the perfect small mirror reflector the spot is really concentrated. Additionally, one can estimate how the smearing due to the real reflector broadens the spot, and that the difference is smaller when the light impinges inclined with respect to the telescope axis. Also, the first impression is that while the broadening of the spot due to the large mirrors in cases of a perfect reflector is high, this is not so much the case when the real reflector conditions apply.

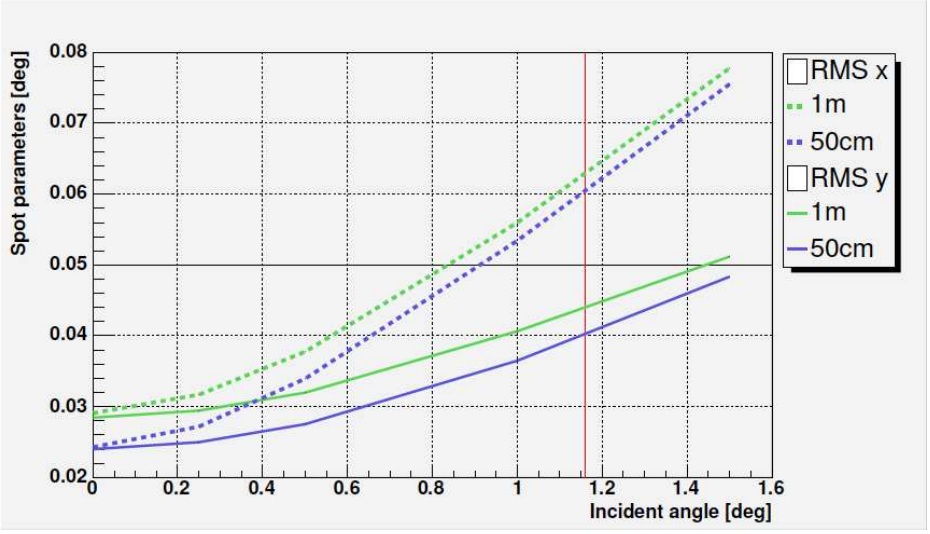

Figure 3.10: Behavior of spot parameters with incident angles and comparison between small and large mirrors configurations.

		Real reflector				Perfect reflector			
Size	angle [deg]	rmsX [cm]	rmsY [cm]	r50 cm]	r90 [cm]	rmsX [cm]	rmsY [cm]	r50 [cm]	r90 [cm]
1 m^2	0.0	0.91	0.89	0.90	1.80	0.56	0.56	0.48	1.14
	0.25	0.99	0.92	0.90	1.86	0.67	0.60	0.54	1.56
	0.5	1.18	1.00	1.02	2.28	0.93	0.72	0.72	2.22
	1.0	1.75	1.27	1.44	3.90	1.59	1.07	1.44	4.14
	1.5	2.43	1.60	2.04	5.82	2.32	1.47	2.46	6.48
0.25 m^2	0.0	0.76	0.75	0.72	1.44	0.28	0.28	0.18	0.54
	0.25	0.85	0.78	0.84	1.62	0.46	0.36	0.36	1.14
	0.5	1.06	0.86	0.96	1.98	0.79	0.52	0.78	2.10
	1.0	1.67	1.14	1.32	3.60	1.50	0.93	1.56	4.20
	1.5	2.36	1.51	1.86	5.46	2.25	1.36	2.34	6.30

Table 3.1: Characteristics of the spot sizes for both the real and perfect reflectors and for small and large mirror configurations. $rmsX, rmsY$ are the RMS along the $x-$axis and the $y-$axis of the spot size. $r50, r90$ are the radii of a circle containing 50% and 90% of the total photons respectively.

In table 3.1 a comparison of the spot characteristics is provided for different angles and both cases of real and perfect reflectors are shown graphically in Figure 3.10.

Let us now analyze the deterioration of the image parameters between small and large mirrors. It is expressed as a percentage of the new parameter with respect to the old one.

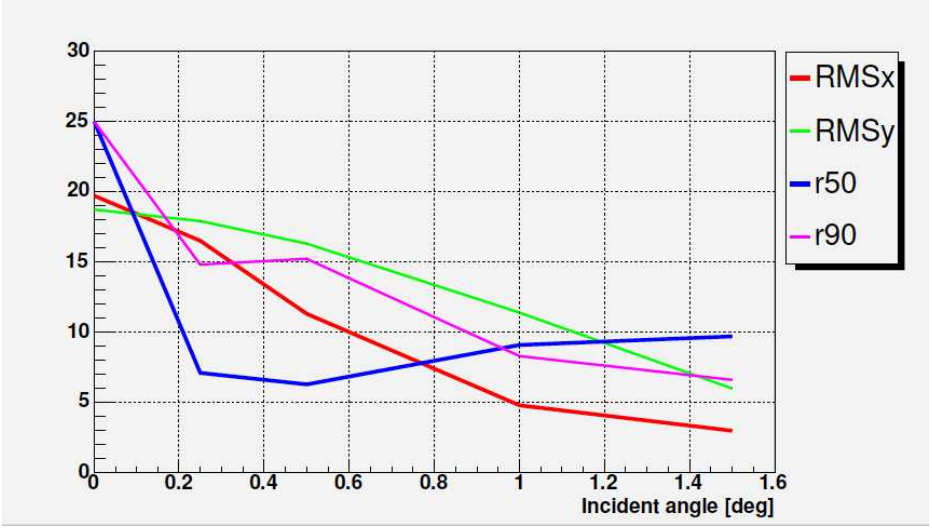

Figure 3.11: Percentage worsening of the spot size with different incident light angles..

One can clearly see from figure 3.11 how fast the degradation is becoming smaller as the incident angle grows. If one wants to estimate an overall degradation parameter, one must take into account also how many times a light ray impinges on the reflector under a certain angle. This of course, depends on the lateral distribution of the showers and the distribution of the impact parameter, which differ from gammas to hadrons, and additionally it depends on the active trigger region in the camera. Thus the camera occupancy is not unique and could differ from MAGIC I to MAGIC II.

It is thus clear that the central camera is the most used, and this is even more valid in cases of low energy showers, which tend to concentrate in the central pixels. In this region,

the performance of the new configuration remains good. This is definitively a good sign to go for an homogeneous reflector all constituted by 1 m^2 mirrors.

3.5 The MAGIC I reflector and its optical performance

MAGIC I is composed by 964 full–aluminum mirrors, 0.5×0.5 m^2 area each, of two slightly different designs. They will both be addressed and discussed in Chapter 4. In this section, I will briefly show how these mirrors were arranged and I will describe the results of some monitoring activities that took place after their installation. In Table 3.2 one can find a more detailed list of the mirrors installed in MAGIC I. In particular, the small mirrors of MAGIC I were installed onto panels. Each panel hosted 3 or 4 mirrors according to its position. A sketch on how they were mounted is shown in Figure 3.12. I want to underline, that the characterization of the optical performance and of the MAGIC I reflector is a fundamental task that qualifies the reflector itself and possibly the entire experiment. This activity was performed by a team of persons, mainly constituted by A. Biland and M. Garczarczyk. A more detailed description of the monitoring activity is reported in Ref. [8].

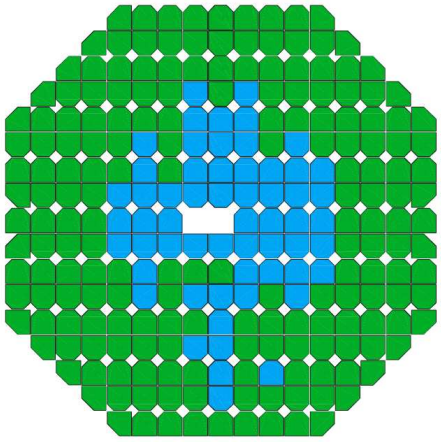

Figure 3.12: Arrangement of full aluminum mirrors on the MAGIC I telescope. MPI mirrors are shown in blue and INFN mirrors in green.

	4–panel	3–panel	N_{mirs}	%	[m^2]
INFN mirrors	165	24	740	23%	179
MPI mirrors	58		224	76%	55
Total	223	24	964	100%	**236**

Table 3.2: Summary of panel and mirror installation for the reflector of MAGIC I for the two designs of MPI and INFN–Padova.

3.5.1 Monitoring activities

Mirror staggering The design of the panels that group 3 or 4 small mirrors for MAGIC I was aimed to minimize the physical gap between mirrors in order to reduce the overall light loss. Nonetheless, this spacing resulted to be too small and panels were touching one another during operation. After MC simulations, the mirrors were *staggered*, i.e. shifted 20 mm backward, or 60 mm forward, according to their position. The time delay introduced in such configuration did not affect the image reconstruction for γ–rays and hadrons, and only slightly degraded the reconstruction of muon showers. Since 2005 we have been recording data with staggered mirrors. The staggering is clearly shown in Figure 3.13.

PSF monitoring The PSF of the reflector is the distribution of photons from a point–like source at the focal plane. It usually is bell–shaped and is fitted with a 2–dim Gaussian function. The PSF of the reflector directly affects the PSF of the telescope. This is defined in the following way. The reconstruction of the direction of a primary γ–ray is performed through

Figure 3.13: The staggering of MAGIC I mirrors. The mirrors are shifted 60 mm forward or 20 mm backward with respect to the original position, without causing any degradation in image reconstruction.

image analysis. As a result, a gamma ray coming from a direction ψ' will be reconstructed to a direction ψ in the sky with a probability distribution that can be fitted to a Gaussian function:

$$B_{\vartheta_r}(\psi' - \psi) = \frac{1}{2\pi\vartheta_r^2} \cdot \exp\left(-\frac{(\psi' - \psi)^2}{2\,\vartheta_r^2}\right). \tag{3.2}$$

The standard deviation ϑ_r of the Gaussian corresponds to the telescope angular resolution, also called Point Spread Function (PSF). As a consequence, any source will appear somewhat blurred. The telescope PSF is also called the *angular resolution* of the telescope. Any target morphology smaller than the telescope angular resolution cannot be correctly reconstructed. In addition, all sources less extended than the angular resolution are considered as point–like. On the center of the reflector, a high sensitive CCD camera is mounted, as already shown in Figure 2.3(d). The aim is to record the image of the reflected light from stars (point–like object) on the focal plane.

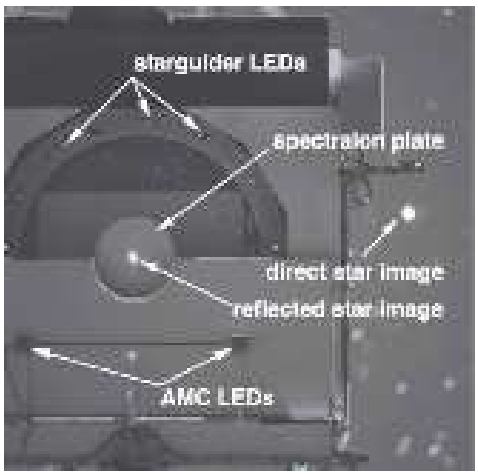

Figure 3.14: The starguider system. From [8].

The result of the monitoring of the PSF over some years of operation is shown in Figure 3.15. During the first years of operation, the PSF systematically increased due to inexperience with the active mirror control and the mentioned problem of mirrors touching themselves. After the staggering, the PSF was kept as stable as possible (different PSFs affect the analysis). Thereafter, the PSF was maintained below 10 mm at the focal plane.

3.6 The arrangement of the MAGIC II reflector

The MAGIC II reflector is composed of 1 m^2 mirrors, as an outcome of § 3.4. On the other hand, MAGIC II has also different types of mirrors: the central part of the reflector is made of 143 full–aluminum 1 m^2 mirror of a similar design as for MAGIC I. The outermost

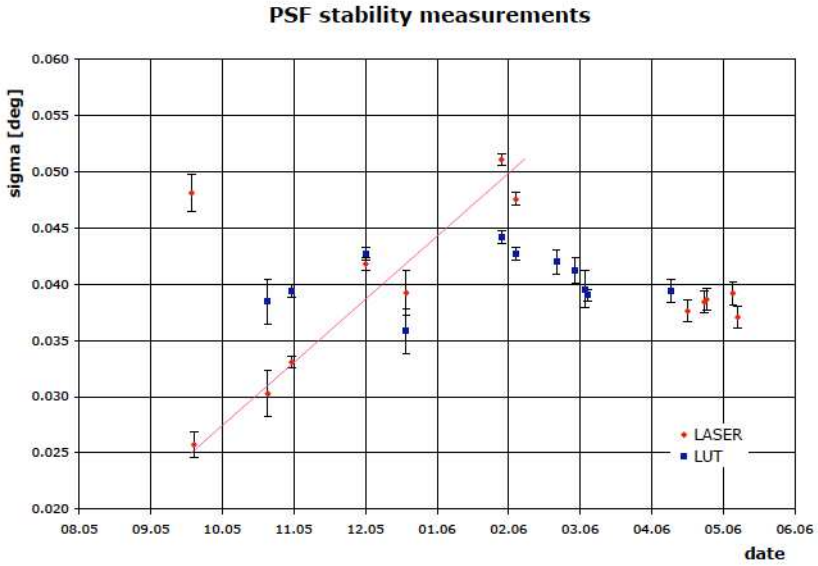

Figure 3.15: Long-term behavior of the PSF measured with the SBIG camera. The PSF obtained with laser focusing (red points) and look up tables focusing (blue points) is shown. The red line indicates the degradation of the laser focusing with the time. [8].

part (104 mirrors) of the reflector is composed of cold–slumped glass–aluminum sandwich mirrors designed and produced by INAF and the Medialario company in Milan (Italy). Both techniques will be described in Chapter 4.

The number of mirrors of each type was decided by budget constraints and political issues. It was decided to use glass mirrors on the edge for two main reasons: *a*) 6 of the mirrors on the edge must be cut at an angle. They correspond to the panels in MAGIC I that housed 3 mirrors instead of 4. The angles must be cut to leave space for the telescope structure. *b*) originally, aluminum mirrors were produced before glass mirrors, and it was easier to proceed for installation from the center outwards.

The mirror mounting is very similar for the two mirrors, with three mounting pads mounted on the back of the mirrors which connect the mirrors to the structure through the actuators of the active mirror control. This will be shown in § 4.5. It is only underlined here that while all INFN mirrors have the same arrangement for the mounting pads, 24 INAF mirrors have the pads fixed at different positions on the back to be placed in the edgemost tubes of the telescope. These mirrors are shown in dark green in Figure 3.16.

3.6.1 Mirror position adjustment

The location of all the mirrors in the telescope is decided via an optimization procedure which minimizes the discrepancies between the *nominal radius of curvature*, associated for the position $x - y$ in the telescope (i.e. the average radius of curvature of the paraboloid calculated in the position $x - y$ corresponding to the center of the mirror), and the *measured radius of curvature* of the mirrors. In other terms, ΔR was minimized.

$$\Delta R = |R_{ideal} - R_{measured}|$$

The optimization procedure was defined and written on a program procedure. For the aluminum mirrors, we had only 1 spare mirror to play with, while for the glass mirrors, we

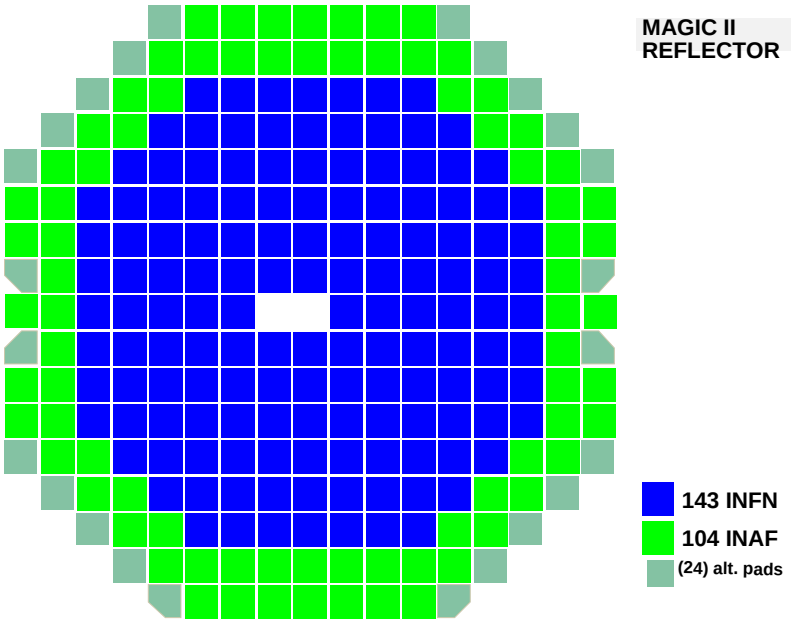

Figure 3.16: Arrangement of full aluminum (INFN) and glass (INAF) on MAGIC II. An optimization procedure was set to optimize the positioning of each mirror in order to minimize the difference with the nominal radius of curvature. Dark green mirrors are glass

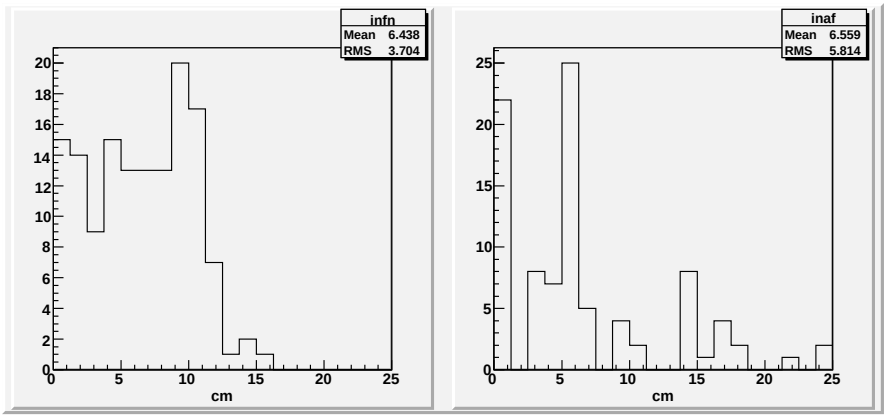

Figure 3.17: Discrepancies between nominal and effective radii of curvatures for the positions on the MAGIC II reflector for INAF and INFN mirrors.

had around 10 spare mirrors. In both cases, a table for the installation was provided. The optimization of the positions led to the results shown in Figure 3.17 where the discrepancies between nominal and effective radii of curvatures for INFN and INAF mirrors are shown.

From the figure one can see that the discrepancies are usually below 15 cm. Given the notation in the Figure 3.18, if ΔS is the increase spot size, therefore $\Delta S \approx \theta \Delta f$, where f is the focal length. Now, $\theta \approx 1/17$ and $\Delta f = \Delta R/2$. Therefore $\Delta S = \Delta R/(2 \cdot 17)$. A difference $\Delta R = 15$ cm, at the focal plane reflects into an increase of 5 mm of the spot size.

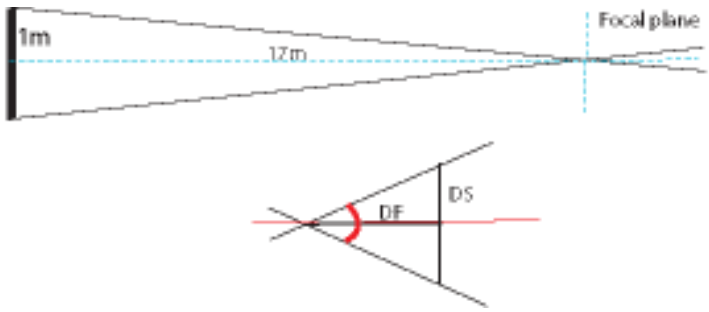

Figure 3.18: Propagation of a mismatch in the radius of curvature to the spot size.

References

[1] A. Akhperjanian, R. Kankanian, V. Sahakian, A. Heusler, C.-A. Wiedner, and H. Wirth. The Optical Layout Of The HEGRA Cherenkov Telescopes. *Experimental Astronomy*, 8:135–152, 1998.

[2] E. Aliu et al. Improving the performance of the single-dish Cherenkov telescope MAGIC through the use of signal timing. 2008.

[3] K. Bernloehr et al. The optical system of the HESS imaging atmospheric Cherenkov telescopes. I: Layout and components of the system. *Astropart. Phys.*, 20:111–128, 2003.

[4] R. Cornils et al. The optical system of the HESS imaging atmospheric Cherenkov telescopes. II: Mirror alignment and point spread function. *Astropart. Phys.*, 20:129–143, 2003.

[5] J. Davies and E. Cotton. *J. Solar Energy Sci. and Eng.*, 1:16, 1957.

[6] M. Doro. Studies on the mirror configuration of the MAGIC-II reflector. MAGIC-TDAS 060704/MDoro. Private use at http://wwwmagic.mppmu.mpg.de, 2006.

[7] M. Doro et al. The Reflectors of the Imaging Atmospheric Cherenkov Telscopes MAGIC I and MAGIC II. Under publication in Journal of Instrumentation.

[8] M. Garczarczyk. First observations of the grb prompt and early afterglow emission phase at $\sim$ 100 gev energy regime with the 17 m $\varnothing$ magic imaging atmospheric cherenkov telescope. Master's thesis, Max-Planck-Institut fuer Physik, Muenchen, Germany, 2006. PhD Thesis. Available at http://wwwmagic.mppmu.mpg.de/publications/theses.

[9] D. A. Lewis. Optical characteristics of the Whipple Observatory TeV gamma-ray imaging telescope. *Experimental Astronomy*, 1:213–226, 1990.

[10] V. N. Mahajan. *Aberration Theory Made Simple*. SPIE Optical Engineering Press, 1991.

4

The Mirrors of the MAGIC Telescope

The design, production, testing and installation of the mirrors for the second MAGIC telescope, dubbed MAGIC II, constituted my major research activity. The design of the new mirrors was subject to major improvements with respect to former MAGIC I mirrors. The production was externalized to a private company which was searched for on the market. Several tests for optical and mechanical qualification were performed at the University of Padova, at the LT-Ultra company and at the Max Planck Institute in Germany. I also managed and participated in the installation of the mirrors on the second telescope which was completed in July 2008. MAGIC II also hosts new design cold–slumped glass mirrors, developed at INAF–Milan. I performed some quality tests and participated in the installation of these innovative mirrors. In this chapter, the general design considerations and the mirror design will be reported. Details on the production and tests will also be given.

This chapter is adapted from: *The reflective surface of the MAGIC telescope*, 2008 [8]; *The Reflectors of the Imaging Atmospheric Cherenkov Telescopes MAGIC I and MAGIC II* [6] and *Glass Mirrors by cold slumping to cover 100 m^2 of the MAGIC II Cherenkov telescope reflecting surface*, 2008 [13].

4.1 MAGIC I mirrors

The development of MAGIC I mirrors started already at the beginning of the design consideration of MAGIC I, early in 1997. The technique was originally developed at MPI, where the initial design and study of materials were performed. Later on, INFN–Padova took the responsibility for the production of the mirrors. As a result, two slightly different designs of mirrors were mounted on the telescope, as will be discussed below. The MAGIC I mirrors have been presented on many occasions. The basic references are the MAGIC design report [2], conference proceedings [5, 4, 3, 9, 7], published general MAGIC contributions [1, 8] and diploma and master thesis [10, 12, 11]. A comprehensive document of MAGIC I mirrors is currently under edition [6]. In this section, I will briefly present the major design considerations of MAGIC I mirrors without entering into detail. This information is used for further considerations. All details about the design of aluminum mirrors are presented in § 4.2.

MAGIC I mirrors are composed of a sandwich of two thin aluminum layers interspaced by a honeycomb structure that ensures rigidity, high temperature conductivity and low weight,

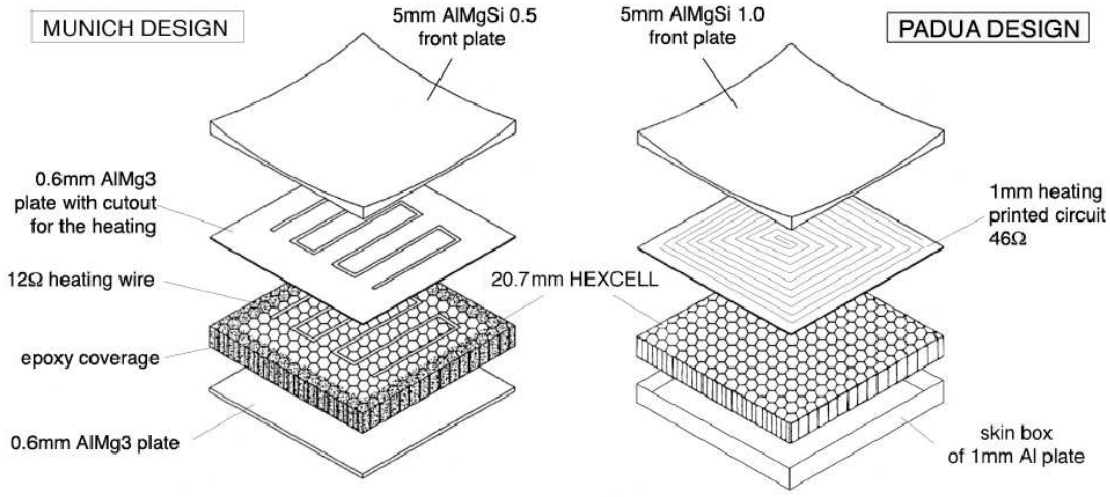

Figure 4.1: The two designs of MAGIC I mirrors: MPI design (left sketch) and INFN design (right sketch).

see Figure 4.1. Two slightly different models were used in MAGIC I: 224 mirrors following a design by MPI–Munich and 740 mirrors designed at INFN–Padova. The skin is a flat square 5 mm–thick AlMgSi–alloy of 495 mm side, with different Si contamination for the MPI and INFN mirrors. The contamination is an extremely relevant fact to guarantee good machinability and resistance to atmospheric conditions. A detailed discussion of the material selection and first tests is found in [2, 6]. A bottom aluminum counterpart is a 2 mm thick plate in the case of the MPI design and a 2 mm thick aluminum box for the INFN case, that encloses the sandwich. In between the two layers, a micro–holed hexcell–honeycomb type 5.2-1/4-003P, 20.7 mm thick is inserted. Between the upper plate and the hexcell a heater board is placed: it consists of a 0.6 mm thick AlMg plate with 12 Ω heating wire in the MPI design, while, for the INFN mirrors, it has a 1mm thick Printed Circuit Board with a 46 Ω impedance. The aim of the heater board is to eventually warm the mirror in order to avoid dew and ice formation. The aluminum parts are glued with the 3M™ Scotch–Weld structural adhesive AF-163-2K specific for aeronautic applications. In the case of MPI mirrors, an additional injection of epoxy foam coverage is done on the perimeter of the mirror for water tightness.

The assembly is sandwiched between two heavy aluminum moulds and the ensemble is enclosed in a vacuum plastic bag. The packet is put in an autoclave, the air is sucked out of the bag to exert pressure on the sandwich, and then a cycle of high temperature and pressure cures the structural glue: As a result a so-called *raw–blank* is produced.

After a rough pre-milling that ensures an approximate curvature of 35 m to the aluminum surface, the mirror is milled with precision by using a diamond-milling machine (see Figure 4.2), which provides high reflectivity and a slightly different focal length to fit the overall parabolic shape on the reflector. The final roughness of the surface is around 4 nm and the average reflectivity 85%. In addition, a thin layer of quartz (with some admixture of carbon) around 100 nm thick is vacuum–deposited for protection against corrosion and acid rain. On average, the reflected light of MAGIC I mirrors is focused within 1 mrad corresponding to 17 mm at the camera focal plane. Each mirror has an approximate weight of 3 kg.

The mirrors are then grouped into panels of 3–4 elements. This required the construction of an additional panel (also a light-weight honeycomb structure) and foresaw an interalignment

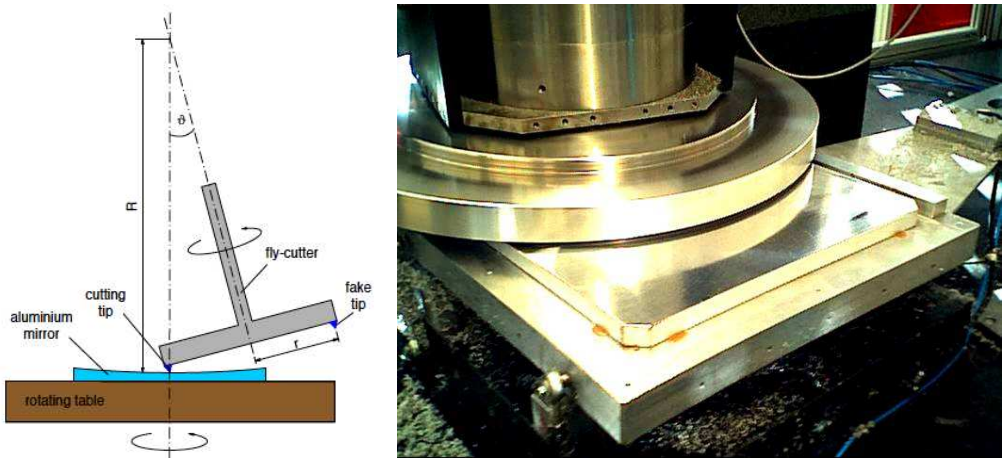

(a) The fly–cutter technique (b) The diamond–milling machine for MAGIC I mirrors

Figure 4.2: (a) Scheme of the fly–cutter technique for MAGIC I mirrors. The angle between the machine head axis and the vertical determines the mirror radius of curvature. The diamonds are mounted on the machine head. From [11](b) Picture of the milling–machine for MAGIC I mirror in operation.

(a) Panel front (b) Panel side (c) Panel mounted

Figure 4.3: Three sketches of the panels onto which the mirrors are mounted. (a,b) the panel viewed from the front and from the side respectively, (c) the panel mounted on MAGIC I.

procedure of the mirrors within the panel, to be done before the mounting. This is shown in Figure 4.3. The use of this panel resulted in some problems during the assembling and had some drawbacks:

- The interalignment is time consuming
- In some cases the fixation of the mirrors inside the panel was not tight enough and this resulted in an overall large telescope point spread function during commissioning, which was corrected by a second fixation of mirrors inside the panel
- The panel adds weight to the structure and the mounting of the structure panel plus mirrors is rather slow.
- The mounting of the mirrors inside the panel is extremely complicated and time consuming directly on the telescope. Exchanging single mirrors inside one panel is therefore very deplorable.

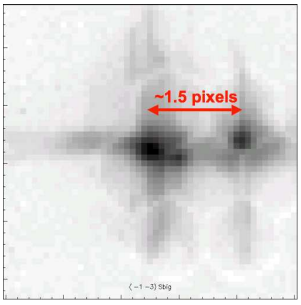

Figure 4.4: The reflection of a panel with one misaligned mirror.

The effect of mirror misalignment inside a panel is clearly shown in Figure 4.4. There one can see the reflection of one single panel at the focal plane. It is clear that while three mirrors are correctly focused on the main central position, one mirror points to a different position on the right at a distance of about 1.5 pixels. In this case, the reason was a loose screw, which was finally solved with a stronger fixation. Nevertheless, this picture shows the risks associated with this procedure. From the same figure, one can also see a cross of dispersed light centered around the spots. This effect is due to a wrong machining of the mirror perimeter, but the effect is marginal in term of light loss (few ‰).

The panel is therefore, fixed to the telescope structure using the AMC system that can correct its precise orientation to counteract for the sagging of the structure during change of the orientation, see § 4.5.

4.1.1 Insulation problem and an upgraded design

Figure 4.5: A damaged mirror from MAGIC I. The bubble created by the internal accumulation of water condensating into ice is clearly visible on the back side.

After the second winter of operation, some mirrors started to show localized deformations on the upper or lower surface, as shown in Figure 4.5. Fortunately, these local deformations always affected less than about 30% of the reflective surface. The reason for the creation of these "bubbles" was water or more likely the humidity entering the mirrors from very small fissures in the sealing. The humidity entering the mirror was free to propagate inside Due to the micro–holes in the honeycomb structure. On the other hand, when in the liquid form, water was not allowed to cross honeycomb cells significantly. For this reason, when water converted into ice, its pressure was exerted on the surfaces which resulted in the appearance of the bubbles. In some cases, the amount of water present inside some mirrors was very large (up to around 1 liter!). As a confirmation of the fact that water was not freely moving inside the mirrors, we observed that the bubbles normally appeared on the edges of the sandwich rather than at the center. Although the first impression was that the mirrors were completely damaged, it was observed that the deformations were only affecting *locally* the surface. Due to the rigidity of the mirror structure, guaranteed by the honeycomb inside, the deformation did not propagate on all the surface. As a result, the appearance of a bubble in one mirror was affecting only less than $10 - -20\%$ of the reflective surface, which summed up over all

the damaged mirrors gives a maximum loss of reflective surface of a few percent for the whole reflector. For this reason, the mirror substitution was not that urgent and a new mirror design was properly studied to solve the problem.

The following design variations were considered: *a*) the upper aluminum plate was made a little larger than the mirror box. This allowed to properly deposit an adhesive on the mirror perimeter to seal the structure. *b*) the upper aluminum plate was made thinner, in order to avoid the pre–milling of the surface. The mirror is sandwiched between two heavy aluminum moulds, that are already curved at 35 m radius. The upper plate therefore bent under the force of vacuum creation. To allow for a small bending of the bottom box, small fissures were striped on the box edges which were then sealed with an epoxy glue.

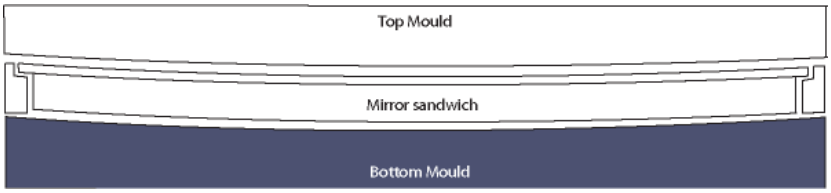

Figure 4.6: Design and production of the MAGIC I upgraded mirrors

Figure 4.6 shows a sketch of the new MAGIC I mirror assembly technique. In October, 2005, 41 mirrors were replaced, and an additional 46 were exchanged in July 2007 for a total of 87 mirrors out of the overall 964 installed. It is foreseen to exchange another 50–100 mirrors in the future and these will probably be substituted by larger mirrors as for MAGIC II. The solution of a thinner aluminum plate resulted in higher quality work at the diamond milling machine, mainly because the internal stresses due to the grinding were avoided. In addition, the overall production became faster.

4.1.2 Reduced mirror ageing

The single mirror reflectivity can be monitored after mounting on the telescope by active mirror control. If the telescope is pointed to a star, it is possible to defocus all mirrors but one. The comparison of the reflected image on the camera of the single mirror with the image of the star allows both to measure the absolute reflectivity and to monitor it during time. The procedure was followed in the past by M. Garczarczyk. Results are described in Ref. [11]. In addition, when focusing all the mirrors properly in the camera, one can monitor the overall reflector reflectivity.

4.2 MAGIC II aluminum mirrors

In § 3.4, the results of a ray-tracing simulation of a reflector for MAGIC II composed of all mirrors of 1 m^2 area were discussed. The basic result was that even if large mirrors slightly worsen the overall reflector performance for vertical incidence of around 20%, in cases of the most–common tilted incidence, the worsening is less evident. On the other hand, having 1 m^2 mirrors had a handful of advantages which are listed below:

- The number of tiles to be produced decreases by a factor 4, from 964 for MAGIC I to only 247 elements for MAGIC II (143 aluminum and 104 glass mirrors);
- The smaller number of mirrors results in faster mirror production, including optical characterization and tests;

– A separate supporting panel as in MAGIC I is avoided; thus the time-consuming internal alignment and the risk of loosing the alignment during the mounting of the panel is no longer necessary.

– The weight per meter square is reduced from around 30 kg to 18/12 kg for the aluminum/glass mirrors respectively with a corresponding gain in weight of the overall structure.

MAGIC II, as anticipated in § 3.6 (refer to Figure 3.6) houses two different types of mirrors:

i) 143 1 m^2 full–aluminum mirrors of similar design compared to MAGIC I in the central part

ii) 104 1 m^2 glass–aluminum sandwich made with the cold–slumping technique in the outer part

While aluminum mirrors were designed and produced by the Padova group and were supervised by me, glass mirrors were designed at the INAF and Medialario company and produced by Medialario. I followed their production and some of the tests performed on these mirrors. In the following, the design of the square meter mirrors installed in MAGIC II is described, together with the production technique and the quality test performed.

4.2.1 Design

The design of the aluminum mirrors follows the idea of the full aluminum sandwich structure as for MAGIC I, and in particular the improved design of MAGIC I upgraded mirrors (see Section 4.1.1). The development of this novel design was carried out principally by A. Pepato, M. Mariotti in 2006. A sketch of a MAGIC II aluminum mirror can be seen in Figure 4.7. In the following, we list the complete materials setup required to build the sandwich:

i) *Back panel box.* A square bottom aluminum box, 973 × 973 × 61.9 mm. The aluminum alloy is 5754 H111[1], having Mg as principal admixture (see Table 4.1), characterized by excellent resistance to corrosion, easy foldability, and resistance to operation at high temperatures as needed during the mirror assembly. The strength is almost comparable to steel. The thickness of the aluminum sheet is 2 mm. 3 small fissures are equally spaced on each lateral side of the box plus one on each corner. Each fissure is of 56 mm height and 3 mm width. A scheme of the box is shown in Figure 4.8. The small fissures allow the bottom box to bend and match the curved shape of a spherical mould of 35 m radius, as will be shown later. They are provided by the company `Me.Co.M` which also treats the surface with pickling before delivering.

Alloy	Si	Fe	Cu	Mn	Mg	Cr	Zn	V	Ti
5086	0.40	0.50	0.10	0.20-0.7	**3.5-4.5**	0.05-0.25	0.25	0.15	0.05
6082	**0.7-1.3**	0.50	0.10	0.40-1.0	**0.60-1.2**	0.25	0.20	0.10	0.05

Table 4.1: Wrought aluminum alloy composition limits (% weight)

[1]We use the International Alloy Designation System standards for the definition of the aluminum alloy. In this system, the wrought aluminum is named with a four digit number which identifies the alloying elements, followed by a dash and a letter identifying the type of heat treatment and a 1 to 4 digit number identifying the specific temper.

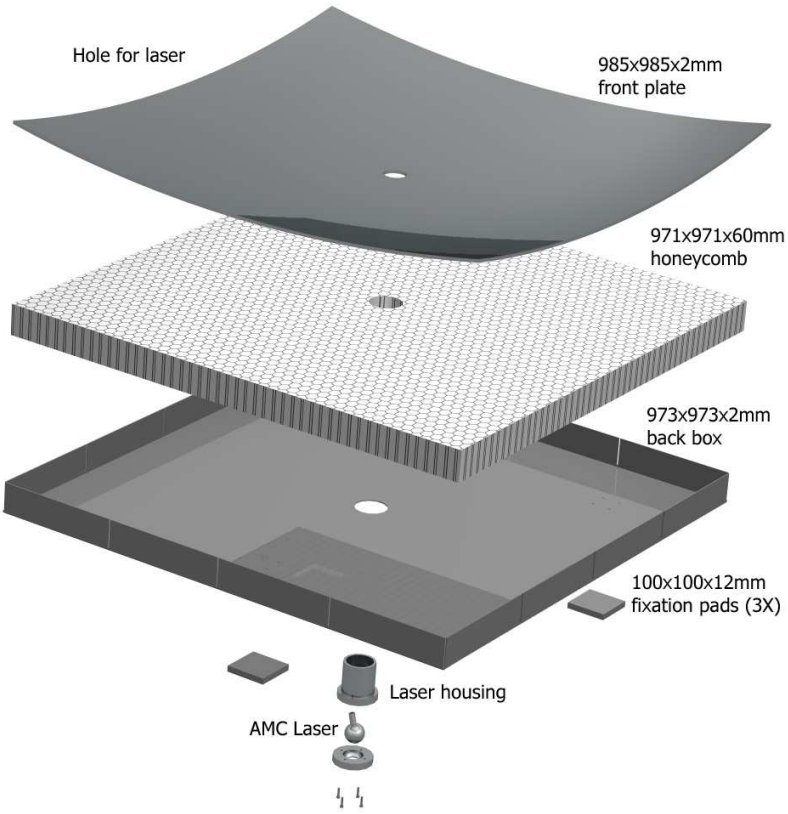

Figure 4.7: Design of the MAGIC II aluminum mirrors. The structure is a sandwich of an aluminum skin $985 \times 985 \times 2$ mm made highly reflective by surface diamond milling, a honeycomb hexcell panel $971 \times 971 \times 60$ mm to provide rigidity, and an aluminum back box $973 \times 973 \times 61.9$ mm (2 mm thick) to close the structure. In addition, a hole is drilled at the center to house the laser for mirror repositioning control and three aluminum inserts inside the panel are inserted for mounting. Schematic from M. Zago.

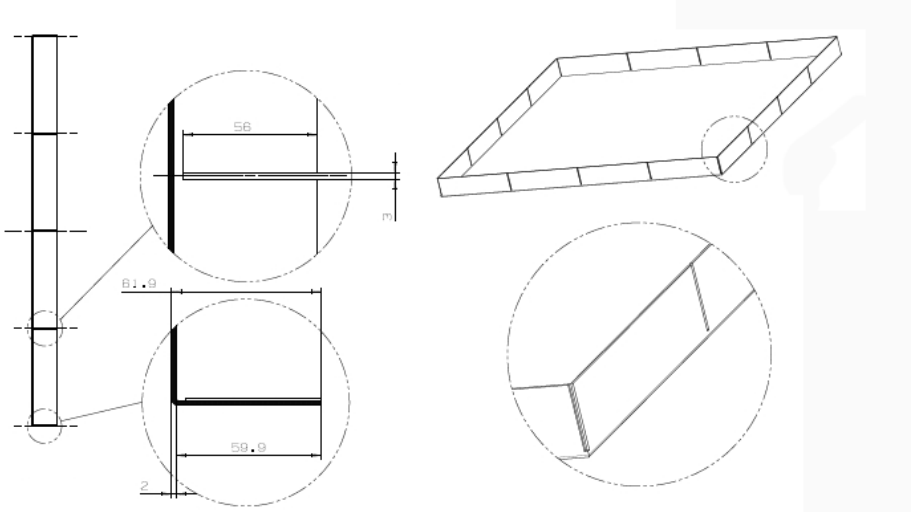

Figure 4.8: Scheme of the back panel box. Right: a sketch of the box is shown, with a zoom on one corner. Left: the schematics of the fissures and the folding of the edges of the box.

ii) *Hexcell Honeycomb.* The honeycomb is a hexcell structure, $971 \times 971 \times 60$ mm of type CRF 1/4 ACG .003 P 5.2[2]. The honeycomb is provided by the company

[2]Respectively: foil treatment, cell size [inch], aluminum foil type, foil thickness P=perforated and density [lb/ft^3]

Hexcel, expanded and shaped by I.Ma.Tec in Milan. It was chosen to maximize the stabilized compression, with a Young Modulus of 1000 MPa for the chosen type. The honeycomb has tiny holes among Its cells for ventilation, pressure equalization and evacuation.

iii) *Surface Skin.* The upper skin is composed of an aluminum alloy of type 6082–T6 which offers good weldability, brazeability, corrosion resistance, formability and very good machinability and is also heat treatable. The principal admixtures are of silicon and manganese, as reported in Table 4.1. It has a dimension of $985 \times 985 \times 3$ mm. It is produced as a flat sheet of material, and is slightly bent to match the concave mould of 35 m radius of curvature. At the center, this reflects into a maximum deformation of ~ 3.58 mm from the flat shape. The surface skin is also pickled by Me.Co.M.

iv) *Laser Housing.* At the center of the mirror, after assembly of the sandwich, a hole is drilled to house a laser for the mirror repositioning control. Details on the laser can be found in a separate paper. The laser housing is mounted as in Figure 4.7 and a sketch of the laser housing can be seen in Figure 4.9 and Figure 4.12(b).

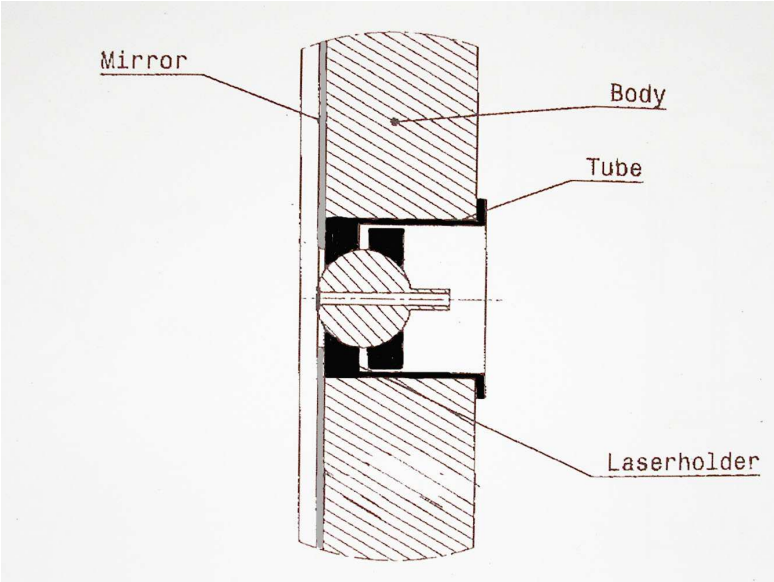

Figure 4.9: Schematics of the laser housing. The laser has a spherical head which can be rotated inside the housing to focus the mirror at the center of the camera. Courtesy of U. Horisberger.

v) *Additional Elements* Three aluminum pads $100 \times 100 \times 12$ mm are glued inside the mirror between the honeycomb and the bottom box to be further perforated to install the mirrors on the telescope. On the pad, the actuators of the AMC motors are directly screwed before being mounted on the telescope. See Figure 4.34a.

To produce the mirrors, additional supplies were used, these are listed below:

- *3M Scotch-Weld™Structural Adhesive Film AF 163-2K (Red).* It is a thermosetting modified epoxy structural adhesive film designed for honeycomb sandwich constructions. It has a high fracture toughness and peel strength, excellent resistance to high moisture environments, short cure time, it is capable of low pressure bonding and vacuum cure capability. It is used to tie the hexcell to the bottom box and the top plate.
- *3M Scotch-Weld™Epoxy Adhesives DP190 (gray).* It is a flexible weld with high shear and peel strength. It is used to seal from outside the sandwich in the lateral perimeter of the bottom box and in all its fissures, as shown in Figure 4.12(b).

– *Mould.* The mould (see Figure 4.10) is a square aluminum chunk of area slightly larger than the mirror size. The surface profile is spherical with a radius of curvature of 35 m. The surface is machined with a cutter. Three similar moulds were produced to work three mirrors at once. The front plate of the mirror is put over the mould. The small fissures on the mould allow air to be sucked out during vacuum creation.

(a) Aluminum mould (b) Zoom on the central area

Figure 4.10: (a) One of the three aluminum moulds of 35 m curvature used to assemble the raw blank mirror. The concave surface is imprinted on the raw-blank. (b) Zoom on the central area of the mould. The radial fissures allow the air to be sucked our during vacuum creation.

Materials

A new search of materials for the production of MAGIC II aluminum mirrors was not performed. The materials and the companies were the same as for the MAGIC I aluminum mirrors (INFN design).

For a detailed study on the initial research of materials, we refer the reader to Ref. [6]. For the purpose of this work, we simply recall that pure aluminum is the best–suited standard metallic reflector material for the spectral range of Cherenkov light. Nonetheless, pure aluminum is rapidly destroyed by corrosion in the open air and has low stiffness and machinability. Therefore, one needs to use aluminum with some admixtures of secondary metals and in particular manganese and silicon, as already shown in Table 4.1 and text. One also has to consider high corrosion resistance and good prospects for anodisation, low internal stress to avoid deformations after machining the spherical surface, high hardness for easy machining during the diamond turning and minimizing surface damage during handling. The aluminum is also delicate for gluing. In a very short time the metal oxidates and a thin layer of Al_2O_3 covers the entire surface. While from one side the layer prevents from further material oxidation, it also hinders gluing. For this reason, the aluminum is normally pickled before delivery, and the surface is always cleaned with acetone.

4.2.2 Production

The assembly of the mirror was performed by the company Compositex in Vicenza (Italy) (points 1 to 5 of the list below). The assembly of the sandwich proceeded as follows:

1. Cleaning. All the aluminum components (top plate, bottom box, inserts) are polished with Acetone and hereafter treated with protective gloves in order not to deposit any kind of

grease which could lead to a defective adhesion of the AF163-2K.

2. Assembly. The AF163-2K film is deposited onto the internal part of the bottom box. The honeycomb and the inserts are introduced into the box. A second layer of AF163-2K is put over the honeycomb and the top plate is put on the top to complete the sandwich. Figure 4.11(a) illustrates the gluing process on a smaller sample of mirror.

(a) Deposition of AF163 2K (b) Vacuum and autoclavation

Figure 4.11: (a) The gluing process of the honeycomb to the top plate and the bottom box with AF163 2K. This picture is shown for a prototype small mirror.

3. Mould and Vacuum Bag. The sandwich is put over the curved mould, which has about the same area. A perfect alignment of the mirror to the mould is ensured by profiles. The entire assembly is put inside a sealed plastic bag and vacuum emptied. This ensures a homogeneous pressure on the surface which allows to match the mould surface. Lateral profiles on the perimeter of the mirror serve as protection against lateral pressure which could damage the sandwich. A sketch of the process is shown in Figure 4.11(b).

4. Curing Cycle. The sandwich is inserted into an autoclave where a cycle of high pressure and temperature cures the adhesive: the temperature is raised from 20° C to 125° C in 35 min and at the same time the pressure is raised to 5 bar. Temperature and pressure are maintained constant for 90 min and then released back to room conditions in another 35 min. Once the cycle is complete, one needs to wait until the sandwich temperature drops below 60° C which ensures a correct and complete cure of the adhesive. At the end of this stage a *raw–blank* is produced, whose surface is still not at all reflective.

5. Preparation. After the raw-blank is produced, the DP190 epoxy glue is deposited onto the perimeter of the bottom box where it is fixed to the top plate and over all the small fissures, see Figure 4.12(a). The DP190 needs a few hours to stick and about 1 day at normal room temperature to cure completely.

Usually one strip of glue is enough. After this, a hole is drilled in the center of the mirror where the laser housing (Figures 4.12(a) and 4.12(b)) is inserted and glued with DP190. In addition, four holes for the three internal pads are drilled in the back of the mirror corresponding to the position of the AMC actuators. The holes are drilled in order to be locally perpendicular to the surface rather than aligned with the optical axis of the mirror.

6. Diamond Milling. The raw–blanks have an average radii of curvature of around 35 m.

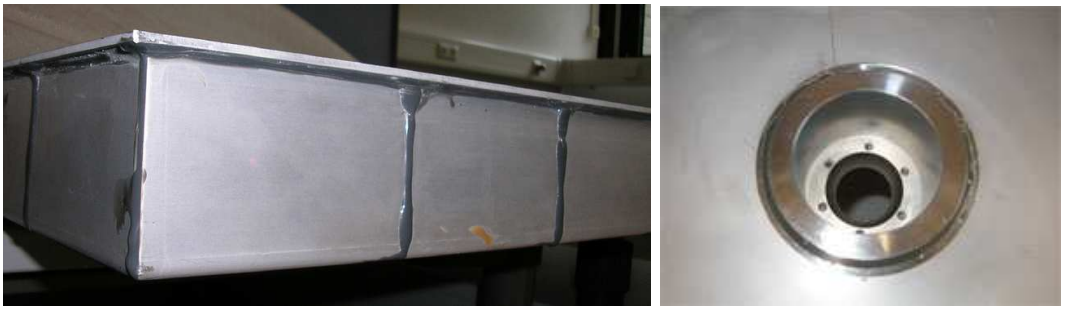

(a) Aluminum mirror. Lateral view (b) Central LASER housing

Figure 4.12: (a) A view of the side of a raw-blank after deposition of the epoxy glue DP190 on the internal perimeter and fissures. The glue prevents humidity and water from entering the mirror. (b) The laser housing hole at the center of the mirror as viewed from the back of the mirror. The housing is glued to the mirror also with DP190. On the bottom, the holes where the laser will be fixed.

To reach the exact value of curvature for the position of the mirror in the telescope, which ranges from around 34 m to around 35.5 m, the surface of the mirror is grinded. This is done by a possibly unique machine in Europe, which operates with a fast rotating diamond head which mills the mirror surface. At the same time, the precision of the diamond milling is such that the aluminum surface acquires an extremely low roughness (order of a few nanometers, see Figure 4.25) and consequently a reflectivity of around 90% at 400 nm (and an average over the Cherenkov range of 85%). The milling technique is called *flying cutting*. The reason for this is that the relevant parts of the machine rotate on a very thin air layer suppressing oscillations and offering the required stability. The schematics of the milling machine is shown in Figure 4.13

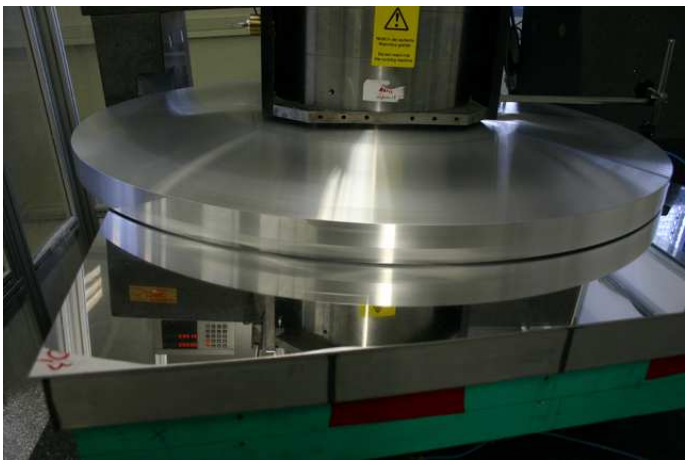

Figure 4.13: A sketch of the LT-Ultra machine used to diamond-mill MAGIC II mirrors.

The raw–blank is mounted onto a mould which must be as close as possible to the mirror back. For this reason, in the case of MAGIC II, we used the epoxy mould (the green mould shown in Figure 4.13) which was used to produce the first prototype mirrors. In general, also the mounting mould should be milled by LT–Ultra to guarantee correct coupling. The mould is mounted onto a granite table that floats on an air layer and slowly rotates back and forth on a horizontal plane at a velocity of around 1 m/h. On the other hand, the head of the diamond machine rotates extremely rapidly ($\simeq$ 20 000 turns/h) around a tilted axis.

The combination of the two movements determines the desired radius of curvature. If d is the diameter of the machine head and β is its adjustable inclination, the mirror radius of curvature is determined by:

$$R = \frac{d/2}{\sin\beta} \tag{4.1}$$

The two diamonds mounted on the head of the machine have a spherical shape with radius of curvature of around 100 mm. At the passage of the diamond over the surface, some material is exported. What is observed is that a regular pattern of grooves where the diamond removes the material is observed. Whenever this pattern is regular over a region of the mirror, a coherent effect of the reflected light is observed, with a consequent loss of light depending on the wavelength[3]. If one considers the velocity of the horizontal plate, the regular pattern appears at a distance of 50 μm. A possible solution to remove this defect is to modify the velocity of the horizontal plate at least for the last diamond cycle on the surface. The diamond should be changed for each mirror, and the mirror should be worked immediately in order to properly take into account the oxidation of its surface due to the different mechanical properties of Al_20_3. To guarantee the quality of the surface, the setup of the milling machine must have a micrometer precision for the positioning and orientation of all the components: the table, the machine head axis, and the centering of the mirror. The milling of the surface proceeds in several cycles until the desired radius of curvatures is reached. Usually it takes around one working day to complete one mirror.

The LT-Ultra company was provided with a list of the required radii of curvature for each mirror. Once the mirror is ready, LT-Ultra was also responsible for making quality measurements and to eventually reject or re-work the surface of the mirror in case our specifications in terms of radius of curvature and optical quality were not satisfied (see Section 4.2.3).

7. Quartz Coating At the Fraunhofer Institute (IFAM) in Bremen (Germany), the surface of the mirror was coated through a vacuum deposition of quartz with an admixture of carbon. The technique is called plasma enhanced vapor chemical deposition (PEVCD). The surface to be coated must be cleaned to a high level in order to guarantee the chemical reaction between the quartz and aluminum. This is done with a chemical treatment. Subsequently the mirror is mounted inside a large autoclave. First the mirror surface is cleaned with a hydrogen gas heated to a plasma state by alternating electrodes in a medium vacuum ambient condition ($\sim$ 10 mbar). After the surface has been cleaned, the quartz is vaporized and deposited onto the surface.

The quartz deposition on the aluminum surface is necessary for protection against mechanical and chemical damage. In particular, acid rains[4] and dust can degrade the aluminum and in general quartz prevents from corrosion. We underline that the degradation rate of the aluminum depends on its width: a larger width slows down the degradation process. This is the main reason why aluminum coated glass mirrors are more rapidly degraded by the atmosphere. In this case, the aluminum mirrors are only a few micrometers thick and therefore, any corrosion which is expanding on the material can only creep in the thin layer and affect much of the surface rapidly. In the case of an aluminum mirror, the few millimeter thick surface allows a creeping of the eventual corrosion into the interior and avoids propagation on the surface.

[3]This can be easily observed when looking at the mirror from the side and close to the surface. A white light is decomposed into its components because of the gratings.

[4]The presence of a large quantity of $C0_2$ in the atmosphere (for example, due to pollution) determines an efficient formation of carbonic acid H_2C0_3 which subsequently dissociates into carbonate ion CO_3^- and bicarbonate ion HCO_3^-. These ions are very active on the metal's surface as they create ionic bounding.

The deposition of the quartz layer introduces unavoidable interferences between the incidence and reflected light, which depend on the wavelength. The choice of the width was chosen to minimize the interference in the region around 300 nm where most of the Cherenkov light from atmospheric showers is concentrated. For a given wavelength λ_0 the interference is minimized when the thickness of the layer is $d = m\,\lambda_0 \,/\, 2\,n\,\cos r$, where m is the interference order number, $n = 1.54$ is the refraction index of quartz and r is the refraction angle. For vertical incidence and a wavelength $\lambda_0 = 300$ nm the minimal layer thickness is therefore 100 nm. In some cases, to favor the process of vacuum creation inside the quartz coating chamber, two small holes were made on the side of the aluminum mirror to allow the air to be sucked out. As described in Section 4.2.3, also the IFAM company performs quality tests on the homogeneity of the coating for each mirror.

After the mirrors were quartz-coated at IFAM, they were sent to MPI-Munich for individual quality tests before installation on the telescope. In the following two sections, all the tests performed on aluminum mirrors are described. They are subgrouped in *a*) tests during production, which were meant to monitor their quality and *b*) after the production, to qualify the mirror before installation.

4.2.3 Quality tests during production

A number of tests was performed by the companies during production to check the quality of each individual mirror before delivery. These tests are discussed below.

Raw-blanks curvature. After each raw-blank is produced, the front surfaces are measured systematically at different points with the use of a hand-made instrument, which we call the *sagittometer*, which measures the sagitta between two points at a fixed distance d which corresponds to the arm of the instrument. As a result, all mirrors have an average value of 35 m with a root mean square error of 20 cm. To have a homogeneous sample of raw-blanks it is important to avoid spring-back problems after milling and to ensure therefore, maximum quality.

First Mirror Qualification at LT-ULTRA After the diamond milling of the aluminum surface, the mirror is tested by the company in order to match our design criteria. The first test is to check whether the radius of curvature matches the table of radii provided to the company. Mirrors were accepted if their radius of curvature was within ± 15 cm of the nominal radius. When this was not fulfilled, the mirror could possibly be re-milled. In our case, no mirrors were rejected based on this criterion. A comparison of the nominal radii distribution and those measured at LT-Ultra is given in Figure 4.17. A more detailed description of the measurement and results are reported below. A second test is performed for the optical quality characterization. One image of the spot is taken at the focus while two additional images are taken 10 cm below and above the focus. The result of the spot diameter for the three points is shown in Figure 4.14.

From the figure one can see that even at a distance of 10 cm from the optimal focus, the quality of the image is still well inside the MAGIC specifications. The last test is performed *by eye*. In case the diamond is of bad quality or deteriorated, the surface of the mirror appears to be *milky*, i.e. opaque in certain zones. In such zones, one can clearly see the scratches of the diamond, and viewed in a transverse direction, one can see the light decomposed into components, with a typical rainbow reflection. Such an effect causes a loss of reflectivity from those zones, which unfortunately cannot be estimated

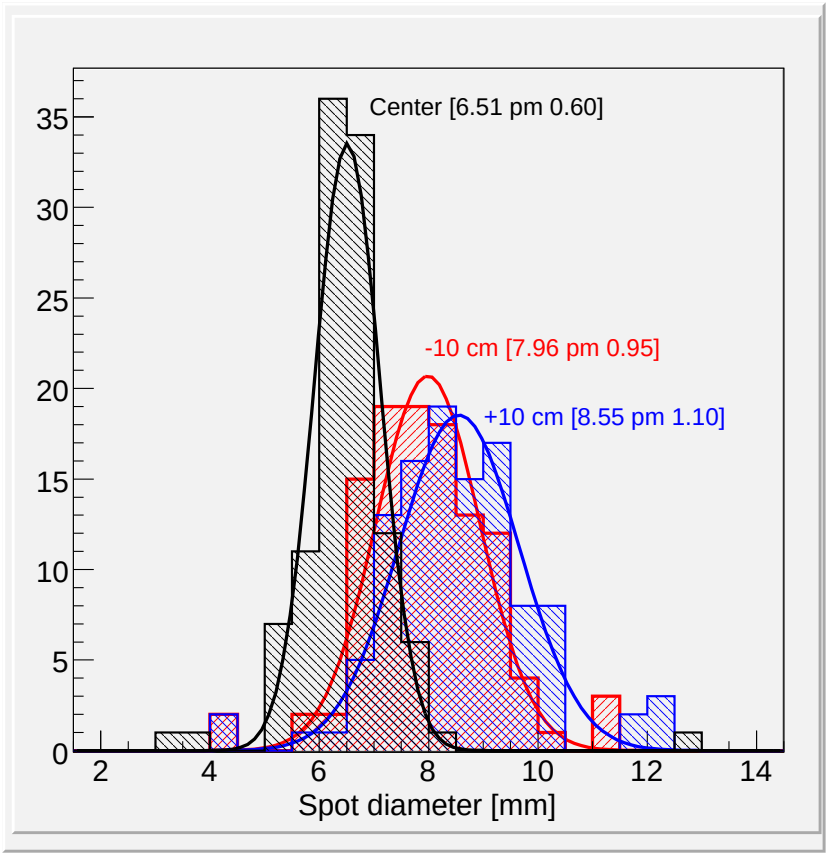

Figure 4.14: Distribution of PSF of the spot of aluminum mirrors taken at three positions: focal length (black), 10 cm below the focus (red) and 10 cm above focus (blue).

with portable reflectometers due to the close distance at which the measurement is performed. In any case, if the mirror presents such an effect, it is usually re-machined and the effect disappears. In general, around 10% of all mirrors presented small zones with a milky surface.

Quartz coating. Coating tests are performed by the IFAM institute to control the thickness and the homogeneity of the quartz deposition. The tests are performed by inserting small aluminum pads around the mirror and in the central hole and performing after the coating cycle some optical interferometric tests. Unfortunately, we did not have access to such tests and we could only rely on our reflectophotometer tests on mirror reflectivity (see below) which give an estimate of the homogeneity and thickness of the coating.

4.2.4 Systematics tests on all mirrors

After delivery from companies, each mirror was tested in the laboratories of MPI-Munich by a team of people mainly composed by me, E. Giro, R. Kosyra, F. Goebel, C. Schultz, and H. Kellermann. Here is the complete description of the optical test setup and the measurements performed.

Estimation of the PSF. To measure the focus of the mirror with a point-like source, one should place it at twice the focal length. As a light source, different bright sources

were used: a blue LED, a halogen lamp or a LASER. The first had the advantage of being rather monochromatic, the second of being very bright and therefore, usable in conditions of limited darkness while the third is also very bright but must be extended in order to illuminate a significant fraction of the mirror. In general, there is no need for a high level of darkness and the measurement was made in the daytime with normal light conditions. The image is acquired using a CCD. The CCD is pointed onto a screen which is a slab of spectralon in the MPI setup and an opaque glass in the INFN setup. In the former case the CCD sees the reflected light from the screen, in the second case, the transmitted light. To reduce the ambient light, a monochromatic filter was used in both setups. For the qualification of the mirror, the optimal focus is found by adjusting the distance of the mirror from the light source. This is done by searching the circle of minimum uncertainty where the spot size is smallest. The uncertainty in this "by-eye" estimation is of the order of ± 5 cm, which is acceptable for our requirements. Once the focal optimum is found, two images are acquired with the CCD: one of the light sources, and a dark image, with the light-source off, to measure the background illumination. In the analysis of the image, the background image is subtracted pixel by pixel. As the image is usually roundish, the determination of the centroid is easy. From the centroid one starts the integration over increasing radius circles and determines the integral profile of the image.

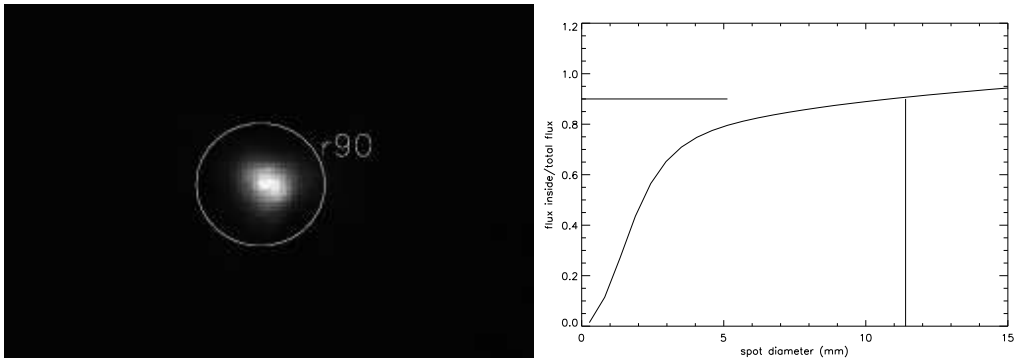

Figure 4.15: (*left*) Image of the reflected spot from one mirror together with the superimposed circle of 90% light containment. (*right*) Integral profile of the spot size.

A check for a correct background subtraction is performed by plotting the integral of the image versus the radius, as shown in Figure 4.15: in case the background is correctly subtracted, the integral asymptotically approaches the reflectivity. If the background is underestimated (overestimated), the integral is indefinitely increasing (decreasing). For the image profile, the R_{90} is defined as the distance from the centroid where 90% of the reflected focused light is enclosed. We underline that this is not an absolute estimate of the reflected light, because, the eventual diffuse light is not taken into account.

Figure 4.16 shows the distribution of R_{90} (hereafter called the mirror PSF) for the INFN mirrors as measured with the INFN setup. One can see that most of the mirrors show a very similar spot profile.

Radius of curvature. With the same procedure as defined above, one can estimate the radius of curvature with the formula $R = 2f = (1/p + 1/q)^{-1}$ where p is the distance between the light source and the mirror and q is the distance between the mirror and the screen. In Figure 4.17 the histograms of ideal curvature radii and those of the real mirrors is provided for INFN mirrors.

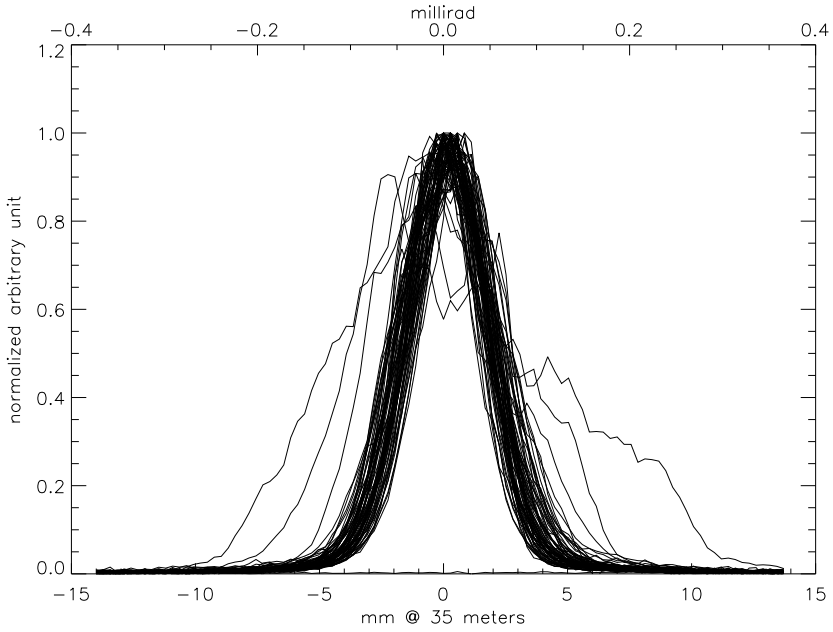

Figure 4.16: Superposition of the spot profiles for all aluminum mirrors.

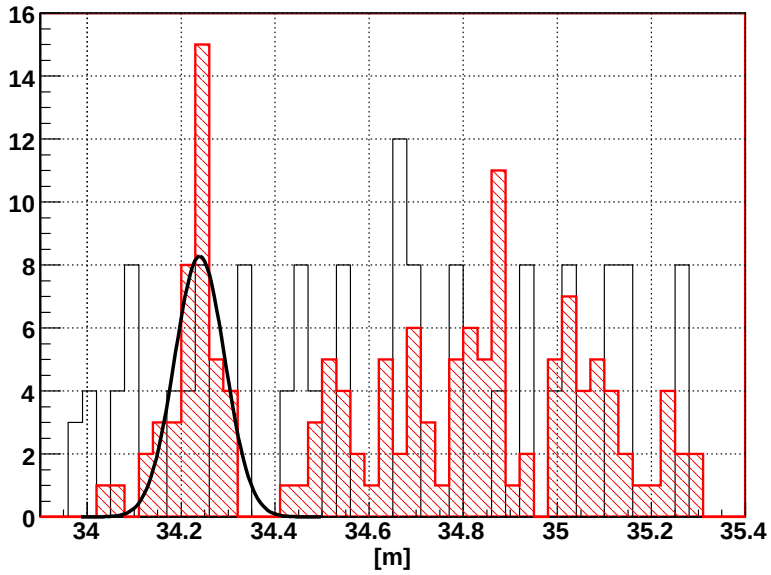

Figure 4.17: Distribution of radii of curvature for the aluminum mirrors of the MAGIC II telescope. Nominal radii are plotted in black and the real produced radii are shown in red. In addition, a Gaussian is plotted over the distribution of mirrors for a given LT-Ultra nominal radius.

In the case of INFN mirrors, the large peak at 34.25 m is due to a misunderstanding with the delivering company, which could be fixed anyhow by rearranging the mirrors on the telescope in a way to fit the best position. In general, it is important to understand the capability of the company in producing one exact radius of curvature. In case of LT-ULTRA, it is recalled that the radius of curvature is fixed by regulating the inclination of the main machine arm, while the final result depends strongly on the rigidity of the mirror and its position on the base. For this reason, the mirror should be put over

a concave surface which has a very similar curvature compared to the back of mirror, otherwise the pressure of the diamond would be so large that it would bend the mirror structure and work the surface improperly. The precision required for the production of the mirrors as asked to LT-ULTRA was that we could accept mirrors within ±15 cm from the nominal radius of curvature. Given this requirement and due to the fact that the orientation of the machine is very delicate, only around six machine setups were used by LT, as clearly visible in Figure 4.17. In the figure, the distribution of radii of curvature for the smaller angle setup is fitted to a Gaussian function to show the accuracy of the setup. As a result, the RMS error of the Gaussian is 9.9 cm. The accuracy of this setup is largely increased compared to MAGIC I mirrors, because the mirrors have better rigidity and were more carefully fixed during the milling process.

Differential reflectivity. The differential reflectivity was measured with two portable reflectometers. A few mirrors were measured with Ocean Optics USB2000+ Miniature Fiber Optic Spectrometer and ISP-REF Integrating Sphere (see Figure 4.18-left), while more systematic tests were done with a Minolta spectrophotometer CM-2600d (Figure 4.18-right).

Figure 4.18: (*left*) Ocean Optics USB2000+ Miniature Fiber Optic Spectrometer and ISP-REF Integrating Sphere, (*right*) Minolta spectrophotometer CM-2600d.

The measurements were made in 12 points of the mirror surface, 8 in the central region, and 4 at the corners. Results are presented in Figure 4.19. The solid lines indicate the average values over the mirrors, and the dotted lines enclose a region within one RMS value from the average. First of all, we observed how three populations of mirrors with different reflectivity curves are present. The first population (upper row in the figure), composed by 35 mirrors, is constituted by the first mirrors produced. Unfortunately, in this population the reflectivity is peaked at around 500-600 nm. This is probably related to the fact that initially, the quartz layer deposited by the company was 160 nm instead of 100 nm, which, following the rule mentioned above, should have a peak at around 450 nm. This was an error of production that was recognized later and we should live with that. The second population (central row in the figure) is composed of the normal production mirrors after the mentioned problem had been diagnosed. A third population (lower row in the figure), composed of only 15 mirrors, is once again another error made by IFAM which coated the mirrors with only a 20 nm thick coating. We also accepted these mirrors believing that their reflectivity was sufficient. In addition, from the figure one can see that in most regions of the surface the reflectivity has a maximum at 400 nm, which is a slightly larger value than expected due to the thickness of the quartz coating and slightly decreased with increasing wavelength. The peak reflectivity

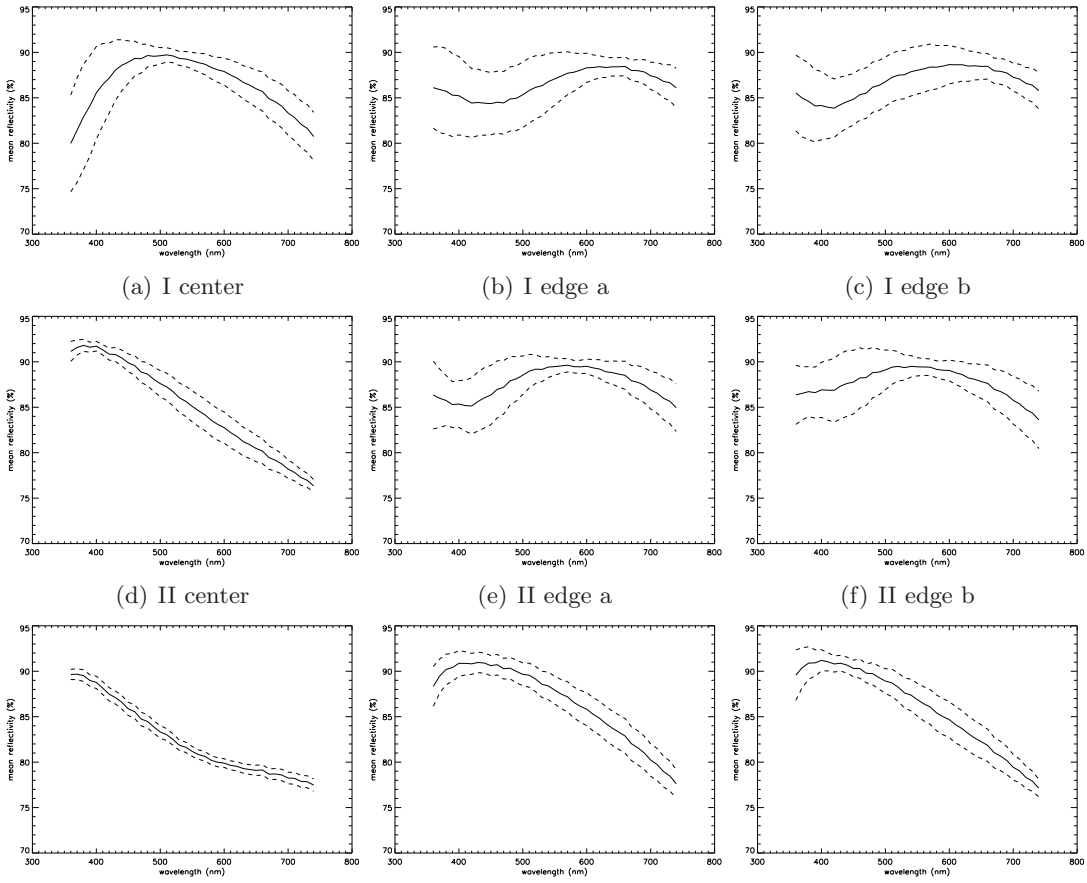

(a) I center (b) I edge a (c) I edge b

(d) II center (e) II edge a (f) II edge b

(g) III center (h) III edge a (i) III edge b

Figure 4.19: Reflectivity measurement on MAGIC II mirrors. From top to bottom. Details in the text.

has an average of 90% with peaks of very large reflectivity. For larger wavelengths, the reflectivity starts to decrease and falls below 80% at wavelengths larger than 600-700 nm. While these values are acceptable for the use of the telescope, it was not possible to measure reflectivities below 350 nm, which is a fundamental region for the Cherenkov spectrum, where most of the light is concentrated. It is indeed difficult to find cheap reflectometers on the market that operate at such small wavelengths. A second important effect which we see is the subtle behavior in the two opposite angles of the mirrors. We see in fact, that the reflectivity curves, probably due to a different quartz deposition on the corners, had peaks respectively at 550 and 600 nm, with a slightly different behavior at the smallest wavelengths. As the reflectivity of each mirrors can be monitored with the AMC, we will make intense follow-up observations on each mirror.

Water tightness. Part of the MAGIC I mirrors suffered a relevant degradation from humidity entering through small fissures and condensating inside, eventually turning into ice and deforming the surface. To cure the problem, an enhanced design and the use of a sealing glue on portions of the mirror were performed, and no significant degradation has appeared on those mirrors in almost 2 years of operation. For MAGIC II mirrors, nonetheless, each mirror was tested by immersion of the entire sandwich into warm water. The water heats the air inside the mirror and bubbles show up. Out of the 143 mirrors tested, only 10% of them showed some air coming out from inside.

This was cured by locally applying a spot of glue DP190. This should eventually stop or drastically reduce the ageing of the reflector, and the mirrors will be monitored to control the quality and degradation of the sealing glue.

4.3 MAGIC II Glass Mirrors

Glass mirrors are mounted on the two edge most rings of the MAGIC II reflector. They are assembled via the innovative technique of cold–slumping of a thin glass sheet onto a honeycomb structure. The technique was developed by Medialario and INAF–Milano in 2006–07.

4.3.1 Design, production and tests by Medialario/INAF

I briefly report about glass mirror design and preliminary tests in the following section. The tests performed on these mirrors will be reported in a separate section.

Design and production

The glass mirrors mounted on the MAGIC II reflector are based on an innovative technique dubbed *cold–slumping* of a thin glass sheet. The technique has been developed by the Media Lario Technologies (MLT) company in collaboration with INAF - Brera Astronomical observatory; MLT has also been in charge of the glass panel production and quality control for MAGIC II. In the cold–slumping technique, a thin glass sheet 1.7 mm thick is elastically deformed in order to retain the shape imparted by a master with a convex profile. The master (see Figure 4.20(a)) is diamond–milled by the same technique used for MAGIC aluminum mirrors by LT-ULTRA. An image of the replica mirror is shown in Figure 4.20(b)

(a) A convex aluminum master (b) Prototype of a glass mirror

Figure 4.20: (a) One of the two aluminum masters used for the cold slumping technique; (b) a mirror produced using the master.

With large curvature radii the glass sheets can be pressed against the master using vacuum suction or a simple heavy weight. In order to provide the necessary rigidity, a honeycomb structure is glued onto the deformed sheet under the vacuum forces. The thickness of the honeycomb layer is 20 mm. Finally, a second glass sheet is glued onto the bottom of the honeycomb structure. The gluing process is realized by heating the aluminum mould up to around 80°C. After this, the panel is aluminized and quartz–coated to protect the reflecting surface by the company ZAOT.

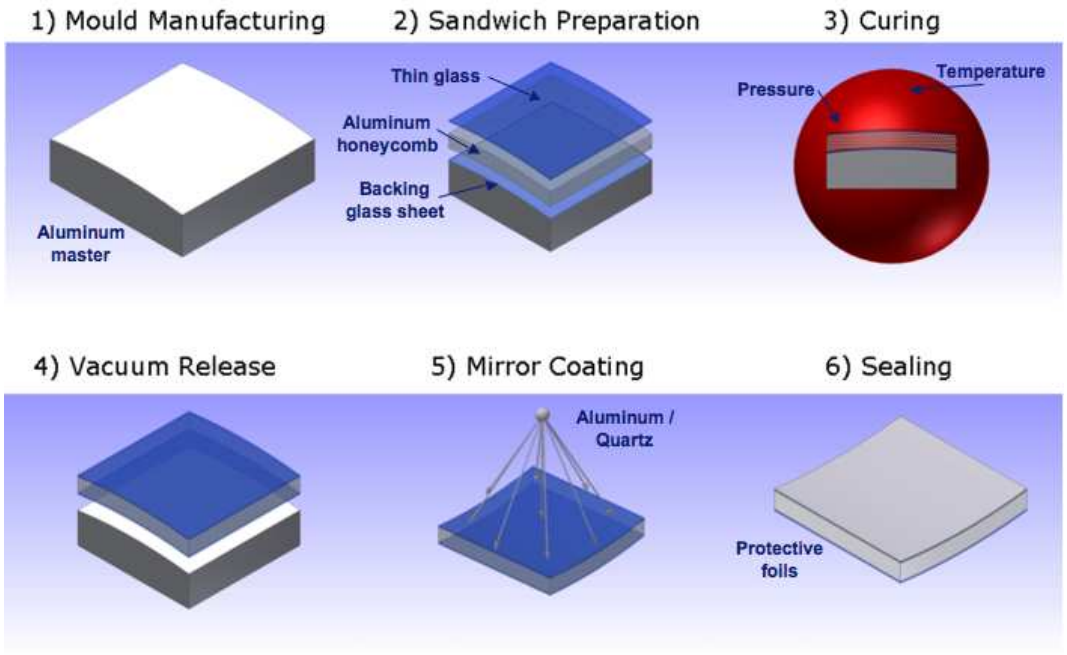

Figure 4.21: The cold glass slumping process for mirror production. Courtesy Vernani.

In Figure 4.21 the various steps of the process are shown. With a careful control of the spring–back effect, from a master with one radius, it is possible to obtain mirrors of different curvatures. In the case of MAGIC II, 12 different curvatures were requested.

The final design for the panel is the following:

i) Dimensions 985 × 985 mm

ii) Sandwich structure with the following characteristics:

- Front glass layer skin 1.7 mm thick
- Epoxy adhesive 0.2 mm thick
- Aluminum honeycomb 20 mm thick
- Epoxy adhesive 0.2 mm thick
- Backing glass skin 1.7 mm thick

iii) Panel total mass: 12 kg

iv) Three rigid supports glued to the back part of the panel (stainless steel plates 80 × 80 mm).

v) A laser holder mounted on one edge for the active mirror control (see Figure 4.22.

According to the position on the telescope, some mirrors must have an adapted design. In particular:

- 80 glass mirrors are standard
- 16 glass mirrors are square but have a different configuration of the mounting of the actuators to fit in the edge most parabola.

Figure 4.22: The laser with its holder applied to the panel

– 8 glass mirrors are not square but have a cut angle in order to not interfere with the structure

Quality Tests at Medialario

In Table 4.2 a summary of the qualification tests is reported. The former tests in the table were performed by Medialario. The latter tests were performed mainly by E. Giro and myself at the LNL.

MLT Qualification test	Prototype	Sample	Each mirror
Curvature radius	YES	YES	YES
PSF spot size	YES	YES	YES
Glass micro-roughness	YES	no	no
Reflectivity	YES	YES	no
Reflectivity b/a weathering test	no	YES	no
Reflectivity b/a salt and fog test	no	YES	no
Coating adhesion test	YES	YES	no
Sealing test	YES	YES	no
INFN cross–check and tests	Prototype	Sample	Each mirror
Differential reflectivity	no	YES	no
Water tightness	no	YES	no
PSF spot size	no	YES	no
Laser mounting stability	no	YES	no
Cross–effect	no	YES	no
PSF at different wavelengths	no	YES	no

Table 4.2: Summary of the qualification tests performed by MLT and by INFN.

Curvature radii distribution The curvature radii of the panels were measured by MLT illuminating the mirror with a point light source at about 35 m and searching for the best image position on a screen with respect to the panel position (see Figure 4.23).

The distance between the mirror and the point source (and between the mirror and the screen) is equal to the nominal curvature radius (or twice the focal length) of the mirror

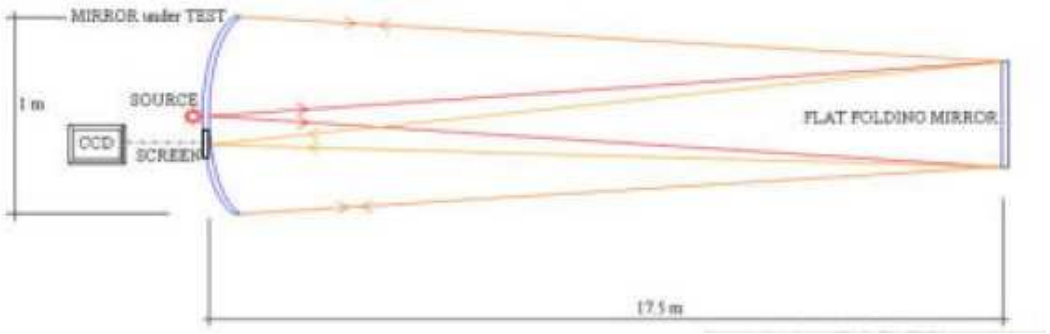

Figure 4.23: Layout of the optical bench used for the measurement of the curvature radius and of the PSF; it is based on a flat folding mirror (see the picture in the right bottom corner) for achieving the right distance from mirror and source.

itself, in such a way that a point image is reflected again into a point image. The image obtained on screen with a CCD camera was used for the PSF evaluation test.

Surface quality and PSF The optical quality of the mirrors was qualified by MLT in two ways:

- Estimating the diameter of the circle which contains 90% of the light reflected by the mirror (d_{90});
- Estimation of the micro-roughness of the glass.

In the first case, they used the same setup described above. The technique was cross–checked with INFN setup by E. Giro and myself, giving similar results. Nevertheless, INFN could cross–check only a few samples, while MLT measured the PSF of all mirrors produced. The mean of d_{90} at 35 m is about 25 mm (1.4 mrad), as shown in Figure 4.24.

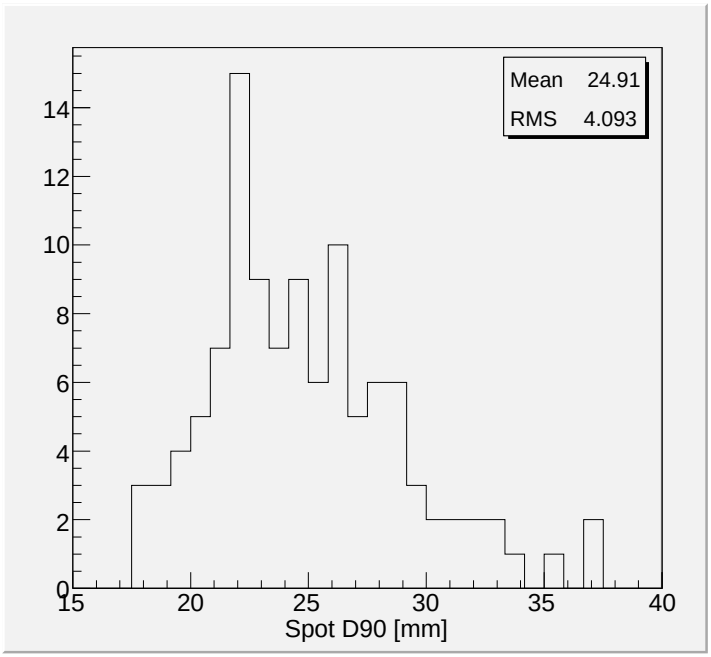

Figure 4.24: Distribution of d_{90} of Medialario mirrors.

Despite the worse focusing compared to MAGIC II aluminum mirrors, the overall quality can be accepted. During prototyping the angular resolution was also tested by MLT before and after thermal cycling (five cycles between −20°C +20°C, plateau of 12 hours, and then between +20°C and +40°C , plateau of 4 hours). No changes in PSF occurred before and after tests. As far as the micro-roughness of the glass is concerned, profiles taken with a WYKO TOPO 2D interferometer system have been taken on a glass sample used for prototypization. Results are shown in Figure 4.25 (lower profile). A comparison

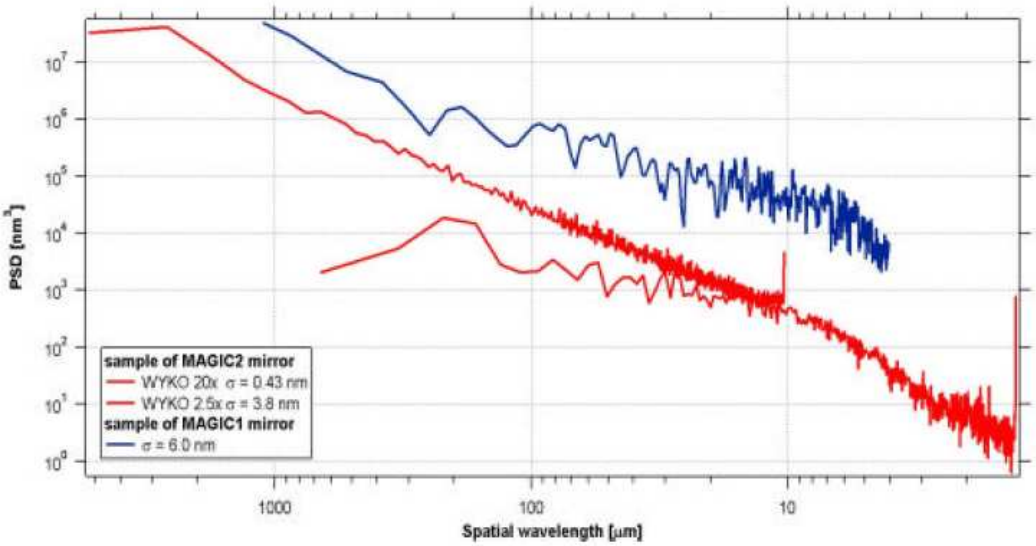

Figure 4.25: Glass micro-roughness PSD in comparison with the MAGIC I mirror one obtained with a WYKO microscope

with a surface sample of the aluminum mirrors used for MAGIC I (upper profile). As expected, glass roughness is an order of magnitude less than Aluminum case, the latter being affected by the typical groove structure due to the diamond milling.

Reflectivity and aging tests Reflectivity of the panels was measured by MLT on samples, before and after salt-fog and weathering tests. Moreover, the same measurement was performed on a prototype installed at the telescope site as in operational situation, after six months. The mean value at 470 nm just after coating was about 88%. Difference before and after aging tests are below 1%.

In Figure 4.26 the spectrum obtained with Oceans optics USB2000 is shown. Good uniformity of the coating on the surface of the mirror is quite evident. Salt-fog test was executed on a dedicated chamber on two glass samples coated as the panels. Weathering test was realized on coated samples with 10 fluorescent lamps and filters to obtain the passband and irradiation needed for the test. During irradiation the humidity of the climatic chamber was changed from 25 to 95%, and the temperature between −40°C and 70°C. The test was performed in 42 days. No change in reflectivity was measured.

4.3.2 Other tests performed by our group

E. Giro and I performed some cross–check tests on a few sample of mirrors. Together with C. Schultz we confirmed the water tightness of the mirror. We measured the differential reflectivity of the mirror, which mostly confirmed the results of Medialario. Two additional tests were performed to understand other particular features of this technique:

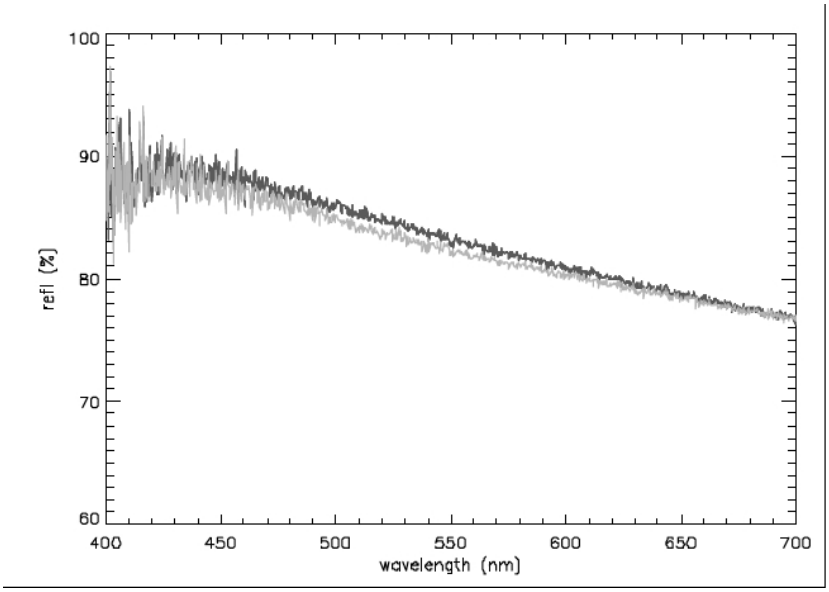

Figure 4.26: Reflectivity in the spectral range between 400 and 700 nm. Different gray tone curves are relative to different portions of the mirror.

Laser mount stability Glass mirrors for MAGIC-II telescope produced by MLT mount a steel holder for the laser on a corner. Nevertheless, the coupling between steel and glass was thought to change properties in function of the temperature, due to the different thermal coefficient of the material; an effect largely amplified by the lever arm due to the non–central position of the laser in the mirror. For this reason, a mechanical test at different temperatures was performed to understand if the laser had misplaced its position. The setup used is shown in Figure 4.27.

An LED at the curvature radius illuminates the mirror, and the image at the focal plane is registered by a CCD camera. The laser on the mirror is oriented to point close to the LED reflection image on the same screen. A camera in front of the screen with a 12 bit A/D converter was used. Due to the fact that the camera has A bayer matrix on the sensor, the blue channel was used for the centroid calculation of the led, while the red one was used for the laser. As we did not possess a thermo–controlled camera large enough to host the mirror, the measurement was a little tricky and possibly far from thermal equilibrium, i.e. we did not have complete control on the flow of heat within the mirror itself. The procedure was to leave the mirror at 9°C until it had thermalized. Afterwards, the mirror was put inside the laboratories, where the room temperature was 19°C, and the reflection was measured while its temperature was increasing.

Nine images were taken between $13 - 19$°C. The temperature was stable inside the mirror within 1°C. The results of the test are shown in Figure 4.28.

In Figure 4.28(a) the absolute positions in the focal plane are shown for the LED and the Laser. An offset has been added to the values of the led to overplot the two curves in the plots. The variations of the led have been divided by two to take into account the reflection on the mirror. It is quite evident that during the temperature transient both the laser and the led spot change in position also if with different behaviors. In Figure 4.28(b) the distance between the two spots is shown during the transient and is plotted both as function of time and of temperature. The plots show the presence of a transient also if the temperature range is very limited.

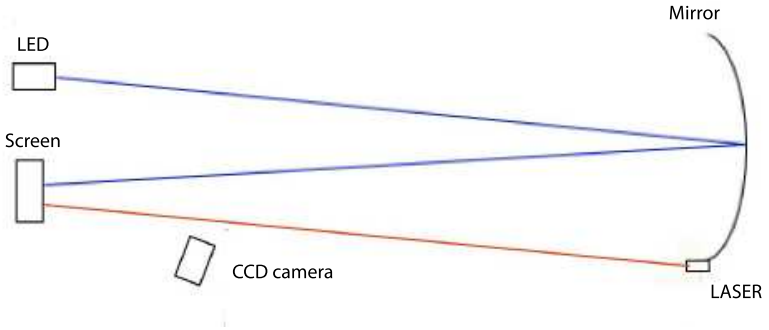

Figure 4.27: Setup of the laser flexure measurement. A CCD camera records the compound images of the LED and the LASER to detect possible mechanical deflections.

The results underlined that during non-thermal equilibrium a rather strong effect in the laser alignment is present, also for very small temperature intervals. Unfortunately, we could not scan the position in stable thermal conditions, so we could not disentangle the effect of transient by a possible intrinsic effect.

While obviously a more advanced test is desirable, this result suggests that during the alignment procedure of the glass mirrors, which are carried out exactly with the use of the laser, special attention should be paid to the temperature to understand if the laser orientation changes with this parameter.

Cross–reflection effect When observing the reflected light of glass mirrors installed in MAGIC II, one can see in some cases the presence of cross of light centered at the spot. A similar effect was observed for aluminum mirrors and described in Figure 4.4. From geometrical point of view, it is clear that the cross is caused by an imperfect curvature at the very edge of the mirror. Figures 4.29 show the effect of masking the perimeter of glass mirrors up to 2 cm in the interior: when covering one side of the mirror, one arm of the cross disappears.

It should be underlined that the amount of light dispersed for such an effect is probably of the order of less than 1%. On the other hand, a simple solution for this effect could be slightly masking the perimeter of the mirror, for example for 1 cm inside (total area loss $\sim 0.4\%$).

PSF at different wavelengths Following a suggestion of A. Foerster, E. Giro and I measured the PSF of a glass mirror and an aluminum one at a different focal length. For our measurement, we used the normal setup for PSF measurement, and we used four LEDs of different wavelengths, see Figure 4.30. The results are shown in Figure 4.31.

From the figure one can see that while for wavelengths larger than 500 nm, the PSF remains quite constant, at shorter wavelengths there is a net increase in both cases.

4.4 Measurement on mounted prototypes mirrors

The first prototypes of MAGIC II mirrors, namely three aluminum mirrors and one glass mirror, were mounted on MAGIC I in substitution of damages panels and to check their performance at the environmental conditions. In the following, a short report is given.

UV–protective varnish For some time, the idea of painting the mirror with a UV–protective varnish has been discussed. While such paints are easily available on the market for

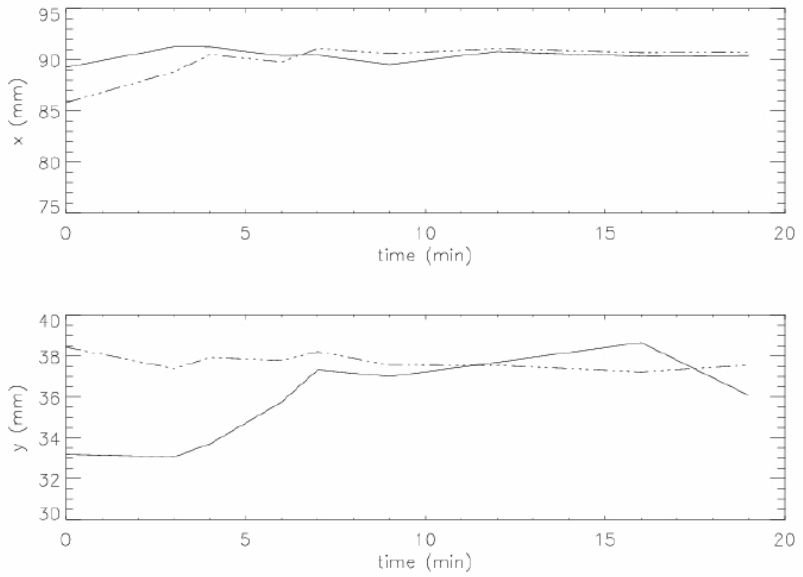

(a) Focal plane position

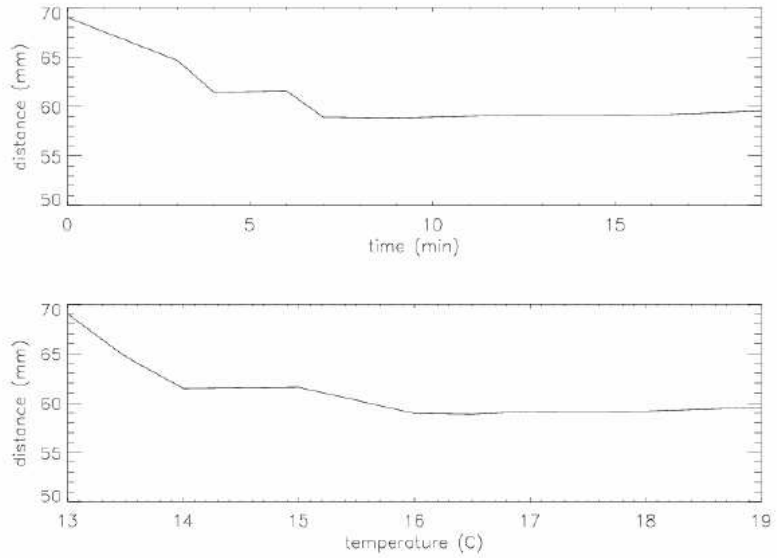

(b) Relative distance

Figure 4.28: Results of the laser flexure measurement for glass mirrors. Figure (*a*) shows the position of the LED and laser spots in the focal plane in function of temperature. Figure (*b*) shows their relative distance.

normal UV fluences, for the conditions of La Palma (high altitude, close to the equator), the UV light is stronger. The result of the deposition of the paint after one winter of operation is shown in Figure 4.32. The detachment is clearly visible.

Quality of the DP190 The quality of the DP190 glue, deposited on the perimeter and

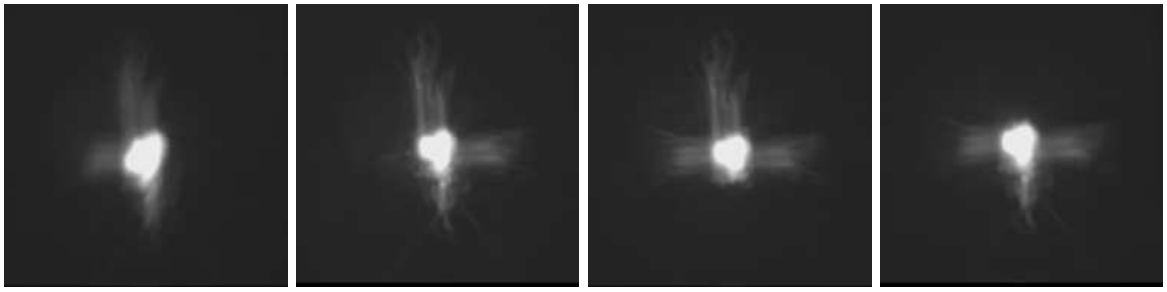

Figure 4.29: The effect of covering one side of the perimeter of a glass mirror on the reflected spot: an arm of the cross of light is disappearing.

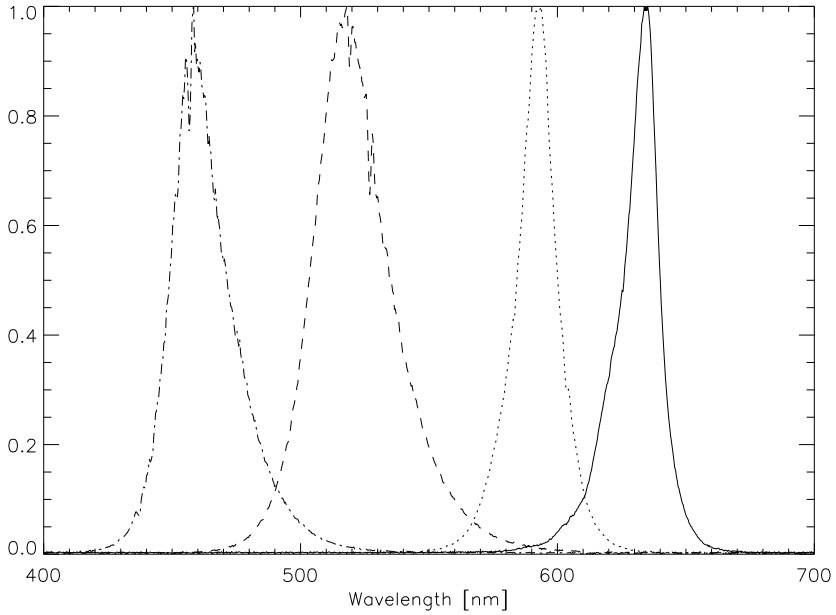

Figure 4.30: Wavelengths of the LEDs.

lateral fissures of the mirrors mounted on MAGIC I (both small mirrors and large mirrors) were checked. No significant sign of degradation was seen after more than one year of operation.

Quality of glass mirror A by–eye inspection of the only glass mirror mounted on MAGIC I showed no sign of degradation neither of the surface nor of the mirror components (glue, plastic, fixation, etc.). Unfortunately, no data are available on the behavior of reflectivity for this mirror.

4.5 Final operations and mounting

Final preparations

Before shipment, all mirrors after tests were covered with an adhesive foil MACal®8129, which is a gloss white soft calandered PVC film, cadmium free and monomeric. The adhesive protects the surface during transportation and allows easier handling during installation on the telescope, with the added advantage of avoiding risks of blinding installers due to sun light reflection and of being allowed to move the telescope during installation without risking

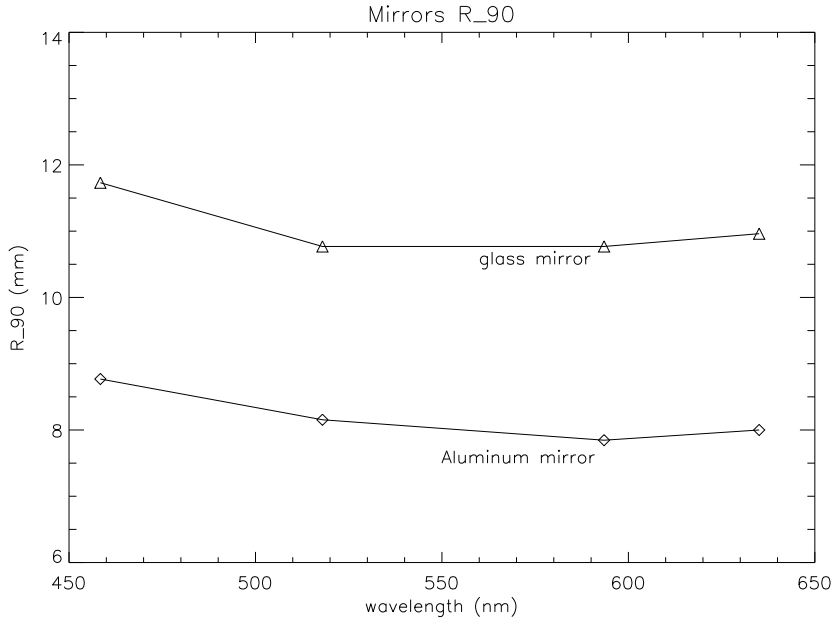

Figure 4.31: PSF for one sample glass and one sample aluminum mirrors at different wavelengths.

Figure 4.32: Detachment of the UV–paint on prototypes MAGIC II aluminum mirrors mounted on MAGIC I.

damage to the structure. The foils were removed after the complete installation of the surface. Even after a winter, the foils are still stuck to the surface of the mirror and are easily removed without breaking or leaving traces of glue on the mirrors. They therefore, constituted an optimum material. Before installation, the actuators are mounted on the back of the mirror, as shown in Figure 4.33. Eventually, the laser is mounted at the center of the aluminum mirror. For glass mirrors, the mounting is very similar, except that the laser is at one corner.

Installation procedure

One could think that the installation procedure is rather a secondary task. Nevertheless, the optimization of this procedure is rather important for the following main reasons:

– It can only be done in good weather conditions, usually from spring to fall. A fast installation rate allows for reducing the risks associated with weather

Figure 4.33: The AMC actuators mounted on the back of the aluminum mirror before mirror installation. There are three types of fixations, all with ball bearings: one fixed point (bottom–right), one single–cardanic point (top–right) and one bi–cardanic point (left). The hole at the laser will host the AMC laser.

– Faster installation times considerably reduce overall costs

– Minimizing installation times is pretty important in view of CTA where a very large number of telescopes have to be installed in the shortest possible time scale.

The installation proceeds as follows: the mirror is lifted via a cherry–picker to the front of the reflector (see Figure 4.34). From inside the telescope, some operators take the mirror and fix it via 6 screws on 3 pads (1 per actuators) mounted directly on the telescope structure. After a rough fixation, the mirror is centered and prealigned. A complete alignment can be achieved subsequently with the use of the AMC.

Figure 4.34: Two phases of the installation of the mirrors in the telescope. The mirror is taken to the reflector front via a cherry–picker (left) and the mirror is fixed by operators to pads mounted on the telescope structure.

4.6 Remarks and outlook

As a conclusion of this part on the activities on the MAGIC II reflector, I would like to draw some general conclusions on the overall quality of the work. In the next section, I will briefly report an outlook for future activities.

i) The optical quality of the new large aluminum mirrors of MAGIC II is unprecedented. The focusing power is almost doubled with respect to MAGIC I mirrors,

reaching less than 0.5 mrad for the diameter of the reflected spot (§ 4.2.4). This is mostly a result of the increased stiffness of the mirror structure, which allows LT–ultra to better machine the surface, and the use of very stiff aluminum alloy.

ii) On the other hand, some mirrors showed so–called "milky " areas on some parts of the surface. This effect is due to a bad machining of the surface, possibly caused by a diamond that is too degraded. While this effect is easy to solve — exchange of the diamond and further milling of the surface — it is hard to determine quantitatively by eye. For this reason, a future work will develop a tool which LT–Ultra will use to determine univocally the surface quality. This could be for example, an adapted tool for reflectivity measurement.

iii) The use of large mirrors and the removal of the intermediate panel as used for small mirrors, carried a general improvement. On the one hand, the number of items produced, tested and shipped were reduced by a factor of 4. Furthermore, the installation was far more simplified with a net result of at least a factor 4 in velocity. In addition, all the problems of mirror interalignment inside the panel (see Figure 4.4) were dropped. The decrease in optical quality due to the fact that a larger spherical facet worse resembles the overall parabolic shape is contained and justified our choice (see § 3.4)

iv) The new design and the use of DP190 should have fixed forever the problem of water/humidity entering MAGIC I mirrors. A by–eye inspection of some prototypes showed no degradation of the epoxy glue.

v) Glass mirrors proved to be a very good solution with acceptable optical quality given the short time in which they were developed. The new technique of cold–slumping replica mirrors is perfectly adapted on MAGIC telescopes. Important work for improvement of the optical quality is currently ongoing at INAF–Milano.

4.6.1 Future plans

i) The reflectivity of the aluminum can be increased by deposition of special coating or by vaporization of aluminum gas onto the surface to smooth out the surface roughness. It is planned for 2009 to develop such studies with the company IFAM and with dedicated studies.

ii) The design of the mirror can be simplified to avoid mechanical activities for construction and in particular decrease the price. It is believed that an increased precision of the raw–blanks could allow for a substantial reduction of costs for the diamond–milling of the surface. This work is already ongoing with A. Pepato.

iii) The quality of the overall reflector can be ameliorated whenever the mirrors more resemble the parabolic shape. In particular, for mirrors far from the center, the discrepancy between radial and tangential radius of curvatures is much more pronounced. For this very position it is planned to develop "aspherical" mirrors, i.e. mirror with different radii of curvatures for the two perpendicular directions. This will be possible after the design of a new head by A. Pepato to be mounted on the LT machine. The mirror surface will Therefore, be a section of a torus. This will be obtained by a misalignment of the rotating head axis and the rotation axis of the mirror at the LT–machine

iv) For the glass mirrors, currently some works are ongoing for the use of new solutions for the cold–slumping technique. These studies are under development by INAF–Milano and are only presented here. In particular, the use of a second ultra–thin glass sheet glued over the surface sheet could increase the surface quality. Furthermore, the use of Glassfoam™ instead of honeycomb inside the mirror could increase the mirror stiffness.

All these activities for MAGIC II mirrors are slightly converging into the activities for the future generation of European Cherenkov telescopes, namely for the Cherenkov Telescope Array (CTA) consortium. The people involved are increasing and future works will be carried out with a European–wide competition, which will result in a better selection of candidates and solutions. In the next chapter, the activities I have already performed are described.

References

[1] C. Baixeras et al. Commissioning and first tests of the magic telescope. *Nuclear Instruments and Methods in Physics Research Section A*, 518(1-2):188 – 192, 2004. Frontier Detectors for Frontier Physics: Proceedin.

[2] J. Barrio et al. MAGIC Design Report. Available at http://wwwmagic.mppmu.mpg.de/publications/proposals/, 1998.

[3] D. Bastieri et al. Development and production of light-weight all-aluminium mirrors for the magic telescope. In *7th Workshop on Towards a Network of Atmospheric Cherenkov Detectors*, Palaiseau, France, 2005.

[4] D. Bastieri et al. The mirrors for the magic telescopes. In *Proc. of 29th Internatial Cosmic Ray Conference (ICRC 2005)*, Pune, India, 2005.

[5] C. Bigongiari et al. The magic telescope reflecting surface. *Nuclear Instruments and Methods in Physics Research Section A*, 518(1-2):193 – 194, 2004. Frontier Detectors for Frontier Physics: Proceeding.

[6] M. Doro et al. The Reflectors of the Imaging Atmospheric Cherenkov Telscopes MAGIC I and MAGIC II. Under publication in Journal of Instrumentation.

[7] M. Doro et al. Realization of Mirrors for the MAGIC Telescopes. In *LNL Annual Report 2007*, 2008. Available at http://www.lnl.infn.it/ annrep/.

[8] M. Doro et al. The reflective surface of the MAGIC telescope. *Nucl. Instr. and Meth. in Phys. Res. A*, 595:200–203, Sept. 2008.

[9] M. Doro and E. Lorenz. Technical solutions for the magic telescope. In *Proc. of 10th ICATPP Conference on Astroparticle, Particle, Space Physics, Detectors and Applications, Como, Italy*, 2007.

[10] N. Galante. Il telescopio magic per l'osservazione dei gamma ray bursts. Master's thesis, Universitá degli Studi di Padova, Padova, Italy, 2002. Diploma Thesis. Available at http://magic.pd.infn.it/Documents/publications.html.

[11] M. Garczarczyk. First observations of the grb prompt and early afterglow emission phase at $\sim$ 100 gev energy regime with the 17 m $\varnothing$ magic imaging atmospheric cherenkov telescope. Master's thesis, Max-Planck-Institut fuer Physik, Muenchen, Germany, 2006. PhD Thesis. Available at http://wwwmagic.mppmu.mpg.de/publications/theses.

[12] N. Tonello. Study of the vhe gamma-ray emission from the active galactic nucleus 1es1959+650. Master's thesis, Max-Planck-Institut für Physik, München, Germany, 2006. Phd Thesis. Available at http://wwwmagic.mppmu.mpg.de/publications/theses.

[13] D. Vernani, R. Banham, O. Citterio, F. Sanvito, G. Valsecchi, G. Pareschi, M. Ghigo, E. Giro, M. Doro, and M. Mariotti. Development of cold-slumping glass mirrors for imaging Cherenkov telescopes. In *Society of Photo-Optical Instrumentation Engineers (SPIE) Conference Series*, volume 7018 of *Presented at the Society of Photo-Optical Instrumentation Engineers (SPIE) Conference*, July 2008.

5

Optics and mirrors for the CTA observatory

The Cherenkov Telescope Array (CTA) is a planned experiment of an array of IACTs with a total mirror area that could be of the order of $10,000$ m^2. CTA constitutes the future of the IACT technique and therefore, the future of MAGIC. Any development activity is now slightly slewing into the CTA consortium. CTA mirrors should have a high optical performance, a high durability and reduced cost. MAGIC II mirrors are optimal candidates. In this chapter, the activities of the CTA mirror working group are reported. The quality demands, the current technologies and the future development are discussed.

This chapter is adapted from (password–protected): *Building Blocks for CTA: existing solutions and new designs. Mount and Mirrors.*, 2008 [4] and *Technical Information for the Development of Mirror Prototypes for the CTA Observatory*, 2008 [3].

5.1 CTA: scientific motivation

During past decades, Imaging Air Cherenkov Telescopes (IACTs) have proven to be the most successful type of instrument to carry out ground-based VHE gamma-ray astronomy. The number of detected sources has increased steadily over time and is foreseen to reach the value of 100 with the current generation. γ–ray emission has been observed from several classes of objects in the entire sky and particularly on the galactic plane. Questions of fundamental physics like dark matter and quantum gravity are possibly round the corner of γ–ray astronomy too.

On the other hand, the observation so far could not help to explain some of the most relevant questions of modern astronomy addressed at the beginning of this thesis: where cosmic rays and how are accelerated? How are γ–rays produced? etc. It is now clear that all these questions can be addressed only if the energy range in which telescopes are sensitive is extended. Observations below 100 GeV are of detrimental importance for pulsar studies to discriminate between accelerations at poles or termination fields or for GRBs. On the other hand, only beyond several TeV and possibly towards a hundred TeV the hadronic and leptonic acceleration mechanisms differ substantially. It is clear that one single array of telescopes of the same size cannot cover the large energy band from a few GeV to several tens of TeV. In

addition, a sensitivity increase of at least a factor of 10 is desired, in particular to be sensitive to γ–ray emission from an extended source on several spatial bins. This in turn will allow for discrimination between hadronic and leptonic emission.

To achieve the goal of increasing sensitivity by a factor of 10 over the currently best installations and to cover an energy band from a few tens of GeV to above 100 TeV in energy, a new generation of IACTs has to use more than one size of telescope to be installed over a large area. Due to the general steeply falling fluxes of gamma-rays, one size of IACT is only optimal for covering about 1.5 to 2 decades in energy, therefore at least two or three sizes of telescopes are needed to cover such a large energy band. Extensive MC simulations are currently ongoing in a few possible different layouts of several telescopes of three sizes. Most probably a few very large telescopes ($>$ 20 m diameter) will cover the lower energies, surrounded by some tens of medium–size telescopes ($\sim$ 10 m diameter) which will record the bulk γ–ray emission at TeV energies in turn surrounded by a large number ($\sim$ 50) of small size telescopes which will record the very high energies at several tens of TeV. Particularly interesting is that small and medium telescopes will also act as veto telescopes for very large telescopes to discriminate hadronic showers (spread more over the ground) from pure γ–ray showers.

While the final layout is far from definitive yet, all other subgroups are developing the necessary technology to develop high quality and reliable telescopes. While the design will probably be similar to that of present Cherenkov telescopes, there will be a big step towards the complete automatization of the telescope operation, which is required when dealing with tens of telescopes. The site–search is still ongoing, and privileged locations are the southern hemisphere (for observation of the galactic center) and high altitude (for low energy showers). Possibly Namibia and Argentina could host such sites. Also different from the current generation of IACTs, CTA will be operated as an astronomical observatory where scientists demand for observation times and professional astronomers follow the operation.

The effort is mainly carried out on a European base, even if already partners from Japan and world–wide are following the progress. It is foreseen that a few prototypes will be built in the following years and that the complete construction of the CTA array will start in 2012–13 and be completed in 2015.

5.1.1 The CTA WP–MIR and WP–TEL

Inside the CTA consortium, I am co–coordinator of the activity of the CTA Working–Package Mirror (WP–MIR). For the design phase of the telescopes, the group works in synergy with the Working–Package Telescope (WP–TEL). The main activities of the WP–MIR are:

i) Discuss the optics for CTA telescopes of different sizes (in synergy with WP–TEL)

ii) Develop a design for a small–size and a large–size telescope prototype for CTA

iii) Develop and test techniques for IACT mirror facets

iv) Develop and test techniques for mirror coatings and protection

v) Find industrial partners and optimize costs

vi) Develop the strategy and technology for a mirror repositioning control system.

vii) Take care of the overall telescope photon detection efficiency

All the updated information on the status and advances are recorded in the CTA webpage http://www.cta-observatory.org/ctawpcwiki/index.php/WP_MIR (password–protected). In February 2008, a meeting–in–person was held in Heidelberg for the joints groups WP–MIR and WP–TEL. During this meeting the main activities of the working package were defined. A second meeting–in–person was held in Padova (Nov 3–5, 2008) where important advances on mirror prototyping were presented.

5.2 Structures of CTA telescopes.

Based on a preliminary work from E. Lorenz, a section for the CTA Letter of Intent (LOI) was prepared. In the document, available at the WP–MIR webpage, two designs of telescopes are presented: a Small Size Telescope (SST) with 5 m diameter and a Large Size Telescope with 23 m diameter. The two designs are briefly presented in § 4.19(i). For a more detailed description the reader is referred to Ref. [4]. Hereafter, some basic design considerations are discussed. The optics design and the mirrors are often the result of a compromise between competing factors, in particular between costs and performance. For this reason, a panoramic view of the main structural subsystems is hereafter reported.

5.2.1 General design considerations

Mounting system

The mounting system of the telescope is the general telescope layout and the basic tracking system. IAC telescopes usually have an *alt–azimuth* mounting, where two perpendicular motions are controlled by servo–motors. The azimuthal motion is on a horizontal plane parallel to the ground and the vertical motion (altitude motion or zenith motion) elevates the telescope structure. The basic reason for alt–azimuth motion is the very large size of the Cherenkov telescopes which makes it technically difficult to build an equatorial design and the simpler construction in remote sites.

Historically two basic mounting designs were used:

- the circular rail system such as used in HESS or MAGIC, see Figure 5.1(a)
- the central support mast as used by HEGRA or VERITAS, see Figure 5.1(b)

The latter design is typically used for radio antennas and solar towers because of its simplicity. On the other hand, it is adapted more for short f/d ratios and requires additional counterweights at the back of the structure for the weight of focal plane instrumentation. The counterweights increase the moment of inertia of the telescope with consequent problems when fast motion is required, as for example, for GRB response. Lately, there is a trend towards placing lots of electronics inside the camera of IACTs which increases its weight and puts several constraints on the central mast design, at least for large telescopes. For small telescopes on the other hand, this is less problematic and a design of a central mast steel small telescopes is currently under development at MPI-Heidelberg. For smaller telescopes, like the SST, different solutions such as a telescope solidly rotating platform, as used in HEGRA, can be considered because of the easier and safer design.

The rail construction is well–suited for large structures. The weight of the camera can be taken by the overall structure with no need of large counterweights, or at least they can be closer to the telescope structure. This allows for a much faster movement of the structure. In cases of large telescopes like HESS and MAGIC, the telescope structures rotate on a rail–like basement. More details on the rails structure are given below.

(a) Rail system (MAGIC) (b) Central Mast (VERITAS)

Figure 5.1: Different mounting systems for Cherenkov telescopes. On the left, the first MAGIC telescope is shown. The entire structure rotates on a circular rail. The camera is supported by a tubular "Gothic" arc which also drives the altitude motion. The entire structure is mounted onto two–bogeys. The space–frame is made of CFRP and the basement structure is made of aluminum tubes. On the right, one of the four VERITAS telescope is shown with only part of the mirror installed. The camera is supported by four steel masts anchored directly onto the reflector dish.

Space–frame construction

The space–frame design is to a certain extent the principal feature of the telescope because the entire structure and the peripheral system is based upon this relevant part. For this reason, a long discussion is currently taking place inside the WP–TEL about which are the best materials and which are the best solutions to adopt for CTA telescopes. It must be premised that different solutions can be taken for telescopes of different sizes.

As regards to the materials, the main solutions adopted for telescope mechanics and for constructions in general are steel and aluminum, while only recently carbon–fibers have started to take a leading role in light–weight structures. Each material has advantages and drawbacks, which are also mostly to be contextualized in the field of telescopes which could be built on very remote sites:

- **Steel.** Steel is the most commonly used material for telescope constructions and of course, for civil construction. Its main advantages are that it is the cheapest material and its production and handling is world–wide known, so one does not have to refer to specialized (and therefore, expensive) private companies. Therefore, for example, one can save costs by obtaining the steel locally and avoiding shipment. Also for installation and mounting of the telescope, there is no need for particularly trained people. A drawback of steel is its very large weight. To maintain rigidity, the steel units must be very big at the expense of the overall light–weight. This particularly constitutes a problem when one wants a telescope with a fast response to GRBs. In this case, a lightweight structure is detrimental. For smaller telescopes, this strong demand is not needed, also because GRBs are thought to be observable at lower energies.
- **Aluminum.** Aluminum is less heavy than steel, and has a higher specific Young modulus. Nevertheless, it has the largest thermal expansion of all three materials. While no full–aluminum mounting structure was ever considered for the telescopes, many relevant

parts of the structure can be made of aluminum, which is also available at the market.

– **CFRP** CFRP is the strongest material of the three, and at the same time is by large, the lightest. It has nearly no thermal expansion and better oscillation damping. Currently, it is probably more expensive than steel or aluminum, however the market crisis and increased development and diffusion of the technique is making this material cheaper and cheaper. This material is now used in many different applications, for example, the company EXEL, in Finland, produces carbon fiber plastics for the pales of wind power plants and at the same time for the doors of buses. From recent discussions with them, we were ensured that they can produced materials of whatever shape under request. At the same time, they are developing a technique for making big tubes at a reduced price. One could also think of building the entire telescope structure made of such materials including structure knots and bearings.

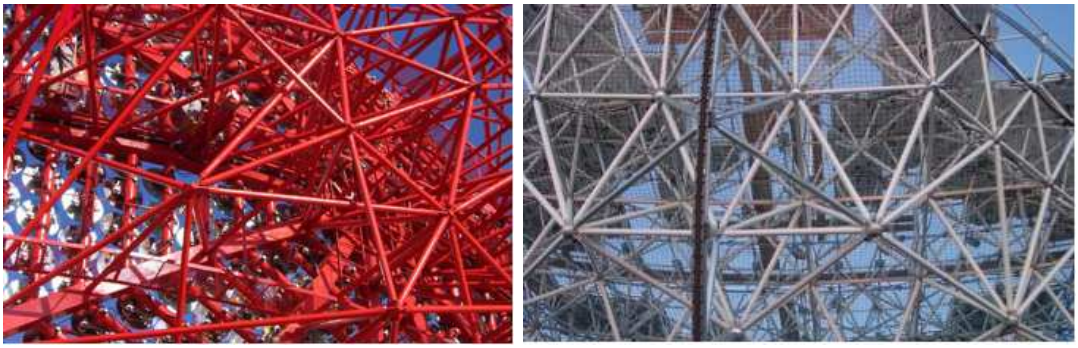

(a) Steel space–frame (HESS) (b) CFRP space–frame (MAGIC)

Figure 5.2: Steel and CFRP solutions for the space–frame of telescopes. On the left, the HESS space–frame is shown, the entire structure is made of steel. On the right, the MAGIC space–frame is shown. In this case, CFRP tubes are joined with aluminum knots.

Camera support

The camera of current IACTs is always mounted on tubes connected to the main reflector. In the case of HESS and VERITAS four masts connect the camera to 4 points dislocated inside the reflector dish. This has the advantage of keeping the structure stiffer and the drawback of shadowing part of the mirrors and consequent loss of effective area. On the other hand, MAGIC mounts the camera on a tubular aluminum arc, called the "Gothic arc" because of its shape, which goes around the structure of the reflector and secures the camera to the telescope bogeys. The tubular arc is maintained in position by pre–stressed steel cables, like the spokes of a bicycle wheel. This solution, long thought to be unhelpful to damping down camera oscillations during telescope motion, provided to be simple and procure little shadowing and weight. In addition, the Gothic arc is linked with the altitude–motors which drive the telescope up and down. The camera supports for MAGIC and VERITAS are shown in Figure 5.1.

Foundations

Figure 5.3: Sketch of an I-beam rail.

An important issue will be the foundation and substructure of the telescopes. Due to their large mirror area, telescopes will be at risk during strong storms. Normally using a very heavy substructure and undercarriage prevents a lift–off. For example, nearly half the weight of the MAGIC telescope is in the bogeys. An alternative, even better suited in cases of adversely structured (non-flat) sites, is to use a foundation composed of some heavy concrete blocks inserted into the ground and a stiff I-beam steel ring on which a lightweight construction is running, see Figure 5.3. By appropriate elements, the telescope can be anchored around the I-beam such that it cannot be lifted off. In such a case the central azimuth axis would not be loaded too much and can be fixed to the I-beam ring by spokes. Removal of such a construction after the termination of the experiments would be rather easy. It is interesting to note how much the I-beam can be bent without any distortion by normal industrial techniques up to very small radius of curvature.

5.2.2 Small size telescope (SST) and large size telescope (LST)

Starting from a rather large preparatory work from E. Lorenz, a document was produced for the design consideration of a small size telescope of 5 m diameter and a large size telescope of 24 m diameter for CTA. All the details can be found in Ref. [4]. For both telescopes, placeholder values for the telescope structure and mirror parameters were provided, which will be briefly discussed below.

Small size telescope – SST

Small size telescopes have already had a glorious history with the HEGRA telescope. The success of this telescope can be pinpointed in a few sentences:

- for small telescopes, the f–number can be quite large, the field of view can therefore, be quite large and with reduced aberrations over the entire focal plane. The construction is in general easy and fast. The cost goes mostly in the electronics equipment rather than in the structure itself.
- The requirements for the PSF of the focused mirror are less critical than for the low threshold LST and MST because from around 1 TeV upwards the γ and hadron shower images are already quite extended and differ significantly in the image parameters Width and Length. In turn no very fine pixel size is needed. A pixel size of 0.25° is sufficient. More important is a camera with a FOV of around 6° ∅.
- the energy threshold for this size of telescope is around 500 GeV. They are therefore, well suited for showers above the TeV, where their sensitivity is maximum. In this region also, the background rejection is extremely efficient and therefore, the sensitivity is very large
- despite the great sensitivity and the goodness of the background rejection, TeV telescopes must deal with the rapidly falling γ–ray fluxes at high energies. Therefore, a large area coverage with a great number of telescopes is desired to increase statistics.

A prototypes SST could have these characteristics:

i) **Energy range.** Optimized for observation in the range 1-100 TeV.

ii) **Optics.** A spherical mirror with 5.3 m diameter and 18 m^2 area. The $f-$number should be large, around 1.4 and therefore, the focal distance should be around 7.5 m. The mirror mount could follow a Davies–Cotton (Whipple, HESS, VERITAS) or a quasi–spherical (HEGRA) design.

iii) **Mirrors.** The preferred mirror shape is hexagonal, with 18 elements. In principle there is no indication about the mirror technique. The mirror should be arranged as in Figure 5.4

iv) **Focal plane instrumentation.** The camera diameter could be as large as 6°, with a pixel size of 0.25° ($\approx$ 475 photon sensors).

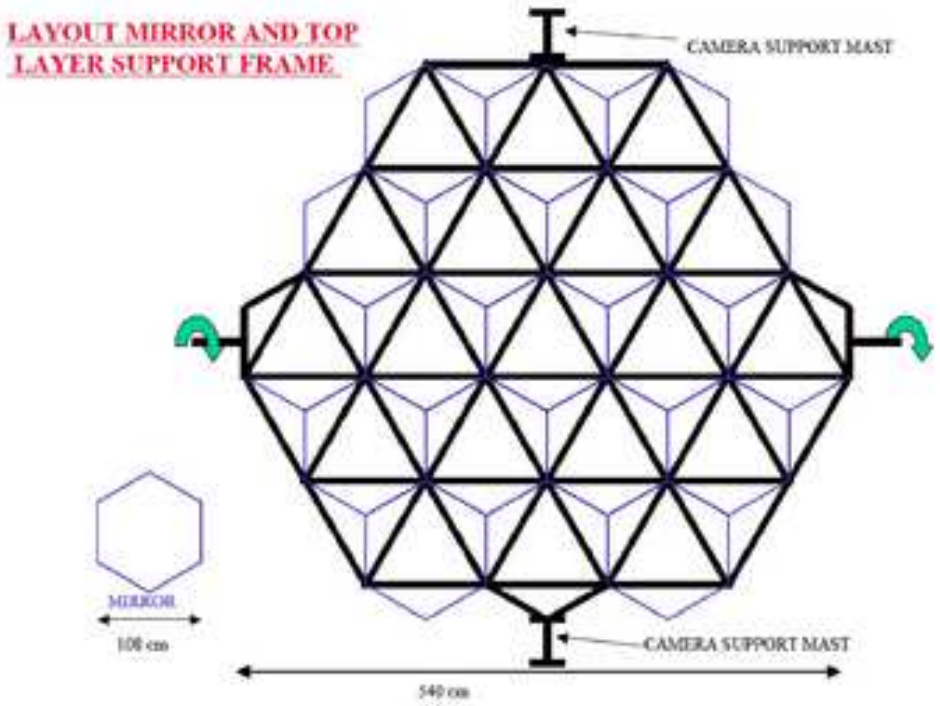

Figure 5.4: Layout of the tessellated mirror of the template SST together with the top layer of the mirror support frame and the dimensions of a single mirror facet. Picture from E. Lorenz.

Large Size Telescope – LST

A telescope of 24 m diameter is quite more challenging than the SST. All parts and subsystems should be optimized, the cost fraction of the structure could probably also be larger than the electronics one. The principal characteristics are hereafter summarized:

– due to its large surface, the LST is best suited for low energy threshold observations. Therefore, the telescope should be optimized only in the very low energy band and cannot compete with medium size telescope in the TeV regime

- the field of view is not required to be very large because low energy showers are usually concentrated towards the center of the camera. In addition, a very large focal plane distance cannot be afforded in the big structure and therefore, the camera size must be kept small. A second reason it that a larger camera is normally heavier and therefore, harder to sustain.
- the structure should be light to be rapidly repositioned in reply to GRBs alert as for MAGIC. For this reason CFRP should be the best solution and a strong effort should be made in structure optimization.
- the optics must be parabolic to preserve the time stamp.
- Deformations of the structure become problematic (material strength does not increase with size), therefore it pays eventually to invest more in light sensors and in the reduction of optical losses.

A prototype LST could have these characteristics:

i) **Energy range.** Optimized for observation between 10 GeV and 2–3 TeV.

ii) **Optics.** A dish diameter of 23 m, with a total area of 410 m^2. $f-$number=1.2 and therefore, a focal length of 28 m. The dish profile must be parabolic, with a deviation of $< 2-3$ cm from the ideal curve. The space frame should be made of CFRP with aluminum knots as in MAGIC and structured in tetraeders.

iii) **Mirror.** The shape of the mirrors should be hexagonal, with A 1.5 flat–to–flat diameter and 1.9 m^2 area. The weight should be minimized and kept below 40 kg/m^2. Therefore, 220 mirrors should cover the entire reflector. The mirror reflectivity should also be maximized $> 95\%$ (300-550 nm) and $> 85\%$ (550-650 nm). There should be a permanent active mirror control. The mirrors could be arranged as in Figure 5.5

iv) **Focal plane instrumentation.** The camera should weigh not more than 1 ton, supported by a Gothic arc shape mast or by 4 independent masts.

5.3 General mirror design considerations

The main mirror of an IACT is, because of the large size, composed of many small elements, which are easier to fabricate than very large elements or single entities. The requirement to observe Cherenkov light emitted by an extended shower and from many scattered tracks relaxes the optical precision of the mirrors. Typically, mirror elements can be staggered and the focusing can be worse by nearly two orders of magnitude compared to optical astronomical mirrors. Too fine fracturing of the main mirror into a large number of elements has the disadvantage of increasing the costs for the mounting and makes final adjustments a problem. As usual, one has to find a balance between costs and performance. Small IACTs normally have a near spherical overall mirror profile (Davies and Cotton [1]) while for very large mirrors the minimization of the light path differences between light hitting the inner and outer region of the mirror is of key importance. Therefore, a parabolic (=isochronous) mirror profile is preferred with a caveat of a worth optical distortion (aberration errors for tilted incidence). In order to keep optical errors in tolerable ranges and at the same time use a sizeable FOV ($> 3°$) camera, it is necessary to use an f/D larger than 1. The caveat is a sizeable shadowing of the

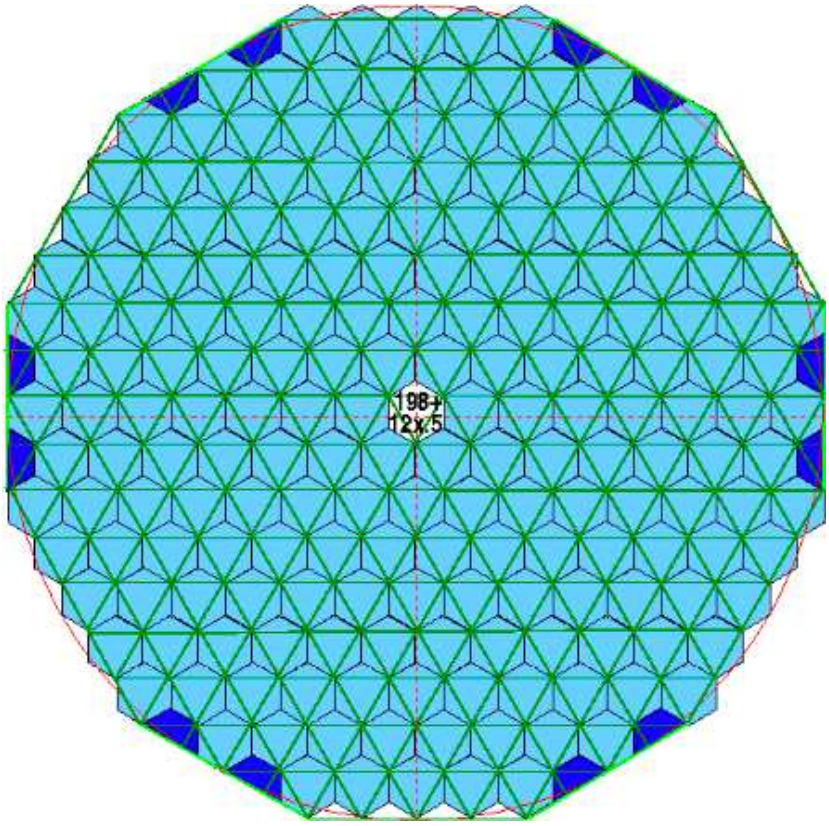

Figure 5.5: Layout of the tessellated mirror of the template LST. Picture from E. Lorenz.

mirror and mechanical constraints for the long camera support masts. While for a spherical mirror all small mirror elements can have the same shape, in the case of a parabolic profile, it is necessary to adapt small elements to their position, i.e., to produce them with different radii. From a certain position outward and for mirrors exceeding a small size, they should be made aspherical. Such mirrors with different focal lengths are clearly more expensive than spherical mirror elements. The situation for CTA might be less critical because the large number of required mirror elements for, say, several $1,000$ m^2 total area, requires anyhow parallel and industrial production.

The production and installation of mirror facets for tens of telescopes is a challenging task. As for the present situation, the production and testing times are rather slow and could be applied for CTA mirror production. There are some general design considerations for the realization of mirrors for CTA, which are listed below [3]:

i) The mirrors should last at least 5 years without the need of human intervention. For a large number of telescopes, a more frequent maintenance is too costly.

ii) The mirrors should be produced and possibly installed by private industrial companies, which guarantee standards for massive production.

iii) An effort to increase mirror reflectivity through innovative surface treatment is desired rather than increasing the telescope size. There is space for a 10% improvement.

iv) The mirror should not cost more than 2–3 kEuro/m^2

An industrial production of mirrors for the CTA observatory is considered basilar. The main reasons are the following

i) The cost of the entire production is hardly sustainable by a private institute rather than from the very CTA consortium itself

ii) The industrial production can minimize costs

iii) Quality standard can be demanded

iv) The installation can be performed by trained people

5.3.1 Mirror mechanical specifications

In particular, a number of specifications that each mirror prototype must fulfill were discussed:

Geometrical shape. The basic idea for CTA telescopes is to use hexagonal mirrors. To reduce the number of facets we aim at sizes larger than those of the current installations resulting in facets between 1 and 2.5 m^2 area. The maximum deviation from the nominal shape shall be ± 1 mm.

Thickness. The thickness of the mirrors is not specified explicitly. The mirrors shall fulfill the requirements of optical quality, mechanical stability, mirror deformation, etc. while meeting weight restrictions. The thickness shall be the same for all mirrors within a tolerance of 1 mm.

Nominal focal length. The focal length is not fixed at present. It will most probably be in the range from $10,000$ to $50,000$ mm depending on the size/type of the telescope. Deviations in focal length are not specified directly, but are implied by the specifications for the resolution, which is measured at the nominal focal length.

Weight. The absolute weight limit will depend on the size of the mirror facets and the construction of the telescope, the mirror alignment system and constraints due to the necessary handling of the mirrors. Manufacturers are asked to provide solutions which are as lightweight as possible but not at the expense of the optical quality or the stability of the facet or a significant increase in price. From the point of view of handling of the facets, a total weight of less than 30 kg would be desirable.

Mirror deformation. Due to the movement of the telescopes the orientation of the mirrors changes between facing 40° down and 90° up relative to a vertical position. The mirror deformation under gravity must be small enough to maintain the specifications for the reflectance and for the resolution for all orientations.

Temperature range. -15°C to $+60$°C. Temperature variations of 30°C between daytime and nighttime are not uncommon. The mirrors shall not suffer any damage or irreversible change of optical properties from temperature variations within this range.

Operating temperature range. -20°C to $+20$°C. The optical specifications shall be maintained within this range.

5.3.2 Mirror optical specifications

Surface shape. The surface shape has not been decided yet. Most probably it will be spherical, especially for the smaller telescopes. For the large telescopes aspherical mirrors better matching a parabolic profile might be an interesting option if in the given production technique the surface shape can be adjusted easily. The surface roughness is not specified directly but is constrained by the requirements on reflectance (for short-scale roughness) and resolution (for long-scale roughness).

Reflectance and Resolution. The final requirements for the resolution of future CTA mirrors, i.e. the spot size of the reflected light on the Cherenkov Telescope Camera, will depend on the pixel size of this camera and the final design of the telescope dish the details of which have not yet been completely fixed. Therefore, the following criteria are for the prototypes and might change slightly for the final CTA mirrors. The reflectance shall exceed 80% for all wavelengths in the range from 300 to 600 nm, ideally close to (or even above) 90%. The range of short wavelengths (300 to 450 nm) contains most of the intensity of the light observed in the experiment and when the optimization of coatings prefers certain wavelength regions, the reflectance should be optimized for this range. The reflectance is always defined as a directed reflectance into the spot.

Measurement technique. Only the intensity collected near the focal spot is of relevance for the performance of the telescope. The following method is employed: A point-like light source at twice the nominal focal length is imaged at twice the nominal focal length and the intensity in the image is determined by scanning the image spot over a circular area with the specified integration diameter. The light flux Q integrated over this area is compared with the light flux F at the location of the mirror and using the nominal mirror area A the effective reflectance is calculated as $R = Q/(FA)$. This is done for different wavelengths separately.

Reflectance of first prototypes. The effective reflectance (as defined above) shall exceed 80% for all wavelengths in the range from 300 to 600 nm, ideally close to (or even above) 90%. In the case of a non-uniform distribution the maximum spectral reflectance shall be between 300 and 450 nm. The required minimum of 80% of the incident light to be reflected shall be contained in a circular area with an integration diameter of 2 mrad. Averaged over all mirrors delivered by one manufacturer, the spot diameter of the circle containing 90% of the reflected light shall be smaller than 0.6 mrad. To meet this criterion, a certain number of mirrors with worse performance might be rejected. A diffuse reflected component is not critical as long as it is spread out over a large solid angle. A diffuse component of 10% of the incident light concentrated over an area of 1 degree diameter, on the other hand, would add a halo to images and would degrade the performance of the instrument. Limits on a diffuse component depend on the angular distribution of the diffuse reflection and need to be addressed individually for manufacturing techniques which result in significant amounts of diffuse reflected light. Scratches and surface imperfections are uncritical to the extent that they (a) do not reduce the reflectance and the resolution below specifications, (b) do not generate a significant diffuse component of reflected light and (c) do not impact the long-term stability of the mirrors. No stains or discoloration are allowed which are readily visible to the unaided eye. The mirrors will be used for a period of up to 10 years. The mirror material shall not exhibit flow or relaxation processes which change the resolution (i.e. beyond specifications) significantly over this time. Most critical is the long-term stability

of the reflectivity under the given environmental conditions. A reflectance loss of no more than 3% per year is expected, in line with results obtained with earlier instruments under similar conditions. The reflective/protective surface shall show no damage under usual adhesion tests, where a 3M Scotch Brand No. 600 tape (or equivalent) is pressed firmly against the front surface mirror coating surface and removed quickly. The surface shall not show damage under moderate abrasion tests, after a standard 200-rub test with a cheesecloth pad. The bearing force shall be nominally one pound.

Accelerated aging: Short term tests of durability include humidity and temperature cycling and a salt fog test. The surface and the optical characteristics shall show no deterioration after exposure to a 10-day humidity test where humidity is cycled between 0 and 100% and temperature between $-15°$C and 60°C. The coating and optical characteristics shall show no deterioration after exposure to a standard 24 hour salt fog test. The mirrors may occasionally be subject to mechanical impact, such as birds flying into the mirrors, birds pecking at the mirrors, or possibly hail. Mechanical impact is simulated by dropping a steel sphere with a diameter of 10 mm from a height of 3 m onto the mirror. Under the impact the mirror shall not shatter, develop cracks, or change its global optical properties as specified above. Local loss of reflectivity or deformation over an area that does not significantly exceed the size of the steel sphere is acceptable.

5.3.3 Surface treatment

The surface treatment is a common operation for all mirrors, even for aluminum mirrors it constitutes only a precautionary measurement to reduce degradation. For glass or other non–reflective materials the coating with aluminum (or other reflective materials) is an unavoidable step. The current situation is very poor: the degradation of glass mirrors is pretty fast and this type of mirrors must be removed and recoated i.e. every 5 years. The coating process is also a very delicate process and only trained companies can perform it with enough precision to guarantee the quality standard of telescope mirrors. Many advances are expected in this field, in particular on a) surface preparation, i.e with chromium [2], b) plasma deposition, c) coating admixtures, d) different coating techniques.

5.3.4 A testing facilities

Two independent test–facilities are foreseen for *a*) a complete qualification of all mirror prototypes until a final decision regarding design is made, *b*) a full characterization of each mirror to be installed on the CTA telescopes. For the former task, two groups are formed: one constituted by E.Giro, M. Mariotti and I, in charge of constituting a facility at the National Laboratories in Legnaro, a second group headed by A. Foerster, to build a facility in Tubingen, Germany.

In the following, the lists of tests to be systematically performed on prototypes and possibly on all mirrors.

1. Focal length at different wavelengths $(250 - 650$ nm) to be done at the best focal point and around these positions to understand spot stability. A rail to move the mirror back and forth is foreseen. The basic setup will be with a CCD camera observing the focal plane where the reflection of LEDs or halogen lamp is created.

2. Focal length dependence on temperature. To perform this test, a dedicated heating chamber will be designed and constructed.

3. Mechanical deformation – rigidity. By putting local weights one can estimate the mechanical rigidity and the shift of the reflected spot. This test mimics the real conditions where the mirrors are operated at different orientations.

4. Differential reflectivity measurement with portable reflectophotometers. Perform full scan of the surface from 300 to 800 nm. The mirror surface can be strongly inhomogeneous, in particular for the coating. For this reason a full scan is desirable.

5. Absolute reflectivity measurement with calibrated diodes. One can scan the focal plane with a diode, and the use of and $x - y$ scanning device.

6. Measurement of surface micro–roughness. To be performed before and after thermal cycles (at least 500 cycles), and salt–fog tests. From the surface roughness one could estimate the reflectivity properties and fully characterize optically the mirror.

7. Adhesion of coating. This is done by stripping a normal desk tape from the surface and checking the coating adhesion.

8. Water–tightness. This is done by inserting the mirror into warm water in a tank. The warm water makes the air inside the mirror expand and facilitates the observation of bubbles.

9. UV–resistance. All plastic parts will be tested with a powerful UV–lamp to understand possible degradations.

5.4 Brief review of current techniques for mirrors

We underlined that mirror elements can be worse by nearly two orders of magnitude compared to optical astronomical mirrors. Many techniques were used in the past, and are under development at present, for the realization of mirrors for Cherenkov experiments. In the following, we describe some of these techniques.

Glass mirrors

Glass mirrors have been the standard solutions for most past and present IACT installations. The mirrors were produced from machined and polished glass blanks that were coated in vacuum with aluminum and some weather–resistant transparent protection layer (normally quartz). The main properties of glass mirrors are good reflectivity, contained costs, extensive production experience and easy production.

Possible drawbacks are fragilities, relatively fast ageing/degradation of the reflective surface when exposed permanently to the atmosphere and large weight. A typical degradation of the reflectivity of at least 6% per year is observed for single 100–200 nm layer quartz protection. It is quite difficult to increase with current technologies the "classical" glass mirrors beyond 1 m^2 area because the required thickness for the solid plate makes the mirrors quite heavy and difficult to handle and to machine. Also, the risk of breaking due to internal stresses or uneven mechanical loads increases

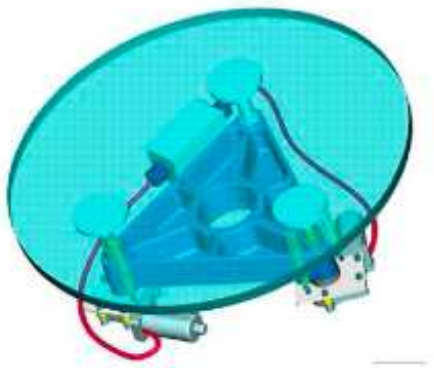

Figure 5.6: Sketch of a glass mirror of HEGRA telescope.

with the increased dimensions. An example of round glass mirrors is proposed in Figure 5.6 for the HEGRA reflector.

Diamond-milled Aluminum mirrors

Quite some knowledge in building and in the performance of aluminum mirrors has been obtained with the HEGRA CT1 and the MAGIC telescopes. The technique is very promising in particular because of the little ageing and high optical performance. This technique was fully addressed in Chapter4. For future applications, it was already mentioned that the production of aspherical mirrors is one of the future goals. On the other hand, already some design work has been done to design an hexagonal mirror of improved design. Particular attention has been given to simplify the design to reduce production costs. In particular, this work is ongoing in the case of LST mirrors.

Cold-slumped glass mirrors

Another ongoing development is the series production of mirror panels by means of the so-called replica technique. The replica technique can be very cost effective and result in very lightweight mirrors. This technique was also described in § 4.3 to which the reader is referred to. The replica method, although long-term tests are still not available, has for the time being the most promising potential for CTA and will be considered as the baseline design. Currently, progress is under development in this technique in particular in two directions:

- the optical quality of the mirror can be increased with a second ultra–thin glass sheet glued in front of the replica mirror. This new sheet will have very reduced roughness and therefore, reduced light scattering and will allow for a better match to the overall spherical shape. On the other hand, the solidity of the new sheet is ensured by the rigidity of the back sandwich.
- the use of honeycomb has some drawbacks with respect to a spring back effect at the moment of assembling the sandwich and in terms of costs. A new solution is currently under development with an innovative glass foam used for acoustic insulation. The rigid glass foam is premachined to the desired shape and the thin glass sheet and the assembly technique is the cold–slumping, where the glass sheet is bent onto a curved mould.

Both techniques are under development at INAF-Merate and are very promising for CTA applications.

Foamed mirrors

Some work has been done to develop a thin glass mirror following the replica method where the rigidity of the mirror is ensured by an expanding foam like polystyrene. Despite positive results in terms of optical quality and reflectivity obtained by the Saclay group, it has been pointed out that a problem of dew formation is always related to the use of foam. Due to the different thermal coefficients of glass and foam, the temperature drops at the surface of the mirror causing dew to form on the front of the mirror which strongly affects its reflectivity in operation in the open environment.

Carbon–Fiber mirrors

At the university of Warsaw, a prototype technology is under development to build carbon fiber mirrors. The basics of the layout is to prepare two surfaces connected together by small carbon–fiber tubes which provides rigidity. The design is currently under tests, despite the first results are not encouraging.

References

[1] J. Davies and E. Cotton. *J. Solar Energy Sci. and Eng.*, 1:16, 1957.

[2] D. Ferenc, A. Chang, L. Johnson, D. Kranich, A. Laille, and E. Lorenz. A new method for vacuum sealing of flat-panel photosensors. *Nuclear Instruments and Methods in Physics Research A*, 567:205–208, Nov. 2006.

[3] A. Foerster and M. Doro. Technical Information for the Development of Mirror Prototypes for the CTA Observatory. Available at http://www.cta-observatory.org/ctawpcwiki/ index.php/WP_MIR (password–protected), 2008.

[4] E. Lorenz and M. Doro. Building Blocks for CTA: existing solutions and new designs. Mount and Mirrors. Available at http://www.cta-observatory.org/ctawpcwiki/ index.php/WP_MIR (password–protected), 2008.

References for Companies and Institutions

CRM Compositi	*http://www.crmcompositi.com/ CRM Compositi, Via Boccherini 2, 57124 Livorno, Italy. Reference person: F. Cavallini.*
Compositex	*http://www.compositex.it. Compositex Srl, Strada Pelosa 179, 36100 Vicenza (Italy). Contact person P. Bernadotto.* Compositex developed the tooling for the construction of the raw–blanks aluminum mirrors for MAGIC II. It also produced around 150 raw–blanks.
INFN–Padova	*http://pd.infn.it University of Padova and Instituto Nazionale di Fisica Nuclare (INFN) Padova. Via Marzolo 8, 35131 Padova, Italia. Reference persons: M. Mariotti, M. Doro for MAGIC II mirror, and F. Dazzi, D. Bastieri for MAGIC I mirrors.*
INAF–Milano	*http://mi.inaf.it Instituto Nazionale AstroFisica (INAF) – Osservatorio Astronomico di Brera–Merate, via E. Bianchi 46, 23807 Merate (Lecco), Italy*
INAF–Padova	*http://www.pd.inaf.it Instituto Nazionale AstroFisica (INAF) – Osservatorio Astronomico di Padova, Vicolo dell'Osservatorio 5, 35122 Padova, Italy*
IFAM	*http://www.ifam.fraunhofer.de. Fraunhofer Institute for Manufacturing Technology and Applied Materials Research, Wiener Strasse 12, 28359 Bremen (Germany). Reference person F. Neese.* IFAM coated with a special quartz coating all mirrors for the aluminum mirrors for MAGIC I and MAGIC II.
I.Ma.Tec.	http://www.imatec.it *I.Ma.Tec S.r.l., Via G. Stephenson 74, 20157 Milano, Italia. Reference person: Rinaldi* I.Ma.Tec provided the honeycomb for MAGIC I and MAGIC II mirrors.
LNL	*http://www.lnl.infn.it/ INFN - Laboratori Nazionali di Legnaro Viale dell'Universitá 2, 35020 Legnaro (Padova), Italy. Padiglione Alte Energie.* In this facility all MAGIC I mirrors were assembled. Measurements on MAGIC II aluminum and glass mirrors were performed. In this place it is foreseen to place the CTA facility for mirror measuring.
LT Ultra	*http://www.lt-ultra.com. LT Ultra–Precision Technologies, Aftholderberg, Wiesenstr.9, 88634, Herdwangen-Schönach (Germany). Reference person J. Arnold.* LT–Ultra developed and built a first machine to diamond–mill MAGIC I mirrors with the fly–cutter technique. It developed a larger machine for MAGIC II mirrors. In total, more than 1000 mirrors were milled at LT.
Me.Co.M	*http://mecomsnc.com Me.Co.M Via dellíndustria, 8/10, 35012 Camposampiero, Padova (Italy).* Me.Co.M provided all the aluminum top and bottom plates for MAGIC I (INFN–design) and MAGIC II aluminum mirrors.

MPI–Munich	*http://www.mppmu.mpg.de Max-Planck-Institut für Physik (Werner-Heisenberg-Institut), Föhringer Ring 6, 80805 München, Germany*

PART TWO

DARK MATTER SEARCHES WITH MAGIC
and
PROSPECTS OF DARK MATTER SEARCHES WITH MAGIC II AND CTA

"Cold, Dark Matter: An Exploded View".
Artistic impression of Cornelia Parker

6 The dark matter paradigm

There are strong evidence that the universe is composed of a new form of matter, which accounts for about 23% of the total energy budget. This matter is observed though its gravitational interactions, and due to its large presence, it must have influenced the structure formation and evolution. Nevertheless, despite recent amazing experimental results, we could not conclude what dark matter is. In this chapter, the dark matter paradigm is introduced. The major experimental evidences will be presented together with the principal theoretical modelization and the particle candidates.

6.1 Evidences

What is dark matter? It is one of the most puzzling questions that physicists are enduring to solve. There is an incredibly large amount of literature, with hundreds of articles written on tens and tens of candidates and proposed solution. On the other hand, possibly the only thing that we know about dark matter is that it is massive, because we see its gravitational effects on various cosmological scales and because we estimate that it accounts for 80% more than ordinary baryonic matter. How is this possible? How could dark matter passed unseen until almost now? The answer is simple: it is very very low interacting, with expected cross–section never larger than the picobarn (10^{-33} cm^2), and no clear interaction with ordinary matter.

On the other hand, the evidence for the existence of dark matter are more and more compelling, and the experiments currently hunting for dark matter and very numerous. A bright future could be round the corner, but first of all, we present a brief history of dark matter, showing the main experimental results that, for almost a hundred years, perplex the scientific community.

Early premises

From the very beginning of astronomical observation many thousands years ago until very recently, astronomers thought the universe was only composed by our solar system planets and the stars, i.e., in other words, by visible baryonic matter. The first hints that some matter was in the form of non–luminous form can be traced back to the end of XIX century, when compact objects like Sirius B and Procyon were observed (1844 and 1862). Another

interesting fact was the prediction of the existence of Neptune from anomalous gravitation in Uranus (1846). At the beginning of the XX century, studies on closeby galaxies started to be more detailed. In particular, the study of the mass estimated by star luminosity of the galaxy Andromeda[1] showed that it should have been three times that expected [28] when compared to the Milky Way. Few years later, the astronomer Oort made a deep study of the MW disk in the solar system surroundings [27] and by combining Poisson's equations with the Boltzmann distribution of particle velocities for the galactic disk, he made predictions of the average density of matter in this region. Oort found that the average density was 0.09 $M_\odot$ pc^{-3}, where the observed density from stellar determination is of 0.03 $M_\odot$ pc^{-3} only.

Rotational curves

Despite these earlier evidences, it was only the brilliant and unprejudiced scientist Zwicky, shown in the picture, who first introduced the paradigm of the missing non–luminous matter. Zwicky studied the gravitational field on the motion of galaxies in galaxy clusters [36]. A *rotational curve* describe the velocity of objects in gravitationally bound systems in function of the distance from the center. In case the system is virialized, which is usually the case for large relaxed gravitational systems, the following relation holds:

$$U = -2K \quad \Longrightarrow \quad v(r) = \sqrt{\frac{G\,M(r)}{r}} \tag{6.1}$$

where $U(r) = G\,M(r)\,m/r$ is the gravitation potential energy for a distribution of mass $M(r)$ contained in a sphere of radius r, m is the mass of the object and G is Newton's constant and finally $K = m\,v^2/2$ is the kinetic energy of the object.

Figure 6.1: The swiss astronomer Fritz Zwicky in a famous picture.

Therefore, if one takes $M(r)$ as constituted by the sole visible matter, then $M(r) \sim r^3$ inside the galactic disk and $M(r) \simeq 0$ outside and the expected rotational curve would be a raising curve up to the extension of the galactic disk followed by a square root decrease, as shown in Figure 6.2. When studying the Coma cluster, Zwicky found that the mass inferred by photometry was only 1/400 of the virial mass used to fit the observed velocities in Eq. 6.1. Despite this observation, the scientific community was not able to accept his theorem for many years. Theories of missing matter were reconsidered only during the 70's. Faber and Gallagher in 1979 measured the mass–to–luminosity ratio (M/L) for many cluster of galaxies finding excess of $80 - 400$ with respect to the Sun, but they underlined that part of this excess could be related to mass in X–ray emitting or microwave absorbing gas. In 1973, Ostriker and Peebles, pursuing the work of Oort, found by numerical studies that the stability of cold disk of gas/matter, as the galactic disk, can be ensured only if a dark component of matter is introduced [29]. Other results came from timing analysis of the dispersion of M31 with respect to the MW [24].

In the years 1978–79, different groups of scientists studied with increased significance the flat rotation curves of galaxies, applying the same argument Zwicky used half a century before. They found an universality in the rotational curve shape, which they ascribed to a cosmological origin of DM in galaxies. They found that the DM distribution is approximately spherical, with a density decreasing from the center with a nearly exponential law. Each

[1] Andromeda is also known as M31, the closest galaxy to the MW, at only 725 Kpc.

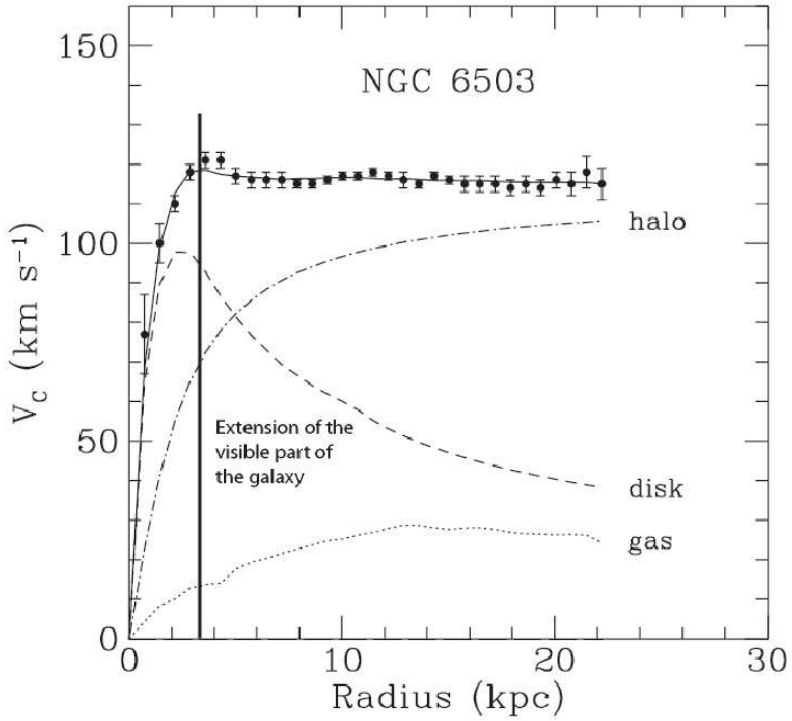

Figure 6.2: Rotation curve for the spiral galaxy NGC 6503 [23]. The points are the measured circular rotation velocities as a function of distance from the center of the galaxy. The dashed and dotted curves are the contribution to the rotational velocity due to the observed disk and gas, respectively, and the dot-dash curve is the contribution from the dark halo.

visible galaxy is therefore embedded inside a larger DM "halo", which can have ten times the diameter of the hosted baryonic galaxy. The results were particularly striking for dwarf galaxies. These objects, characterized by a little amount of stars and reduced luminosity, showed rotational curve even harder than normal galaxies, presuming a larger fraction of DM to ordinary matter. Dwarf galaxies are currently main target for DM observation for γ–ray astronomy. Two galaxies, namely Draco and Willman 1, were observed by MAGIC. The latter object was observed and analyzed and the detail of the observation and results can be found in Chapter 10.

After 30 years, the study of gravitational curve is still a very active field. A large amount of data is already available for a large number of objects. A compilation of more than 1000 rotational curve for example is found in Ref. [30]. A major observational difficulty is currently estimating the rotational velocity in the inner part of galaxies. Important information are expected from this region, which much influence the estimation of the amount of DM and its profile. Future spectroscopic observation could disentangle the question. One of the best experiments performing such searches is the Sloan Digital Sky Survey telescope (http://www.sdss.org/).

Gravitational lensing

Einstein's theory of gravitation predicts that light–rays travel into geodesic and that the energy–matter density introduces a local curvature of the space–time. As a result, the light coming from distant object traveling close to massive object, like cluster of galaxies, can be substantially deflected. As seen from the earth, this light–rays appear to come from a circle (the Einstein's ring) centered around the real source position. A clear example is shown in the picture of the Abell2218 cluster observed with the Hubble telescope reported in Figure 6.3.

This effect was indeed observed already by Eddington in 1919, but only in the last years, the results were able to make detailed estimation of the amount of mass causing the deflection. In particular, the result of strong lensing [35], confirm the rotational curve paradigm that

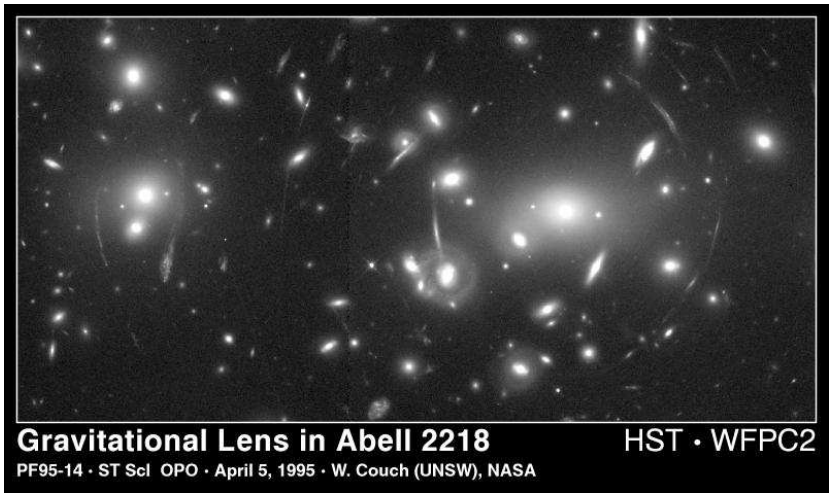

Figure 6.3: Strong gravitational lensing as observed by the Hubble Space Telescope in Abell 1689 indicates the presence of dark matter - Enlarge the image to see the lensing arcs.

galaxies are dominated by DM which accounts for more than 90% of the total mass for these galaxies.

Imprint on the CMB

The measurement of the cosmic microwave background (CMB) from the satellite COBE [33] moved cosmology into the so–called "precision era", where most of the parameters of the Standard Model for Cosmology are known with few percents precision. The model predicts that in the first instants of life, the universe was subject to an extremely violent acceleration, due to a quantum scalar field, called *inflaton* that pervaded the vacuum, characterized by a negative–pressure. Until the scalar field reached the minimum of its potential, the universe expanded exponentially at dramatic superluminal motion. As a result most of the regions of the universe were spread outside the *horizon*, i.e. the region connected with causality relations by the known physical interactions. At the end of the inflation, the universe continued to expand as a result of the pressure or ultrarelativistic radiation field. As the universe expanded, more and more regions re–entered the horizon, and the universe was refilled with particles and radiation. This is called the *re–heating era*. The inflaton causes the universe inside the horizon to be homogeneous to a very large extent. At $z \simeq 1100$, the universe became rapidly transparent to photons: the temperature was low enough to impede the photons to destroy the electromagnetic boundings in the atoms through ionization. The electrons thus combine for the first time with atomic nuclei of hydrogen and helium. Thereafter, photons propagated freely in the universe while their energy was doppler shifted by the expansion of the universe. This radiation is what now forms the *cosmic microwave background* (CMB), which pervades the universe with a perfect black–body spectrum peaked at 2.73 K, isotropically distributed over the sky within 10^{-5} fluctuations. This is shown in Figure 6.4, where the results of the WMAP mission satellite [7, 34, 25], the successor of COBE, are reported. This result is really amazing: the imprint of the *re–combination* era is now seen as the most perfect black–body radiation, meaning that the universe at that epoch was homogeneous at the 10^{-5} precision. These fluctuations are perfectly describe as quantum primordial fluctuations of the inflaton field, making the inflation theory even more appealing. Most of the ideas were developed in 1980 by Guth [18].

The power spectrum of the cosmic microwave background perturbations, shown in Figure 6.5 and nicely explained in Ref. [34], carries an astonishing large amount of information, which cannot be reviewed completely here. The power spectrum is known to be connected to

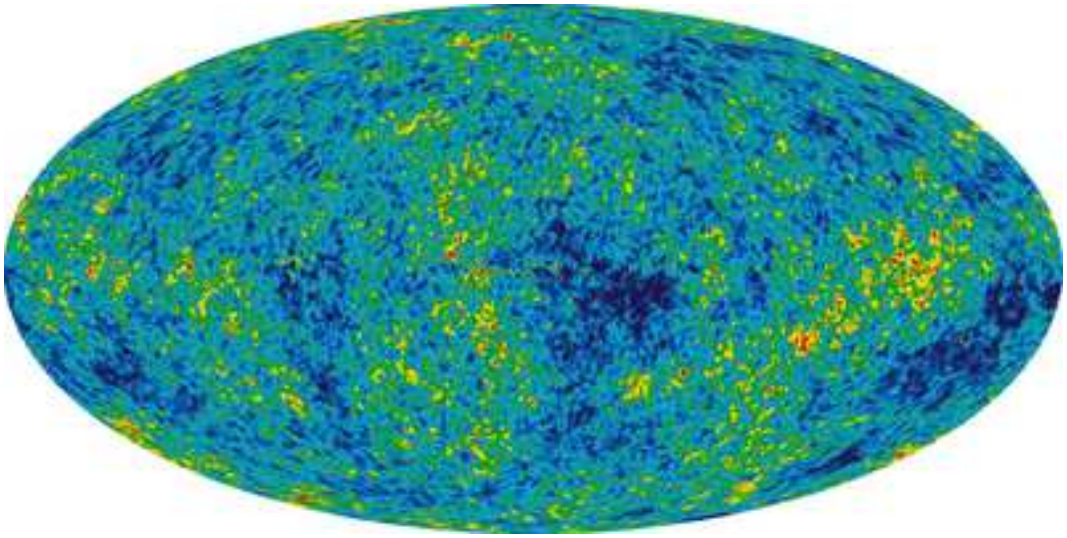

Figure 6.4: The cosmic microwave background fullsky measured by the WMAP mission [34]. Fluctuations are of the order of 10^{-5}, the radiation is a perfect black–body emission peaked at 2.73 K.

so–called baryonic oscillations of matter related to the re–entering of primordial fluctuations inside the Hubble radius after the inflation epoch. The key idea is that the energy density of radiation and matter field leaves trace on this plot and therefore we test now what happened almost 14 billions years ago!

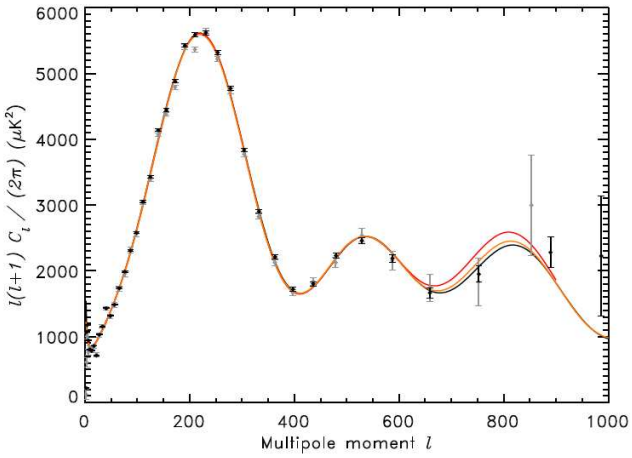

Figure 6.5: The power spectrum of the cosmic microwave background perturbations, from [34]

We restrict our considerations for the DM case. We only mention that the position and height of the first peak of the power spectrum of CMB fluctuations in Figure 6.5 are related to the amount of matter (DM and baryons) at the re–combination era. The amount of matter and radiation is therefore measured to a high precision from the basis of this plot at the moment of re–combination and is extrapolated to present time[2]. A sketch of the contributions at the two epochs is shown in Figure 6.6.

WMAP's most astonishing results is that the energy budget of the Universe is composed of only 4.6% is in the form of visible and unvisible baryonic matter (star, gas, clouds, etc.),

[2]It must be underlined that the way in which the energy densities are extrapolated is model dependent. The current model used is the ΛCDM scenario with cold DM and cosmological constant.

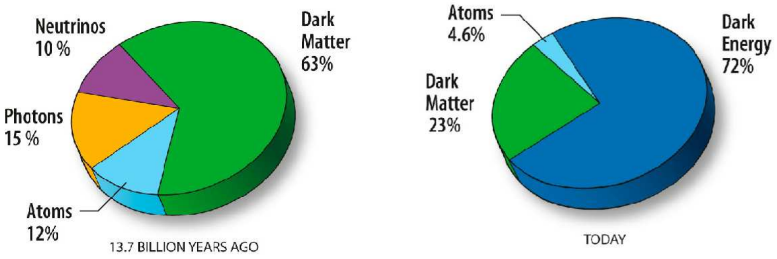

Figure 6.6: The relative contribution of matter and radiation fields at the re–combination epoch (left) and today (right).

23% is the in the form of an unknown DM component and the remaining 72% must be a new exotic form of energy, called *dark energy*. The DM is therefore 83% of the total observed matter in the Universe! What was thought to constitute the entire universe, the baryons, are only a tiny fraction of the entire universe. To be more precise, the extrapolated density of CDM is $\Omega_{\rm CDM}h^2 = 0.10541^{+0.0080}_{-0.0079}$. We will see that this value is already strongly restricting the parameter space for any theory of DM.

The bullet cluster

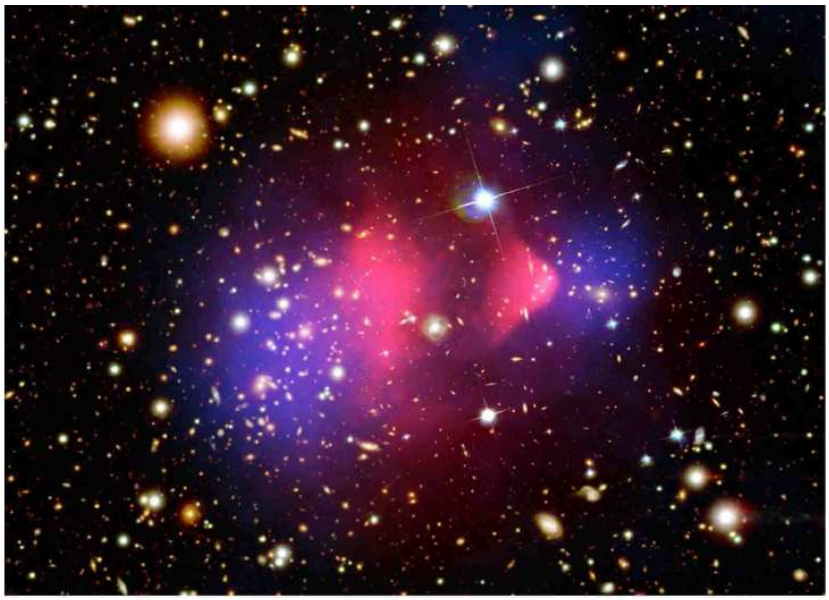

Figure 6.7: False color image of Bullet Cluster 1E0657-558. The surface density map reconstructed from X–ray imaging observations is shown in red and the convergence map as reconstructed from strong and weak gravitational lensing observations is shown in blue. The displacements between the two components is evident. Image provided of Chandra X–ray Observatory

The second extremely exciting result of recent years, and sometimes considered the first *direct* evidence of DM, is the observation of spatial segregation between the radio emission and the luminous emission in two compenetrating galaxies in the merging system 1E0657–558, also called the *bullet–cluster* [15], as one can see in Figure 6.7.

The distinguishing feature between baryonic and non–baryonic matter is in fact that the former interact electromagnetically and therefore emit light and radiate energy. The energy dissipation caused by the friction of baryons causes the matter to concentrate as for example in galactic disks or bulges. On the other hand, DM is only gravitationally and possibly very weakly interacting and is therefore unable to condense through energy dissipation (even if some interplay between the two types of matter can play a role in structure formation). Two compenetrating systems therefore see the DM intersecting almost undisturbed and the baryonic matter strongly frictioning.

The bullet–cluster data are also one of the main argument used to rule out theories of

modified gravity, in particular after the recent strong–lensing data.

Recent controversial evidences

In this section, we report some very recent results which were interpreted as possible detection of DM. In most cases, astrophysical explanations are available.

2003. The 511 KeV excess in INTEGRAL data. The SPI spectrometer on board the INTEGRAL satellite measured a bright emission of 511 keV photons from the region of the galactic bulge [22], orders of magnitude larger than what expected from pair creation via CR interactions with the interstellar medium. The signal comes from a sphere of 6° around the galactic bulge. If the origin is astrophysical, a mechanism of transportation of electrons from the bulge should be considered. While supernovae do not have enough power to inject such an photon flux, perhaps GRBs and hypernovae can [20]. In any case, it is difficult to explain the intensity and morphology of the emission with those astrophysical mechanisms. An explanation based on DM was given by Boehm et al [12], which stated that light DM ($\simeq$ 1MeV) could produce positrons during annihilations that in turn emit synchrotron radiation at 511 keV. Such a light DM would nevertheless require a particular tuning of the annihilation process (s–wave suppression). Another solution could come from excited DM matter, i.e. a 500 GeV DM particle, collisionally excited to a $1-2$ MeV state, that de-excite followed by electron–positron pair, thus generating the positrons needed to account for the observed signal [16].

2004. The WMAP "haze". The WMAP mission revealed an excess of microwaves in the inner 20° around the center of the Milky Way, distributed with approximate radial symmetry. This excess was defined the "WMAP haze". While an astrophysical interpretation is rather complicate, it has been suggested that the WMAP haze could be generated as a product of DM annihilations. In particular, annihilating DM particles produce relativistic electrons and positrons which travel under the influence of the Galactic magnetic field and emit synchrotron photons, which naturally fall within the frequency range measured by WMAP.

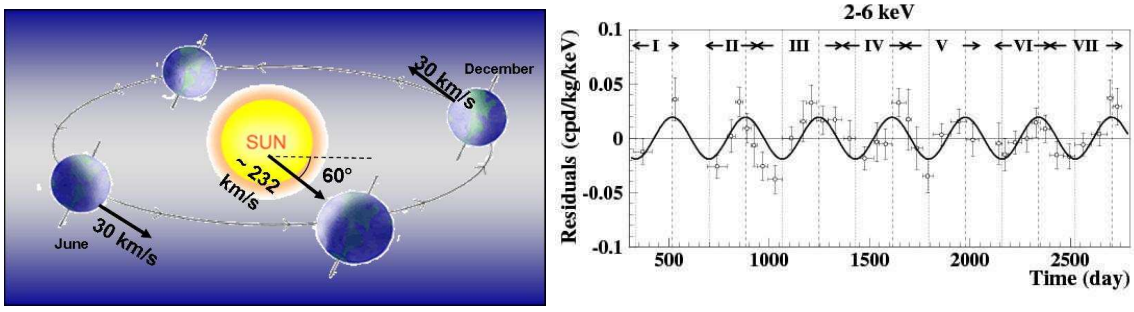

Figure 6.8: The scheme of the dark matter signal modulation in the annual motion of the Earth around the sun (left). The modulation in the range 2–6 keV observed in DAMA results.

2007–08. Annual modulation in DAMA data. It is commonly agreed that DM clusters around galaxies in the form of a spherical halo, whose distribution is peaked toward the center and exponentially decrease moving outward. The local density of DM at the Sun distance from the galactic center is estimated to stay in the range $\rho_0 \simeq 0.2 - 0.5$ GeV cm^{-3}. Due to combined motion of the Sun around the galactic center and the annual Earth motion around

the Sun, the Earth's velocity with respect to the halo, i.e. with respect to the DM background distribution, is modulated. Therefore, if one is able to detect a signal from diffuse halo DM annihilation, one should observe the regular modulation.

Indeed this modulation was seen by the DAMA experiment at Gran Sasso laboratories [9]. Despite the sensitivity of this result is very high, the DM interpretation is in contradiction with the negative detection of other similar underground experiment. It is therefore believed that while the modulation is present, the DM interpretation is not correct. Future experiments, in particular with cryogenic noble gas detector, will soon clarify this statement.

2008. Positron excess in PAMELA data. Positrons are known to be produced in interactions between CR nuclei and interstellar matter. There is in fact no evidence for positrons of relic origin and therefore only in secondary processes, and also by DM particle annihilations in the galactic halo or in the magnetospheres of nearby pulsars. The PAMELA satellite experiment recently reported an excess on the positron abundance in the cosmic radiation for the energy range $1.5 - 100$ GeV [1], see also Figure 6.9(a). Their data deviate significantly from predictions of secondary production models, and may constitute the first indirect evidence of DM particle annihilations, or the first observation of positron production from near–by pulsars.

2008. Electron–positron excess in ATIC data. Very recently, the Advance Thin Ionization Calorimeter (ATIC) collaboration, reported an excess of electrons–positrons in the energy range $300 - 800$ GeV than that expected from the diffuse electron composition of the CRs [13]. Such an excess could be either due to an unseen astrophysical closeby object like a pulsar or a micro–quasar, or possibly by WIMP DM. Many authors tried to explain and to understand the implication of those data. In particular, Hall & Hooper [19] investigated the Kaluza–Klein scenario but Bertone et al [10] showed that the DM scenario is hard to be adjusted with previous observations. In particular because the synchrotron emission from secondary electrons emitted by a DM distribution as modeled for the ATIC result, would violate the HESS and radio observations of the galactic center and HESS observation of dwarf spheroidal galaxies in term of flux. The astrophysical explanation seems therefore more appropriate.

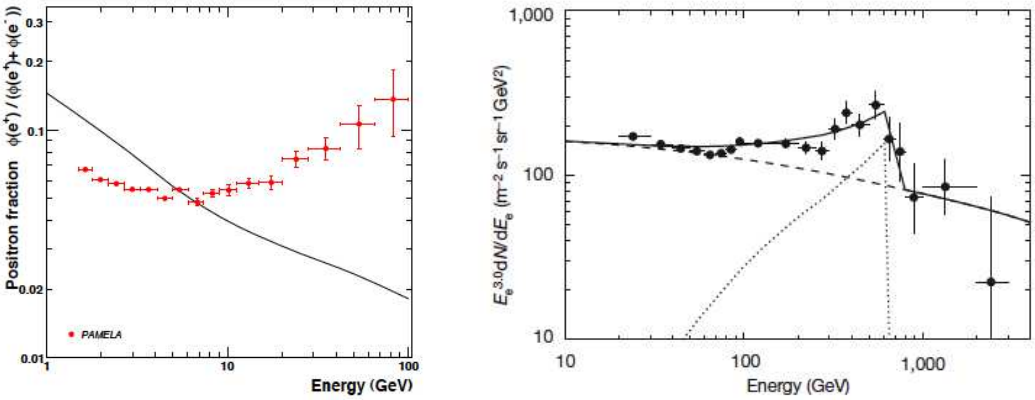

(a) Pamela positron excess

(b) ATIC positron excess

Figure 6.9: (a) PAMELA positron fraction (red point) compared with theoretical models (black line), calculated for pure secondary production of positrons during the propagation of cosmic-rays in the galaxy. Figure from [1]. (b) The ATIC excess and the fit with KK DM particle. Figure from [13].

6.2 The WIMP paradigm

It is particularly intriguing of DM that its understanding is based on a mix of knowledge in astrophysics, cosmology and particle physics. In this section, a little cosmological introduction is given. The rest of the chapter is dedicated to introduce the main DM scenarios and the principal particle candidates so far proposed. This part is only introductory and the specific literature is vast. An recent complete review of DM candidates, with a detailed bibliography, can be found in Ref. [11].

6.2.1 Cosmological introduction

The Standard Model of Cosmology is based on the theory of gravitation from Einstein's General Relativity. From the Einstein's field equations we learn that the local geometry of space–time is strictly related to the local distribution of energy–matter. When applied to the universe evolution, we understand that the universe expansion, which we know to have happened after Hubble's discovery, can be related to the amount of energy in the form of matter or radiation in each and every moment of its evolution. The basic equation that rules the universe evolution is the Friedmann equation:

$$\left(\frac{\dot{a}}{a}\right)^2 + \frac{k}{a^2} = \frac{8\,\pi\,G}{3}\,\rho \tag{6.2}$$

where $a(t)$ is the scale factor, $k = -1, 0, +1$ governs the universe topology (hyperbolic, flat, spherical respectively) and ρ is the actual energy density of the universe equal to the sum of all components:

$$\rho = \rho_m + \rho_r + \rho_\Lambda \tag{6.3}$$

where $\rho_m = \rho_{dm} + \rho_b$ is the energy density of the matter, the sum of baryonic matter and DM, ρ_r is the energy contribution from the radiation fields (massless) and ρ_Λ is the contribution of the so–called vacuum energy or cosmological constant.

One of the main outcome of the inflation theory, is that the universe is flat to a very large extent, i.e., $k = 0$. We do not go into details in the motivation and just use this fact to define the critical density as the density associated to a flat–universe. Following Friedmann's equation, and defining the Hubble's constant as $H \equiv \dot{a}/a$, the definition of critical density is:

$$\rho_c = \frac{3\,H^2}{8\,\pi\,G} \tag{6.4}$$

The Hubble's parameter has the dimension of the inverse of time, and its inverse is about the age of the universe. As H is function of time, also the critical density value evolves. An important cosmological parameter is the present critical density, and its value is $\rho_c \simeq 1.3 \cdot 10^{-38}$ kg m^{-3} ($= 0.7 \cdot 10^{-5}$ GeV cm^{-3}). With this definition, the energy densities of Eq. 6.3 can be written by the use of the relative density $\Omega_i \equiv \rho_i/\rho_c$.

We now use this terminology to understand what happened in the early times of the universe. After the inflation era finished, the universe was still very hot, with temperature above the MeV which kept electrons, positrons and neutrinos in equilibrium. The equilibrium is guaranteed whenever the interaction rate ($\Gamma = n\,\sigma\,v$, where n is the number density, σ is the cross–section and v the particle relative velocity) is larger than the Hubble rate. This condition guaranteed that particles of different type have enough interactions to thermalize, i.e. to share the same spectral energy distribution. In this ambient where different particles

coexists in thermal equilibrium, the density of each type is governed by the Boltzmann's equations. In particular, for non–relativistic particles ($m_i \gg T$), the particle density at equilibrium is:

$$n_{nr} \propto (m_i\, T)^{3/2}\, e^{-m_i/T} \tag{6.5}$$

where m_i is the $i-th$ particle mass and T the universe temperature. For relativistic particles ($m_i \ll T$), the particle density is instead:

$$n_r \propto s_i\, T^3 \tag{6.6}$$

where $s_i = 1$ and $3/4$ for bosons or fermions respectively. One can see that, in case of relativistic particles, the density decreases much slower than for non–relativistic particles as the temperature decreases, with the net result that relativistic particles outweighs their non–relativistic companions (at least until the thermal condition is ensured). Therefore, the energy density is dominated by relativistic particles:

$$\rho \sim \rho_r \propto u_i\, T^4 \tag{6.7}$$

where $u_i = 1$ for bosons and $7/8$ for fermions.

When particles of a certain type drops out of equilibrium, they have a fixed comoving density (excluding the secondary interactions) and their energy is redshifted and cooled down. And now comes the crucial point: By knowing the particle density at the equilibrium drop (also called the particle's freeze–out), and scaling the volume of the universe, one can estimate the relic density particle now and their energy/temperature. This is what happened to the photons of the CMB which were redshifted to energy of 2.73 K. When making this calculation for a massive particle χ, the resulting energy density now is:

$$\Omega_\chi \simeq \frac{10^{-27}\ \mathrm{cm}^3\ \mathrm{s}^{-1}}{<\sigma_a v>} \tag{6.8}$$

where the cross–section times the velocity is averaged over the temperature. Therefore, to ensure a relic density of the order of 1, one can see that the *natural* cross–section for dark matter is of the order of 10^{-27} cm^3 s^{-1}. This condition, is curiously automatically fulfilled by massive particles with weak interactions, at around hundreds GeV scale. For this strong motivation, the search for DM particle is usually focussed on *weakly interacting massive particles* (WIMPs). At the same time, for WIMPs, at the freeze–out, the temperature is typically $4-5\%$ of the particle mass and the particle is therefore non–relativistic, and the DM is therefore called *cold DM*.

6.2.2 Astrophysical implications

After the freeze–out, the DM expands comovingly with the universe, while standard model bosons and fermions are still in thermal equilibrium and strongly interact. DM starts to interact gravitationally before baryons. For the gravitational interaction to be efficient, it is required that the particle pressure due to the free–streaming velocity is smaller than the gravitational pressure due to its mass. This condition is fulfilled in different ways according to the mass and the velocity of the DM particle at the freeze–out. This in turn depends on the ambient temperature at that moment. According to this, usually DM candidates are grouped into three families:

i) *hot DM* (HDM), when the DM particle was relativistic at the freeze–out because

its mass is at the eV scale or smaller. An example of this class is the neutrino,

ii) *warm DM* (WDM), when the particle has masses around the keV scale, e.g. the gravitino,

iii) *cold DM* (CDM), at the GeV—TeV scale, whose most important representatives are the neutralino and the Kaluza–Klein state.

There are other particles which behave like CDM being less massive, as the axion, but this is due to their non–thermal origin. The axion will be discussed below.

6.3 Dark matter Candidates

Since the renovated interest in DM of the '70s, many theories were proposed. Some of them have an *ad hoc* nature, i.e. they were created specifically to solve the DM problem. Others, called *natural theories,* were developed independently to solve the theoretical problems of the Standard Model (SM), but they provided, *naturally*, a good candidate for DM. These theories are normally preferred, and among them, the most discussed is the Super–Symmetrical development of the SM.

A complete list of DM candidates is out of the target of this thesis and will not be discussed here. In this section, a brief recall to the most discussed candidates is presented, with particular attention to the case of the *neutralino*, which is one of the most studied candidates. It is also used as reference for DM interpretation of MAGIC data in Chapter 8, 9 and 10. Some of the basic candidates are also schematically represented in the famous plot by Roszkowski in Figure 6.10. For recent reviews about DM candidates, we refer the reader to [8, 26, 11, 4].

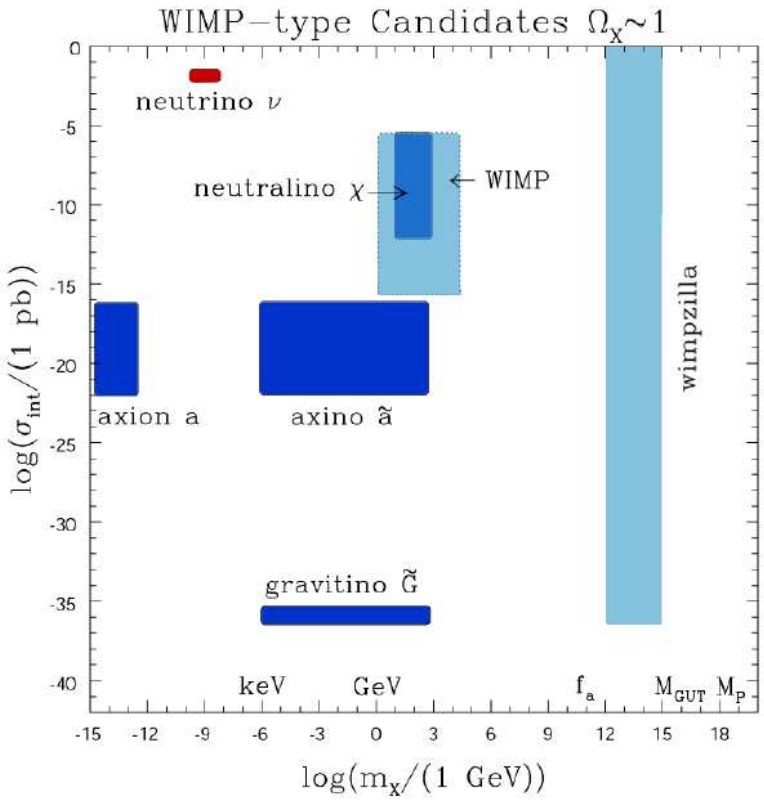

Figure 6.10: A schematic representation of some well–motivated DM candidate particles. σ_{int} represents a typical order of magnitude of interaction strength with ordinary matter. The box marked "WIMP" stands for several possible candidates, e.g., from Kaluza–Klein scenarios. Figure from [32].

Axions. The strong interaction violates the CP–simmetry 10^9 times more often than expected from theory. A possible solution to this problem is found by introducing a new light pseudoscalar boson, called the *axion* [31]. This is a chargeless, spin–0 particle associated with the spontaneous breaking of the Peccei–Quinn symmetry. The axion acquires small mass by non–perturbative effects, in the range $10^{-5} - 10^{-2}$ eV. The upper limit in the mass comes from observation of SNRs: larger values would make the axion cool down stars through its emission in place of the photons emission. Axions are largely produced in the Big Bang scenario, but never in thermal contact with other particles. Axion is a non–relativistic DM candidate despite its low mass. Axions interact very poorly with matter and could be detected only by oscillations into photons in magnetic fields or in cosmic distances as discussed in § 1.6. Some searches are already performed in radio–frequency cavity where axions can couple to the electric field in a tunable resonant cavity plus a magnetic field [3]. It is plausible that future experiments can start to put serious constraints on the nature of this hypotethic particle.

Neutrinos. Until few years ago, neutrinos were considered the perfect candidate for being the DM: They were known to exist, to pervade the entire universe in large quantity, to interact very little with matter, and to have a small mass. Indeed, they are part of the DM fraction of the universe, but only to a small extent. The reason is the following. From the observation of the cosmic microwave background, the photon energy and number density are known with high precision: T=2.725 K and $n_\gamma^{CMB} = 410.5$ cm^{-3}. From the Friedmann equation of evolution of the universe, the neutrino number density after the decoupling is frozen at a value of $n_\nu = 3/11\, n_\gamma^{CMB}$. Given the critical density value of Eq. 6.4, the neutrino density is therefore:

$$\Omega_\nu = \frac{\rho_\nu}{\rho_c} = \frac{\Sigma_i\, m_i\, n_\nu}{\rho_c} \simeq \frac{\Sigma_i\, m_i}{30 \text{ eV}} \tag{6.9}$$

As the measured oscillations between neutrino's flavour by Superkamiokande in Japan is of the order of 0.05 eV [17], the mass of the neutrinos cannot be but of the same order, and therefore, from Eq. 6.9, follows that the its contribution to the total DM density cannot be but a little percentage. The WMAP bound [34], allows for a neutrino relic density of $\Omega_\nu\, h^2 < 0.0067$, which is far below the estimated amount of total DM today. The only possible solution is that there is a fourth family of neutrinos, whereas it should have been already observed at underground experiments. Another fact againts the total neutrino nature of DM is that the primordial neutrino would have had a "hot" i.e. relativistic nature. Its free–streaming length would have been of the order of ~ 40 kpc and therefore structures could have collaped only at size larger than this length, leading to a *top-down formation* scenario which is strongly ruled out today. For example, top–down scenarios foresee structure formation at epochs more recent than $z \leq 1$, while indeed structures are observed at $z \geq 4$, as for example our Local Group.

Light Scalar – MeV DM. The INTEGRAL (INTErnational Gamma-Ray Astrophysics Laboratory, www.rssd.esa.int/Integral/) satellite detected an excess of positrons with energy 511 keV coming from the galactic bulge [22]. As this excess is difficult to reconcile with astrophysical origins, it was proposed [12] that the origin was from MeV DM. Candidates for DM at this scale were already presented in the '70s with light scalar fermions not belonging to the SM. Nevertheless, theoretical motivations for this particles are weaker than for other particles.

Extra–dimensions, Kaluza–Klein states. In theories of Unified Extra Dimensions (UED), it is believed that the 4–dim space–time is embedded into a larger frame [2, 21]. UED is

a model with flat extra dimensions where all the SM fields are allowed to propagate. UED predicts the existence of a tower of Kaluza-Klein (KK) states for each SM particles. It is believed that a symmetry called KK parity exists (similar to momentum conservation) that has two implications: first, the contributions to SM observables arise only at loop level, and KK states can only be pair-produced, and second, the *lightest KK particle* (LKP) is stable, providing a suitable particle DM candidate. The LKP is likely to be associated with the first KK excitation of the hypercharge gauge boson. This state is also called $B(1)$. Unlike in the case of supersymmetry, the bosonic nature of the LKP implies that there are no chirality suppression in its annihilations, and thus the LKP can annihilate efficiently to fermionic pairs. In particular, since the annihilation cross section is proportional to the hypercharge4 of the final state, a large fraction of LKP annihilations goes into charged lepton pairs.

Super–heavy DM – Wimpzillas At the end of inflation, it is believed that the gravitation interaction could have led to the direct production of particles of 10^{13} GeV mass [14]. These particles could decay into standard model particles with dramatic energies (for example, directly into UHE or EHE CRs. This could for example explain the observed GZK cutoff in the CR spectrum.

Other candidates. Little higgs, sterile neutrinos, primordial black holes, mirror matter, Q–balls, charged massive particles, cryptons, D–matter, brane DM, etc are nothing but a comprehensive list. The reader is referred to dedicated reviews as for example [8].

6.3.1 Introduction to super–symmetry

The super–symmetric theory (SUSY) was developed since the 80's to explain few theoretical problems of the SM, in particular:

- The hierarchy problem. All interactions are thought to be unified at the unification scale, which roughly corresponds to the Unification scale at $\sim 10^{14}$ GeV. The enormous gap between the scale at which the known forces act and the unification scale causes serious problem to the SM in the radiative corrections of the Higgs boson mass, which are removed in SUSY by an all–orders intrinsic cancellation of the radiative corrections connected to the existence of superparticles,
- The unperfect unification of the gauge couplings at the Plank scale is perfectly obtained when SUSY partners are taken added into the particle family,
- The observation of CP violation in experiments.

The basic of SUSY is that it pairs bosons with fermions. For each SM particle, a particle with similar quantum numbers and spin added by 1/2 is predicted. There are many ways in which the SUSY can be carried out. Normally, only the minimal extension is considered (Minimal SUSY Model or MSSM). In this model, the number of new particle (superpartners) is kept at minimum. MSSM associated superpartners which are named after the SM partner with the addition of the prefix *s–* in case of SM fermions and the suffix *–ino* in case of SM bosons, so for example the photon becomes the *photino* and the electron becomes the *selectron*. However, the MSSM cannot result in a simple duplication of SM particles. In fact, an additional Higgs field must be added to give mass to both the u, d quarks. Table 6.1 reports the members of the MSSM family.

The super–symmetry between particles and superparticles is violated: otherwise, having the SUSY spartners the same mass of SM particles, they should already have been seen in

Mass eingenstates		Interaction eigenstates		SM particle/fields	
$\widetilde{q_1}, \widetilde{q_2}$	squark	$\widetilde{q_L}, \widetilde{q_R}$	squark	u, d, s, c, b, t	quark
$\widetilde{l_1}, \widetilde{l_2}$	slepton	$\widetilde{l_L}, \widetilde{l_R}$	slepton	e, ν, τ	lepton
$\widetilde{\nu}$	sneutrino	$\widetilde{\nu}$	sneutrino	ν_e, ν_μ, ν_τ	neutrino
$\widetilde{g}$	gluino	$\widetilde{g}$	gluino	g	gluon
$\widetilde{\chi_{1,2}}^{\pm}$	chargino	$\widetilde{W}^{\pm}$	wino	$W^{\pm}$	W-boson
		$\widetilde{H}^{-,+}$	charged Higgsinos	$H^{-,+}$	Higgs bosons
$\widetilde{\chi}^0_{1,2,3,4}$	neutralinos	$\widetilde{B}$	bino	B	B-field
		$\widetilde{W}^3$	wino	W^3	W^3-field
		$\widetilde{H}^0_{1,2}$	neutral Higgsinos	$H^0_{1,2,3}$	Higgs bosons

Table 6.1: Standar models particle and their superpartners in the MSSM, adapted from [11]

experiments. The SUSY breaking allows for a proton lifetime far shorter than the age of the universe. To avoid this thoretical problem, a new *ad–hoc* symmetry is included in the MSSM, the so–called $R-$parity. The parity is defined as $R = (-1)^{3(B-L)+2S}$ where B, L, S are the baryonic, the leptonic numbers and the spin eigenvalue respectively. In particular, for SM particles $R = +1$ and for superpartner $R = -1$. It must be said that there are other SUSY extension were $R-$parity is not conserved and the proton lifetime is large but not infinite.

The number of free parameters in a general MSSM extension is quite large and can excess 100. For this reason, some theories were developed to simplify the scenario, by adding some additional constraints or physical interpretation, thus reducing dramatically the number of free parameters:

i) the *mSUGRA* extension, where the symmetry breaking is mediated by the graviton, with 5 free parameters defined at the SUSY breaking scale,

ii) the phenomenological SUSY extension, or *pMSSM*, with about 10–20 free parameters defined at the EW scale.

mSUGRA

It is a grand unification theory (GUT), where gravity is unified to the other forces at high energies. mSUGRA is completely characterized once few parameters are defined at the grand unification (GU) scale: the gaugino unification mass $m_{1/2}$, the scalar unification mass m_0, the universal trilinear coupling constant A_0, the ratio of the vacuum expectation values of the two Higgs fields $\tan\beta$ and by the sign of the higgsino mass parameter $\text{sign}(\mu)$. Despite the reduced number of parameters, the parameter space of mSUGRA is still quite wide. Fortunately, there are important constraints coming from experiments which much exclude parts of the space:

– the WMAP results on the power spectrum of the cosmic microwave background determines the relic density of DM particles. The effect of this is shown in Figure 6.3.1.

– Absence of new particle at LEP below 100 GeV put constraints on the higgsino and gaugino masses

– the agreement with the SM in the decay $b \to s\gamma$

– measurement of the anomalous magnetic momentum of the muon g_μ (the so–called $g_\mu - 2$ effect).

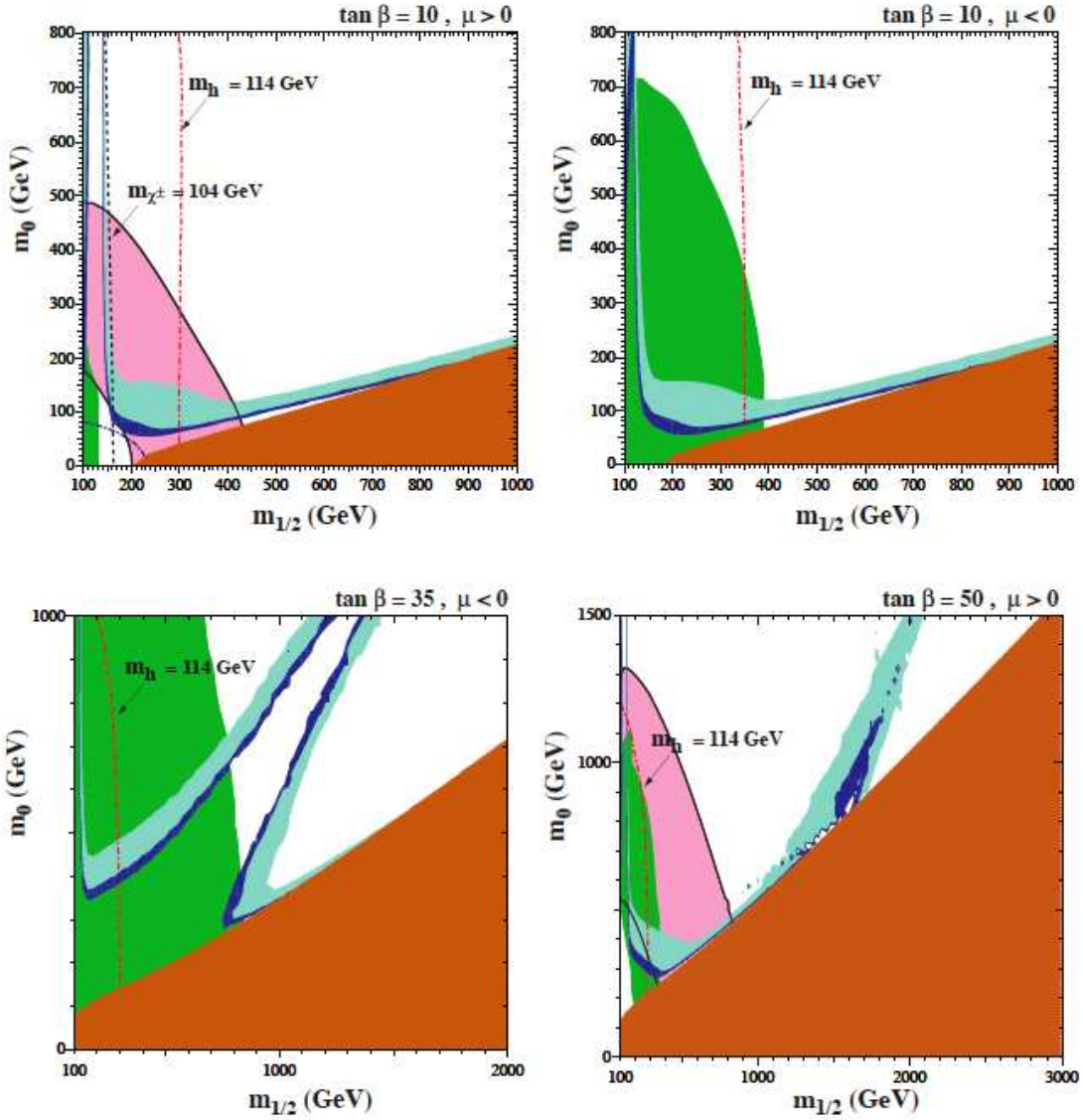

Figure 6.11: A convenient expression of the mSUGRA parameter space in the $(m_{1/2}, m_0)$ for four neutralinos with $(\tan\beta, sign(\mu)) = (10, > 0), (10, < 0), (35, < 0), (50, > 0)$. For comparison, the region allowed by the older cosmological constraint has medium shading, and the region allowed by the WMAP cosmological constraint $0.094 < \Omega_{DM}h^2 < 0.129$ has dark shading. The region excluded by LEP is in red shading. The regions excluded by $b \to s\gamma$ decay have green shading, and those in panels (a,d) that are favoured by $g_\mu - 2$ anomaly at $2\sigma-$level have pink shading. Image taken from Ref. [5]

There are many studies on the mSUGRA parameter space, and we refer the reader to [5, 6].

From Figure 6.3.1 one can see that the WMAP constraints define a very narrow region allowed in the paramater space. Nuclear physic results, on the other hand, excludes neutralinos with too low mass.

pMSSM

The pMSSM is the second most–discussed model for SUSY. It is not based on particular theoretical assumptions but few phenomological considerations that reduce the number of free parameters at 10–20. The main difference with respect to mSUGRA is that pMSSM free parameters are described at the electroweak scale, and not renormalized from the unification scale. In particular, the most common free parameters are $\tan\beta, \mu, m_0, M_A M_2, A_b, A_t$, where the first three terms were already presented for mSUGRA, M_A is the mass of the pseudo–scalar Higgs boson, M_2 of the second gaugino, A_b, A_t are the trilinear coupling constants.

Other SUSY extensions

Other common SUSY extensions are the anomaly mediated SUSY breaking model (AMSB), the heterotic orbifold model or other gauge mediated SUSY breaking (GMSB) models and gaugino mediates SUSY breaking models. For more details, see for example [11].

6.3.2 The neutralino

In the MSSM there are four neutralinos $\widetilde{\chi}^0_{1\ldots4}$. They are a superposition of fermionic spartners of SM bosons: *a*) the $\widetilde{B}^0$, called the *bino* is the superpartner of the gauge boson corresponding to weak hypercharge. It mixes with one of the gauginos corresponding to weak isospin to give the *photino* and the *zino*, *b*) the $\widetilde{W}^0_3$, called *wino*, which is the superpartner of the W boson mediating the electroweak interaction, *c*, *d*) the two *Higgsinos* $\widetilde{H}^0_u$, $\widetilde{H}^0_d$ that are superpartners of the neutral Higgs bosons. The lightest of the four neutralinos is $\widetilde{\chi}^0_1$, which is also called *the* neutralino or simply $\chi \equiv \widetilde{\chi}^0_1$. All SUSY particles can therefore decay into χ (if it is the LSP) while χ itself is stable if the $R-$parity is a conserved symmetry. The neutralino mass matrix can be diagonalized and the neutralino can therefore be written as a superposition of the four spartners:

$$\chi = n_{11}\widetilde{B}^0 + n_{12}\widetilde{W}^0_3 + n_{13}\widetilde{H}^0_d + n_{14}\widetilde{H}^0_u \tag{6.10}$$

A parameter $P = |n_{11}|^2 + |n_{12}|^2$ is defined to characterize the neutralino's gaugino content: $P > 0.9$ defines an gaugino–like neutralino, $P < 0.1$ an higgsino–like neutralino and the other values defined a mixed neutralino. We will see in Chapters 9 and 10 that the nature of the neutralino affects the prospects of detection.

Other super–symmetrical candidates

Gravitino In GMSBs, the gravitinos can be the lightest particles and therefore stable. Despite being theoretically well–motivated, they would interact only gravitationally, making their detection challenging.

Sneutrino In MSSM, the sneutrino, being chargeless and massive, fulfill the basic criteria for being a DM candidate. In particular, if its mass is in the range $500 - 2000$ GeV the relic density matches that required by WMAP results. On the other hand, sneutrinos of this masses, would have been already detected at underground experiment for DM direct detection.

Axino They share similar properties with gravitinos, in particular, very little interaction with matter.

6.4 Remarks

From the above discussion, it is clear that when one refers to the *neutralino*, one is discussing about a particle with properties which span over a large parameter space according to the underlying specifications of the theory. Usually, to make calculations, physicists use some different approaches. The first is to use the neutralino with highest prospects of detection, which is usually a neutralino with maximum cross section. A second approach is to scan extensively the parameter space, which is normally pretty time consuming. In addition, for example for γ–ray observation, this practice is even more complicated by the fact that different neutralinos have rather different annihilation modes, and consequently their different spectra. For this reason, another commonly used approach is to defined benchmark models for neutralinos. This approach was for example used by Battaglia et al. to define benchmarks for LHC searches [5, 6]. This approach was used throughout this work, with the definitions of 5 benchmark neutralinos, adapted from Battaglia et al. Other details on the benchmarks are found in Chapters 9 and 10.

References

[1] O. Adriani et al. Observation of an anomalous positron abundance in the cosmic radiation. arXiv:0810.4995 [astro-ph], 2008.

[2] T. Appelquist, H.-C. Cheng, and B. A. Dobrescu. Bounds on universal extra dimensions. *Phys. Rev.*, D64:035002, 2001.

[3] S. J. Asztalos et al. An improved RF cavity search for halo axions. *Phys. Rev.*, D69:011101, 2004.

[4] E. A. Baltz. Dark matter candidates. Preprint astro-ph/0412170, 2004.

[5] M. Battaglia et al. Proposed post-LEP benchmarks for supersymmetry. *Eur. Phys. J.*, C22:535–561, 2001.

[6] M. Battaglia et al. Updated post-WMAP benchmarks for supersymmetry. *Eur. Phys. J.*, C33:273–296, 2004.

[7] C. L. Bennett et al. First Year Wilkinson Microwave Anisotropy Probe (WMAP) Observations: Preliminary Maps and Basic Results. *Astrophys. J. Suppl.*, 148:1, 2003.

[8] L. Bergstrom. Non-baryonic dark matter: Observational evidence and detection methods. *Rept. Prog. Phys.*, 63:793, 2000.

[9] R. Bernabei et al. First results from DAMA/LIBRA and the combined results with DAMA/NaI. *Eur. Phys. J.*, C56:333–355, 2008.

[10] G. Bertone, M. Cirelli, A. Strumia, and M. Taoso. Gamma-ray and radio tests of the e+e- excess from DM annihilations. 2008.

[11] G. Bertone, D. Hooper, and J. Silk. Particle dark matter: Evidence, candidates and constraints. *Phys. Rept.*, 405:279–390, 2005.

[12] C. Boehm, D. Hooper, J. Silk, M. Casse, and J. Paul. MeV dark matter: Has it been detected? *Phys. Rev. Lett.*, 92:101301, 2004.

[13] J. Chang et al. An excess of cosmic ray electrons at energies of 300.800 GeV. *Nature*, 456:362–365, 2008.

[14] S. Chang, C. Coriano, and A. E. Faraggi. Stable superstring relics. *Nucl. Phys.*, B477:65–104, 1996.

[15] D. Clowe et al. A direct empirical proof of the existence of dark matter. *Astrophys. J.*, 648:L109–L113, 2006.

[16] W. de Boer et al. Excess of EGRET galactic gamma ray data interpreted as dark matter annihilation. Preprint., 2004.

[17] S. Fukuda et al. Determination of Solar Neutrino Oscillation Parameters using 1496 Days of Super-Kamiokande-I Data. *Phys. Lett.*, B539:179–187, 2002.

[18] A. H. Guth. The Inflationary Universe: A Possible Solution to the Horizon and Flatness Problems. *Phys. Rev.*, D23:347–356, 1981.

[19] J. Hall and D. Hooper. Distinguishing Between Dark Matter and Pulsar Origins of the ATIC Electron Spectrum With Atmospheric Cherenkov Telescopes. 2008.

[20] D. Hooper. Indirect Searches For Dark Matter: Signals, Hints and Otherwise. Preprint., 2007.

[21] D. Hooper and S. Profumo. Dark matter and collider phenomenology of universal extra dimensions. *Phys. Rept.*, 453:29–115, 2007.

[22] P. Jean et al. Early SPI/INTEGRAL measurements of galactic 511 keV line emission from positron annihilation. *Astron. Astrophys.*, 407:L55, 2003.

[23] M. Kamionkowski. Possible relics from new physics in the early universe: Inflation, the cosmic microwave background, and particle dark matter. In *Proc. of Workshop on The Early and Future Universe, Beijing, China, 22-27 Jun 1998*, 1998.

[24] F. Kane and L. Woltjer. *Astrophys. J.*, 130:705, 1959.

[25] E. Komatsu et al. Five-Year Wilkinson Microwave Anisotropy Probe WMAP Observations:Cosmological Interpretation. preprint, arXiv:0803.0547, 2008.

[26] C. Munoz. Dark matter detection in the light of recent experimental results. *Int. J. Mod. Phys.*, A19:3093–3170, 2004.

[27] J. Oort. *Astr. Inst. Netherlands*, 6:249, 1932.

[28] E. Opik. *Astrophys. J.*, 55:406, 1922.

[29] J. Ostriker and P. Peebles. A numerical study of the stability of flattened galaxies: or, can cold galaxies survive? *Astrophys. J.*, 186:467, 1973.

[30] M. Persic, P. Salucci, and F. Stel. The Universal rotation curve of spiral galaxies: 1. The Dark matter connection. *Mon. Not. Roy. Astron. Soc.*, 281:27, 1996.

[31] L. J. Rosenberg and K. A. van Bibber. Searches for invisible axions. *Phys. Rept.*, 325:1–39, 2000.

[32] L. Roszkowski. Particle dark matter: A theorist's perspective. *Pramana*, 62:389–401, 2004.

[33] G. F. Smoot et al. Structure in the COBE differential microwave radiometer first year maps. *Astrophys. J.*, 396:L1–L5, 1992.

[34] D. N. Spergel et al. Wilkinson Microwave Anisotropy Probe (WMAP) three year results: Implications for cosmology. *Astrophys. J. Suppl.*, 170:377, 2007.

[35] J. A. Tyson, R. A. Wenk, and F. Valdes. Detection of systematic gravitational lens galaxy image alignments - Mapping dark matter in galaxy clusters. *Astrophys. J.*, 349:L1–L4, 1990.

[36] F. Zwicky. Spectral displacement of extra galactic nebulae. *Helv. Phys. Acta*, 6:110–127, 1933.

7 Dark Matter Searches

In this chapter, a brief review of the experimental techniques for DM detection (direct production at accelerators, direct detection through nuclear recoils and indirect detections) is provided. The places in the universe were DM is expected are also discussed.

7.1 Dark matter detection

In Chapter 6, we saw that the zoo of candidates for being DM is very crowded. While only some candidates are *natural* as they arose from non *ad–hoc* theories, most candidates still do not contradict the experimental evidences. A recent review of those experimental constraints are given in the *ten–point test* described in Ref. [40]. An important figure of merit of a theory is the fact that its proposed candidate is more or less likely to be observed. Theories whose candidates have small or null chance of being observed are less appealing than others. Undoubtedly, the best chances of observation are for WIMP DM, with masses at the reach of modern accelerators and cross–sections close to current experimental sensitivities.

We saw that DM is embedding our galaxy, in the form of a spherical halo extended several times the extension of the observed galaxy. The estimated density of DM in the solar system is around ≈ 0.3 GeV/cm^3. Furthermore, DM tends to accrete gravitationally on central cores which constantly grow to larger and larger densities. In those places, the probability of observing DM through its annihilations are increased.

From the experimental point of view, DM can then be observed in three modes: *direct detection* through nuclear recoils, *indirect detection* through DM annihilation or decay products as γ–rays, antiparticles and neutrinos and *direct production* at accelerators. In the following, we will briefly review the methods.

7.1.1 Direct detection

Because electromagnetic and strong interactions are not accomplished by DM, DM particles can cross cosmological distances without significant absorption or scattering. However, when crossing dense targets, DM can be observed indirectly through the outcomes of nuclear recoils. A nuclear recoil determines measurable signals from ionization, scintillation and phonon release. There are many detectors operating since two decades that are based on this technique.

A reasonable interaction rate is $1-10^5$ recoil kg^{-1} week^{-1}, with cross–section of the order of 10^{-43}cm^2 [4], and therefore very large detectors are needed to acquire enough statistics. At such small cross–sections, the control of the background, constituted mainly by natural radioactivity and electronic noise, is determinant. The detectors for direct DM detection must therefore be placed in underground laboratories and the electronics must be as much as possible noise–free. As the radioactivity background is an irreducible component, it must be estimated through Monte Carlo statistical simulation.

The detectors of this class can be sub–classified into:

- *heat and ionization* detectors, which reveal both charge signal from ionization after nuclear recoil and heat signal. They require crystal semiconductor material and cryogenic cooling (EDELWEISS, CDMS),
- *scintillation* detectors, which use the light emitted by scintillating materials at DM passage (DAMA, ANAIS)
- *phonon and light* revelation detector (CRESST).

The basic output of such experiments is an upper limits in the rate of recoils per kg of detector, which is interpreted within a given theoretical model in terms of limits in the WIMP–nucleon interaction cross–section.

A specific example: the EDELWEISS experiment

EDELWEISS is operating since 2000 at the Frejus tunnel laboratories (1780 m overburden, 4800 mwe, muons: 4.5 m^{-2} day^{-1}, neutrons [2−10 MeV]: 1.6×10−6 cm^{-2} s^{-1}). The detector is composed of a stacks of Ge plates, 120 in total. To reduce the background, the stacks are housed into a tank, which in turn is surrounded by 10 cm copper and 15 cm lead and a pure nitrogen pool which absorbs the radon. The whole detector is finally screened by 30 cm paraffin against neutrons and operates at 17 ± 10^{-5} K.

The recoil material is germanium ($_{32}$Ge) which is in pads of 70 mm diameter, 20 mm thickness, 320 g weight. A Neutron Transmutation Doped (NTD)-Ge thermometric sensor (4 mm^3) is mounted on a gold pad directly onto the germanium pad. The ionization signal is obtained by collection of the electron–hole pairs created at the passage of DM in the Ge crystal polarized through a bias voltage applied to the electrodes.

Each signal is analyzed through templates obtained from Monte Carlo simulations. To calibrate the detector, a ^{57}Co radioactive source emitting γ–rays at 122 keV is used. Let E_I be the total ionization signal amplitude, i.e. the electrodes signal and E_H heat signal measured as resistance drop in the sensor resistance with constant current flood, then the recoil energy E_R is the phonon signal converted and corrected for the Neganov–Luke effect of heating[1]:

$$E_R = \left(1 + \frac{|V_{bias}|}{\epsilon_\gamma}\right) E_H + \frac{|V_{bias}|}{\epsilon_\gamma} E_I \tag{7.1}$$

where ϵ_γ is the electron-hole pair creation potential for Ge (3 V). Only part of the energy from the recoiled nucleus is recovered through ionization. The quenching factor Q is defined as $Q = E_I/E_R$. Nuclear and electronic recoils correspond to different ionization efficiencies: $Q = 1$ corresponds to electronic interaction (example from γ–rays) and $Q \simeq 0.3$ is for nuclear

[1]The Neganov-Luke effect consists of the enhancement of heat deposited by an ionizing particle in a bolometer at low temperatures, when the induced charges are collected by an applied voltage.

recoil in Ge. The result is expressed in differential counts rate in energy bins. In the year 2006 they published the following results: 15-20 keV, 18 events; 20-30 keV, 16 events; 30-100 keV, 3 events; 100-200 keV: 3 events. There is no WIMP DM model that could fit the data and only upper limits on the cross sections were found.

There is a wide literature on direct detection and the field is currently very active and developing. Important news are expected from the experiments in the following years. Two recent reviews can be found in Refs. [33, 36].

7.1.2 Direct production at LHC

SUSY models contains massive particles with color charge associated that generate the mass of SM particles. The electro–weak symmetry breaking arises as a result of radiative corrections due to the spartner particles. The resulting WIMP candidates should have masses at the GeV–TeV scale and couple to quantum cromo-dynamics (QCD). Particles of this class are expected to be produced in pairs at the LHC, with cross sections around the picobarn [7]. The particle pairs will subsequently decay to quark or gluon jets plus a WIMP that can escape the detector without interactions. Therefore, the LHC experiments will observed events with many hadronic jets and a *missing–energy* event which should be signature of SUSY. The rate of these missing–energy events strongly depends on the mass of the WIMP rather than on the details on the model. It will be unknown how much of the missing momentum of an event is taken by the center of mass of the massive particle produced, since no final states will be observed from a WIMP.

LHC is therefore believed to be able to produced DM particles extensively, but only marginally to put constraints on its nature.

7.1.3 Indirect detection.

Indirect DM detection experiments search for the annihilation or decay products of DM particles, which include γ–rays, neutrinos, positrons, antiprotons, antideuterons and synchrotron radiation. These products usually mix with the CRs background and it is often very complicate to disentangle the origin. Indirect DM searches are basically performed by satellite or balloon–borne experiments, and ground–based telescopes. In the space, experiments are able to directly observe the products of DM annihilations that interact inside the detectors, while ground–based experiments normally observe the secondary products of the interaction of γ–rays in the atmosphere.

In the class of satellite experiments, we recall the EGRET experiment on board the CGRO satellite. EGRET detected more than 200 sources, out of which, more than 100 have an unknown origin, which could in principle be associated to DM overdensities, as will be discussed below and is the argument of Chapter 8. Furthermore, EGRET detected a diffuse γ–ray emission which can be associated also to a DM origin [21]. Currently, the Fermi–LAT experiment is following the footsteps of EGRET with increased sensitivity and larger energy window.

Some detectors are launched inside balloon–borne vectors, which travel the top atmosphere for days or weeks and are subsequently recollected and analyzed after landing. These detectors usually study the charged components of the CRs, which interact in calorimeters. The cost of those experiments is also contained. Recent result from HEAT or ATIC have shown the possibilities of this rather inexpensive technique, as shown in Chapter 6.

The ground–based detectors for γ–rays were already described in § 1.2.2. The IACT technique is well–fitted for DM searches for the reason that the WIMPs have masses expected at the order of the GeV–TeV scale, where IACTs operate.

7.2 DM annihilations/decay products.

In Chapter 6, we showed that many DM candidates fulfill both theoretical and experimental constraints. In the worst cases, the DM has barely no interaction, apart from gravitational, with the ordinary matter, like in the case of axions. In other cases, in particular for WIMPs, the DM can either decay or annihilate into ordinary matter. In the latter case, we could be able to observe DM indirectly via its products. Due to its large relic density, the DM must be very stable. However, it is not very clear whether it has infinite lifetime, and therefore it can be seen only through annihilations, or it slowly quasi–stable, and can only slowly decay into other particles.

In the following, we restrict our description for the case of the neutralino as lightest stable particle (LSP) in mSUGRA framework, while most of the discussion can remain valid also in other cases, in particular for the LKP, introduced in the previous chapter. The basic modes of annihilations of the neutralino are treated more extensively in Ref. [14].

7.2.1 Primary products

The WIMP has normally QCD interactions with ordinary matter, and therefore ordinary matter can be produced as a result of annihilation events. The primary products are hereafter presented.

1. *Annihilation into fermions.* Two neutralinos can annihilate into a fermion–antifermion pair (to conserve charge). This $t-$channel can be mediates by a sfermion (a squark or a slepton). The $s-$channel must be mediated by neutral particles, as the Z^0 boson or the pseudoscalar Higgs A^0. The amplitudes of the annihilation reactions are proportional to the final state mass, if there is enough energy, because of the cold nature of neutralino. Therefore annihilations into fermion–antifermion pairs will be dominated by heavy states and in particular $b\bar{b}, \tau\bar{\tau}$ and if allowed $t\bar{t}$. In addition, the cross sections depends on the mixing angle $\tan\beta$: if this is large, down–type quarks are favored compared to up–type quarks despite their higher mass.

2. *Annihilation into gauge bosons.* Neutralinos can annihilate into gauge bosons (W, Z) in several ways, whereas the $t-$channel processes are favored in the CDM scenario. These processes occur either via chargino $(\tilde{\chi}^{\pm}_{1,2})$ or neutralino $(\tilde{\chi}^{0}_{n})$ exchange. It is useful to underline that only higgsino–like and mixed neutralinos can annihilate into gauge bosons.

3. *Annihilation into Higgs bosons.* The annihilation into Higgs bosons can be into Higgs boson pairs and a Higgs boson and gauge boson. Favored processes are $\chi\chi \to Z^0 h^0$, $\chi\chi \to Z^0 H^0$ and $\chi\chi \to W^{\pm} H^{\mp}$ or $\chi\chi \to h^0 A^0$.

4. *Annihilation into photons.* There is no tree level process for neutralino annihilation into photons. They are produced only at one loop processes and of course as secondary products. Example of two level processes are $\chi\chi \to \gamma\gamma$ where the photon energy is exactly $E_\gamma = m_\chi$. A second process is $\gamma\gamma \to Z^0\gamma$ where the energy now is almost a delta expect for the width of the boson $E_\gamma = m_\chi + m_Z^2/m_\chi^2$. There are plenty of these one–loop processes, as shown in [14]. A third process, even if less relevant can contribute to line γ–ray emission, the annihilation into the Higgs boson and a gamma $\chi\chi \to H^0\gamma$ [17].

5. *Internal Bremsstrahlung.* Recently Bringmann et al. (2008a), following an earlier idea from Bergström (1989), showed that in some regions of the mSUGRA parameter space, a hitherto neglected contribution to $\gamma-$ray emission comes directly from charged sparticles mediating the annihilation into leptons, in processes like $\chi\chi \rightarrow l^+l^-\gamma$. They defined this intermediate state radiation as *internal bremsstrahlung* (IB). The IB mechanism permits to restore the helicity balance in processes that would otherwise be strongly forbidden, and supplies $\gamma-$rays towards high energies ($E > 0.6\ m_\chi$) of up to several orders of magnitude. This boosted emission is particularly interesting for ground–based $\gamma-$ray observation, as performed by Imaging Atmospheric Cherenkov Telescopes (IACTs), which are usually sensitive above ~ 100 GeV where normally the IB boost takes place.

The effect of this emission on IACTs was extendedly studied for MAGIC II and CTA. The study is discussed in Chapter 9.

7.2.2 Secondary products

There is a large number of secondary products that can come after the products of annihilations or decays of DM particles.

Positrons

Positrons are produced after decay of W bosons for those candidates DM particles that foresee that boson among the final states. It is therefore expected to have a contribution in the astrophysical background of positrons of secondary origin, from DM products. For the neutralino, only some models predict a high positron flux. Bino–like neutralino for example does not produce efficiently antiprotons, because binos do not couple with W. Instead, they can be largely found in secondary leptonic decays of τ^+, or after fragmentation of τ jets. However, Higgsino– and wino–like neutralino may have a strong positron flux: If the mass is larger than W, these neutralinos annihilate efficiently in WW pairs that can produce positrons through $W^+ \rightarrow X + e^+$ (see for example [8, 28]).

A strong impulse to the study of antiprotons signal from DM came after the discovery of the HEAT experiment of an excess in the CRs positrons [10] between 1 and 30 GeV and more recently, as already reported, by the more significant determination of the PAMELA experiment [1], which triggered a large number of studies.

Antiprotons

In the final states, antiprotons can be found after direct production of quarks and gluons, generation of quarks through the intermediate production of Higgs bosons, gauge bosons and the top quark [23]. On the other hand, antiprotons are naturally produced by the nuclear interactions of CRs with the interstellar medium. The differential rate (per unit volume and per second) for the production of antiprotons from $\chi\chi$ annihilations is given by [19]:

$$q_{\bar{p}}(E_{\bar{p}}) =< \sigma v > \left(\frac{\rho_\chi}{m_\chi}\right)^2 \sum_f B_{\chi f} \left(\frac{dN_{\bar{p}}^f}{dE_{\bar{p}}}\right) \tag{7.2}$$

where $E_{\bar{p}}$ denotes the antiproton energy, $< \sigma v >$ is the thermal averaged cross section times the velocity, ρ_χ, m_χ is the DM density and mass respectively, $B_{\chi f}$ is the branching ratio into the quarks or gluons f, and $(dN_{\bar{p}}^f/dE_{\bar{p}})$ the corresponding spectrum.

It is particularly puzzling that the PAMELA recent results show a perfect agreement in the antiproton spectrum with theoretical modelization of the astrophysical background. There is therefore no evidence for antiproton from DM. This result is difficult to combine with the positron fraction excess observed by PAMELA: it is complicate to model a DM particle that have strong positron flux and small or null antiproton flux among the final states. There are a number of articles that try to explain the problem [], but the solution has not yet come.

Neutrinos

If the annihilation/decay processes are helicity suppressed, leptons are not efficiently produced. This may imply that, in order for the DM particle to produce charged leptons efficiently, the relevant interactions should be flavor–blind. Furthermore, charged leptons (μ, τ) produced in the annihilation/decay of the dark matter decay into neutrinos. Thus it is natural to expect that when the DM mainly annihilates or decays into leptons, it also produce large amount of neutrinos. Possible production processes of neutrinos are direct production $(\chi\chi \rightarrow \nu_i \bar{\nu_i})$ where $i = 1, 2, 3$ distinguishes flavors and the decay of primary μ and τ $(\mu^- \rightarrow \nu_\mu + \bar{\nu_e} + e^-)$ which are directly produced by the DM annihilation/decay $\chi\chi \rightarrow \mu^- u^+,' tau^-, \tau^+$.

One of the best way to detect those neutrinos is from the Galactic center. The detectors in the northern hemisphere observe the upgoing muon induced by neutrinos from the Galactic center. See also Ref. [9, 27] and references therein.

Gamma–rays

As a result of annihilations of DM, γ–rays are always found in the final states. For example, the hadronization of quarks is normally accompanied to a broad–band emission of γ–rays. This is the dominant component of the flux from DM annihilations and governs the shape of the spectrum. The corresponding spectrum is typically a continuum similar to a power–law with spectral index -1.5 followed by an exponential cutoff at the DM mass. Some examples of this behavior is shown in Figure 7.1.

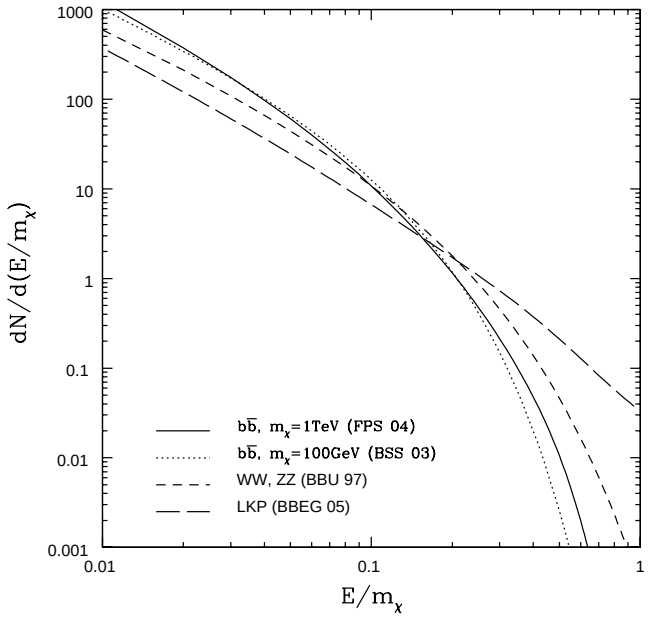

Figure 7.1: Energy spectra of photons per annihilation for different annihilation channels. The *solid* and line correspond to the $b\bar{b}$ annihilation channel for a neutralino with $m_\chi = 1$ TeV [25] and the *dotted* line shows the same for for a neutralino with $m_\chi = 100$ GeV [15]. The *short-dashed* line corresponds to the spectra for annihilation through the WW and ZZ channels [13]. The *long-dashed* shows the spectrum of Kaluza-Klein DM from Ref. [12]. Figure from Ref. [16].

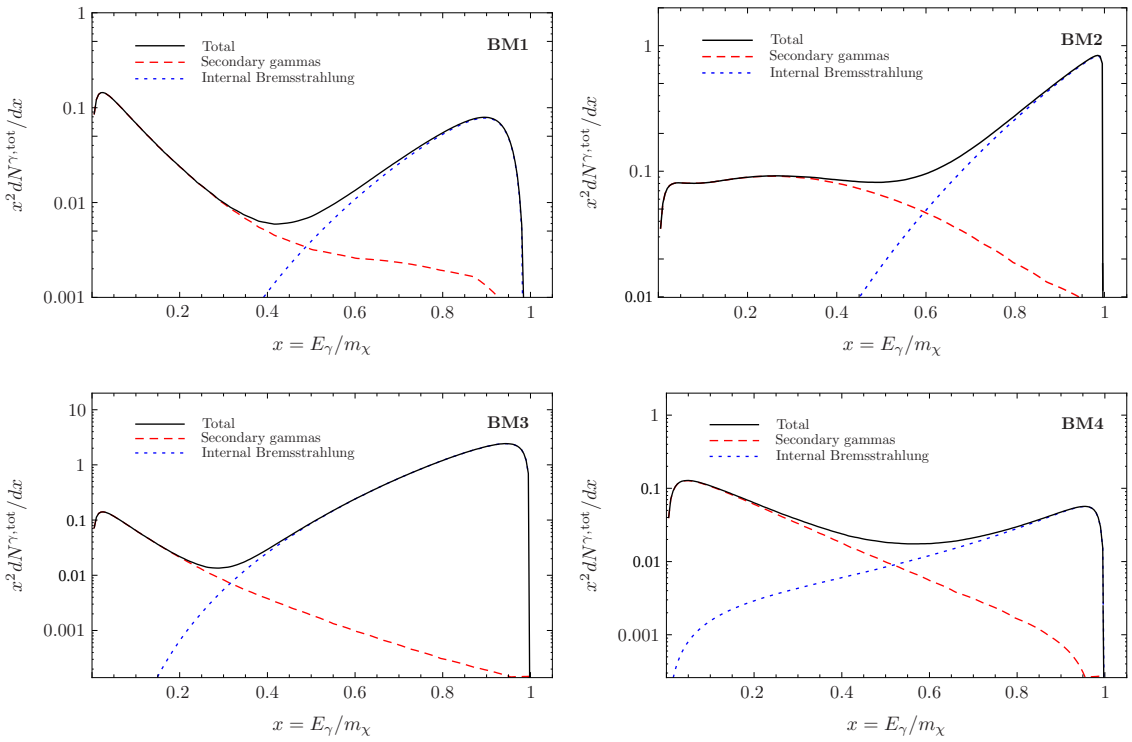

Figure 7.2: The γ–ray spectra for the different benchmark models of neutralino as defined in Tab. I of Ref. [18]. The contributions from IB and secondary photons is indicated separately (in these figures, the line signal is not included. Figures from Ref. [18].

In the past, this recipe was used to define an universal spectrum for WIMP annihilation γ–rays signal. Recently, the studies on the effect of internal bremsstrahlung have shown that this assumption was only partially correct and that a universal profile cannot be defined for the neutralino [18]. The presence of a "bump" close to the DM mass and due to the γ–rays from internal bremsstrahlung is in fact largely dependent on the neutralino specifications, and can vary by orders of magnitude. An example of the effect for some neutralino models is shown in Figure 7.2.

In Chapters 9 and 10 we study for the first time the effects of the discovery of the internal bremsstrahlung on the detection of DM from IACT.

7.2.3 Multi–wavelengths signals from secondary interactions.

Colafrancesco et al. [20] recently observed that electron–positron pairs created at DM annihilations (or decays), in case they escape the emission region, could produce a strong radio signal via inverse Compton and synchrotron processes. Characterizing this emission is normally complicated because one has to track the injection of positrons and electrons, their energy distribution and their propagation in space, therefore one needs to know very well the local environment around the emitting source. The radio emission is not coming from a nearly point–like source as in the case of γ–rays, but from an extended region around the target where the electrons have streamed. The authors made predictions for the Draco dwarf galaxy. They found that the basic parameter affecting the radio emission is the local magnetic field, and that normally larger magnetic fields tend to boost the radio emission, even if the dependence is not trivial because magnetic fields also affect the electrons–positrons propaga-

tion. In some cases, the radio emission could be more constraining that the γ–ray emission. Unfortunately, no radio observations are hitherto performed on Draco.

7.3 Sites of interest

When searching for DM annihilation products, as γ–rays or neutrinos, one should look for "hot spots", i.e. places were DM is particularly concentrated. The reason is that the DM interaction is an annihilation process and therefore depending on the square density: $\Phi \sim \rho^2$. The flux also decreases with the square of the distance of the target, and therefore the closer the object the more probable its observation.

7.3.1 The galactic center

One of the closest and more DM dominated region is the Galactic Center (GC). Located at a distance of 8.5 kpc, the GC is a very crowded region. The astrophysical description was already given in § 1.4.3. Making estimation for the DM annihilation flux from the GC is complicated by the large presence of baryons that could have modeled the DM distribution in a complicated way. While the well–studied motion of stars around the GC gives us important information on the average matter density, there is no clear indication on the density in the very central core, from where the most signal is expected.

The GC was observed and detected in γ–rays by all current IACTs. The HESS experiment gave the most robust observation [3]. They measured a featureless spectrum from 200 GeV to several TeV. The spectrum was associated to the contribution from the several astrophysical emitters, while the study of the DM interpretation was performed by Profumo in Ref. [31]. In particular, only very massive neutralino of the order of 10–20 TeV could explain the observed HESS data, and in addition boost factor of the 2–3 orders of magnitude are required to match the flux. The GC was also observed by MAGIC, which confirmed the HESS data [5]. In Figure 7.3 the GC spectrum is shown.

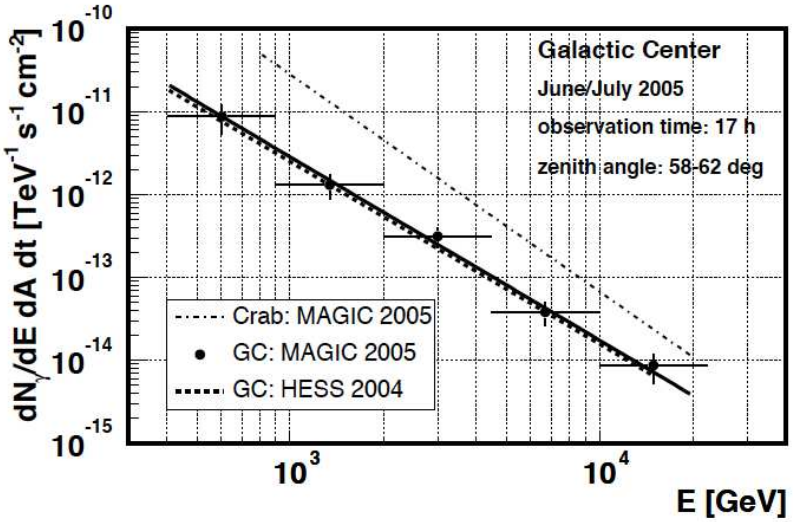

Figure 7.3: Reconstructed VHE spectrum of the GC. The full line shows the result of a power–law fit to MAGIC data points. The dashed line shows the result of the HESS collaboration. The dot-dashed line shows the energy spectrum of the Crab nebula as measured by MAGIC. Image from [5]

It is therefore believed now that, if a DM signal exists in the GC, it is orders of magnitude smaller than the astrophysical signal. For this reason, only very accurate, and prolonged, observation of the GC could unveil eventual spectral features that could be sign of DM. It is underlined that the GC is well–observed from the southern hemisphere, because it culminates higher in the sky.

To overcome this problem, it was recently studied the possibility of observing an annulus around the GC instead the GC itself [37, 34]. The authors observed that this region is less affected by background or foreground astrophysical γ–ray emission. The DM signal will be therefore integrated over a larger area, and one should therefore pay attention to the loss of signal to noise ratio to the growth of the background.

7.3.2 LSB objects

Dwarf Spheroidal Galaxies (dSph) are believed to be the smallest (size $1 \sim$ kpc), faintest (luminosities $10^2 - 10^8$ $L_\odot$) astronomical objects whose dynamics are dominated by DM (DM) ([26] and references therein). They are found as satellites orbiting in the gravitational field of a larger host galaxy (e.g., the Milky Way (MW)). Usually, their member stars show large circular velocities and velocity dispersions that, combined with their modest spatial extent, can be interpreted by the presence of a large DM halo of the order of $10^5 - 10^8$ $M_\odot$. In recent years the Sloan Digital Sky Survey (SDSS) [44] led to the discovery of a new population of MW satellites, comprising about as many (new) objects as were previously known [42, 45, 41, 11]. This population of extremely low–luminosity galaxies can be very interesting for DM searches and for investigating galaxy formation at the lowest mass scales. The existence of a new class of ultra–faint MW satellites is also relevant because it provides a partial solution for the so-called "missing satellite problem" [29, 35, 38, 30] by partially filling the gap between the predicted and the measured number of galactic sub-halos. These new galaxies represent a population of extremely low–luminosity objects, very interesting in the context of DM searches and concerning galaxy formation at the lowest mass scales.

In this family is Willman 1, discovered by Willman et al. [42] and soon established as potentially the most DM dominated dSph satellite of the MW [39]. The observation of Willman 1 with the MAGIC telescope is described in Chapter 10. Dwarf galaxy satellites of the MW represent very good candidates, since they are the most DM dominated systems known in the Universe, with very high mass–to–light ratios (M/L), close distance and reduced γ–ray background from unresolved conventional Galactic sources (i.e. stellar evolutionary remnants).

Some dSphs have already been studied in γ–rays: Draco by MAGIC [6] and Whipple [43]; UMi by Whipple [43] and Sagittarius by HESS [2] without any significant observation of DM annihilations and only flux upper limits were estimated.

7.3.3 Galaxy cluster

Clusters of galaxies are the largest and most massive gravitationally bound systems in the universe, with radii of the order of the Mpc and total masses around $10^{14} - 10^{15}$ $M_\odot$. Galaxies, gas and DM contribute roughly for 5, 15 and 80%, respectively (see Ref. [32] for a general review). While no cluster has been firmly detected as a γ–ray source so far, they are expected to be significant γ–ray emitters because are very active regions now, and therefore a substantial non–thermal emission is expected. They also contain large amounts of gas and strong magnetic fields, therefore are natural place for CR acceleration.

Clusters are undergoing active processes of formation today, in general agreement with the Standard Model of Cosmology which foresees structures to grow hierarchically through merging and accretion of smaller systems into larger ones. Clusters are the latest stage of these processes.

Galaxy clusters are thought to host enormous amount of DM, which should gravitationally cluster on their center and present numerous local substructures which could led to a

significant boost in the flux. The large amount of DM should counteract their large distance compared to the already mentioned galactic targets.

Three nearby clusters: Perseus, Coma and Virgo, are the most promising candidates for observation with MAGIC and not only in the DM scenario. Particularly a signal from the proton–induced pion decay emission should be very bright. The HESS collaboration observed two galaxy clusters, Abell 496 and Coma, without any significant detection and only upper limits on the γ–ray emission were found [22]. More recently, INTEGRAl observed the Perseus cluster [24]. The authors conclude that the high energy emission above 30 keV is dominated by the AGN, even if this statement is under debate.

7.3.4 Intermediate mass black holes.

It is currently believed that a new class of black holes exists beyond the class of stellar mini black holes (with $M < 20M_{\odot}$) and that of supermassive black holes (SMBH) with masses larger than $10^{6-9}M_{\odot}$. Members of this class are intermediate mass black holes (IMBHs) with masses in between the two limits. The main observational evidences are two–folds. First, the existence of ultra–luminous X–ray objects (ULXs). This objects must be characterized by high mass content, nevertheless, they are not associated to active galactic nuclei. If they were IMBHs, the strong radio emission could be explained by infalling materials. IMBHs could also explain the stellar kinematics in globular clusters, where SMBH cannot.

There are also theoretical motivation for the existence of IMBHs. From SDDS data, there are strong indication for quasar at z.6. This in turn lead to the hypothesis that SMBHs were already in place at the very beginning of structure formation, some 1 Gy after the Big Bang. For the current knowledge, there normal growth of black holes by infalling materials is not sufficient to explain their early existence. It is therefore believed that SMBHs form as the result of major merging events between *seeds* black holes of lower mass. IMBHs are perfect candidate in this scenario.

There are two basic scenarios which describe the formation of IMBHs, which differ for their mass scale:

A. in the first scenario, IMBHs are formed as remnants of collapse of Population III stars (the "first" stars ever formed, with very low metallicity). These stars could have formed after the collapse of large molecular clouds after they become unstable. The average number of *unmerged* IMBHs in the MW halos is predicted by numerical simulation to be in the order of $\mathrm{N}_A \simeq 1027$.

B. In the second scenario, IMBHs originate from massive objects formed directly during the collapse of primordial gas in early-forming halos. The total number of *unmerged* IMBHs in the MW for this scenario black holes per Milky Way halo is $N_B \simeq 101 \pm 22$.

The distribution of IMBHs in function of the distance from the center of the galaxy is very simple and common to both scenarios and foresees a behavior of $dN/dr \sim r^{-3}$. They all agree that a number of them should be still wanderer in the galactic halo, grown mostly undisturbed, without major merging events, where matter and dark matter could have had the time to concentrate enormously.

The dark matter signal from IMBHs

As a result of increase gravitational potential due to infalling baryons on a central accreting system, also the dark matter readjust and shrink and give rise to the formation of what were

defined "spikes". On the other hand, spikes are rapidly disrupted as result of dynamical processes like black hole formation or merging events. The DM component, despite being significantly reduced, is nevertheless enhanced in the core of these systems. Some of the IMBHs, as suggested in numerical experiments, could not have suffered major merging events. In this case, one can see that "mini-spikes" of DM forms around IMBHs with greatly enhances densities. Starting from a NFW distribution for the dark–matter (see Eq. 9.1), the adiabatic growth of the mini–spike lead to a final power–law profile of the form of:

$$\rho_{\rm sp}(r) = \rho(r_{\rm sp}) \left(\frac{r}{r_{\rm sp}}\right)^{-\gamma_{\rm sp}} \tag{7.3}$$

where r_h is the black hole radius, $r_{\rm sp} \approx 0.2 r_h$ is the spike radius and $\gamma_{\rm sp}$ is related to the initial power-law index γ by:

$$\gamma_{\rm sp} = \frac{9-2\gamma}{4-\gamma} \ . \tag{7.4}$$

In the case of the profile of NFW, this reduces to $\gamma_{\rm sp} = 7/3$. The flux of γ–rays from a mini-spike around an IMBH at a distance D can be expressed as:

$$\Phi(E, D) = \frac{{\rm d}N}{{\rm d}E} \frac{\rho_{\rm sp}^2}{4\gamma_{\rm sp} - 6} \frac{\sigma v}{m_\chi^2} \frac{r_{\rm sp}^3}{D^2} \left(\frac{r_{\rm cut}}{r_{\rm sp}}\right)^{-2\gamma_{\rm sp}+3}$$

where we assumed $r_{\rm sp} >> r_{\rm cut}$ where $r_{\rm cut}$ is the central evacuated region where DM annihilations are particularly active. For scenario B, which foresee more luminous objects, the corresponding γ–ray luminosity *is of the order of the gamma-ray luminosity of the entire Milky Way halo*, making IMBHs very interesting targets for DM searches. In particular, for scenario B, it is expected that a number of IMBHs around 100 could be observed with IACTs of MAGIC sensitivity.

Interestingly, the prospects of indirect detection in this scenario do not depend strongly on the particle physics parameters. In fact, while e.g. in the case of annihilations from the Galactic center the annihilation flux is proportional to $\sigma v / m_\chi^2$, the flux from mini-spikes is limited by the plateau in the number density due to DM annihilation itself For mini-spikes growing from $\gamma = 1$ profiles, we have shown that the annihilation flux is instead proportional to $(\sigma v)^{2/7} m_\chi^{-9/7}$.

The determination of a common cut-off in the spectra (possible only with ACTs for DM particles heavier than 300 GeV) will provide an estimate of the mass of the DM particle, while spectral features, such as annihilation lines or sharp edges, may provide important information on the nature of the DM particle.

In this contest, MAGIC observed a putative IMBH in 2005. The results of the observation are described in Chapter 8.

References

[1] O. Adriani et al. Observation of an anomalous positron abundance in the cosmic radiation. arXiv:0810.4995 [astro-ph], 2008.

[2] F. Aharonian. Observations of the Sagittarius Dwarf galaxy by the H.E.S.S. experiment and search for a Dark Matter signal. *Astropart. Phys.*, 29:55–62, 2008.

[3] F. Aharonian et al. HESS observations of the galactic center region and their possible dark matter interpretation. *Phys. Rev. Lett.*, 97:221102, 2006.

[4] D. S. Akerib and R. J. Gaitskell. Deep Underground Science and Engineering Lab: Dark Matter Working Group 2007 White Paper. 2009.

[5] J. Albert et al. Observation of gamma rays from the galactic center with the MAGIC telescope. *Astrophys. J.*, 638:L101–L104, 2006.

[6] J. Albert et al. Upper limit for gamma-ray emission above 140 GeV from the dwarf spheroidal galaxy Draco. *Astrophys. J.*, 679:428–431, 2008.

[7] E. A. Baltz, M. Battaglia, M. E. Peskin, and T. Wizansky. Determination of dark matter properties at high-energy colliders. *Phys. Rev.*, D74:103521, 2006.

[8] E. A. Baltz and J. Edsjo. Positron Propagation and Fluxes from Neutralino Annihilation in the Halo. *Phys. Rev.*, D59:023511, 1999.

[9] V. D. Barger, F. Halzen, D. Hooper, and C. Kao. Indirect search for neutralino dark matter with high energy neutrinos. *Phys. Rev.*, D65:075022, 2002.

[10] S. W. Barwick et al. Measurements of the cosmic-ray positron fraction from 1- GeV to 50-GeV. *Astrophys. J.*, 482:L191–L194, 1997.

[11] V. Belokurov et al. Cats and Dogs, Hair and A Hero: A Quintet of New Milky Way Companions. *Astrophys. J.*, 654:897–906, 2007.

[12] L. Bergstrom, T. Bringmann, M. Eriksson, and M. Gustafsson. Gamma rays from Kaluza-Klein dark matter. *Phys. Rev. Lett.*, 94:131301, 2005.

[13] L. Bergstrom, P. Ullio, and J. H. Buckley. Observability of gamma rays from dark matter neutralino annihilations in the Milky Way halo. *Astropart. Phys.*, 9:137–162, 1998.

[14] G. Bertone, D. Hooper, and J. Silk. Particle dark matter: Evidence, candidates and constraints. *Phys. Rept.*, 405:279–390, 2005.

[15] G. Bertone, G. Servant, and G. Sigl. Indirect detection of Kaluza-Klein dark matter. *Phys. Rev.*, D68:044008, 2003.

[16] G. Bertone, A. R. Zentner, and J. Silk. A new signature of dark matter annihilations: Gamma-rays from intermediate-mass black holes. *Phys. Rev.*, D72:103517, 2005.

[17] T. Bringmann. Searching for point-like dark matter sources. Prepared for 5th Workshop on Science with the New Generation High Energy Gamma-ray Experiments (SciNeGHE07): The Light of the Dark: Solving the Mysteries of the Universe, Frascati, Rome, Italy, 18-20 Jun 2007.

[18] T. Bringmann, L. Bergstrom, and J. Edsjo. New Gamma-Ray Contributions to Supersymmetric Dark Matter Annihilation. *JHEP*, 01:049, 2008.

[19] P. Chardonnet, G. Mignola, P. Salati, and R. Taillet. Galactic diffusion and the antiproton signal of supersymmetric dark matter. *Phys. Lett.*, B384:161–168, 1996.

[20] S. Colafrancesco, S. Profumo, and P. Ullio. Detecting dark matter WIMPs in the Draco dwarf: a multi- wavelength perspective. *Phys. Rev.*, D75:023513, 2007.

[21] W. de Boer et al. Excess of EGRET galactic gamma ray data interpreted as dark matter annihilation. Preprint., 2004.

[22] W. Domainko et al. H.E.S.S. observations of galaxy clusters. 2007.

[23] F. Donato, N. Fornengo, D. Maurin, and P. Salati. Antiprotons in cosmic rays from neutralino annihilation. *Phys. Rev.*, D69:063501, 2004.

[24] D. Eckert and S. Paltani. INTEGRAL observations of the Perseus cluster. 2008.

[25] N. Fornengo, L. Pieri, and S. Scopel. Neutralino annihilation into gamma-rays in the Milky Way and in external galaxies. *Phys. Rev.*, D70:103529, 2004.

[26] G. Gilmore et al. The Observed properties of Dark Matter on small spatial scales. preprint, arXiv:0703308, 2007.

[27] J. Hisano, M. Kawasaki, K. Kohri, and K. Nakayama. Neutrino Signals from Annihilating/Decaying Dark Matter in the Light of Recent Measurements of Cosmic Ray Electron/Positron Fluxes. 2008.

[28] G. L. Kane, L.-T. Wang, and J. D. Wells. Supersymmetry and the positron excess in cosmic rays. *Phys. Rev.*, D65:057701, 2002.

[29] A. A. Klypin, A. V. Kravtsov, O. Valenzuela, and F. Prada. Where are the missing galactic satellites? *Astrophys. J.*, 522:82–92, 1999.

[30] P. Madau, J. Diemand, and M. Kuhlen. Dark matter subhalos and the dwarf satellites of the Milky Way. 2008.

[31] S. Profumo. TeV gamma-rays and the largest masses and annihilation cross sections of neutralino dark matter. *Phys. Rev.*, D72:103521, 2005.

[32] C. L. Sarazin. X-ray emission from clusters of galaxies. *Rev. Mod. Phys.*, 58:1–115, 1986.

[33] R. W. Schnee. Status of direct searches for WIMP dark matter. *AIP Conf. Proc.*, 903:8–15, 2007.

[34] P. D. Serpico and G. Zaharijas. Optimal angular window for observing Dark Matter annihilation from the Galactic Center region: the case of γ^- ray lines. *Astropart. Phys.*, 29:380–385, 2008.

[35] J. D. Simon and M. Geha. The Kinematics of the Ultra-Faint Milky Way Satellites: Solving the Missing Satellite Problem. *Astrophys. J.*, 670:313–331, 2007.

[36] N. J. Spooner. Direct Dark Matter Searches. *J. Phys. Soc. Jap.*, 76:111016, 2007.

[37] F. Stoehr, S. D. M. White, V. Springel, G. Tormen, and N. Yoshida. Dark matter annihilation in the Milky Way's halo. *Mon. Not. Roy. Astron. Soc.*, 345:1313, 2003.

[38] L. E. Strigari et al. Redefining the Missing Satellites Problem. preprint, arXiv:0704.1817, 2007.

[39] L. E. Strigari et al. The Most Dark Matter Dominated Galaxies: Predicted Gamma- ray Signals from the Faintest Milky Way Dwarfs. preprint, arXiv:0709.1510, 2007.

[40] M. Taoso, G. Bertone, and A. Masiero. Dark Matter Candidates: A Ten-Point Test. *JCAP*, 0803:022, 2008.

[41] S. M. Walsh, H. Jerjen, and B. Willman. A Pair of Bootes: A New Milky Way Satellite. *Astrophys. J.*, 662:83, 2007.

[42] B. Willman et al. A New Milky Way Dwarf Galaxy in Ursa Major. *Astrophys. J.*, 626:L85–L88, 2005.

[43] M. Wood et al. A Search for Dark Matter Annihilation with the Whipple 10m Telescope. preprint, arXiv:0801.1708, 2008.

[44] D. G. York et al. The Sloan Digital Sky Survey: technical summary. *Astron. J.*, 120:1579–1587, 2000.

[45] D. B. Zucker et al. A Curious New Milky Way Satellite in Ursa Major. *Astrophys. J.*, 650:L41–L44, 2006.

8

DM searches at IMBHs. Observation of 3EG 1835 with MAGIC

IMBHs are thought to populate the MW halo in a number comprised between one hundred and one thousand. Most of them should be observable with IACTs. They should be brilliant γ–ray emitters with no counterpart at other wavelengths. Perfect candidates for being IMBHs are the unidentified EGRET sources, even if their characteristics are not well–known. In this chapter, a search among the unidentified EGRET catalog is performed. The best candidates which emerges from the selection procedure, namely 3EG 1835, was observed by MAGIC in 2006. The telescope was suffering serious technical problem and the data treatment was challenging. This give us the opportunity of describing into detail the data treatment. As a result, only upper limits in the flux from 3EG 1835 are reported.

This chapter is adapted from: *Dark matter searches at intermediate mass black hole with the MAGIC telescope.*, 2007 [7] and *Upper limits on the emission of 3EG J1835* , 2005 [5].

8.1 Introduction

In Chapter 7, the scientific paradigm of IMBHs was presented. It was observed that 100–1000 of such objects can populate the MW halo. They should be completely dark in visible light, with no counterparts at other wavelengths and bright γ–ray emitters. A detection through gravitational effects is not possible due to their vicinity and relatively small mass.

Until few years ago, the EGRET satellite recorded the γ–ray sky below few GeV. As a result, more than 250 sources were observed, out of which almost 200 remained unidentified. In the year following the publication of the III EGRET catalog [11], all the possible associations at other wavelengths, from radio to X–ray, were investigated. The problem of association of EGRET unidentified sources is complicated the fact that the error box of EGRET sources is very large, i.e. the position of the γ–ray excess is known only with precision of few degrees where too many radio and X–ray sources are coexisting.

On the other hand, the unidentified EGRET sources represent good candidates for being IMBHs, as they do not have counterparts at other wavelengths. For the MAGIC telescope, the catalog of unidentified EGRET sources was studied to select sources which could have

characteristics similar to IMBHs and could be observable by MAGIC. This is discussed in § 8.2. The main criteria for the selection are steadiness of the flux and observability with MAGIC.

Around ten targets were selected out of the catalog. Out of this list, only one candidate, the brightest among them and the brightest of all the unidentified sources, was chosen for observation with the MAGIC telescope. The analysis of this source is reported in this chapter. Due to some telescope technical problems, the analysis was complicated and the overall quality of the data spurred.

In the following, we report the result of the analysis of the source 3EG J1835 with the MAGIC telescope.

8.2 Search among EGRET unidentified sources.

The EGRET experiment, hosted on board the CGRO satellite, took data until the year 2000. It recorded γ–rays through electron–positron pairs production events. While the energy is reconstructed with precision, the major uncertainties were present in the determination of the arrival direction. For each source, an "error–box" is determined. The PSF was energy dependent, with a FWHM of approximatively 6° at 100 MeV and decreasing at higher energies. At few GeV, the PSF is of the order of 1° but can vary according to amount of data.

In the third EGRET catalog [11], 271 sources ($E > 100$ MeV) are included, around 70 out of which have been subsequently identified as blazars, 7 are rotation powered pulsar, 2 are the nearby Radio Galaxy Cen A and the Large Magellanic Cloud. Therefore around 196 sources [17, 16] remains unknown. Statistical studies indicate that the unidentified EGRET sources belong to basically two groups, namely a galactic population and an isotropic extragalactic population. The identification of the unidentified sources is made more difficult from the large typical error circle in the position estimation which put hindrances to the association of the gammas observed with observation at other wavelengths.

For each γ–ray source, the EGRET catalog adds the following information:

i) **EGRET source name.** The named is based on the $J2000$ (the Julian day corresponding to year 2000), following the IAU naming convention. Due to uncertainties in the position, also the name coding could not be definitively conforming to the source position.

ii) **RA and DEC**. The J2000 convention of RA and Dec. These have been then transformed to MAGIC local coordinates with the use of the MAGIC standard analysis and reconstruction code (MARS[1]).

iii) **Galactic Coordinates**. As above.

iv) **θ_{95}:** The 3EG catalog defines this measure as *"the radius in degrees of the circle containing the same solid angle as the* 95% *confidence contour"*. This means that the source is situated in a circle with radius θ_{95} around the mean position with 95% probability.

v) **Flux and its statistical uncertainty**. There are different flux values for different observation periods (each with a defined name type). P1234 means all EGRET periods. The EGRET catalog provides then a most significant flux (mostly corresponding to P1234) which has been used in the following analysis. The flux is

[1]MARS is the MAGIC Analysis and Reconstruction Software. Developed in C++.

calculated above 100 MeV with an assumed spectral index of -2 for most sources. However, the authors of the 3EG catalog are quite unclear about the systematic uncertainty of the thus calculated flux: *"If the spectral index differs substantially from 2.0 some additional error should be assumed for the flux F"*. The flux is given in units of 10^{-8} photons cm^{-2} s^{-1}. We do not have a clear opinion on this choice.

vi) **Γ:** The photon spectral index derived from the P1234 sum period.

vii) **Sqrt(TS):** The statistical significance of the observation.

viii) **VP:** The Viewing Period.

ix) **ID:** P pulsar, G galaxy, S solar flare, (a)A (presumed)AGN

x) **Other names:**. "E" extended source, "em" possibly extended source, "C" possible source confusion

8.2.1 Selection of the candidates

In the following search we tried to individuate the best candidates for signals from IMBHs among the unidentified EGRET sources. The following selection criteria were used:

- Minimum galactic latitude of 15 deg. This reduces the probability that the putative source is mis-interpreted as different types of typically Galactic source, especially pulsars or SNRs.
- Minimum source culmination at $\theta = 45°$. This cut assures the low energy threshold of the telescope.
- All entries with ID "a", "A" "S", with notes "E" or "em" were filtered out.
- Steady source: We used the variability indexes δ and their minimum values δ_{min} from [18]. All sources incompatible with steadiness (variability indexes $\delta_{min} > 0$) have been rejected.

Considering that several years have passed, we searched for associations with known sources that could have happened after the EGRET catalog publication. In Table 8.1 the result of the selection is reported. For each candidate, a list of parameters and a selection of articles that describe the target are reported.

Extrapolation of the EGRET fluxes to MAGIC energies

In order to estimate the observability of EGRET unidentified sources with MAGIC, we have to extrapolate their flux (measured principally at 100 MeV) to the MAGIC energy domain, i.e. above 100 GeV. The fluxes reported by EGRET are integral above 100 MeV, assuming a fixed spectral index of -2:

$$F_{EG} = \int_{100\,\mathrm{MeV}}^{\infty} \frac{dN}{dE} \cdot dE \quad \text{where} \quad \frac{dN}{dE} = N_{EG} \cdot E^{-2} \tag{8.1}$$

Because of the rapidly falling flux, the integral in the equation above can be approximated by:

$$F_{EG} \simeq N_{EG} \cdot \frac{1}{100\,\mathrm{MeV}} \tag{8.2}$$

We extrapolate the flux for a given spectral index $-\beta$ different from -2, by considering that the differential spectrum dN/dE must be the same at 100 MeV in both cases:

$$N_{EG} \cdot (100\ \mathrm{MeV})^{-2} = N_\beta \cdot (100\ \mathrm{MeV})^{-\beta} \quad \rightarrow \quad N_\beta = N_{EG} \cdot (100\ \mathrm{MeV})^{\beta-2} \tag{8.3}$$

The integral flux above 100 GeV, extrapolated with a power–law of spectral index $-\beta$ is therefore:

$$\begin{aligned}
F_\beta^{MAGIC} &= \int_{100GeV}^{\infty} \frac{dN}{dE}\, dE && (8.4)\\
&= \int_{100GeV}^{\infty} N_\beta\, E^\beta\, dE && (8.5)\\
&= \int_{100GeV}^{\infty} N_{EG}\, (100\ MeV)^{-2+\beta}\, E^{-\beta}\, dE && (8.6)\\
&= \int_{100GeV}^{\infty} F_{EG}\, (100\ MeV)^{-1+\beta}\, E^{-\beta}\, dE && (8.7)\\
&= \int_{10^5}^{\infty} F_{EG}\, (100)^{-1+\beta} \left(\frac{E}{MeV}\right)^{-\beta} dE && (8.8)\\
&\simeq F_{EG} \cdot \frac{(100\ \mathrm{MeV})^{\beta-1}}{\beta-1} \cdot (10^5\ \mathrm{MeV})^{-(\beta-1)} && (8.9)
\end{aligned}$$

The flux in the EGRET catalog is given in terms of 10^{-8} photons cm^{-2} s^{-1}.

In Chapter 7, we discussed the principal feature of the γ–ray spectrum from DM annihilation. We saw that the effect of internal bremsstrahlung significantly affects the γ–ray spectrum (see for example Figure 7.2). On the other hand, extrapolating the EGRET flux with a different γ–ray spectrum for each neutralino candidate would constitute a rather complicate task, compared to the much simpler extrapolation shown in Eq. 8.4 obtained with a power–law.

For this reason, a basic simplification was made. We neglected the contribution of internal bremsstrahlung and discussed only the spectrum emerging from $b\bar{b}$ annihilation branches, as suggested by G. Bertone:

$$\frac{dN}{dx} = x^{-1.5} \cdot e^{0.37 - 16.05 \cdot x + 18.01\, x^2 - 19.50\, x^3} \tag{8.10}$$

where $x = E/M$ is the ratio between the energy of emitted gamma-ray and the rest mass of the DM particle M.

This spectrum has the interesting advantages of being *universal*, i.e. almost independent for the neutralino composition, and only dependent of its mass. The mass affects the spectrum in determining the cutoff position. A further simplification can be used. As done in Eq. 8.2, we can extrapolate the spectrum with a power–law of index -1.5 without taking into account the cutoff.

With this assumption, the integral flux above 100 GeV can be calculated from Eq. 8.4 and leads to:

$$F_{DM}^{MAGIC} \simeq F_{EG} \cdot \frac{(100)^{0.5}}{0.5} \cdot (10^5)^{-0.5)} \simeq 0.063 \cdot F_{EG} \tag{8.11}$$

These values were used for Table 8.1

a	Source Name b	Ra c	Dec d	Θ_{95} [deg.] e	Variability δ $[\delta_{min}, \delta_{max}]$ f	culmin. θ_{min} g	Sp.index γ h	EGRET Flux 10^{-8}ph/cm^2/s i	CrabFlux j	Day k	Comments
Good candidates											
A	J0407+1710	2.56	9.74	0.24	0.9 [0, 1.59]	11	2.93 ± 0.37	32.1 ± 8.6	46%	256	Obs.at >100 TeV by [12] Def. as non-blazar [20, 15] Radio ass. B0404+1743 [15]
B	J0439+1105	69.81	11.09	0.92	0 [0, 0.74]	17	2.44 ± 0.29	9.4 ± 2.4	14%	204	HVC 186.2-22.8-206 [8] GC Abell497 [4]
C	J1337+5029	204.38	50.48	0.72	0.53 [0, 1.3]	21	1.83±0.29	9.2 ± 2.6	13%	310	GC Abell1758 [4] Def. as non-blazar [20, 15] Radio ass. B1329+5023, B1340+5125 [15]
D	J1600-0351	240.22	−3.86	0.86	0.01 [0, 1.62]	32	2.65±0.59	58.4 ± 19.9	84%	87	Ass. to radio NVSS J160117-030231 [2] Def. as non-blazar [15]
E	J1719-0430	259.79	−4.51	0.44	0 [0, 0.81]	33	2.2±0.24	16.2 ± 3.3		61	No ref.
F	J1835+5918	278.87	59.32	0.15	0.15 [0, 0.47]	30	1.69± 0.07	60.6 ± 4.4	87%	355	GC Abell1758 [4] Def. as best prot. for new source [17, 16] Def. as non-blazar [15]
G	J2248+1745	342.24	17.77	0.94	0.65 [0, 1.48]	10	2.11±0.39	12.9 ± 3.5	18%	160	Def. as non-blazar [20] NVSS A2486 [4] Def. as non-blazar [15]
Discarded candidates											
H	J1133+2304	173.35	0.55	1.02	0.82 [0, 1.51]	28	2.73 ± 0.63	10.6 ± 3.0		248	Def. as featureless BL-Lac [20] SRM 2003 with multi-epoch photometry obs. [21]
I	J1212+2304	183.15	23.08	0.88	0 [0, 1.13]	5	2.76±0.6	50.8 ± 16.6		319	Def. as BL-Lac RXJ1211+2242 [1] SRM 2003 with multi-epoch photometry obs. at Tenagra[21]
L	J1310-0517	197.60	−5.30	0.78	n.a.	34	2.34±0.22	7.9 ± 1.8		59	GC Abell1688 [4] Defined as Bl Lac IWGA J1311.3-0521 [10]
M	J1347+2932	206.80	29.54	0.95	0.64 [0, 1.6]	0.8	2.51±0.61	21.0 ± 6.8		343	GC Abell1781 [4] Claim as pulsar [3] Def. as Bl Lac FSRQ [22] Def. as FSRQ [20]
N	J1424+3734	216.22	−37.58	0.88	n.a.	8.8	3.25±0.46	16.3 ± 4.9		322	Def. blazar-like [24] Defined as Bl Lac TEX 1428+370 [10]
O	J2243+1509	340.78	15.17	1.04	1.06 [0, 1.79]	13	—	73.1 ± 25.1		189	Pulsar [3]

Table 8.1: Candidates for observation. The column definitions are: (^{a}) candidate ID, (^{b}) 3EG source name, (^{c}) 3EG mean Ra and (^{d}) Dec, (^{e}) 3EG 95% source position confidence radius θ_{95}, (^{f}) variability parameter as defined in [18], (^{g}) MAGIC telescope zenith angle at culmination, (^{h}) 3EG estimation of spectral index γ, (^{i}) most significant 3EG flux level, (^{j}) percentage of the flux w.r.t. Crab flux using spectral index $\gamma = -1.5$, (^{k}) first day of observation since May,13 th 2006

From the table, one can see that:

- Most sources have been already observed in the radio domain, but due to the large uncertainty of the 3EG position, the association is not strong enough to claim a striking source association.

- Almost every source has been observed also in X–rays. In case of a steady counterpart in this domain, the source is often associated with a pulsar, while in case of a variable X–ray counterpart, usually the source is putatively defined as blazar. Those candidates are therefore higher chance to be a new class of sources.

- Several sources have error–boxes larger than 1°. This constituted a problem for small field of view experiment like MAGIC.

Figure 8.1(a) shows more accurate extrapolations of EGRET spectra, including the exponential cut-off for two possible χ-masses: 400 GeV and 1.5 TeV, together with the Crab spectrum and a line indicating the equivalent flux level at which $3\,\sigma$ significance can be obtained in 20 hours of observation. One can see that assuming masses around 1.5 TeV, all source become visible. Note however that the integral EGRET flux values have considerable errors and can easily vary by 30%. Figure 8.1(b) shows the EGRET fluxes, extrapolated to MAGIC energies with the use of the spectral index, as given in the 3EG catalog.

8.2.2 Discussion of the EGRET candidates for MAGIC

From the results of Table 8.1 and Figure 8.1, we report the best three candidates for detection with MAGIC telescope:

1. **J1835+5918.** This source has been deeply investigated at many wavelengths (optical photometry, X-ray,, radio) by [17, 16] in 2000. The authors state that in case of an AGN, its beamed emission is at least a factor 100 suppressed, and in case of an isolated neutron star, it lacks the steady thermal X-rays flux from a cooling surface. In case of a pulsar it would show very atypical emission features. For these reasons the authors define the source as a new class of high–energy gamma-ray emitters. Thus, even in the case of different origin, a counterpart search above 50 GeV would be of out–standing importance. Additionally, this source shows the highest flux among the other EGRET candidates and a spectral index which is compatible with -1.5. Finally, this source is the only candidate with a good position estimate: θ_{95}=0.15°. The only negative point is the rather high zenith angle at culmination which results to be 30 deg.

2. **J1719-0430.** This source has never been observed by other experiments or at other wavelengths. The flux is very steady and its level quite high. The position estimation is good (θ_{95}=0.44°).

3. **J0407+1710** This candidate has a strong flux level and a good position estimate. It has a low zenith angle at culmination. However, the EGRET spectral index is very steep and inconsistent with -1.5. Moreover, it has been claimed to be observed above the 100 TeV by a scintillator detector [12].

For the following three targets, the uncertainty in the EGRET position is large and they are therefore less attractive targets.

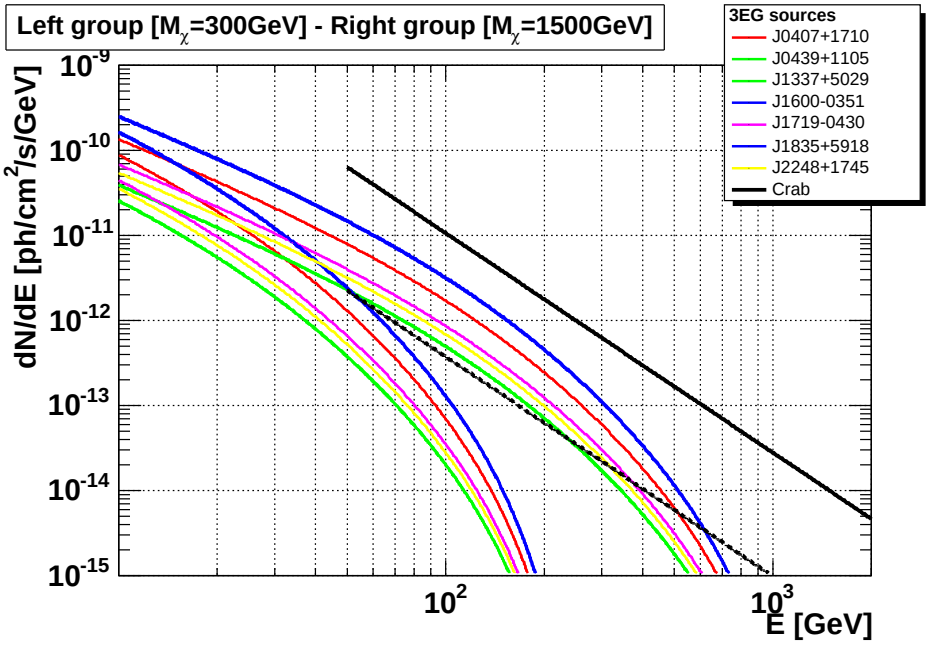

(a) Extrapolation of EGRET spectra with Eq. 8.10

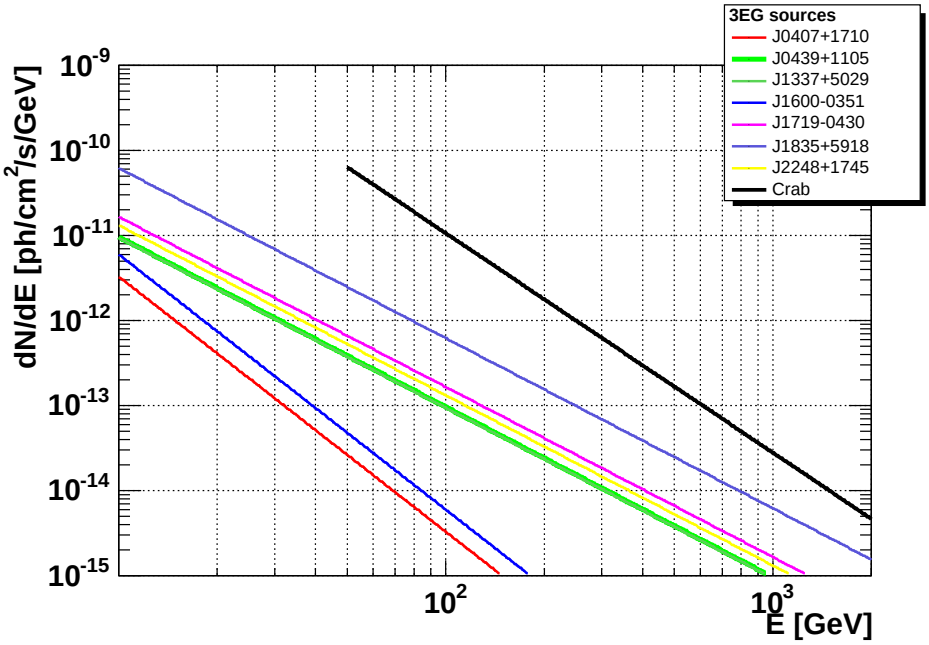

(b) Extrapolation of EGRET spectra with $1 - .5$ power–law

Figure 8.1: (a) Spectra of the EGRET source calculated with a spectral index of -1.5 together with an exponential cutoff for two different DM masses value of 300 GeV and 1.5 TeV. The differential flux for the Crab (black line) is also shown for comparison. The dotted line is the flux of a 1/20 Crab intensity: this ideal source, according to MAGIC integral sensitivity, can be observed in 10 hours with 3 sigmas significance. (b) The spectra for each source is presented with a spectral index as defined in 3EG.

a) **J2248+1745.** The source has been defined as non-blazar and the spectral index is consistent with -1.5 within 2 sigmas. An advantage is the high culmination, a disadvantage is the average precision of the position estimate.

b) **J1337-5029** Even if the flux of this source is the weakest, its spectral index is consistent with -1.5, making it a candidate. An inconvenient is the low positional uncertainty of 0.72 deg. also requiring various pointings.

c) **J1600-0351** The source has a high flux, however the positional uncertainty is 0.86 deg. This source would need to be observed with various pointings and require more time for this reason. Also the zenith angle at culmination lies at the edge (32 deg.)

Finally, J0439+1105, due to the low flux and bad parameters, is excluded from being a suitable candidate.

Approval of 3EG 1835

In the phase of approval of the proposal of observation of IBMHs by the MAGIC collaboration time allocation committee, only one target was guaranteed, namely the best candidate, 3EG 1835. The source was observed for around 30 hours between May and June 2006, The results of the observation are reported below. The analysis was made with F. Zandanel, and these results were already presented in his Diploma Thesis [23].

8.3 Observation of 3EG 1835 with the MAGIC I telescope.

The source was observed for around 30 hours in ON/OFF observation mode between May and June 2006. Unfortunately, this happened after a major upgrade on the telescope electronics, which caused some technical problems exactly in the two weeks of observation. The quality of the data was therefore affected. Nevertheless, we tried to recover as much data as possible from the period, and in addition we performed a very detailed analysis, monitoring the quality run per run. The peculiarity of the analysis is hereafter described with the particular aim to introduce the reader to the MAGIC analysis. It must be underlined that since 2006, many changes on the software took place, and most of the checks and procedures which are here described are now included into automated routines. The main technical problems are hereafter discussed:

– **Part of the camera not triggering.** The Level1 trigger of MAGIC is a topological coincidence trigger. The trigger area is divided into n independent cells. The trigger checks whether pixels inside the single cells are activated above a threshold energy, and in case fires the trigger signal. The scheme of the trigger cells is shown in Figure 8.2.

  Due to an overheating problem in the trigger system, one of the trigger chips was burnt. As a result, around ten of the trigger cells (micro–cells) of Figure 8.2 were not active. This meant that while the photomultipliers were operating normally, with their signal charge read–out functioning, they were not properly triggering. Each microcells control 8 pixels. In case of event with large energy (i.e above 300 GeV) the number of photomultipliers illuminated is around 50 (this depends strongly on the shower impact parameter). This means that many trigger microcells are activated by such shower. In the case of low energy showers, the number of activated microcells can be of the order of unity. Because to trigger the trigger only one microcells need to be activated, the probability of loosing one event was way larger for low energy events than for high energies events. We will show this on the text and how this problem was overcome in the analysis.

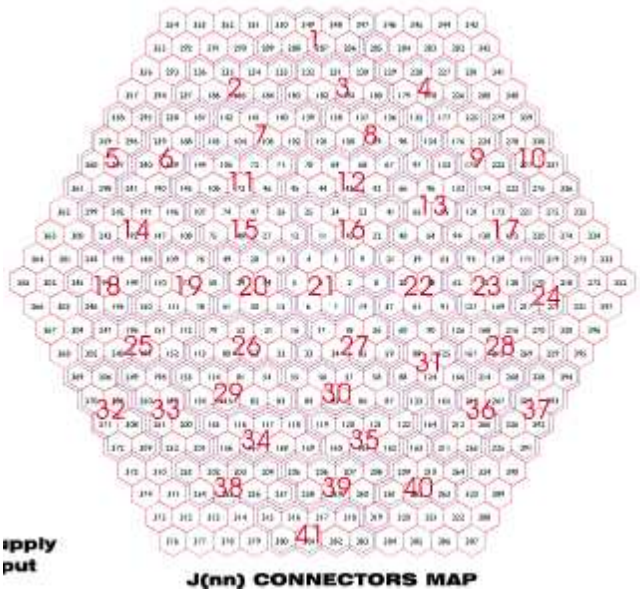

Figure 8.2: The trigger configuration of MAGIC camera. Numbered are the trigger cells (micro–cells). Each microcells control 8 pixels. Courtesy F. Dazzi.

– **Wrong pointing in a sub–period.** In the period between May 16 and 25, 2005, the telescope was wrongly focussed due to an incorrect positioning of all the mirrors in the telescope. While the telescope was focussed properly, the reflector was focussing on a point 18.5 mm (half a camera pixel) far from the camera center. The source was therefore shifted in the camera and rotating around this new center during observation. While in principle the problem could have been recovered in the analysis by repositioning the shower on a event by event basis. It was decided to remove those events because the events were already affected by the trigger problem.

Other factors added to the above problems and made even more complicated the analysis of this source:

– **Low energy searches.** Given the expected DM spectrum of Eq. 8.10, a reduction of the analysis energy threshold is accompanied by an increase of the flux. It was therefore particularly important for us to look for low energy events and to push the analysis to the lowest achievable threshold. Of course, this demand collided with the technical problems described above and complicated the analysis.

– **EGRET error–box.** The error–box of 3EG J1835 is smaller compared to other EGRET sources, but still larger than the MAGIC angular resolution. For this reason, we were aware that we could have a signal slightly off–center with respect to the nominal telescope pointing.

– **Spread in zenith angle range.** The source was observed between 29 and 47 degrees in zenith angle (ZA). It was shown in [13], that almost all Hillas parameters have distributions that change with the zenith angles. More into detail, they are constant for incidence between 0 and 30° ZA. They approximatively vary of 10% every 0.1 change in the $\cos(ZA)$. It is important that the Hillas parameters are homogeneous in the data sample, because quality cuts on Hillas parameters are used as main technique for gamma/hadron separation. In light of this, it was decided to perform the analysis in zenith angle bins, with around equal bins widths in the cosine of the zenith angle. The used bins are reported in Table 8.2.

Zbin	13–19	16–23	24–28	24–32
Angle	29.0–36.4	32.3–40.1	40.1–44.4	40.1-47.6

Table 8.2: Conversion between zenith angles and zbins

The final dataset, after quality selection which will be described below, is listed in Table 8.3.

Zbin	ON Eff.Time [h]	OFF Eff.Time [h]
13–19	10.92	1.97
16–23	9.31	1.92
24–28	1.39	1.47
28–32	3.34	-
Total	24.96	5.36

Table 8.3: 3EG 1835 ON and OFF data ordered and grouped according to zenith angles and date.

Several particularities of the these data sample have to be mentioned:

- The amount of OFF data is clearly undersized with respect to the ON sample. This will result in a worse background estimation and in a corresponding loss in sensitivity. Any attempt to find additional proper OFF data from the same period failed.
- OFF data in the zbin 28–32 were not taken. Therefore a larger zbin 24–32 was used.

We performed the full analysis for all the three ZA range, but we will report the result mainly for the first ZA bin considered, which is that with most data. The other bins were always not significant. To mix them with lower ZA data in general further worsen the quality of the analysis.

8.4 Data preparation

Analysis of the star–field

Bright stars ($M > -5$) in the field of view of the telescope, could be observed through an increase of the pedestal RMS in those pixels which are illuminated by the star itself. Normally those pixels are replaced in the analysis as described below. On the other hand, it is important to check the sky around the source preliminarily. In Figure 8.3 the star–field map of the region of the sky around 3EG 1835 is shown. One can see that only faint stars are present.

Exclusion of misbehaving pixels.

A description of the some types of electronics and environmental background of MAGIC was given in § 1.2.2. Pedestal runs are taken to estimate the contribution of the electronic noise. In addition, they give information on the state of the single photomultiplier (PMT) in the camera. PMTs in fact age quite fast, and their performance decreases with time. Misbehaviors and breaks can happen and pixels are seldom replaced in the camera. In our dataset, we had to exclude pixels because of fluctuating RMS of their pedestal value. We recall that the pedestal value is fixed artificially to keep all the signals positive and that the photomultipliers are read out in AC–coupling mode. The pedestal RMS is connected in

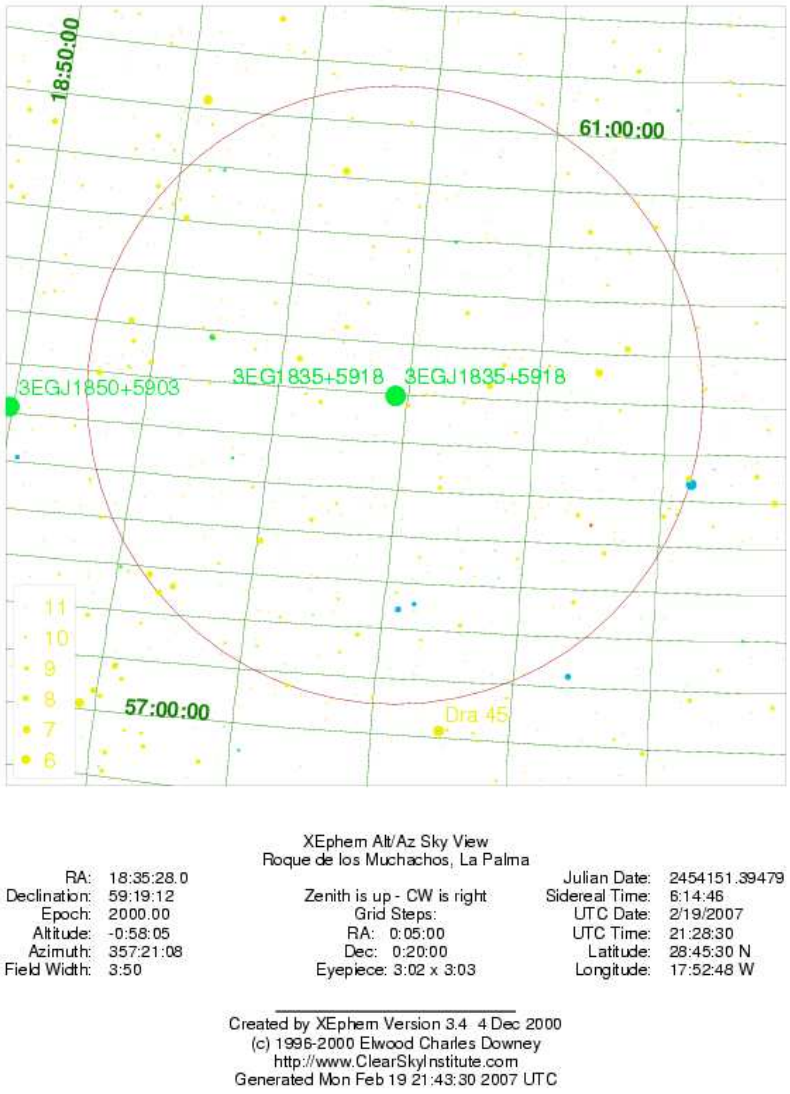

Figure 8.3: Star field map of the sky around 3EG 1835

normal operating conditions to the average level of illumination of the pixel. A fluctuating RMS is therefore symptomatic of a pixel misbehavior. On average 10–15 pixels ($\sim 2\%$) out of 577 were excluded because of this problem.

The calibration runs are instead obtained via artificial illumination of the camera homogeneously with a calibrating systems of ultra–fast LEDs [9, 6]. The signal from each photomultiplier is extracted and corrected with a conversion factor obtained after calibration runs. Sometimes a pixel cannot be calibrated. Again, this is often related to a technical problem in the photomultiplier. In this case, the pixel is excluded from further analysis. Following this method, we rejected another 10–15 pixels in the camera. Summed together, we excluded around 4–5% of the camera pixels from the analysis.

The signal of these pixels is not completely lost and is recovered by averaging on the adjacent pixels signal. This is done automatically in the analysis.

Image cleaning.

The image cleaning is the analysis process that isolates the pixels of the camera which were illuminated by Cherenkov light and remove the others. It is a rather important process, because it directly affects the overall performance of the telescope: energy threshold and sensitivity.

In order to reach a low energy threshold we used two image cleaning configurations:

i) **Cleaning "absolute 7–5".** Core pixels must have more than 7 photoelectrons (phes) each and then all the pixels with more than 5 phes close to the core pixels are considered as contributing to the shower.

ii) **"Time and Relative" cleaning.** The reconstructed pulse arrival time for each pixel is taken into account, and the selection between core and neighbor pixels is not based on an absolute number of phes but on the relative charge signal with respect to an average pedestal signal for that pixel.

Our aim was to determine which of the two had better performance. The comparison is described below.

8.4.1 Treatment of the camera inhomogeneity

The trigger problem has the direct effect of mining the camera homogeneity. A good test to monitor the homogeneity of the camera is the study of the distribution of the center of gravity (*cog*) of the hadronic events in the camera. This distribution is shown in Figure 8.4, for two separate energy bins. The *cog* is the centroid of each event in the camera. In normal operating condition, one expects the distribution to be almost flat in the variable ϕ, the angle between the *cog* and a chosen axis (i.e. the x axis pointing left). This corresponds to the physical fact that atmospheric showers have not a preferential azimuthal direction (excluding the effect of the earth magnetic field). A perfect flatness is unreachable due to the difference acceptance of the camera for different ϕ, dependent from the trigger design (Figure 8.2).

Strong inhomogeneities are visible on two regions in the upper part of the camera. These parts correspond to those trigger cells which were not triggering, as described in the introduction of this chapter. The effect is more noticeable at lower energies as already anticipated.

To perform the analysis, i.e. to compare correctly the ON data with the OFF data and the MC simulations, we had to perform what we call the $\phi-$cut, i.e. we took out part of the camera in all data sample (ON,OFF,MC) and analyzed only the shower triggering outside this region. The $\phi-$cut we used to match the ON and OFF distribution on Figure 8.4 was:

$$180^\circ < \phi < 240^\circ \qquad \text{and} \qquad 280^\circ < \phi < 325^\circ \tag{8.12}$$

The result of the cut is shown in Figure 8.5. The homogeneity of the camera is only partial, particularly at low energies. We observed indeed the presence of red "bumps" in the *cog* plot which are region more triggering than others. Low energy data were therefore treated with caution.

Counter-check of the $\phi-$cut on the Crab

In order to test the feasibility of the analysis after the $\phi-$cut, a test check was needed on a well–known source. It is usual behavior to use the Crab Nebula, but it is also important to reproduce as close as possible the observational condition of the source under study . We used

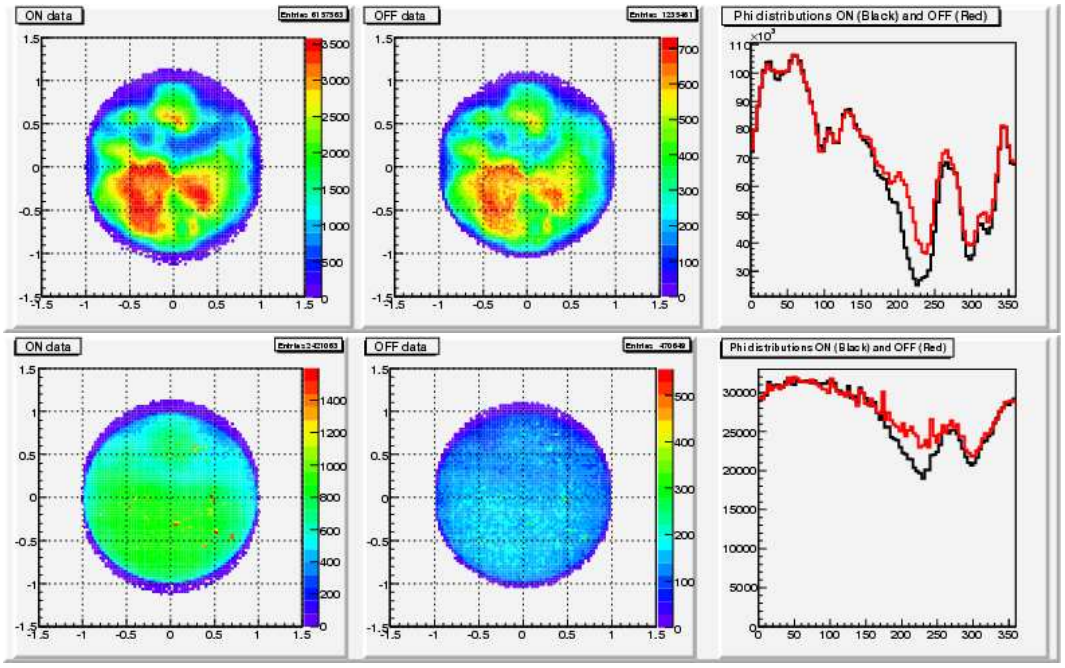

Figure 8.4: Distribution of the center of gravity of the ellipses in the camera. The upper pad refers to the range 120-300 GeV and the lower to 300-700 GeV. The left plots show ON data, the center plots OFF data and the right plots are the projection of the camera onto the azimuth angle ϕ.

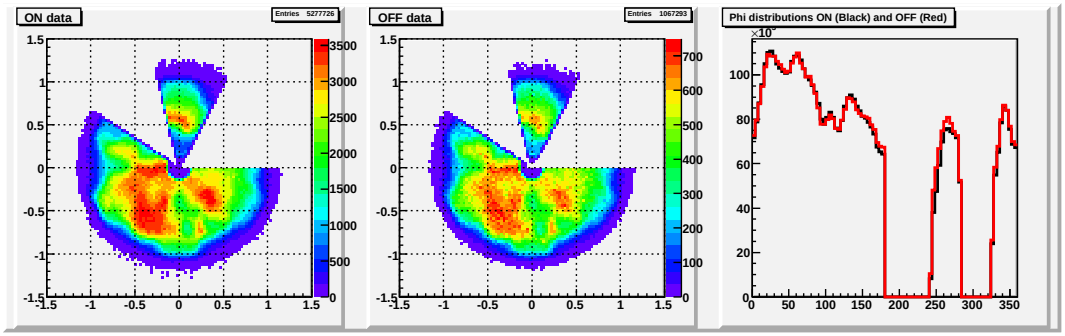

Figure 8.5: Distribution of the *cog* after all cuts as in relation (8.12) and effectively used in the further analysis.

a set of Crab data observed at similar ZAs. Two analyses were performed: one on a *normal* Crab data sample where the $\phi-$cut was not applied (hereafter *u–Crab*, for uncut–Crab) and the second on a *cut* Crab data sample (hereafter *c–Crab*, for cut–Crab), i.e. with the same $\phi-$cut of Eq. 8.12.

The distributions of the *alpha* Hillas parameter for *u–Crab* and *c–Crab* are shown in Figure 8.6 for one energy bin. One can see that when the $\phi-$cut is applied a loss of excess events appears, followed by a loss of sensitivity. The studies was extended for all three energy bins and in addition the *theta2* Hillas parameter was studied. We recall that *theta2* is the angular distance between the expected position of the source estimated on the basis of image parameters and the real position of the source in the camera [14]. The complete set of results is shown in Table 8.4.1.

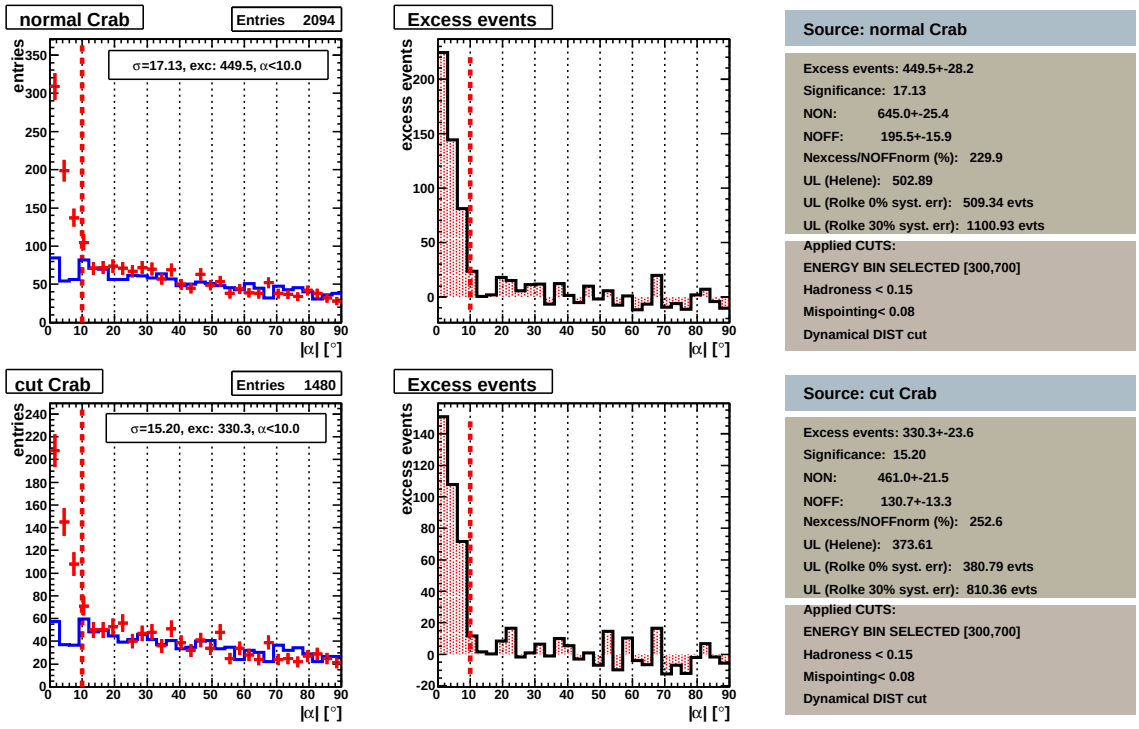

Figure 8.6: From up to down: Alpha plots and *theta2* plots for the for the *u–Crab* and *c–Crab*. Energy range: $300 - 700$ GeV.

		alpha–plot		*theta2*–plot	
Energy [GeV]	Source	Excess	Significance	Excess	Significance
120-300	*u–Crab*	698±62	11.4	545±60	9.14
	c–Crab	460±53 (-34%)	8.7 (-24%)	382±51 (-30%)	7.5 (-18%)
300-700	*u–Crab*	449±28	17.1	331±28	12.1
	c–Crab	330±23 (-26%)	15.2 (-11%)	254±24 (-23%)	11.1 (-8%)
700-10^4	*u–Crab*	141±14	10.1	118±13	9.5
	c–Crab	114±12 (-19%)	9.8 (-3%)	95±11 (-19%)	9.1 (-4%)
120-10^4	*u–Crab*	1309±72	18.6	1027±71	14.6
	c–Crab	918±61 (-30%)	15.2 (-18%)	747±60 (-27%)	12.5 (-15%)

Table 8.4: Alpha and Thetaii plots results of the *u–Crab* and *c–Crab*

One can see that:

i) The loss of events is larger than than the loss of significance. This is due to the fact that the significance scales with the square root of the excesses number.

ii) The loss of events in the lower energy bin ($\simeq 30\%$) is comparable with the portion of excluded camera, while this value decreases in the second and third energy bin. This demonstrates that at low energies there are much more events which are affected by the trigger loss then at higher energies.

iii) The *theta2* analysis is only marginally less affected by the $\phi-$cut, but the results are quite similar.

The effect of the $\phi-$cut was also checked on the spectrum and the effective area of the Crab. The latter, shown in Figures 8.7, decreases of around 20–30% after the $\phi-$cut, again

corresponding to the rejected part of the camera. This is because the effective telescope area is proportional to the effective trigger area of the camera. The γ–ray flux is calculated via the formula:

$$\Phi(> E_0) \;=\; \frac{N_\gamma^{cuts}(> E_0)}{t_{eff} \cdot A_{eff}(> E_0)}, \tag{8.13}$$

where E_0 is the energy threshold, $N_\gamma^{cuts}(> E_0)$ is the number of gammas after analysis cuts above the energy threshold, t_{eff} is the effective observation time and $A_{eff}(> E_0)$ is the effective telescope area above the energy threshold.

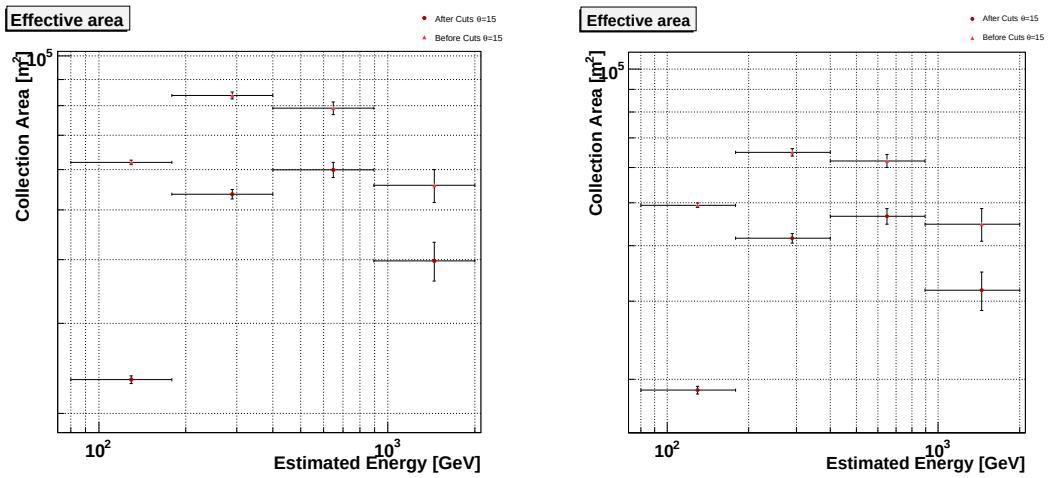

Figure 8.7: Effective areas for the *u–Crab* (left) and *c–Crab* (right).

Given that the effective time is constant between the *c–Crab* and *u–Crab*, it is clear that the flux remains constant because a decrease in the number of excess is compensated by a decrease in the effective area. For what deals the spectrum, no significant differences are found between the *c–Crab* and the *u–Crab*, as shown in Figure 8.8.

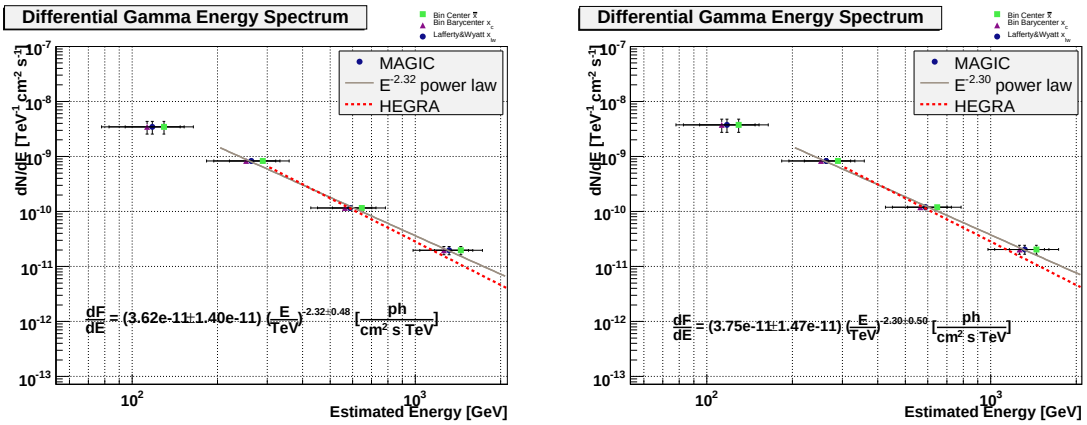

Figure 8.8: Differential spectra for *u–Crab* (left) and *c–Crab* (right).

From all the discussion above, we conclude that *an analysis on this set of data is possible and gives reliable results. The exclusion of a part of the camera affects the data sample*

especially in the lower energy bin, while for energies above the 300 *GeV the analysis is almost unaffected.*

8.4.2 Compatibility ON–OFF

Due to the particular condition of the telescope, an extended check of the compatibilities between ON and OFF data was performed, on a daily–based check. Without γ-hadron, both samples are constituted basically of hadrons and therefore their distribution of the Hillas parameters should be compatible. Again, these checks were performed on all the analysis energy bins and over all the zenith angle bins ($120-300$ GeV, $300-700$ GeV, $700-10^4$ GeV and $30-36$ deg, $33-40$ deg, $40-44$ deg, $40-48$ deg, respectively).

On average, a good agreement was found, as shown in Figure 8.10. This ensure an overall robustness of the results.

8.4.3 Determination of the analysis energy threshold

The analysis energy threshold can be defined in several ways. We determined it as the peak of the MC data estimated energy distribution. In Figure 8.9, the estimated energy distribution and the energy resolution, from the MC data, for the Time cleaning (upper plots) and for the Absolute cleaning (lower plots), are shown.

Two important differences between the cleaning methods can be found:

i) the lowest energy threshold is obtained with the Time cleaning, and is about 120 GeV. With the Absolute cleaning, it increases to 150 GeV.

ii) the Time cleaning has also a better energy resolution compared to the Absolute cleaning.

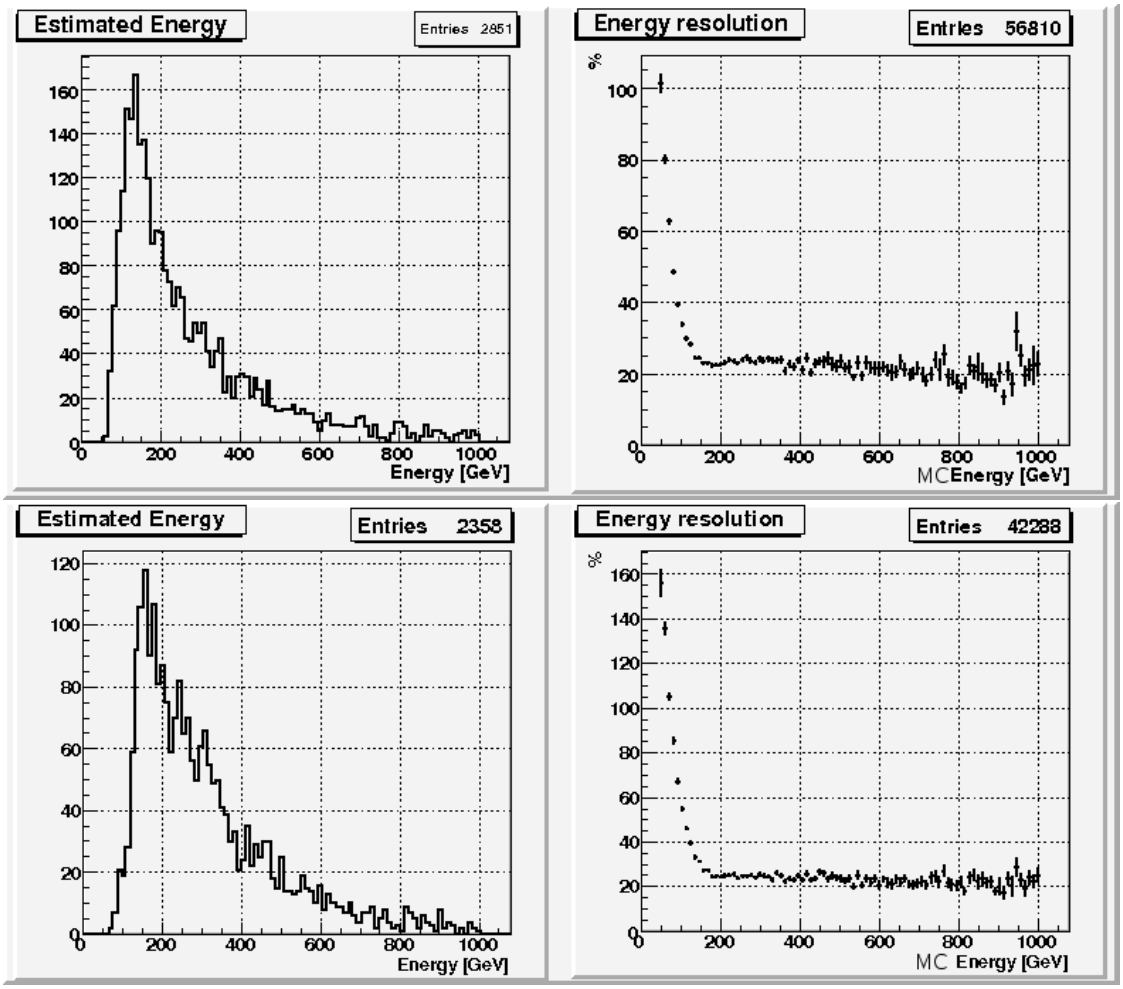

Figure 8.9: Energy reconstruction and resolution for the Monte Carlo data with the Time cleaning (upper plots) and Absolute cleaning (lower plots). The energy reconstruction distribution peak is around 120 GeV for the Time cleaning data and around 150 GeV for the Absolute ones.

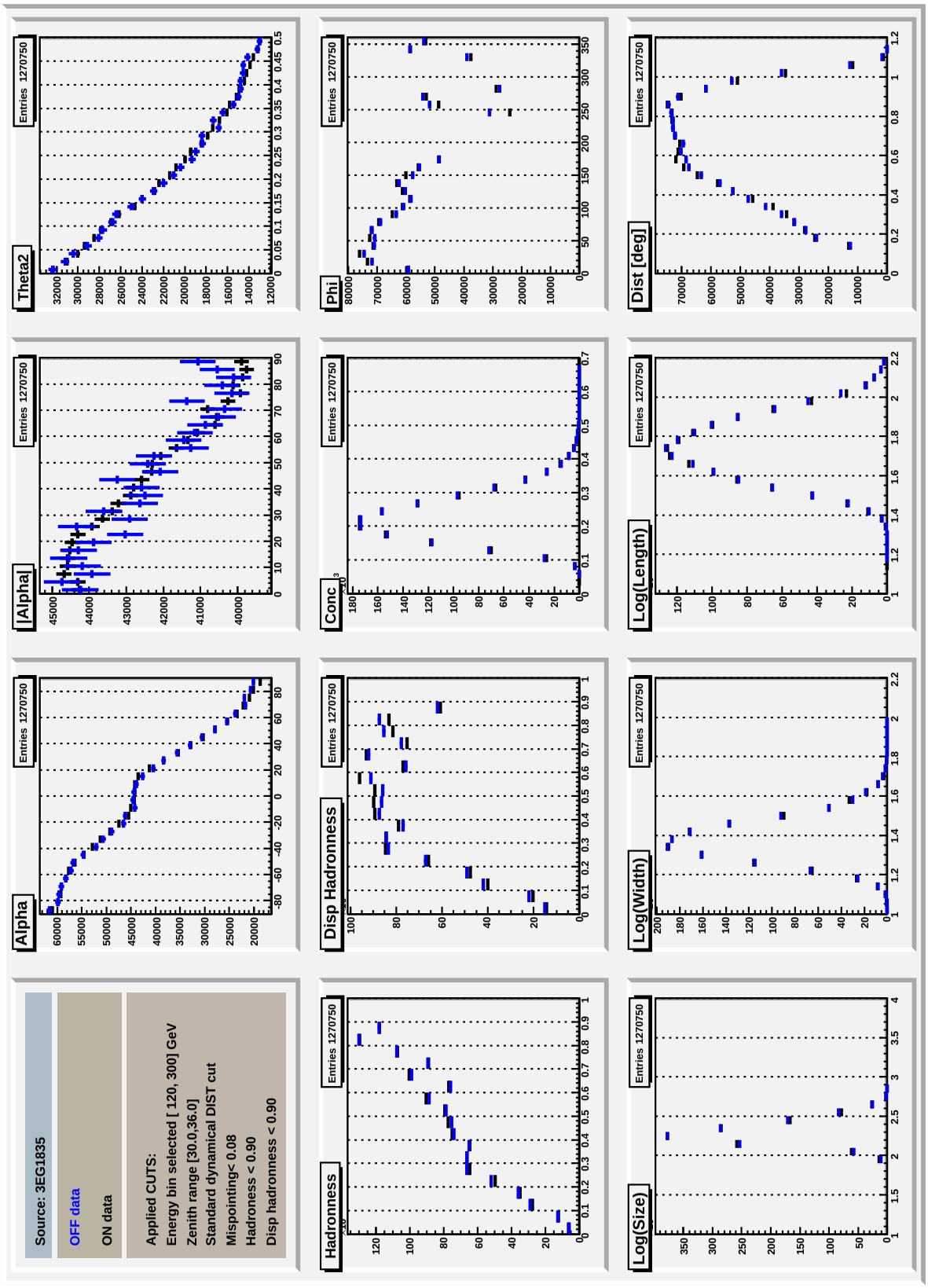

Figure 8.10: Distribution of several Hillas parameters for ON and OFF data sample without any *hadronness* cut for $120 - 300$ GeV and $30 - 36$ deg.

8.5 Results

As mentioned above, we performed the analysis of the detection plots in energy bins, equally spaced on a logarithmic scale:

$$120 - 300 \text{ GeV} \qquad 300 - 700 \text{ GeV} \qquad 700 - 10^4 \text{ GeV} \tag{8.14}$$

We also performed separated studies for different zenith angles bins:

$$30 - 36 \text{ deg} \qquad 36 - 40 \text{ deg} \qquad 40 - 44 \text{ deg} \qquad 40 - 48 \text{ deg} \tag{8.15}$$

For the reason that the $\phi-$cut we applied could have affected the distribution of the angular Hillas parameters in the camera, we compared to results for several estimators of the orientation of the shower:

$$alpha \quad |alpha| \quad theta2 \quad alpha180 \quad alphapow \tag{8.16}$$

where *alpha* and its modulus are the usual Hillas parameter, the *theta2* is calculated using the *disp* method, *alpha* 180 is calculated using the the third order asymmetries of the shower, and *alpha* pow is a way of calculating *alpha* using the vector pointing to the peak of the image in the camera, as described in [14].

		$120-300$ GeV			$300-700$ GeV			$700-10^4$ GeV		
	Had	Exs	%	σ	Exs	%	σ	Exs	%	σ
alpha	0.1	172±156	4.6	1.09	-2±77	-0.3	-0.03	18±32	11.5	0.54
	0.2	98±325	0.6	0.31	-17±103	-1.1	-0.17	-2±43	-0.8	-0.05
	0.3	313±482	0.9	0.65	74±129	3.0	0.57	6±51	1.8	0.12
	0.4	460±625	0.8	0.73	213±153	6.1	1.38	-16±60	-3.4	-0.28
	0.5	380±754	0.4	0.51	197±179	4.1	1.09	38±65	6.5	0.58
theta2	0.1	-42±169	-0.9	-0.25	-20±27	-5.6	-0.75	-53±52	-17.1	-1.07
	0.2	177±317	1.1	0.56	-84±138	-2.9	-0.81	-23±60	-5.5	-0.39
	0.3	685±467	2.0	1.46	1±155	0.0	0.01	15±64	3.1	0.23
	0.4	1177±605	2.1	1.94	-40±175	-0.8	-0.23	99±64	18.6	1.49
	0.5	1711±726	7.2	2.34	232±198	3.9	1.16	61±72	8.5	0.83
alpha 180	0.1	-69±125	-2.9	-0.56	5±60	0.9	0.08	21±24	23.9	0.83
	0.2	-138±251	-1.4	-0.55	75±76	8.7	0.98	21±32	14.5	0.64
	0.3	-18±366	-0.1	-0.05	69±94	5.1	0.72	16±39	7.9	0.41
	0.4	214±488	0.6	0.46	217±110	11.9	1.91	-26±48	-8.4	-0.56
	0.5	270±561	0.6	0.48	219±129	8.9	1.67	-6±51	-1.6	-0.11
alpha pow	0.1	168±136	6.0	1.22	-27±86	-2.6	-0.35	-24±31	-16.7	-0.81
	0.2	371±285	2.9	1.29	57±112	3.0	0.51	-21±36	-11.0	-0.59
	0.3	781±426	2.8	1.82	32±143	1.0	0.22	-40±44	-15.4	-0.94
	0.4	771±552	1.6	1.39	328±166	7.8	1.94	-16±47	-5.5	-0.35
	0.5	770±803	0.8	0.96	378±194	6.6	1.92	-44±54	-10.8	-0.84

Table 8.5: Table of significances for different angular parameters and different *hadronness* cuts.

Unfortunately, *no significant detection was reached in any of the energy bins.* In Figure 8.11, the *theta2* plot for the lower energy bins is shown.

8.5.1 Skymaps

The skymap is a the bidimensional reconstruction of the direction of incoming γ–rays after subtraction of background. It is usually expressed on a RA–Dec plane and centered on the

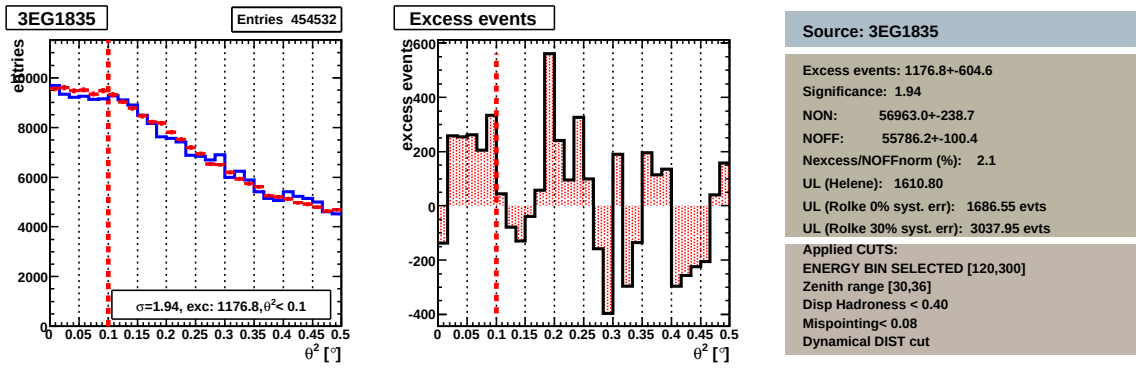

Figure 8.11: From up to down: Alpha plot, Alpha 180 plot, Alpha Pow plot and *theta2* plot. Range: $120 - 300$ GeV, $30 - 36$ deg.

target source observed. As the MAGIC mounting is alt–azimuthal, the sky rotates around the position where the telescope is pointing to. For this reason, a deconvolution with the sky rotation must be performed on the data to reconstruct correctly the bidimensional position. For the ON data, the derotation is performed with the time stamp of the event. In case of the OFF data, the derotation is performed by taking random values from the distribution of the derotation angles of the ON data sample.

It must be underlined that for point–like sources (i.e. sources whose extension is smaller than the telescope angular resolution), the skymap has little meaning. On the other hand, it is good practice to create it, because serendipitous sources can be observed in the skymap field of view, and most of all to check that that the background sky is homogeneous over the plane. In our case, due to particular telescope conditions, the fact that the EGRET error–box was larger than the telescope angular resolution, and because of the particular analysis we performed, we performed a detailed skymap analysis.

There are two ways in which the skymap reconstruction can be produced:

i) *"False Source" method.* In this method, the full field of view of the telescope is investigated without any hypothesis of where the source is localized. It goes as follows: first, the events are derotated, then the field of view is divided into $n \times n$ bins. For each *i–th* bin, all events are reprocessed and the *alpha* parameter is calculated *with respect to the center of the i–th bin.*. Therefore for each bin one obtains an independent *alpha*–plot. The false source plot is therefore a $n \times n$ diagram where in each bin the number of excess of the corresponding *alpha*–plot is plotted. We call this plot, the "false source plot (FSP)".

ii) "disp" *method.* We observed above that the *disp* method reconstructs event by event the position of the source in the camera without aprioristic assumptions. After derotation, by plotting the *disp* variable on a bidimensional plane, one obtains directly the skymap. The ON and OFF distributions are normalized to each other using all events 0.5 degrees from the center. The plot obtained with the *disp* method is also called directly, *the* skymap .

Test of the method on a Crab sample

The $\phi-$cut was checked again on the Crab data. Skymaps and FSPs were hereafter produced. The bidimensional reconstruction was also checked in energy bins to understand a possible

energy dependent effect. The results are shown in Figures 8.12.

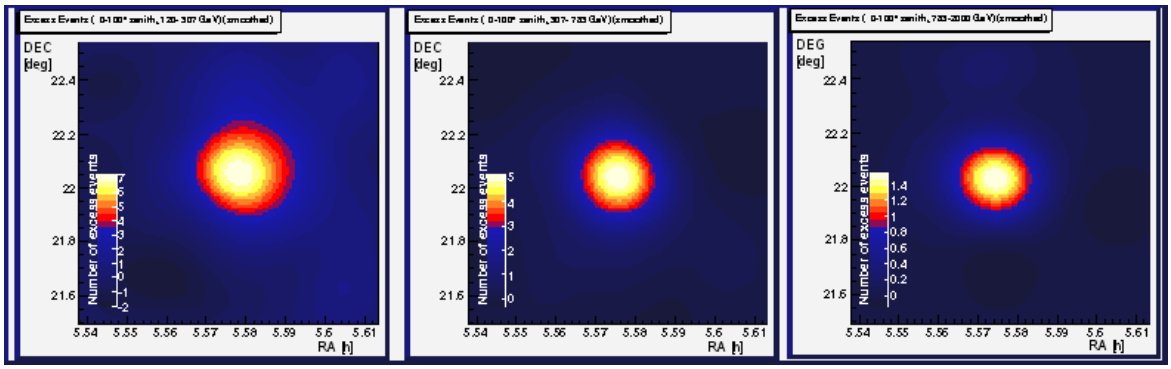

(a) Skymap of *c–Crab* for the energy bins (left-to-right)120 − 300 GeV, 300 − 700 GeV and 700 − 2000 GeV.

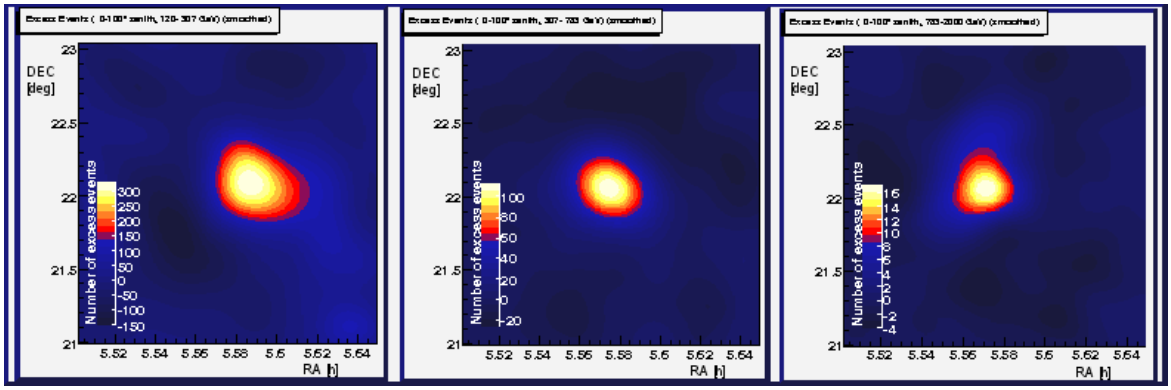

(b) FSP of *c–Crab* for the same energy bins

Figure 8.12: Skymaps (top) and FSPs (bottom) for the *c–Crab* sample. From the left to the right increasing energy bins are used: 120 − 300 GeV, 300 − 700 GeV and 700 − 2000 GeV, respectively.

Here are the main results:

- The centroid reconstruction is unaffected by the $\phi-$cut at energies larger than 300 GeV,
- In the first energy bin (leftmos plots), the effect of the $\phi-$cut is to slighly shift the centroid rightward. The effect is larger in the case of the FSP.

To investigate further the effect of the $\phi-$cut, we reconstructed the skymaps using only a portion of the camera, i.e. the upper–right quadrant. In case of *u–Crab*, no effect is visible and the skymaps look similar to the normal skymaps but with lower significance, as expected because of the loss of 3/4 events. In the case of *c–Crab*, the skymap is largely affected. The results are shown in Figure 8.13. One can see how the combination of the effects of having the $\phi-$cut which strongly decrease the number of triggering events and the low energies, creates a sort of "bubble" in the skymaps located outside the center of the camera. The appareance of this excesses can be misintrerpreted with the existence of a γ–ray source, which is not the case.

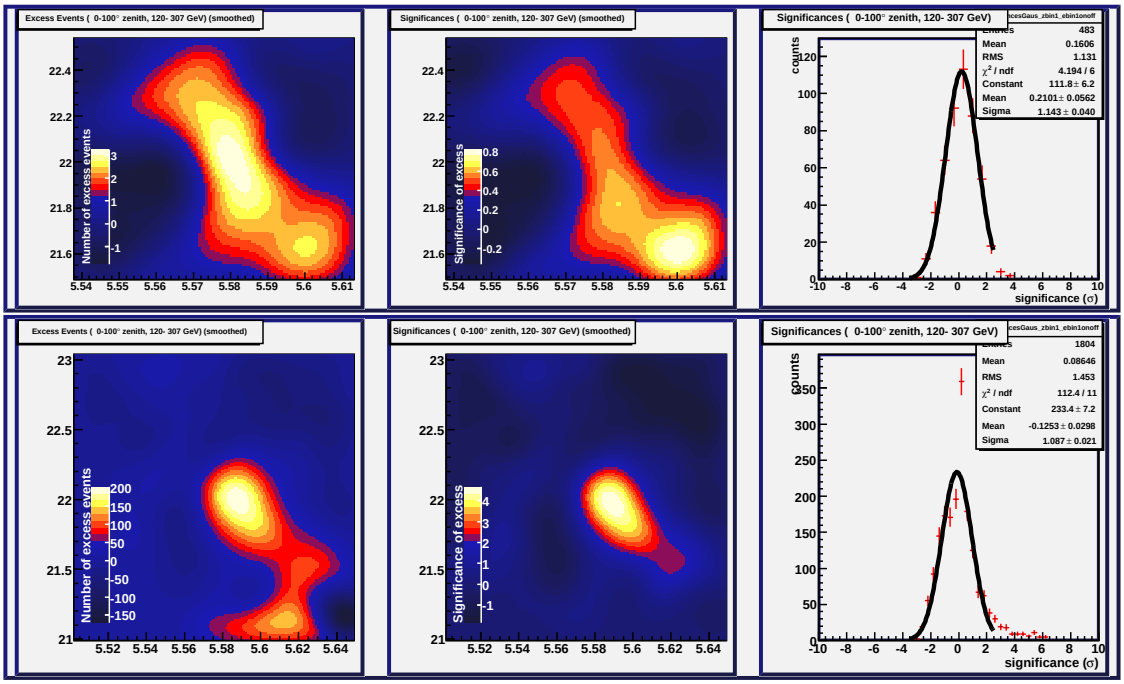

Figure 8.13: Skymap (upper plots) and false source plot (lower plots) for the *c–Crab* in the energy bin $120 - 300$ GeV using only the up–right quadrant of the camera (where the $\phi-$cut is located)

Skymaps of 3EG J1835

In figure 8.14, the FSPs for the 3EG J1835+5918 is shown for the three different energy bins used during all the analysis.

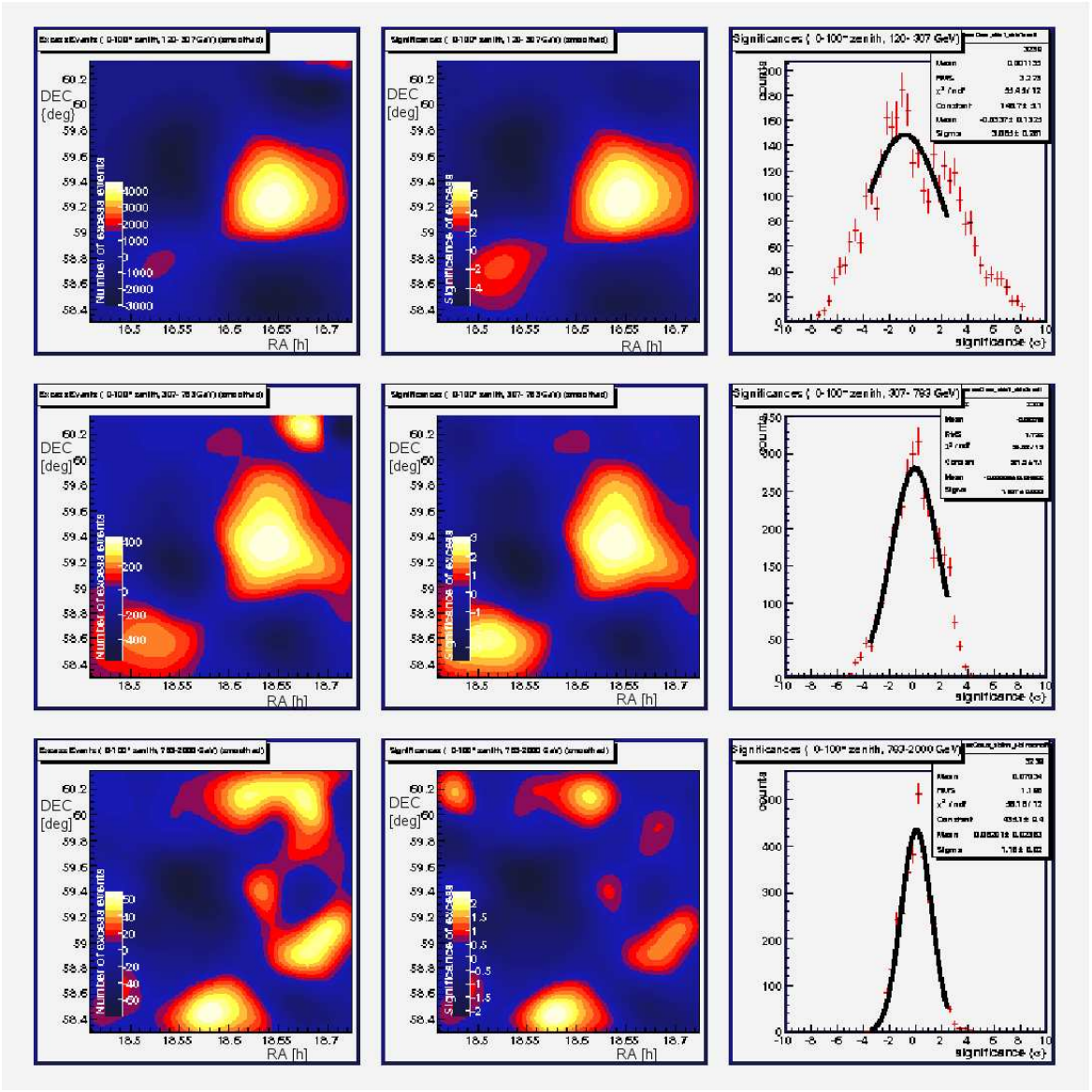

Figure 8.14: False Source plot for the 3EG J1835+5918 sample. From up to down, increasing energy bins. From left to right: excesses, significances and one-dimensional significance plot with a gaussian fit superimposed.

The presence of an apparent tail in the distribution of sensitivities, which normally could be related to the real existence of excesses in γ–rays, is due to the effect of the $\phi-$cut in the camera.

8.6 Estimation of upper limits

As no signal detection was reached, upper limits for the flux were calculated. The upper limits is obtained using the Rolke, Lopez and Conrad method [19], considering a 30% of systematic

errors. It is important to remember that the presented upper limits are also affected by another 20% of uncertainty on the absolute energy scale.

Upper limits on the differential flux f_0 were calculated with a test power–law spectrum of spectral index 1.5, and with an exponential cut-off. The tested break energies were 200 GeV and 800 GeV. The upper limits were calculated in the three energy bins used during all the analysis. In each energy bin, the four ZA bins were considered, since different ZA ranges have different effective collection areas. For each energy bin, the best upper limit estimation obtained from the four ZA bins was taken. The upper limits refer to the Time cleaning method:

- $E_{cut-off} = 200$ GeV:
  - $f_0|_{181\ \mathrm{GeV}} = 3.3 \times 10^{-10}$ ph cm^{-2} s^{-1} TeV^{-1} $\rightarrow$ 0.142 C.U.
  - $f_0|_{403\ \mathrm{GeV}} = 3.8 \times 10^{-12}$ ph cm^{-2} s^{-1} TeV^{-1} $\rightarrow$ 0.014 C.U.
  - $f_0|_{1196\ \mathrm{GeV}} = 1.9 \times 10^{-13}$ ph cm^{-2} s^{-1} TeV^{-1} $\rightarrow$ 0.011 C.U.
- $E_{cut-off} = 800$ GeV:
  - $f_0|_{181\ \mathrm{GeV}} = 3.1 \times 10^{-10}$ ph cm^{-2} s^{-1} TeV^{-1} $\rightarrow$ 0.138 C.U.
  - $f_0|_{403\ \mathrm{GeV}} = 3.6 \times 10^{-12}$ ph cm^{-2} s^{-1} TeV^{-1} $\rightarrow$ 0.013 C.U.
  - $f_0|_{1196\ \mathrm{GeV}} = 2.9 \times 10^{-13}$ ph cm^{-2} s^{-1} TeV^{-1} $\rightarrow$ 0.017 C.U.

where C.U. is the Crab Unit[2]. The energies 181, 403 and 1196 correspond to the mean energy for each energy bin ($120 - 300$ GeV, $300 - 700$ GeV and $700 - 10^4$ GeV, respectively) evaluated by the MC data.

8.6.1 Constrain on the DM mass.

The upper limits in the flux from 3EG J1835 can be used naïvely to estimate an upper limit in the DM mass of the particle. This calculation is here presented more as an exercise rather than a physical constraints because several are the hypothesis:

i) the first big assumption is that 3EG J1835 is an IMBH. There are not any experimental evidence on this,

ii) we take the EGRET estimation of the flux as true without propagating its error, and we naïvely extrapolate the flux at higher energies,

iii) we assume a simplified version of a neutralino with no contribution from internal bremmstrahlung and $b\bar{b}$ main annihilation branch.

In order to put constraints of the neutralino mass, the upper limits must be calculated on the integral flux above a certain energy $\bar{E}$:

$$\begin{aligned} f_0(>181\ \mathrm{GeV}) &= 2.9 \times 10^{-10}\ \text{ph cm}^{-2}\ \text{s}^{-1}\ \text{TeV}^{-1} &\rightarrow 0.129\ \text{C.U.} \\ f_0(>403\ \mathrm{GeV}) &= 3.3 \times 10^{-12}\ \text{ph cm}^{-2}\ \text{s}^{-1}\ \text{TeV}^{-1} &\rightarrow 0.012\ \text{C.U.} \\ f_0(>1196\ \mathrm{GeV}) &= 2.5 \times 10^{-13}\ \text{ph cm}^{-2}\ \text{s}^{-1}\ \text{TeV}^{-1} &\rightarrow 0.014\ \text{C.U.} \end{aligned}$$

In Figure 8.15, the upper limits are reported. On the same figure, a curve is drawn in correspondence of a neutralino mass of 800 GeV. A neutralino with larger mass would have crossed our estimation of upper limits and therefore would have been observed with MAGIC.

[2] 1C.U. $= 1.5 \times 10^{-3}\,(E/\mathrm{GeV})^{-2.58}$ph cm^{-2} s^{-1} TeV^{-1} .

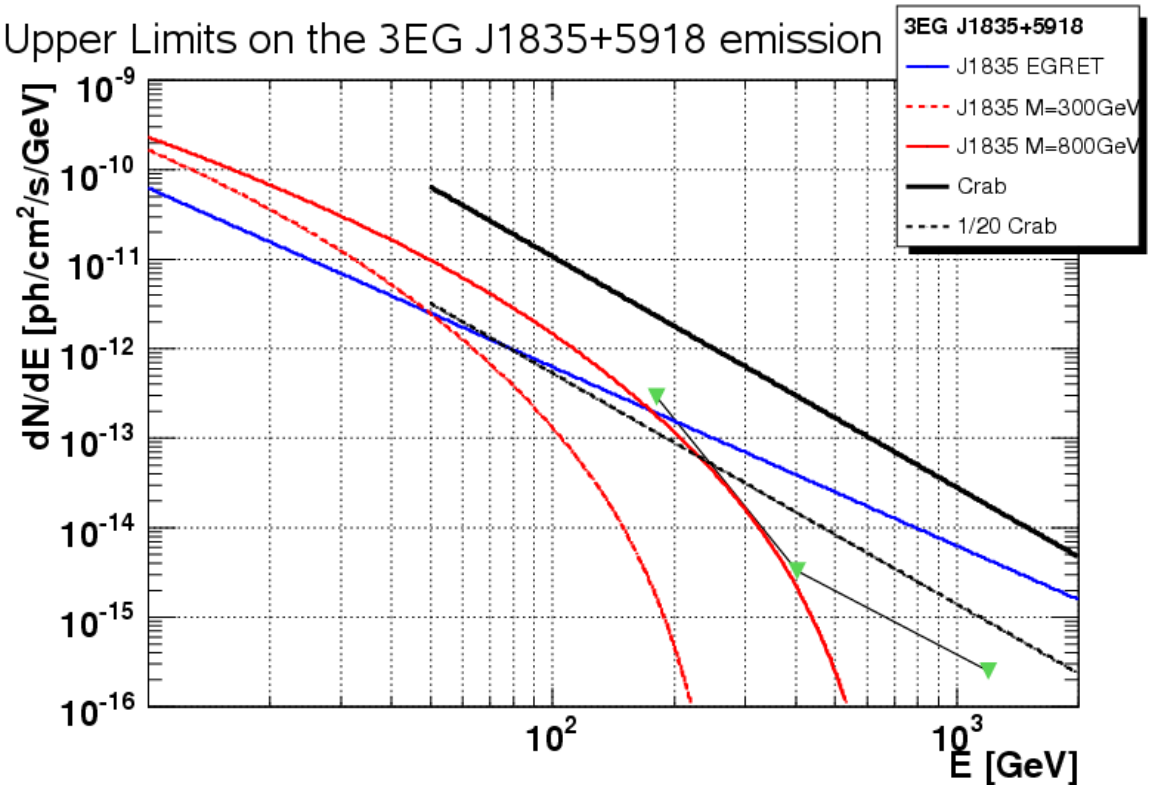

Figure 8.15: In the plot the upper limits (without any cut-off) are shown (green triangles) with the "limit spectrum" for a DM mass of about 800 GeV. In the plot, are also shown the Crab spectrum, the 1/20 of Crab spectrum, the extention of the EGRET given spectrum for the 3EG J1835+5918 and the spectrum in the case of a DM mass of about 300 GeV.

Therefore, under the naïve assumptions written above, we obtain an upper limit in the mass of the neutralino of:

$$m_\chi \precsim 800 \text{ GeV} . \tag{8.17}$$

8.7 Conclusions

Unfortunately, the 3EG J1835+5918 data sample was affected by several problems. The missing trigger determined a loss of about a 30% of the low energy events. The large inhomogeneities affecting the data sample below 300 GeV implied the determination of poor upper limits at these energies. The lack of OFF data reduced the sensitivity of the observation. The constrain of the DM neutralino mass is only an exercise and the intrinsic hypothesis prevent from making any physical constraint.

The source remains a interesting target for MAGIC, and in particular for MAGIC II. It is the brightest EGRET unidentified source and its existence only in γ–ray is intriguing. There are strong expectation or at least curiosities on the result that the Fermi–LAT satellite could bring upon this source. Until the release of a new spectrum and new flux measurement, there is no reason to observe the source again with IACTs, particularly in the context of DM searches.

References

[1] V. Beckmann. Ultra High Frequency Peaked BL Lac Objects. In *High Energy Blazar Astronomy ASP Conference Series*, volume 299, 2003.

[2] S. D. Bloom et al. An Optical Survey of the Position Error Contours of Unidentified High Energy Gamma-Ray Sources at Galactic Latitude b ¿—20— degrees. 2004.

[3] D. J. Champion, M. A. McLaughlin, and D. R. Lorimer. A survey for pulsars in EGRET error boxes. *Mon. Not. Roy. Astron. Soc.*, 364:1011–1014, 2005.

[4] S. Colafrancesco. First gamma-rays from galaxy clusters. Preliminary evidence of the association of galaxy clusters with EGRET unidentified gamma-ray sources. *Astron. Astrophys.*, 396:31–52, 2002.

[5] G. M. Doro, M. and F. Zandanel. Upper limits on the emission of 3EG J1835. MAGIG internal note. Not published., 2005.

[6] M. Doro. The commissioning and characterization of the calibration system of the magic telescope. Master's thesis, Universitá degli Studi di Padova – Institut de Física des Altes Energies de Barcelona, Padova, Italy, 2004. Diploma Thesis. Available at http://wwwmagic.mppmu.mpg.de/publications/theses.

[7] M. Doro et al. Dark Matter searches at intermediate mass black hole with the MAGIC telescope. In *Proc. of the 30th ICRC*, Merída, Mexico, 2007.

[8] J. Flix et al. Do the Unidentified EGRET Sources Trace Annihilating Dark Matter in the Local Group? 2004.

[9] M. Gaug. Calibration of the magic telescope and observation of gamma ray bursts. Master's thesis, Institut de Física des Altes Energies, Barcelona, Spain, 2006. Available at http://wwwmagic.mppmu.mpg.de/publications/theses.

[10] D. S. Gorbunov, P. G. Tinyakov, I. I. Tkachev, and S. V. Troitsky. Evidence for a connection between gamma-ray and highest- energy cosmic ray emissions by BL Lacs. *Astrophys. J.*, 577:L93, 2002.

[11] R. C. Hartman et al. The Third EGRET catalog of high-energy gamma-ray sources. *Astrophys. J. Suppl.*, 123:79, 1999.

[12] M. Khakian Ghomi, M. Bahmanabadi, and J. Samimi. Observation of EGRET gamma-ray sources by an extensive air shower experiment. 2004.

[13] S. Lombardi. Studio sistematico del fondo e del segnale nei dati dell'esperimento MAGIC con applicazione all'analisi della sorgente CRAB, 2006. Diploma Thesis.

[14] S. Lombardi. Development of new techniques for the selection and analysis of rare events in astroparticle physics experiments, 2007. PhD Thesis.

[15] J. R. Mattox, R. C. Hartman, and O. Reimer. A Quantitative evaluation of potential radio identifications for 3EG EGRET sources. *Astrophys. J. Suppl.*, 135:155–175, 2001.

[16] N. Mirabal and J. P. Halpern. A Neutron-Star Identification for the High-Energy Gamma- ray Source 3EG J1835+5918 Detected in the ROSAT All-Sky Survey. 2000.

[17] N. Mirabal, J. P. Halpern, M. Eracleous, and R. H. Becker. Search for the Identification of 3EG J1835+5918: Evidence for a New Type of High-Energy Gamma-ray Source. 2000.

[18] P. L. Nolan, W. F. Tompkins, I. A. Grenier, and P. F. Michelson. Variability of EGRET Gamma-Ray Sources. *Astrophys. J.*, 597:615–627, 2003.

[19] W. A. Rolke, A. M. Lopez, and J. Conrad. Limits and confidence intervals in the presence of nuisance parameters. *Nuclear Instruments and Methods in Physics Research Section A*, pages 493–503, 2005.

[20] D. Sowards-Emmerd, R. W. Romani, and P. F. Michelson. The Gamma-Ray Blazar Content of the Northern Sky. *Astrophys. J.*, 590:109–122, 2003.

[21] P. M. Wallace, S. D. Bloom, and M. S. Lewis. A Multiwavelength Investigation of Unidentified EGRET Sources. 2005.

[22] J.-H. Yang and J.-H. Fan. The correlation between gamma-ray and radio emissions in gamma-ray loud blazars. *Chin. J. Astron. Astrophys.*, 5:229–237, 2005.

[23] F. Zandanel. Dark Matter Search with the MAGIC Telescope: Analysis of the Unidentified EGRET Source 3EG J1835+5918, 2007. Diploma Thesis.

[24] S. Zhang, W. Collmar, W. Hermsen, and V. Schonfelder. Spectral constraints on unidentified EGRET gamma-ray sources from COMPTEL MeV observations. *Astron. Astrophys.*, 421:983–990, 2004.

9

Draco and Willman 1: Prospects for MAGIC II and CTA

The next generation of ground–based IACTs will play an important role in indirect DM searches. In this chapter, we consider two particularly promising candidate sources for DM annihilation signals, the nearby dwarf galaxies Draco and Willman 1, and study the prospects of detecting such a signal for the soon operating MAGIC II telescope system as well as for the planned installation of CTA, taking special care of describing the experimental features that affect the detectional prospects. For the first time in such studies, we fully take into account the effect of internal bremsstrahlung, which has recently been shown to considerably enhance, in some cases, the γ–ray flux in the high energies domain where IACTs operate, thus leading to significantly harder annihilation spectra than traditionally considered. While the detection of the spectral features introduced by internal bremsstrahlung would constitute a smoking gun signature for DM annihilation, we find that for most models the overall flux still remains at a level that will be challenging to detect, unless one adopts somewhat favorable descriptions of the smooth DM distribution in the dwarfs.

This chapter is adapted from *Dark Matter Signals from Draco and Willman 1: Prospects for MAGIC II and CTA*, JCAP 2009:01 (016) [18].

9.1 Introduction

The search for DM is a vast field where different experimental techniques can provide complementary information. At the Large Hadron Collider (LHC), the detection of new supersymmetric particles through missing energy signatures, would provide valuable information about the composition of the neutralino and its role as a DM candidate (see, e.g., [8, 6], and the discussion in Chapter 7). The neutralino could also be observed through nuclear recoils in direct detection experiments. A new generation of cryogenic detectors is aiming to improve the already impressive recent limits reported by Angle et al. [4] and Ahmed et al. [2], thereby probing significant regions of the parameter space. Finally, DM can be searched for through *indirect detection*, i.e. by looking for primary and secondary products (mainly gamma rays, neutrinos, positrons and anti-protons) of DM annihilation. Our attention will be focused on the detection of very–high–energy gamma rays. In this field, Imaging Air Cherenkov Telescopes (IACTs) play a leading role, exploring the possibility of tracing Cherenkov photons

from electromagnetic showers produced by gamma rays impinging on the Earth's atmosphere. Ground–based gamma ray astronomy has become a very active field in recent years and it has now reached a mature stage. In the near future, new installations with improved sensitivity will investigate those regions in the sky where DM signatures can be expected. In particular MAGIC II, already in the commissioning phase, will perform observations in the northern hemisphere, while a new generation of IACTs is currently in the design phase, the Cherenkov Telescope Array (CTA), where an array of several tens of telescopes will have an improved angular and energy resolutions, as well as a very low energy threshold and a much increased sensitivity.

In this chapter, we provide an update on the possible future of the indirect detection of DM with IACTs. In particular, we discuss the prospects for the detection of DM in dSphs with MAGIC II and make tentative predictions in view of the expected characteristics of CTA. We choose to focus on two dSphs, Draco and the recently discovered ultra–faint Willman 1. While the choice of Draco is supported by the large set of available data, Willman 1 will be discussed as a very promising target for future detection.

A key ingredient in estimating the gamma ray flux for IACTs is the computation of the energy spectrum for photons produced by neutralino annihilations. Bringmann et al. [17] have recently shown that internal bremsstrahlung (IB) provides an important, hitherto neglected, contribution to the spectrum. While the effect of IB is largely model dependent, it appears in general as an pronounced "bump" at energies close to the kinematic cutoff at the neutralino mass. The importance of this effect is two–fold: first, the flux at high energies, where IACTs are most sensitive, is significantly increased; secondly, the introduction of spectral features allows an easier discrimination of a DM source from potential astrophysical sources located in the vicinity, whose spectrum is usually a featureless power law. This is the first time that IB is fully included in studying prospects of DM detection for IACTs.

The chapter is organized as follows: in Section 9.2, we will review principal properties of Draco and Willman 1 and discuss how their DM profiles are constrained by observations. The following Section 9.3 is dedicated to a short description of the IACT technique, with particular attention on the features that are relevant for DM observations. In Section 9.4, we introduce a set of five benchmark neutralinos, representative for the relevant regions of the parameter space, and estimating the corresponding flux based on the technical specifications for MAGIC II and CTA. Results are discussed in Section 9.5, and in Section 9.6 we present our conclusions.

9.2 Phenomenology of Draco and Willman 1

9.2.1 Draco

Draco is located at a distance of 80 ± 7 kpc from the Earth [40] and it is one of the best known and most often studied dSph. Discovered by Wilson [58], the first estimation of its DM content was performed only 30 years later by Aaronson [1] from the analysis of its stellar velocity dispersion. Nowadays, a large set of data is available for Draco [49, 5, 43, 48, 55]. Even though the formation of the DM halo cannot be traced back with great precision, it can be inferred that the system is composed of very old, low–metallicity stars, without any significant sign of star formation in the last 2 Gyrs. Draco is in a privileged position relative to other dSphs, since it actually has fewer stars, which makes its kinematics more clearly determined. In addition, it does not show any active evidence of tidal disruption. The observed stellar distribution (that ranges from 50 pc to 1 kpc) and velocity dispersion can be used to infer the DM profile: The result of the fit (assuming a Navarro–Frenk–White profile,

hereafter NFW [41]) indicates a virial mass of the order of 10^9 $M_\odot$ [55], with a corresponding mass–to–light ratio of $M/L \gtrsim 200$ $M_\odot/L_\odot$ that characterizes Draco as highly DM dominated.

Many groups analysed the available data for Draco and modelized its DM profile [54, 34, 36, 39, 24, 46]. We are going to discuss here the two extreme cases of a *cusp* profile and a *core* profile[1], which span the range of possible configurations. For the former, we take the NFW profile,

$$\rho_{\,\mathrm{NFW}}\,(r) = \frac{\rho_s}{(r/r_s)\;(1+r/r_s)^2}, \tag{9.1}$$

and for the latter we take a Burkert [20, 45] profile,

$$\rho_{\,\mathrm{Burkert}}\,(r) = \frac{\rho_s}{(1+r/r_s)\;(1+(r/r_s)^2)}. \tag{9.2}$$

For the scale radius r_s and the scale density ρ_s, we use the values summarized in Table 9.1, taken from Mashchecnko et al. [39]. Note that both profiles produce good fits to the velocity dispersion profiles, down to the pc scales where the innermost stars are observed. No direct observational information is available for distances even closer to the centre, where the two profiles differ significantly.

Possible DM annihilation signals from Draco have already been searched for in the past: after the CACTUS experiment had claimed the detection of an excess of ~ 7000 very–high–energy photons in only 7 hours [23], almost all IACTs tried to reproduce the result, but the claim was not confirmed [26, 59]. MAGIC observed Draco for 7.8 hours during 2007 above 140 GeV [3]. Within a 2σ confidence limit, the collaboration reported an upper limit for the integral flux of $\Phi^{u.l.}(E > 140\ \mathrm{GeV}) < 1.1 \times 10^{-11}$ ph cm^{-2} s^{-1}.

9.2.2 Willman 1

Willman 1 (SDSS J1049+5103) is a very peculiar object, located at a distance of 38 ± 7 kpc from the Earth in the constellation of Ursa Major. Discovered in 2004 by B. Willman [56, 57], using data from the Sloan Digital Sky Survey [60], it was then further observed with Keck/DEIMOS [38] and more recently by Siegel et al. [50]. With an absolute magnitude of $M_V \sim -2.5$ and a half–light radius (i.e. the radius of a cylinder, pointing to the Earth, that encloses half of the luminosity of the object) of 21 ± 7 pc, it looks very similar to a globular cluster, even if its narrow distribution of stellar velocities and the large spread in stellar metallicities suggests that it is indeed the smallest dSph ever observed. The object may show evidence for tidal disruption from its tri-axial stellar distribution [57]. On the other hand, the difference in the stellar luminosity function between the central and outermost stars reveals a strong mass segregation. With a luminosity of 855 $L_\odot$, and a mass of the order of 5×10^5 $M_\odot$ [38], Willman 1 could feature a mass–to–light ratio in the range $500 - 700$ $M_\odot/L_\odot$, or even more, making it one of the most DM dominated objects in the Universe [52].

The small number of stars that belong to this dSph hinder, however, an accurate determination of the DM density profile. Following Strigari et al [52], we parametrize its DM halo with an NFW profile, as specified in Table 9.1, although these parameters are subject to somewhat larger uncertainties than in the case of Draco.

[1] It should be underlined that core profiles are not compatible with current CDM simulations: recent results predict DM halos well–fitted by an Einasto profile without converging to a precise value for the inner slope [51].

	Draco–Burkert	Draco–NFW	Willman 1–NFW
r_s (kpc)	0.35	0.50	0.18
ρ_s ($M_\odot$/kpc^3)	3.6×10^8	1.3×10^8	4.0×10^8
θ_{90} (°)	0.52°	0.35°	0.20°
D (kpc)		80 ± 7	38 ± 7

Table 9.1: Scale radius (kpc) and scale density ($M_\odot$/kpc^3) that appear in the DM density profiles. The NFW and the Burkert profiles in the case of Draco represent models N3 and B2, respectively, from Mashchenko et al [39]. In the case of Willman 1, the NFW fit is taken from Strigari et al [52]. In addition, the semiaperture of the solid angle corresponding to 90% of emission θ_{90} (°) is reported together with the target distance D (kpc).

9.3 Observation with IACTs: MAGIC II and CTA

In this paper, we will address observational prospects for the upcoming MAGIC II telescopes system and for the future generation of IACTs, focusing on the case of CTA. MAGIC II is a stereoscopic system of telescopes, composed of MAGIC and a second telescope currently under commissioning on the island of La Palma, which will start operation in 2009. The stereoscopic view of two telescopes (pioneered by HEGRA, [44]), together with the improved technical characteristics of the second detector, will allow a general improvement in the overall performance of the experiment, in particular in terms of energy and angular resolution, as well as energy threshold. The performance of the MAGIC II array were simulated with Monte Carlo (MC) tools by Carmona et al [21]. CTA, on the other hand, is the result of an effort for a next generation Cherenkov observatory with increased capabilities: normally, one single telescope can cover 1.5–2 orders of magnitude in energy range. With the combined use of many telescopes of 2–3 different sizes, CTA should be able to extend the energy range to almost 4 orders of magnitude, from roughly ~ 30 GeV to ~ 100 TeV. The experiment is still in the early design phase and the final layout of the array is thus far from defined yet; the performance, therefore, is still subject to changes. For this paper, we will refer mainly to the work of Bernlöher et al [13] and several private communications within the collaboration. The CTA prototype construction could start in 2010, at least for some of the main components, and the final installation is foreseen in 2012–15.

The performance of an IACT in terms of its prospects to detect a DM annihilation signal can generally be characterized by a small number of basic parameters, which are described in the following (see also Table 9.2 for a compilation of characteristics for MAGIC II and CTA):

- *Energy threshold:* The energy threshold of an IACT can take slightly different values according to the definition. Hereafter we consider it to be the peak of the reconstructed MC energy distribution (other definitions being analysis threshold, trigger threshold, etc.). This value depends mainly on the reflector area of the telescope: A larger mirror area allows, in particular, to collect more photons from the showers and thus increases the chance of discrimination against the night sky background light, in particular for low energy showers. The use of a stereoscopic system also plays an important role because it enhances the gamma/hadron (g/h) discrimination power which is weaker at low energy. The energy threshold changes with the zenith angle of observation, and sources culminating high in the sky are preferred. Reaching a low energy threshold is an important feature for DM studies with IACTs, both because of the increased number of photons and because of the enhanced possibility to observe the spectral cutoff even for low-mass neutralinos. Making use of stereoscopic observations, MAGIC II will have an energy threshold of 60-70 GeV [21], with possible extension to even lower energies with

improved analysis techniques and new trigger systems currently under development [47]. This value will be further lowered to at least 30 GeV for CTA. The telescope acceptance for gamma rays around 30 GeV starts to decrease rapidly, but a very strong gamma ray signal could probably even be detected at an energy as low as about 10 GeV.

- *Energy resolution:* The true energy of the primary gamma ray E' is reconstructed on the basis of a comparing analysis between the shower image parameters and MC events. The probability to assign, after the analysis, an energy E to the primary gamma ray can be approximated by

$$R_\epsilon(E - E') \approx \frac{1}{\sqrt{2\pi}E} \cdot \exp\left(-\frac{(E - E')^2}{2\epsilon^2 E^2}\right). \tag{9.3}$$

  Typical values for the energy resolution ϵ are of the order of 10-30% for IACTs, depending on the energy. The reason for such large uncertainties is the combined effect of many sources of uncertainties (for a more detailed discussion, refer to [3]). The energy resolution is an important parameter when observing spectral features as bumps and cutoffs that can provide clear signatures for a DM signal. MAGIC II will have an energy resolution of 15% above 300 GeV (up to 20% at 70 GeV). The situation could radically improve for CTA. Finally, let us note that further systematic errors might hide in the absolute energy calibration; the recent MAGIC observation of a clear cutoff in the Crab Nebula spectrum[2], when compared with a corresponding future observation by Fermi-LAT [28], may allow for the first robust calibration of gamma ray energies [15].

- *Angular resolution:* The reconstruction of the direction of a primary gamma ray is performed through image analysis. As a result, a gamma ray coming from a direction ψ' will be reconstructed to a direction ψ in the sky with a probability distribution that can be fitted to a Gaussian function:

$$B_{\vartheta_r}(\psi' - \psi) = \frac{1}{2\pi\vartheta_r^2} \cdot \exp\left(-\frac{(\psi' - \psi)^2}{2\,\vartheta_r^2}\right). \tag{9.4}$$

  The standard deviation ϑ_r of the Gaussian corresponds to the telescope angular resolution, also called Point Spread Function (PSF). As a consequence, any source will appear somewhat blurred. The stereoscopic system exploited in MAGIC II will improve the PSF, allowing values as low as 0.05°, while for CTA we expect an even smaller PSF. It is hard to predict an exact value given the current lack of knowledge of the CTA design, but a realistic value that we use for this study is 0.02° (see also [32]). For extended sources, as in the case of dSphs, the PSF plays an important role in the reconstruction of the DM density profile, as discussed in the next section.

- *Flux sensitivity:* The sensitivity of an IACT is usually defined as *the minimum flux for a $5\,\sigma$ detection over the background, after 50 hours of observation time and based on at least 10 collected photons.* For operating experiments, the sensitivity can be computed by using real data and following Equation (17) of Li & Ma [35], while for planned experiments the sensitivity has to be estimated on the basis of MC simulations and is therefore subject to larger uncertainties. The procedure is as follows: a full data

[2]The Crab Nebula is a supernova remnant that is conventionally taken as reference source for cross–calibrations in gamma ray astronomy due to its very stable and intense flux.

	MAGIC	MAGIC II	CTA*
E_0 (GeV)	100	70	30
ϵ	30-20%	20-10%	10%
ϑ_r (°)	0.10°	0.05°	0.02°
S($> E_0$) (cm^{-2} s^{-1})	5×10^{-11}	1.4×10^{-11}	1.5×10^{-11}

Table 9.2: Comparison of the performance of the MAGIC, MAGIC II and CTA* telescopes. E_0 (GeV) is the energy threshold, ϵ the energy resolution and ϑ_r(°) the angular resolution. The sensitivity S($> E_0$) (cm^{-2} s^{-1}) is given for a Crab-like spectrum above the energy threshold.
*For CTA, the numbers have to be taken as placeholders because the telescope design is not yet fixed.

analysis is performed on two samples of MC simulations, one for gamma ray events and one for background events (basically protons and helium), during which a number of parameters ("cuts") is optimized to maximize the analysis quality factor $Q = \epsilon_\gamma/\sqrt{\epsilon_h}$, i.e. the ratio between the efficiency for gamma rays and the square root of the hadron efficiency ("efficiency" refering here to the ratio between the number of events passing the analysis cuts and the number of events at MC, input, level). After the optimization, one can estimate the number of hadrons $N_h(> E)$ above some energy E. Given the Poissonian distribution of events, a $5\,\sigma$ detection is obtained whenever the number of gamma rays detected is larger than $5\,\sqrt{N_h\,(> E)}$. The integrated sensitivity above E is thus given by:

$$\Phi^{min}(> E) = \frac{5\sqrt{N_h\,(> E)}}{A \cdot t_{50}} \frac{1}{\epsilon_\gamma}\,, \tag{9.5}$$

where A is the MC gamma ray simulation area and t_{50} is the time interval corresponding to 50 hours.

$N_h(> E)$ and ϵ_γ, and thus the sensitivity, are usually determined assuming a featureless power law spectrum of MC gamma ray events of index -2.6. This corresponds approximately to the spectrum of the Crab. For this reason, the sensitivity is often also expressed in terms of "Crab" units (C.U). In the case of the benchmark neutralinos under study (see next section), the gamma ray spectra are usually harder than that of the Crab and no longer featureless; it is therefore natural to ask how much this would change the sensitivity.

To address this question, let us note that the sensitivity mainly depends on the g/h discrimination power. The g/h separation, however, is very efficient at intermediate and large energies, where the shower parameters are firmly distinguishable between hadronic and gamma events. At energies below $\sim$ 30 GeV, on the other hand, the differences are more subtle and the sensitivity *is* affected. Hence we expect that the differential sensitivity does not depend too strongly on the spectrum of the source, unless in the case of rather low energies. An exact treatment of this effect would require dedicated studies with MC simulations, which is beyond the aim of this work. Based on a preliminary MC analysis, however, we generally expect that the sensitivity at a given energy will not change by more than a factor of two compared to that defined for the Crab. A full analysis of this effect is left for future work.

9.4 Flux estimation

The gamma ray flux from DM annihilation can be factorized into two different contributions:

$$\frac{d\,\Phi}{dE} = J(\psi) \cdot \frac{d\,\Phi^{PP}}{dE}\,. \tag{9.6}$$

The term $J(\psi)$, also called the *astrophysical factor*, depends on the DM morphology at the emission region. The *particle physics factor* $d\,\Phi^{PP}/dE$, on the other hand, depends on the microscopic properties of the DM candidate, in particular its mass and cross section, as well as the annihilation modes and branching ratios, that define the gamma ray spectrum. For a given telescope energy threshold E_0, the integral flux is thus $\Phi(>E_0) = J \cdot \Phi^{PP}(>E_0)$.

The ability to reconstruct the two factors depends on the experimental performance of the IACT; in the following, we will estimate the expected flux for Draco and Willman 1.

9.4.1 Astrophysical Factor

The astrophysical factor depends on the source distance and geometry (as well as the PSF of the telescope), but for a given DM profile it does not depend on the particular DM candidate. As a consequence, the discussion here remains valid for any generic WIMP candidate. Pointing the telescope towards a direction ψ in the sky, and taking into account its finite angular resolution, the astrophysical factor is given by:

$$J(\psi) = \frac{1}{4\pi} \int d\Omega \int d\lambda \;\left[\rho^2(r(\lambda,\psi)) \cdot B_{\vartheta_r}(\theta)\right]\,, \tag{9.7}$$

where the angular integration $d\Omega = d\varphi\, d(\cos\theta)$ extends over a cone centered around ψ, with an opening angle a few times the PSF ϑ_r. The integration over λ is along the line-of-sight, in the direction ψ, such that $r = \sqrt{\lambda^2 + D^2 - 2D\lambda\cos(\Psi)}$, where D is the distance of the source from the Sun and $\cos(\Psi) \equiv \cos(\theta)\cos(\psi) - \cos(\varphi)\sin(\theta)\sin(\psi)$. Defined as above, $J(\psi)$ is conventionally expressed in units of $\mathrm{M}_\odot^2\,\mathrm{kpc}^{-5}\,\mathrm{sr}^{-1}$ or $\mathrm{GeV}^2\,\mathrm{cm}^{-5}\,\mathrm{sr}^{-1}$. In order to translate it to the dimensionless quantity $J(\psi)$ as defined in Bergström [12], one simply has to multiply it by $5.32 \times 10^{-21}\,\mathrm{GeV}^{-2}\mathrm{cm}^5\mathrm{sr}$ ($= 2.37 \times 10^{-14}\,{\mathrm{M}_\odot}^{-2}\mathrm{kpc}^5\mathrm{sr}$).

Integrating Eq. 9.7 over the full angular extension of the source gives:

$$\widetilde{J} \equiv \int d\Omega_\psi\, J(\psi) \simeq \frac{1}{4\pi D^2} \int dV\; \rho^2(r)\,, \tag{9.8}$$

where the second integral is over the *spatial* extent of the source. Note that this expression is now given in units $\mathrm{M}_\odot^2\,\mathrm{kpc}^{-5}$ (or $\mathrm{GeV}^2\,\mathrm{cm}^{-5}$) and no longer depends on the telescope PSF.

Using the DM profile parameters of Table 9.1, we now show in Figure 9.1 the quantitity $J(\psi)$ for Draco and Willman 1. While the two sources, from this plot, appear similar in terms of their angular size ψ, we recall that their spatial extension is quite different: By comparing, e.g., their respective scale radii for an NFW profile, one sees that Willman 1 ($r_s = 0.18$ kpc) is considerably smaller than Draco ($r_s = 0.50$ kpc). In the case of Draco, the cusp and core profiles are almost identical (up to an overall normalization factor of ~ 2) for angular distances larger than about $\psi \sim 0.3^\circ$, below which the cusp profile starts to increase more rapidly. At the center, the two profiles differ by around one order of magnitude, the difference increasing with decreasing PSF. Whenever an extended emission would be observed, one could thus in principle be able to discriminate between different profiles by comparing the flux at different distances from the center. As it becomes obvious from Figure 9.1, and as already stressed by Sanchez–Conde et al [46], the angular resolution of the telescope would play an important

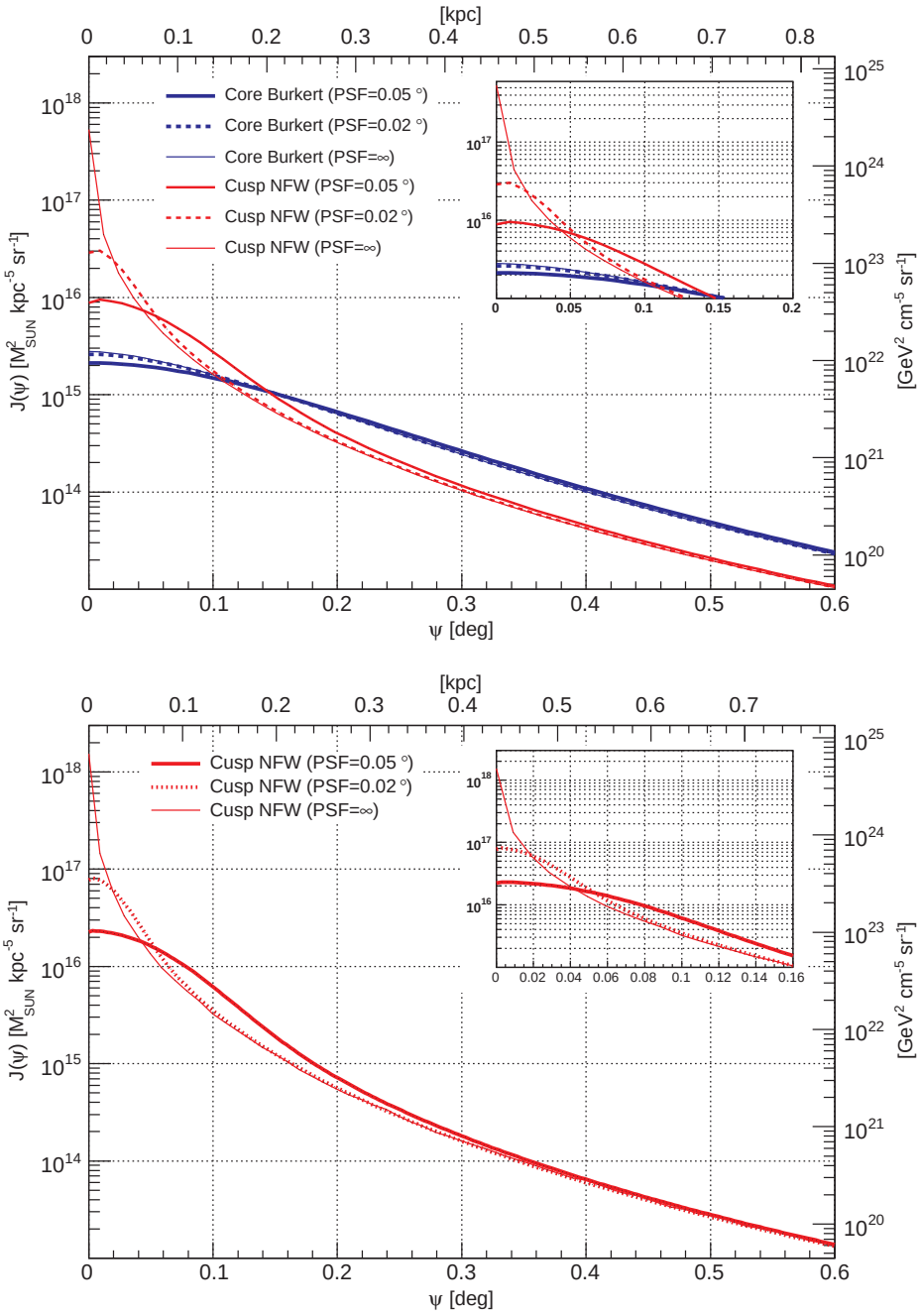

Figure 9.1: The $J(\psi)$ factor in the case of Draco (upper plot) and Willman 1 (lower plot). Core profiles are shown in black, cusp profiles in red. Solid lines represent profiles smeared with the MAGIC II angular resolution while dashed lines with the CTA expected angular resolution. The upper right panel in each figure shows a zoom-in of the region close to the center.

role. Taking into account the full range of profiles consistent with the observational data [52], we note that the astrophysical factor for dSphs is far better constrained than for, e.g., the galactic center, where the uncertainty in the inner part spans several orders of magnitude [27].

Given a telescope PSF of the order of 0.1°, and the expected feableness of the signal, however, the capability of reconstructing the morphology of extended sources is limited. This

$\widetilde{J}$	Draco–Burkert	Draco–NFW	Willman 1–NFW
$(\mathrm{GeV}^2/\mathrm{cm}^5)$	3.84×10^{17}	4.71×10^{17}	9.55×10^{17}
$(\mathrm{M}_\odot/\mathrm{kpc}^5)$	8.63×10^{10}	1.06×10^{11}	2.15×10^{11}

Table 9.3: Comparison of the integrated astrophysical factor $\widetilde{J}$ for Draco and Willman 1, for the profiles specified in Table 9.1.

is particularly true in the case of non-stereo IACTs where the shower direction is reconstructed with less precision. Even when making the rather optimistic assumption that a signal could be discriminated against the background out to a distance where the annihilation flux is a factor of 3 less than from the direction towards the center, the source would appear at a size of only roughly twice the PSF for both Draco and Willman 1, in the case of a cuspy profile. For a core profile, the same measure would indicate an apparent extension out to $\lesssim 0.2^\circ$, still well contained in a normal IACT camera ($\sim 3^\circ$ aperture). As we will see, the expected annihilation fluxes are rather low and we find it therefore premature to discuss in depth the possibilities to distinguish between different profiles in the way indicated above; rather, we will in the following focus on the total, i.e. integrated, flux.

Table 9.3 reports the calculation of the *integrated* astrophysical factor $\widetilde{J}$ for the two dSphs studied here. For Willman 1, the uncertainty in the DM profile translates into a 95% confidence interval of about $8 \times 10^{17}\,\mathrm{GeV}^2/\mathrm{cm}^5 \lesssim \widetilde{J} \lesssim 4 \times 10^{19}\,\mathrm{GeV}^2/\mathrm{cm}^5$ [52]. In the case of Draco, the astrophysical factor lies in the range $10^{17}\,\mathrm{GeV}^2/\mathrm{cm}^5 \lesssim \widetilde{J} \lesssim 2 \times 10^{18}\,\mathrm{GeV}^2/\mathrm{cm}^5$ [53]. Again, these astrophysical uncertainties are rather small when compared to other potential sources of DM annihilation signals – but one should keep in mind that our choices of DM profiles are actually quite conservative: taking into account the above quoted range of possible values for $\widetilde{J}$ that are consistent with current observations of velocity dispersions in the dwarfs, one could thus win a factor of up to about 4 (in the case of Draco) or 40 (in the case of Willman 1) in the annihilation flux.

9.4.2 Particle Physics factor and Benchmarks

The particle physics factor in Eq. 9.6 is given by:

$$\frac{d\Phi^{PP}}{dE} = \frac{\langle\sigma v\rangle}{2m_\chi^2} \cdot \sum_i B^i \int dE' \frac{dN_\gamma^i(E')}{dE'} R_\epsilon(E - E')\,, \tag{9.9}$$

where $\langle\sigma v\rangle$ is the total annihilation rate of the DM particles, m_χ the mass of the DM particle, B_i the branching ratio into channel i and dN_γ^i/dE the corresponding differential number of photons per (total) annihilation. The integration over $R_\epsilon(E - E')$ (see Eq. 9.3), takes into account the finite energy resolution of the instrument. The *total* number of photons above some energy E_0 of course no longer depends on the energy resolution (as long as $1 - E_0/M_\chi \gg \epsilon$) and is given by:

$$N_\gamma(> E_0) \simeq \sum_i B^i \int_{E_0}^{m_\chi} \frac{dN_\gamma^i(E)}{dE}\, dE\,. \tag{9.10}$$

Three different contributions to the spectrum can, in general, be distinguished: first of all *monochromatic γ lines*, where photons are primary products of neutralino annihilations through the reactions $\chi\chi \to \gamma\gamma$ and $\chi\chi \to \gamma Z^0$ [12]. These processes are very model-dependent; while providing a striking experimental signature, they are usually subdominant (for a recent analysis, see [17]). As a further contribution, *secondary photons* are produced

BM	$m_{1/2}$	m_0	$\tan\beta$	A_0	s(μ)	m_χ	$\Omega_\chi h^2$	$\langle\sigma v\rangle\vert_{v=0}$
I'	350	181	35.0	0	+	141	0.12	$3.6\cdot10^{-27}$
J'	750	299	35.0	0	+	316	0.11	$3.2\cdot10^{-28}$
K'	1300	1001	46.0	0	−	565	0.09	$2.6\cdot10^{-26}$
F^*	7792	22100	24.0	17.7	+	1926	0.11	$2.6\cdot10^{-27}$
J^*	576	108	3.8	28.3	+	233	0.08	$9.2\cdot10^{-29}$

BM	r	$2\cdot\sigma v\vert_{\gamma\gamma}$	$\sigma v\vert_{Z\gamma}$	$\Phi^{PP}_{>70\ GeV}$	$\Phi^{PP}_{>30\ GeV}$
I'	4	$7.9\cdot10^{-30}$	$8.5\cdot10^{-31}$	$1.6\cdot10^{-33}$	$9.9\cdot10^{-33}$
J'	34	$3.4\cdot10^{-30}$	$4.1\cdot10^{-31}$	$2.2\cdot10^{-34}$	$1.1\cdot10^{-33}$
K'	<0.1	$1.8\cdot10^{-31}$	$2.2\cdot10^{-32}$	$1.5\cdot10^{-32}$	$7.5\cdot10^{-32}$
F^*	11	$5.8\cdot10^{-30}$	$1.6\cdot10^{-29}$	$9.6\cdot10^{-34}$	$2.4\cdot10^{-33}$
J^*	2300	$5.5\cdot10^{-30}$	$1.8\cdot10^{-30}$	$7.9\cdot10^{-34}$	$8.9\cdot10^{-34}$

Table 9.4: Parameters defining the benchmark models and some relevant quantities related to the annihilation spectrum. $m_{1/2}$ and m_0 (expressed in GeV) are the uniform masses of gauginos and scalars, respectively. $\tan\beta$ is the ratio between the vacuum expectation values of the two Higgs bosons. A_0 (in GeV) is the coefficent of the trilinear scalar term and μ is the coefficent of the mass term in the Higgs potential. m_χ (in GeV) is the neutralino mass, $\Omega_\chi h^2$ its relic density and $\langle\sigma v\rangle\vert_{v=0}$ (expressed in cm^3 s^{-1}) its annihilation rate today. r is the ratio of IB photons over secondary photons (above $0.6\,m_\chi$) and $\sigma v\vert_{\gamma\gamma}$, $\sigma v\vert_{Z\gamma}$ are the annihilation rates for the γ lines. Φ^{PP} (expressed in cm^3 s^{-1} GeV^{-2}), finally, is defined in Eq. 9.9 and given for MAGIC II ($E_0 = 70$ GeV) and CTA ($E_0 = 30$ GeV) energy thresholds, respectively.

in the hadronization and further decay of the primary annihilation products, mainly through the decay of neutral pions, resulting in a featureless spectrum with a power law like behaviour at small photon energies and a rather soft cutoff at m_χ. These contributions, which always dominate the total spectrum at low energies, are highly model-independent and have a spectral shape that is almost indistinguishable for the various possible annihilation channels (see, e.g. [14, 27]).

For charged annihilation products, a third contribution has to be included; *internal bremsstrahlung*, where an additional photon appears in the final state. As it has been pointed out recently [17], these photons generically dominate the total spectrum at energies close to the kinematical cutoff at m_χ. Moreover, they add pronounced signatures to the spectrum that would allow for a clear identification of the DM origin of an observed source; viz. a very sharp cutoff at m_χ and bump-like features at slightly smaller energies. While photons directly radiated from charged final states give rise to a rather model-independent contribution [16], photons radiated from charged virtual particles strongly depend on the details of the underlying DM model.

As anticipated in the introduction, for what concerns the particle physics content, we will restrict ourselves to supersymmetric DM. While the Minimal Supersymmetric Standard Model (MSSM) needs more than 100 parameters for its full characterization, in the following we will only consider a constrained version, minimal supergravity (mSUGRA [22]), where gravity is supposed to mediate SUSY breaking and the number of parameters is reduced to 4 plus a choice of sign after certain commonly adopted, physically well-motivated assumptions such as neglecting CP violating or flavour-changing-neutral-current interactions and imposing the grand unification theory (GUT) condition for the gauge couplings, $\mathrm{M}_1 = 5/3\tan^2\theta_w\mathrm{M}_2 \approx 0.5\ \mathrm{M}_2$. The parameters defining a mSUGRA model are: universal

masses for gauginos ($m_{1/2}$) and scalars (m_0), a common trilinear coupling term A_0 in the SUSY breaking part of the Lagrangian, the ratio $\tan\beta$ of the vacuum expectation values of the two Higgs bosons and the sign for the coefficient μ of the mass term in the Higgs potential. By solving the renormalization group equations, these parameters, defined at the GUT scale, can be translated into masses and couplings at observable, i.e. low, energies.

Even if highly constrained, these models permit a rich phenomenology. From a cosmological point of view, one can single out five regions of the underlying parameter space that are particularly interesting as they correspond to models with a neutralino relic density in accordance with the value measured by WMAP: the *bulk region* at low m_0 and $m_{1/2}$, where the mass spectrum contains light sleptons $\widetilde{\ell}$ and, as a consequence, the relic density is mainly determined by annihilation processes $\chi\chi \to \ell^+\ell^-$ in the early universe (through a t-channel exchange of $\widetilde{\ell}$); the *funnel region* at intermediate values for m_0 and $m_{1/2}$, where $m_A \approx 2m_\chi$ and annihilations in the early universe are thus enhanced by the presence of the near-resonant pseudoscalar Higgs boson; the hyperbolic branch or *focus point region*, where $m_0 \gg m_{1/2}$ and the neutralino becomes an almost pure Higgsino, with large annihilation rates into gauge bosons; the *stau coannihilation region* at large $m_{1/2}$ but small m_0, where $m_\chi \approx m_{\widetilde{\tau}}$ and coannihilations with staus (and usually other sleptons as well) are important in determining the relic density; and finally the *stop coannihilation region* (arising when $A_0 \neq 0$) where $m_\chi \approx m_{\widetilde{t}}$.

In what follows, we choose to work with a set of benchmark models, representative of the different regions in parameter space described above. From an experimental point of view, the advantage of benchmark models is that they allow a direct comparison between data from different experiments (most of the benchmarks that we use have already been extensively studied in other contexts) and, in general, a more detailed *per case* analysis than for, e.g., parameter scans. Our particular choice of benchmark models is summarized in Table 9.4.

The features of these models that are important in our context are the following:

- I': This model (like the following two) was introduced by Battaglia et al [7], where also phenomenolgy at colliders was extensively studied. It is a typical example of a model in the *bulk region*. While the annihilation into lepton pairs is strongly suppressed for neutralinos with the small velocities they exhibit today (unlike in the early universe), annihilation into $\ell^+\ell^-\gamma$, which does not suffer from helicity suppression [9], gives a considerable contribution due to the lightness of the sleptons.

- J': This model lies in the *coannihilation tail*. The sleptons being close to degenerate with the neutralino, IB from lepton final states gives even higher enhancement of the flux than in the previous case.

- K': A representative model for the *funnel region*, where the annihilation dominantly occurs through an s-channel pseudoscalar Higgs boson. Consequently, the additional emission of a photon does not lift the helicity suppression in this case and therefore IB contributions have to be subdominant.

- F^*: Introduced by Bringmann et al [17] as BM4, this model exhibits a large neutralino mass, as typical in the *focus point* region. In this regime, the chargino is close to degenerate with the neutralino (in this case an almost pure Higgsino) and large IB contributions result from charged gauge boson final states [10].

- J^*: Introduced by Bringmann et al [17] as BM3, this is another example of a neutralino in the co-annihilation region, characterized by a particularly large IB contribution.

We used DS[3], which in its most recent public release 5.0.1 [29], contains a full implementation of the IB contributions focused on here, to compute the annihilation spectra for the benchmark models defined above. Line signals are also taken into account, but they turn out to be completely subdominant in the cases studied here (except for model F^*). The resulting spectra are plotted in Figure 9.2, both before taking into account the finite energy resolution of the detector and for the case of an energy resolution of 10%. The main characteristics of these spectra are also summarized in Table 9.4.

9.5 Results and Discussion

	Draco-NFW			
	MAGIC II		CTA_{30}	
I'	0.75	$(1.9{\cdot}10^4, 1.3{\cdot}10^4, \mathbf{2900})$	4.7	$(3100, 2100, \mathbf{490})$
J'	0.10	$(1.4{\cdot}10^5, 3.2{\cdot}10^4, \mathbf{7600})$	0.52	$(2.8{\cdot}10^4, 4900, \mathbf{1200})$
K'	7.0	$(2000, 2000, \mathbf{470})$	35	$(410, 260, \mathbf{61})$
F^*	0.45	$(3.1{\cdot}10^4, 1.6{\cdot}10^4, \mathbf{3800})$	1.1	$(1.3{\cdot}10^4, 2800, \mathbf{670})$
J^*	0.37	$(3.8{\cdot}10^4, 7400, \mathbf{1700})$	0.42	$(3.4{\cdot}10^4, 1200, \mathbf{290})$

	Willman 1			
	MAGIC II		CTA_{30}	
I'	1.5	$(9200, 6200, \mathbf{150})$	9.4	$(1500, 1000, \mathbf{25})$
J'	0.21	$(6.9{\cdot}10^4, 1.6{\cdot}10^4, \mathbf{380})$	1.1	$(1.4{\cdot}10^4, 2400, \mathbf{58})$
K'	14	$(990, 990, \mathbf{24})$	71	$(200, 130, \mathbf{3})$
F^*	0.92	$(1.5{\cdot}10^4, 8100, \mathbf{190})$	2.2	$(6500, 1400, \mathbf{34})$
J^*	0.76	$(1.9{\cdot}10^4, 3700, \mathbf{88})$	0.85	$(1.7{\cdot}10^4, 610, \mathbf{15})$

Table 9.5: Expected integrated flux $\Phi(E > E_0)$ for our neutralino benchmark models (in units of 10^{-15} ph cm^{-2} s^{-1}), where we used the experimental parameters listed in Table 9.2. In parentheses, we state the boosts in the signal that would be needed for a 5σ detection as (B1,$B2$,**B3**). Here, B1 is the often cited boost factor that is obtained by simply comparing the sensitivity and annihilation fluxes above the telescope energy threshold E_0. $B2$ is more realistic in that it gives the corresponding quantity *above a certain energy E^*, depending on the benchmark, where the integrated flux to sensitivity ratio is greatest* and **B3** is the same as $B2$, yet for the most favourable halo profile consistent with current observations (still not taking into account the effect of substructures, however). See text for further details.

Combining the astrophysical factor of Table 9.3 and the particle physics factor from Table 9.4, we can finally make predictions about the expected gamma ray flux above the telescope energy threshold E_0. A summary of the results is reported in Table 9.5, where we also quote the boost in the flux that would be necessary to meet the required sensitivity for a 5σ detection (referred to as B1 in the table). While it is customary to quote sensitivities

[3]For the calculation of the low-energy features of these models (i.e. mass spectra etc.), we use version 4.01 of DS[30] that relies on the public code **Isajet 7.69** [42]. One should be aware, however, that these calculations are highly sensitive to how the renormalization group equations are implemented and different codes, or even different versions of the same code, may give rather different results (see, e.g., Battaglia et al.,2001;2004b). Typically, the *qualitative* low-energy features of a given model can still easily be reconstructed by allowing for slight shifts in the parameter space (defined at high energies). From a practical point of view, this situation therefore does not constitute a severe problem as one may always regard a set of low-energy quantities like the mass spectrum, annihilation cross section and branching ratios as a valid *effective* definition of the model.

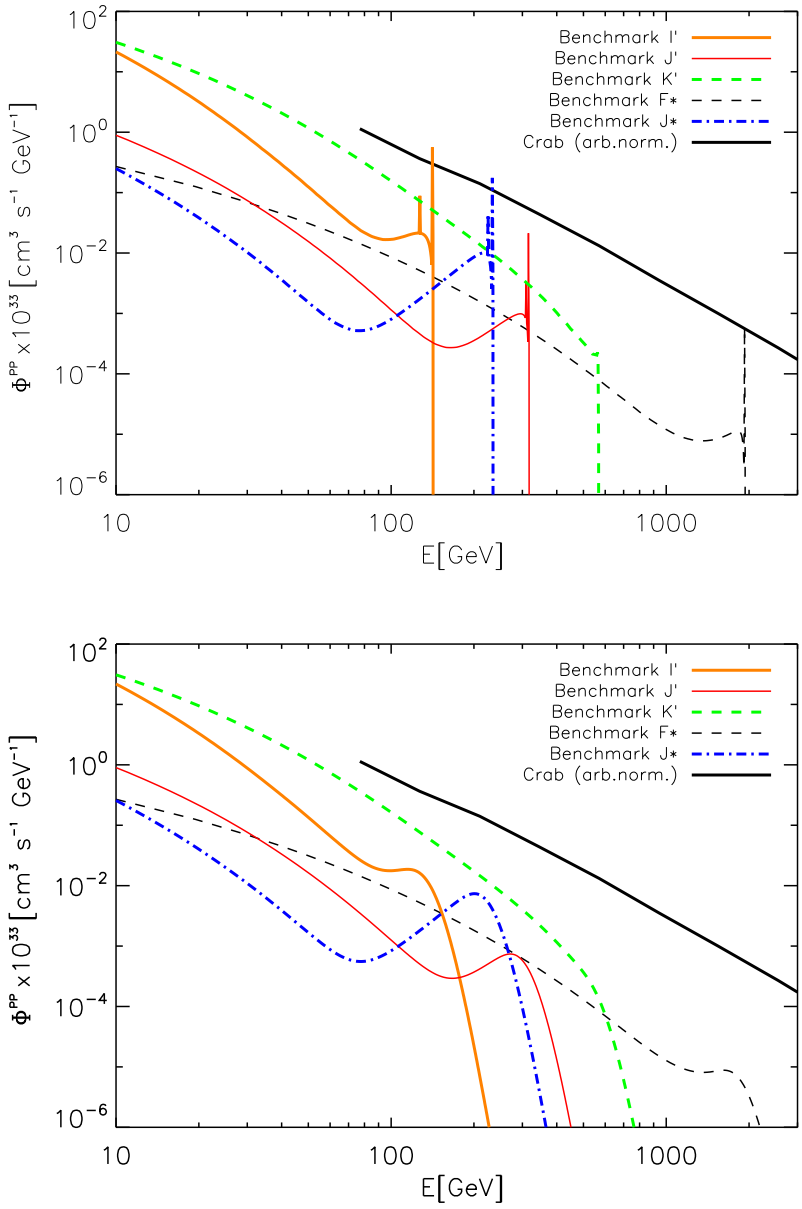

Figure 9.2: The particle physics factor $d\Phi^{PP}/dE$, as defined in Eq. 9.9, for the benchmarks models introduced in Section 9.4.2. The upper panel shows the case of a hypothetical detector with perfect energy resolution, and a line width of $\epsilon \sim v \sim 10^{-3}$, while the lower case shows the more realistic example of $\epsilon = 10\%$. For comparison, we also show the spectrum of the Crab Nebula, taken from Albert et al [3] with an arbitrary normalization.

and actual fluxes above E_0 in this kind of analysis, we recall that DM annihilation spectra are rather hard, in particular when taking into account possible spectral features at photon energies close to the spectral cutoff at the mass of the DM particle. On the other hand, the sensitivity of IACTs is considerably better at energies somewhat larger than the telescope energy threshold. We therefore take the projected sensitivites for the integrated flux above some energy $E^* > E_0$, using the sensitivity curves as provided by Bernlöher et al [13] for CTA and Carmona et al [21] for MAGIC II and, by comparing those to the annihilation spectra,

compute the *minimal* boost factor that is required to see at least part of the DM annihilation spectrum above E^*. This is referred to as the quantity $B2$ in Table 9.5; finally, we also state as **B3** the corresponding value for the most favourable *smooth* halo profile that is consistent with the observational data, as discussed in Section 9.4.1.

So far, we have only discussed smooth DM distributions. On the other hand, it is well known from both theory [31] and numerical N-body simulations [25] that cold DM is expected to cluster and thereby to form substructures with masses all the way down to the small–scale cutoff in the spectrum of matter density fluctuations, which can be determined to a great accuracy from the underlying DM model [19]; if surviving until today, such inhomogeneitis in the DM distribution would greatly enhance the DM annihilation rate [11]. For the case of typical dSphs, this would result in an additional boost of the signal by a factor of 10-100 [53]. Another considerable boost in the annihilation flux could also result from the existence of a hypothetical black hole at the center of the dwarfs [24]. In the most optimistic astrophysical configuration, the required boost stated as **B3** in Table 9.5, would thus further be *reduced* by up to two orders of magnitude.

Let us now discuss some details of the results:

- *Sources.* For Draco, the model-dependent fluxes for the Burkert and NFW profiles are very similar, and therefore we presented only the latter in Table 9.5. For the astrophysical benchmark profiles introduced in Section 9.4.1, detectional prospects for Draco and Willman 1 only differ by a factor of around 2, and are obviously not very encouraging. When considering the most optimistic astrophysical configurations, however, things change considerably, making Willman 1 an interesting and indeed very promising target for DM searches. Allowing for an additional, in fact well-motivated, boost due to the presence of DM substructures in the dwarfs, this may give at least CTA the chance to see also Draco in some cases.

- *Telescopes.* Depending on the DM model, the ability of CTA to detect gamma rays from DM annihilation is a factor of $6-8$ better than for MAGIC II. Focusing on Willman 1, and assuming very favourable astrophysical conditions, CTA would in principle be able to see *all* the benchmark models considered here, while MAGIC II should be able to see at least some of them. We recall that the above stated boost factors are calculated with respect to an observation time of $t_{obs} = 50$ hrs and scale like $t_{obs}^{-1/2}$. For prolonged observation times, one could thus win a factor of a few for both telescopes. Furthermore, as the CTA parameters are still quite preliminary, an additional factor of 2 in the sensitivity of the operating instrument seems quite feasable.

- *Benchmark models.* The best prospects for detection are found for the neutralino in the funnel region (model K'), the reason simply being a rather large annihilation rate. The second-best prospects are found for model J^* in the coannihilation region. Recalling from Table 9.4 that J^* is actually the model with the *smallest* annihilation rate, this may come as some surprise and nicely illustrates the importance of including IB contributions when estimating the flux from DM annihilation. The model F^* is yet another example with rather pronounced IB contributions; a mass of almost 2 TeV, however, efficiently suppresses the annihilation flux (in this case, the required boost actually depends significantly on the details of the — so far not sufficiently well known — integrated sensitivity of CTA for TeV photons and could thus eventually be significantly improved).

When compared to previous work, we thus arrive at considerably more optimistic conclusions than what has been reached by Sanchez–Conde et al [46] for the analysis of present-day

gamma ray telescopes – not the least due to our fully taking into account all the contributions to the expected annihilation spectrum. On the other hand, we find the conclusions of Strigari et al [52] overly optimistic, a fact that we trace back to the very large particle flux factor of $\Phi^{PP} = 5 \times 10^{-29}\mathrm{cm}^3\mathrm{s}^{-1}\mathrm{GeV}^{-2}$ that the authors assumed as a fiducial value (this should be compared to Table 9.4 and the corresponding values for our benchmark models, which were chosen such as to represent typical neutralino DM candidates). While it may indeed be possible to find DM models with higher gamma ray yields than considered here, we recall that there exist rather tight general bounds on the allowed annihilation cross section and the number of high-energy photons that are produced [37]. Finally, we would like to remark that it is certainly promising to combine the DM searches in gamma rays, as described here, with observations of the same dSphs at other wavelengths (see also [24, 33]).

9.6 Conclusions

In this chapter, we have computed the prospects of detecting gamma rays from annihilating DM in two nearby dwarf galaxies, Draco and Willman 1, for the upcoming ground–based Imaging Atmospheric Cherenkov Telescopes MAGIC II and the CTA telescope array (the latter still being in the early design phase). We have focused our analysis on a set of five benchmark models, representatives for the parameter space of neutralino DM in mSUGRA framework, and paid special attention in describing those telescope features that are most relevant in this context. For the first time in this kind of analysis, we have fully taken into account the contributions from radiative corrections that were recently reported by Bringmann et al [17]. As it turned out, in fact, taking realistic DM spectra has an important impact on the analysis and, although common practice, *it can be a rather bad approximation to simply assume a featureless DM spectrum like from $b\bar{b}$ fragmentation and/or to only focus on the total flux above a given energy threshold E_0* in these kind of studies. The basic underlying reason for this is that *realistic DM annihilation spectra show a harder energy dependence than the sensitivity of IACTs*. Once detected, clear spectral features would, of course, have the additional advantage of providing a rather fool-proof way of discriminating DM spectra against astrophysical background sources – which is even more important in view of the still rather large astrophysical uncertainties involved.

Although these effects do provide a considerable enhancement of the detectional prospects, the expected flux remains at a level that, for conservative scenarios, will be challenging to detect with the next generation of IACTs. This, rather than the angular resolution of these instruments, is the reason why the potential of IACTs to discriminate between different DM profiles in dSphs is limited even in the case of the detection of an annihilation signal; the eventual disentanglement between cored and cuspy profiles is probably more promising to perform at other wavelengths.

On the other hand, if one adopts the most optimistic astrophysical configurations that are compatible with current observational data of Willman 1, i.e. a favourable DM profile and an $\mathcal{O}(10-100)$ flux enhancement due to the existence of substructures, *all* of our benchmark models approach the reach of at least the CTA which, for the models studied here, is a factor of $6-8$ more sensitive to the annihilation signal than MAGIC II (this is, of course, independent of the source). The most promising case of our analysis turns out to be a neutralino in the funnel region, characterized by no sizeable IB contributions to its spectrum but a rather large annihilation rate; the second best case is a neutralino from the coannihilation region, making up for its small annihilation rate with enourmously large radiative corrections.

Having demonstrated that the prospects of indirect DM detection through gamma rays do

depend on the details of the annihilation spectrum, and thus the underlying particle nature, it would be interesting to perform similar analyses also for other targets of potential DM annihilation. Another further direction of extending the present analysis would be to perform a full scan over the parameter space of viable models. Finally, we have stressed that the very concept of sensitivity of an IACT depends on the spectrum that is observed; in the context of DM searches, this is particularly important as DM annihilation spectra can significantly deviate from the usually assumed Crab-like spectrum. While we have provided a first estimate of how to proceed in such a case, it would be warranting to perform a dedicated analysis, using the full power of state-of-the-art MC tools, in order to accurately determine the importance of this effect.

Finally, we would like to mention that even in the case of negative detection, IACTs could in principle put interesting upper limits on the flux which in turn would translate into constraints on the combined space of astrophysical and particle physics parameters. Though much smaller than for other sources like, e.g., the galactic center, the main uncertainty in this case lies in the overall scale of the flux as determined by the details of the DM distribution. This, unfortunately, will therefore greatly obstacle any stringent constraint from null searches on the particle physics nature of DM for quite some time ahead.

To conclude, nearby dwarf galaxies – and in particular Willman 1 – are very interesting and promising targets for DM searches with the next generation of IACTs. An excellent performance of these experiments, in particular in terms of the sensitivity at energies slightly below the DM particle mass, will be paramount in such searches. In fact, given the low level of fluxes involved, a factor of 2 in sensitivity might decide whether a signal will be seen or not. Complementary to such demanding requirements on the experiments, the above discussion should also have made clear that it will be very important to collect more astrophysical data and to improve the theoretical understanding of how DM is distributed in order to reduce the still unpleasantly large astrophysical uncertainties involved.

References

[1] M. Aaronson. *Astrophys. J.*, 266:L11, 1983.

[2] Z. Ahmed et al. A Search for WIMPs with the First Five-Tower Data from CDMS. preprint, arXiv:0802.3530, 2008.

[3] J. Albert et al. Upper limit for gamma-ray emission above 140 GeV from the dwarf spheroidal galaxy Draco. *Astrophys. J.*, 679:428–431, 2008.

[4] J. Angle et al. First Results from the XENON10 Dark Matter Experiment at the Gran Sasso National Laboratory. *Phys. Rev. Lett.*, 100:021303, 2008.

[5] A. Aparicio, R. Carrera, and D. Martinez-Delgado. The Star Formation History and the Morphological Evolution of the Draco Dwarf Spheroidal Galaxy. *Astronom. J.*, 123:2511, 2002.

[6] E. A. Baltz, M. Battaglia, M. E. Peskin, and T. Wizansky. Determination of dark matter properties at high-energy colliders. *Phys. Rev.*, D74:103521, 2006.

[7] M. Battaglia et al. Updated post-WMAP benchmarks for supersymmetry. *Eur. Phys. J.*, C33:273–296, 2004.

[8] M. Battaglia, I. Hinchliffe, and D. Tovey. Cold dark matter and the LHC. *J. Phys.*, G30:R217–R244, 2004.

[9] L. Bergstrom. RADIATIVE PROCESSES IN DARK MATTER PHOTINO ANNIHILATION. *Phys. Lett.*, B225:372, 1989.

[10] L. Bergstrom, T. Bringmann, M. Eriksson, and M. Gustafsson. Gamma rays from heavy neutralino dark matter. *Phys. Rev. Lett.*, 95:241301, 2005.

[11] L. Bergstrom, J. Edsjo, P. Gondolo, and P. Ullio. Clumpy neutralino dark matter. *Phys. Rev.*, D59:043506, 1999.

[12] L. Bergstrom, P. Ullio, and J. H. Buckley. Observability of gamma rays from dark matter neutralino annihilations in the Milky Way halo. *Astropart. Phys.*, 9:137–162, 1998.

[13] K. Bernloehr, E. Carmona, and T. Schweizer. In *Proc. of the 30th ICRC*, Merída, Mexico, 2007.

[14] G. Bertone, D. Hooper, and J. Silk. Particle dark matter: Evidence, candidates and constraints. *Phys. Rept.*, 405:279–390, 2005.

[15] A. Biland. In *Proc. of IDM 2008*, Stocholm, Sweden, 2008.

[16] A. Birkedal, K. T. Matchev, M. Perelstein, and A. Spray. Robust gamma ray signature of WIMP dark matter. preprint, arXiv:hep-ph/0507194, 2005.

[17] T. Bringmann, L. Bergstrom, and J. Edsjo. New Gamma-Ray Contributions to Supersymmetric Dark Matter Annihilation. *JHEP*, 01:049, 2008.

[18] T. Bringmann, M. Doro, and M. Fornasa. Dark Matter signals from Draco and Willman 1: Prospects for MAGIC II and CTA. *JCAP*, page 016, 2009.

[19] T. Bringmann and S. Hofmann. Thermal decoupling of WIMPs from first principles. *JCAP*, 0407:016, 2007.

[20] A. Burkert. The Structure of dark matter halos in dwarf galaxies. *IAU Symp.*, 171:175, 1996.

[21] E. Carmona et al. Monte Carlo Simulation for the MAGIC-II System. preprint, arXiv:0709.2959, 2007.

[22] A. H. Chamseddine, R. L. Arnowitt, and P. Nath. Locally Supersymmetric Grand Unification. *Phys. Rev. Lett.*, 49:970, 1982.

[23] M. Chertok et al. Search for dark matter annihilations in Draco with CACTUS. *AIP Conf. Proc.*, 842:995–997, 2006.

[24] S. Colafrancesco, S. Profumo, and P. Ullio. Detecting dark matter WIMPs in the Draco dwarf: a multi- wavelength perspective. *Phys. Rev.*, D75:023513, 2007.

[25] J. Diemand, B. Moore, and J. Stadel. Earth-mass dark-matter haloes as the first structures in the early universe. *Nature.*, 433:389–391, 2005.

[26] D. D. Driscoll et al. Search for Dark Matter Annihilation in Draco with STACEE. preprint, arXiv:0710.3545, 2007.

[27] N. Fornengo, L. Pieri, and S. Scopel. Neutralino annihilation into gamma-rays in the Milky Way and in external galaxies. *Phys. Rev.*, D70:103529, 2004.

[28] N. Gehrels and P. Michelson. GLAST: The next-generation high energy gamma-ray astronomy mission. *Astropart. Phys.*, 11:277–282, 1999.

[29] P. Gondolo, J. Edsjo, L. Bergstrom, P. Ullio, M. Schelke, E. Baltz, T. Bringmann, and G. Duda. Darksusy 5.0.1, 2005.

[30] P. Gondolo et al. DarkSUSY: Computing supersymmetric dark matter properties numerically. *JCAP*, 0407:008, 2004.

[31] A. M. Green, S. Hofmann, and D. J. Schwarz. The first WIMPy halos. *JCAP*, 0508:003, 2005.

[32] W. Hofmann. Performance limits for Cherenkov instruments. preprint, arXiv:astro-ph/0603076, 2006.

[33] T. E. Jeltema and S. Profumo. Searching for Dark Matter with X-ray Observations of Local Dwarf Galaxies. preprint, arXiV:0805.1054, 2008.

[34] S. Kazantzidis et al. Density Profiles of Cold Dark Matter Substructure:Implications for the Missing Satellites Problem. *Astrophys. J.*, 608:663–3679, 2004.

[35] T. P. Li and Y. Q. Ma. Analysis methods for results in gamma-ray astronomy. *Astrophys. J.*, 272:317–324, 1983.

[36] E. L. Lokas, G. A. Mamon, and F. Prada. Dark matter distribution in the Draco dwarf from velocity moments. *Mon. Not. Roy. Astron. Soc.*, 363:918, 2005.

[37] G. D. Mack, T. D. Jacques, J. F. Beacom, N. F. Bell, and H. Yuksel. Conservative Constraints on Dark Matter Annihilation into Gamma Rays. *Phys. Rev.*, D78:063542, 2008.

[38] N. F. Martin, R. A. Ibata, S. C. Chapman, M. Irwin, and G. F. Lewis. A Keck/DEIMOS spectroscopic survey of faint Galactic satellites: searching for the least massive dwarf galaxies. arXiv:0705.4622, 2007.

[39] S. Mashchenko, A. Sills, and H. M. P. Couchman. Constraining global properties of the Draco dwarf spheroidal galaxy. *Astrophys. J.*, 640:252–269, 2006.

[40] M. Mateo. Dwarf Galaxies of the Local Group. *Ann. Rev. Astron. Astrophys.*, 36:435–506, 1998.

[41] J. F. Navarro, C. S. Frenk, and S. D. M. White. A Universal Density Profile from Hierarchical Clustering. *Astrophys. J.*, 490:493–508, 1997.

[42] F. E. Paige, S. D. Protopopescu, H. Baer, and X. Tata. ISAJET 7.69: A Monte Carlo event generator for p p, anti-p p, and e+ e- reactions. preprint, arXiv:hep-ph/0312045, 2003.

[43] S. Piatek, C. Pryor, T. E. Armandroff, and E. W. Olszewski. Structure of the Draco Dwarf Spheroidal Galaxy. *Astronom. J.*, 123, 2002.

[44] G. Pulhofer et al. In *Proc. of the 28th ICRC*, Tsukuba, Japan, 2003.

[45] P. Salucci and A. Burkert. Dark Matter Scaling Relations. *Astrophys. J.*, 537:9, 2000.

[46] M. A. Sanchez-Conde et al. Dark matter annihilation in Draco: New considerations of the expected gamma flux. *Phys. Rev.*, D76:123509, 2007.

[47] T. Schweizer. private communication, 2007.

[48] M. Segall, R. Ibata, M. Irwin, N. Martin, and S. Chapman. Draco, a flawless dwarf galaxy. *Mon. Not. Roy. Astron. Soc.*, 375:831–842, 2007.

[49] M. Shetrone, P. Cote, and W. L. W. Sargent. Abundance Patterns in the Draco, Sextans and Ursa Minor Dwarf Spheroidal Galaxies. *Astrophys. J.*, 548:592–608, 2001.

[50] M. H. Siegel, M. D. Shetrone, and M. Irwin. Trimming Down the Willman 1 dSph. arXiv:0803.2489, 2008.

[51] V. Springel et al. The Aquarius Project: the subhalos of galactic halos. 2008.

[52] L. E. Strigari et al. The Most Dark Matter Dominated Galaxies: Predicted Gamma- ray Signals from the Faintest Milky Way Dwarfs. preprint, arXiv:0709.1510, 2007.

[53] L. E. Strigari, S. M. Koushiappas, J. S. Bullock, and M. Kaplinghat. Precise constraints on the dark matter content of Milky Way dwarf galaxies for gamma-ray experiments. *Phys. Rev.*, D75:083526, 2007.

[54] C. Tyler. Particle dark matter constraints from the Draco dwarf galaxy. *Phys. Rev.*, D66:023509, 2002.

[55] M. G. Walker et al. Velocity Dispersion Profiles of Seven Dwarf Spheroidal Galaxies. 2007.

[56] B. Willman et al. A New Milky Way Dwarf Galaxy in Ursa Major. *Astrophys. J.*, 626:L85–L88, 2005.

[57] B. Willman et al. Willman 1 - A Galactic Satellite at 40 kpc With Multiple Stellar Tails. preprint, arXiv:astro-ph/0603486, 2006.

[58] A. G. Wilson. In *Publications of the Astronomical Society of the Pacific*, volume 67, page 27. 1954.

[59] M. Wood et al. A Search for Dark Matter Annihilation with the Whipple 10m Telescope. preprint, arXiv:0801.1708, 2008.

[60] D. G. York et al. The Sloan Digital Sky Survey: technical summary. *Astron. J.*, 120:1579–1587, 2000.

10

Observation of Willman 1 with the MAGIC telescope

Although the scenario presented in the previous chapter was not optimistic for the detection of Willman 1 with MAGIC telescope, it was underlined that still the possible combinations of boosting effects could lead to an observable flux or at least upper limits could start to be constraining observations. It was therefore considered worth to observe Willman 1 with the MAGIC telescope in 2008. In this chapter, we present the result of the observation. No significant gamma–ray emission was found above 100 GeV. We derived upper limits of the order of 10^{-12} ph cm^{-2} s^{-1} on the integral flux above 100 GeV, which we compare with predictions from several of the established neutralino benchmark models in the mSUGRA parameter space already introduced in the previous chapter. Flux boost factors of three orders of magnitude are required even in the most optimistic scenario to match our upper limits.

This chapter is adapted from *MAGIC upper limits on the VHE gamma-ray emission from the satellite galaxy Willman 1*, 2008 [4].

10.1 Introduction

In Chapter 9, it was shown that, even in the case of increased telescope sensitivity, both Draco and Willman 1 could hardly be detected by MAGIC II, and that applies of course for MAGIC I too. On the other hand, the combined effect of the uncertainties already discussed could lead to an (undefined) increase in the γ–ray flux. While it is not realistic to consider too large boost factors, and it is also unelegant to make such assumptions, there is still theoretical space for thinking that we could be at a step from DM detection from dSphs. On the other hand, as we are hunting in the dark, it is a good practice to look where the probability is higher. This mainly motivated the observation of Willman 1 with the MAGIC telescope during the third cycle of observation in 2008, which is hereafter described.

An introduction about the target source was already given in § 9.2.2. In § 10.2 we recall the basic of the estimation of the flux using benchmark models for the neutralino and a typical DM density profile. In § 10.3 we describe the data treatment and present the calculation of upper limits. A discussion follows in § 10.4

10.2 Theoretical modeling of the gamma-ray emission

At a distance of 38 kpc, the scale radius of Willman 1 corresponds to an extension of 0.54° in the sky, which is well inside the MAGIC field of view ($\sim 3.5°$), but is rather extended if one considers the telescope angular resolution of 0.1°. This evidence is mitigated by the fact that the main emission still comes from the very core of the source, due to the very steep NFW profile at the center and the square density dependence (see Eq. 9.7). Normally, all MAGIC targets are point–like source, i.e. their intrinsic extension is smaller than the telescope PSF. Therefore the analysis is adapted for this type of sources. On the other hand, the observation of extended sources is very better carries out by telescopic observation, as already observed. Recently, Sitarek and Mirzoyan [16] showed that the analysis of extended sources can be also computed with MAGIC I by a slight readjastement of the optimal cuts. We used the results of their analysis here.

10.2.1 Particle Physics Factor

Hereafter, we use a subset of four slightly modified Battaglia models of Ref. [5], as defined in Chapter 9, which include the contribution of IB in the computation of the cross sections and spectra: models *I', J', K', F** for the bulk, co-annihilation, funnel and focus point regions respectively. All the defining parameters of the benchmarks were already listed in Table 9.4. The total estimated flux due to DM annihilation computed according to Eq. 9.6 is given in Table 10.1.

There are some sources of uncertainty that may largely affect the values for the predicted flux, as already mentioned: *a*) our lack of knowledge of the DM density profile, which may change the astrophysical factor by more than one order of magnitude, *b*) the possible boost due to the presence of substructures in the dwarf, which may enhance the $\gamma-$ray flux at least by a factor of $2-3$ according to $N-$body simulations [7, 8, 11]. Substructures are in fact expected to be present not only in Willman 1 but also in any other DM halo, since CDM halos are approximately self-similar until a cutoff scale mass (which lies in the range of 10^{-4}–10^{-12} $M_\odot$ [14] *c*) the exclusion of the baryons in the modelization of the total density profile. However, the effect of the adiabatic compression [13, 9], although important for larger DM halos, will probably play a marginal role in the case of Willman 1, given its relatively low amount of baryons even in the central regions, where the effect is expected to be more important.

10.3 MAGIC I data

MAGIC I observed Willman 1 between March and May 2008. The source was surveyed at zenith angles between 22° and 30°, which guarantees the lowest energy threshold. The source was tracked for 16.8 hours plus another 9.3 hours in OFF observation mode, i.e. pointing to a dark patch in the sky close to Willman 1 where no γ–ray emission is expected, to estimate the background.

10.3.1 Data preparation

The analysis proceeds as follows (for a detailed description see [3]): data are calibrated and the number of photoelectrons per pixel extracted [1], then an image cleaning selects pixels with at least 6 photoelectrons (3 photoelectrons for pixels in the boundary of the image).

Additional suppression of pixels containing noise is achieved by requesting a narrow time coincidence between adjacent pixels (~ 7 ns). Based on the Hillas parameterization algorithm [10], the shower parameters are reconstructed. The hadronic background is suppressed with a multivariate method, the Random Forest [6, 2], that uses the Hillas parameters to define an estimator called *hadronness* by comparison with Monte Carlo (MC) $\gamma-$ray simulations. The hadronness expresses the likeness of an event to be a hadron and runs from 0 for gammas to 1 for hadrons. The Random Forest method is also used to estimate the energy of a reconstructed shower: the energy threshold is defined by the peak of the distribution of reconstructed MC gamma events. The g/h separation is optimized on a real data sample from the Crab Nebula. The optimization yields a best set of cuts in the Hillas parameters which defines the gamma and hadron acceptance of the analysis. In our case, the optimal set of cuts is obtained for an energy threshold of 100 GeV and a hadronness cut of 0.15. The overall data quality is very high, with only 7% data rejection, resulting in 15.5 hours effective observation time.

The analysis was performed together with S. Lombardi. Independent cross–checks were performed on the data by D. Nieto and F. Zandanel giving compatible results.

10.3.2 Results

No significant $\gamma-$ray excess beyond 100 GeV above the background was observed in 15.5 hours of observation of the sky region around Willman 1. This is also shown in Figure 10.1, where the "*alpha*–plot" is reported. The *alpha*–parameter is the angular distance between the shower image main axis and the line connecting the image barycenter and the camera center. Due to their isotropic origin, hadronic events, in case they survive the analysis, are randomly oriented in the camera both in the ON–data and OFF–data sample. This is reflected into a more or less smooth distribution of events in the *alpha*–plot, the non–perfect flatness being due to an increased camera acceptance for showers with small *alpha*. On the other hand, $\gamma-$rays trace back the source, and thus the orientation of the shower image is toward the center of the camera. Therefore, in case of positive detection, an excess of events in the ON–data above the OFF–data sample is expected at small *alpha*. A fiducial region $alpha < 12^\circ$ is chosen where the signal is assumed with a cut slightly larger than for a point–like source to take into account the moderate source extension. The OFF–data are normalized to the ON–data in the region where clearly no signal is expected, i.e. between $alpha = 30^\circ$ and $alpha = 80^\circ$.

The significance of the detection is calculated using Eq. (17) of [12]. The number of excess events $N_{exc}(> 100 \text{ GeV}) = -223 \pm 223$ is calculated as the difference between the number of ON–events and the number of OFF–events in the fiducial *alpha*$-$region. From $N_{exc}(> 100$ GeV), an upper limit in flux can be extracted.

10.3.3 Calculation of upper limits

We applied the Rolke method [15] to estimate the upper limit in the number of excess events with a 90% confidence level and including 30% of systematic errors, giving as a result $N^{ul}_{exc}(> 100 \text{ GeV}) \sim 191.4$ events. This value is used to reconstruct the corresponding photon flux for a general $\gamma-$ray spectrum $S(E)$. The method for calculation for upper limits was adjusted for the general DM spectrum, in contrast with the common use of power–law. A preparatory study was developed with D. Nieto, which we reported in Appendix D.

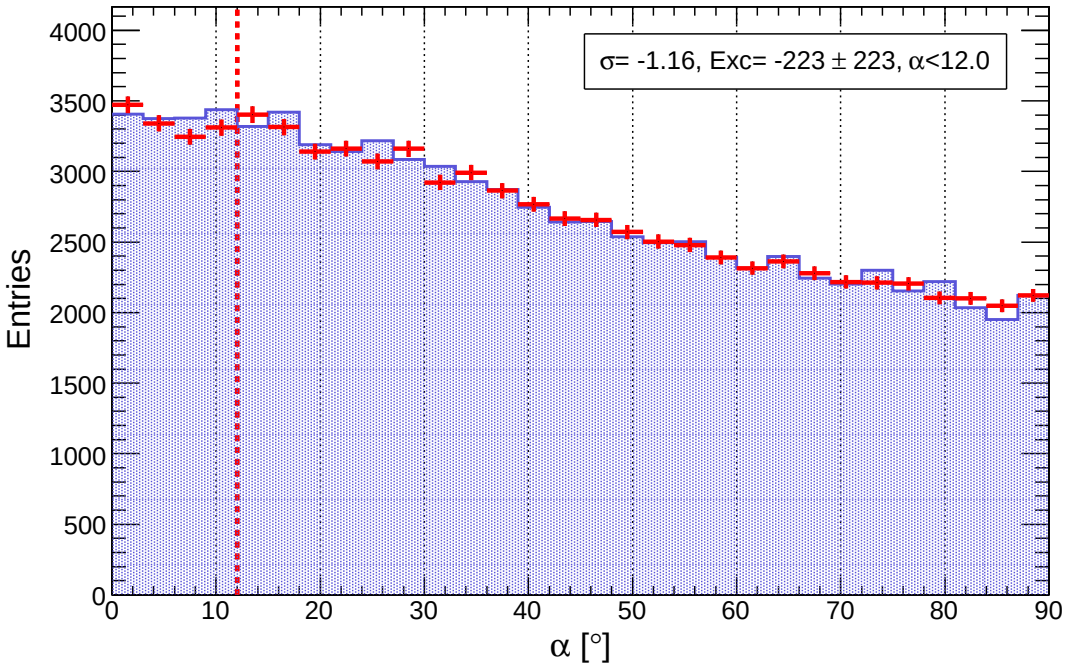

Figure 10.1: Willman 1 *alpha*–plot as seen by MAGIC in 15.5 hours above a fiducial energy threshold of 100 GeV and using a hadronness$<$ 0.15. The red crosses represent the ON–data sample, the blue shaded region is the OFF–data sample normalized to the ON–data sample between $30° - 80°$. The vertical red dotted line represents the fiducial region *alpha* $< 12°$ where the signal is expected.

The upper limit is calcuated using Eqs. D.11 and D.12, reported here for clarity:

$$\Phi^{u.l.}_{>E_0} = \frac{N^{u.l.}_{exc}}{\int S(E)\, A^{cuts}_{eff}(E)\, \mathrm{d}E\, \Delta T} \int_{E_0} S(E) \mathrm{d}E \ , \tag{10.1}$$

where E_0 GeV is the energy threshold, $A^{cuts}_{eff}(E)$ is the effective telescope area after analysis and ΔT is the effective observation time.

We applied Eq. 10.1 for the four neutralino benchmarks defined. Results are reported in Table 10.1, where we also compare $\Phi^{u.l.}_{>E_0}$ with the estimated model–dependent flux of Table 9.4. We also report the upper limits on the *boost factors* that are required to match the two fluxes, calculated again for each neutralino model. The boost factor is defined as the ratio between the upper limit and the theroretical flux, and defines the minimal boost that the theoretical flux should be subject to in order to allow for a positive detection of the source. In order to provide results less dependent of the particular benchmark spectrum, we also calculated flux upper limits in four different energy bins [100–170, 170–350, 350–1000, 1000–20 000] GeV for a generic annihilation spectrum without cutoff and spectral index -1.5. Respectively, the resulting upper limits are $[\,9.94,\ 4.75,\ 0.68,\ 0.35\,]\times 10^{-12}$ photons cm^{-2} s^{-1}.

10.4 Discussion

Table 10.1 reveals that although we derived upper limits of the same order of magnitude for the four models considered, there are evident differences in the prospects of detection for

BM	$\Phi^{model}(>100$ GeV)	$\Phi^{u.l.}(>100$ GeV)	$B^{u.l.}$
I'	2.64×10^{-16}	9.87×10^{-12}	3.7×10^{4}
J'	4.29×10^{-17}	5.69×10^{-12}	1.3×10^{5}
K'	2.32×10^{-15}	6.83×10^{-12}	2.9×10^{3}
F^*	2.09×10^{-16}	7.13×10^{-12}	3.4×10^{4}

Table 10.1: Comparison of estimated integral flux above 100 GeV using Eq. 9.6 for the benchmarks models defined in Table 9.4 and the upper limit in the integral flux $\Phi^{u.l.}$ above 100 GeV coming from MAGIC data in units of photons cm^{-2} s^{-1}. On the rightmost column, the corresponding upper limit on the boost factor $B^{u.l.}$ required to match the two fluxes is calculated.

different neutralinos. The boost factor largely depends on the benchmarks, but the main differences are connected to the particle physics factor, which varies by orders of magnitude among the different benchmarks, as shown in Table 9.4. The best prospects are for neutralinos in the $funnel$ region (model K') of the parameter space, for which the mass is large enough to place the cutoff well within the MAGIC energy threshold but still small enough to not reduce the particle physics factor Φ^{PP} of Eq. 9.9 too much. Next, with similar boost requirements follow the I' and F^* models. In the former case, the effect of the IB plays an important role at energies close to the cutoff even if the neutralino mass is very close to the MAGIC energy threshold. In the latter case, although the IB effect is negligible, the signal is very extended in the energy region suitable for MAGIC, whereas the large mass makes the flux suppression too large. The worst case scenario is the co–annihilation neutralino. In this case, even if the IB contribution is large, the intrinsic total cross section is very low, which makes the flux very low compared to the others. The IB effect cannot counteract this intrinsic deficit.

Although the results of Table 10.1 seem to show that we could still be far from DM detection (the most promising scenario being three orders of magnitude below our sensitivity), we should keep in mind that there are important uncertainties in our modeling that may play a crucial role in detectability issues, as already discussed in Section 10.2.1. In particular our imperfect knowledge of the exact DM density profile as well as the presence of substructure in the dwarf, which is theoretically well–motivated, may increase the astrophysical factor and therefore the flux of more than one order of magnitude. Furthermore, since the parameter space was not fully scanned, it is likely that there are models of neutralino with higher Φ^{PP}.

References

[1] J. Albert et al. FADC signal reconstruction for the MAGIC telescope. *Nuclear Instruments and Methods in Physics Research A*, 594:407–419, Sept. 2008.

[2] J. Albert et al. Implementation of the Random Forest method for the Imaging Atmospheric Cherenkov Telescope MAGIC. *Nuclear Instruments and Methods in Physics Research A*, 588:424–432, Apr. 2008.

[3] J. Albert et al. VHE Gamma-Ray Observation of the Crab Nebula and its Pulsar with the MAGIC telescope. *Astrophys. J.*, 674:1037–1055, 2008.

[4] E. Aliu et al. MAGIC upper limits on the VHE gamma-ray emission from the satellite galaxy Willman 1. 2008.

[5] M. Battaglia et al. Updated post-WMAP benchmarks for supersymmetry. *Eur. Phys. J.*, C33:273–296, 2004.

[6] L. Breiman. Machine learning. 2002.

[7] J. Diemand, M. Kuhlen, and P. Madau. Dark matter substructure and gamma-ray annihilation in the Milky Way halo. *Astrophys. J.*, 657:262, 2007.

[8] J. Diemand, M. Kuhlen, and P. Madau. Formation and evolution of galaxy dark matter halos and their substructure. *Astrophys. J.*, 667:859, 2007.

[9] O. Y. Gnedin, A. V. Kravtsov, A. A. Klypin, and D. Nagai. Response of dark matter halos to condensation of baryons: cosmological simulations and improved adiabatic contraction model. *Astrophys. J.*, 616:16–26, 2004.

[10] A. M. Hillas. In *Proc. of the 19th ICRC*, La Jolla, January 1985.

[11] M. Kuhlen, J. Diemand, and P. Madau. The Dark Matter Annihilation Signal from Galactic Substructure: Predictions for GLAST. 2008.

[12] T. P. Li and Y. Q. Ma. Analysis methods for results in gamma-ray astronomy. *Astrophys. J.*, 272:317–324, 1983.

[13] F. Prada, A. Klypin, J. Flix, M. Martinez, and E. Simonneau. Astrophysical inputs on the SUSY dark matter annihilation detectability. *Phys. Rev. Lett.*, 93:241301, 2004.

[14] S. Profumo, K. Sigurdson, and M. Kamionkowski. What mass are the smallest protohalos? *Phys. Rev. Lett.*, 97:031301, 2006.

[15] W. A. Rolke, A. M. Lopez, and J. Conrad. Limits and confidence intervals in the presence of nuisance parameters. *Nuclear Instruments and Methods in Physics Research Section A*, pages 493–503, 2005.

[16] J. Sitarek and R. Mirzoyan. The study of MAGIC I performance for extended sources. MAGIC-TDAS 080901/JSitarek. Private use at http://wwwmagic.mppmu.mpg.de, 2008.

APPENDIXES

.

A

Acceleration of cosmic–rays and photon–matter interactions.

In this appendix, the principal mechanisms of cosmic–ray acceleration are presented. The main mechanisms of production of VHE γ–rays from energetic cosmic–rays are also presented. A brief discussion on the processes of interaction and transport of cosmic–rays and γ–rays during propagation is also discussed.

A.1 Acceleration mechanisms

The production of γ–rays is typically accompanied by the presence of leptons of hadrons of energies above the GeV. The acceleration of charged particles can be a direct effect of very large electric and magnetic field like in pulsar (see Chapter 1) or via statistical diffusive shock acceleration mechanisms. The basic of this theory was formulated by Fermi, hence the name of two acceleration mechanisms. We redirect the interested reader to the following selected literature [5, 6, 1, 4].

Second order Fermi mechanism

Historically the first mechanism proposed by Fermi, the so–called second order Fermi mechanism describes the acceleration of a charged particle scattering off *magnetic irregularities*.

To describe the mechanism, we consider a black box with some magnetic field, a cosmic–ray (CR) with quadri–momentum $E_1, \boldsymbol{p_1}$ entering the black box at an angle θ_1, and exiting the black box with $E_2, \boldsymbol{p_2}$ at an angle θ_2. The relativistic relations between the laboratory (lab) and black box reference frame (the center of mass system or CM) are:

$$\begin{aligned} E_1' &= \gamma E_1(1 - \beta\cos\theta_1) \\ E_2 &= \gamma E_2'(1 + \beta\cos\theta_2') \end{aligned} \tag{A.1}$$

where E_i, E_i' are the CR energy in the CM and lab frames respectively, $\beta = V/c$ is the ration between the velocity of the magnetic cloud and the velocity of light and $\gamma = 1/\sqrt{1-\beta^2}$.

Applying the law of conservation of energy in CM ($E_2' = E_1'$), we can calculate from

Eq. A.1 the energy gain ϵ of a single event of CR scattering after exiting the magnetic cloud:

$$\epsilon = \frac{E_2 - E_1}{E_1} = \frac{1 - \beta\cos\theta_1 + \beta\cos\theta_2' - \beta^2\cos\theta_1\cos\theta_2'}{1-\beta^2} - 1 \tag{A.2}$$

We want to calculate the average energy gain per CR $\bar{\epsilon}$. If the magnetic cloud is large, the exit angle is random, and therefore $< \cos\theta_2' >= 0$, while the average of the first angle can be demonstrated to be $\cos\theta_1 = -\beta/3$ [4], therefore:

$$\bar{\epsilon} = \frac{1+\beta^2/3}{1-\beta^2} - 1 \simeq \frac{4}{3}\beta^2 \tag{A.3}$$

The second order Fermi mechanism has the following properties:

i) on average the energy gain is positive ($\bar{\epsilon} > 0$),

ii) the average energy gain depends on the square of the magnetic cloud velocity. For typical values of $\beta = 10^{-5}$, the energy gain is therefore only $10^{-10}E_1$ per crossing. The acceleration efficiency is therefore quite low.

iii) the resulting energy spectrum is strongly dependent on magnetic cloud properties and is quite unpredictable

Points ii) and iii) are colliding with the rate of observed CRs and with the classic featureless power–law shape of their spectrum.

First order Fermi mechanism (Diffusive Shock Acceleration mechanism)

After a supernova events, a dense shell of material is expelled at large velocity in the surroundings of a compact star. As the shell propagates, a *shock* is formed. It can in fact be demonstrated [4] that small adiabatic compressions of local regions inside the shell, generate sound waves that propagate. However, as the sound speed increases in compressed regions, the dense regions become denser and denser and the shell self compacts. A discontinuity surface or "shock" is therefore formed at the head of the propagating shell. As the shock propagates, it interacts with local ambient gas fields. It can be demonstrated that, as a result of the passage of the shock, the ambient gas (if monoatomic) can be compressed not more than a factor four. Therefore the gas particles get accelerated by a factor of four which result in generic prediction for the spectrum of accelerated particles of E^{-2}.

In the shock configuration, the average enter and exit angles of Eq. A.1, are calculated as $< \cos\theta_1 >= -2/3, < \cos\theta_2' >= 2/3$, and therefore:

$$\bar{\epsilon} \simeq \frac{4}{3}\beta = \frac{4}{3}\frac{v_1 - v_2}{c} \tag{A.4}$$

where $v_1 - v_2 = V$ is the relative velocity of the CR and the magnetic cloud.

In this case, the acceleration is more efficient that in the second order case. The first order Fermi acceleration mechanism is believed to be the most diffuse mechanism of acceleration of CR at the TeV scale, i.e.in case of non–relativistic shock. The diffusive shock acceleration at relativistic shock is a highly non–linear theory, and could account for CRs at energies up to UHE regime. An introduction on this theory can be found in Ref. [2].

A.2 Interaction in matter

While propagating, high–energy CRs interacts with local gas field or dust. After interactions, normally γ–rays can be emitted. In the following we will discuss such mechanisms.

Bremsstrahlung

Bremsstrahlung is one of the most efficient way in which charged CRs lose energy when crossing matter. The interaction is with the electromagnetic field of the nuclei:

$$q\,(\gamma) \rightarrow q\,\gamma. \tag{A.5}$$

The deceleration produces a beamed photons emission in the forward direction of the particle, within an angle $\theta \simeq 1/\Gamma$, if the particle is relativistic (Γ is the particle Lorentz factor).

Bremsstrahlung occurs when the energy of the charged CR $E = \Gamma\, m\, c^2$ is above a *critical energy* E_0 which depends on the material crossed. Below this value, the most efficient energy loss mechanism is ionization. The bremsstrahlung energy loss rate is proportional to the particle energy, and therefore the mean free path is independent on the particle energy. The energy loss follows the Beth and Heitler law:

$$E(x) = E_0\, e^{-x/X_0}, \tag{A.6}$$

where X_0 is the *radiation length* X_0 and corresponds to the path length that gives an energy fraction loss of $1/e$. The radiation length depends on the material atomic numbers and density:

$$X_0 \sim \frac{Z^2}{A}\,\rho. \tag{A.7}$$

Therefore high density material have a larger radiation length and CRs are more penetrating. Sometimes it is also expressed as $X_0 = Z^2/\rho$ so that it is an intrinsic parameter of a material and is not depending on the its density. In this case it is expressed in units of g cm^{-2}. The radiation length is connected to the mean free path of the particle ($\lambda = (n\sigma_0)^{-1}$) by the well–known relation $X_0 = 9/7\,\lambda$.

The fact that the energy loss through bremsstrahlung depends linearly on the particle energy has the interesting effect that the emitted photons follow the same spectral distribution of the charged particles. All charged particles can produce bremsstrahlung, but the process is very efficient mainly for electrons because the total radiated power goes as m^{-4} where m is the mass of the particle.

This mechanism is observed in astrophysical regions that contain ionized gas, such as gaseous nebulae, which emit in radio–waves and in the hot intracluster gas within cluster of galaxies, which emit in X–rays. If the electrons are accelerate to TeV energies or more, emission at γ–rays is also observed.

Electron–positron annihilations

CR electrons suffer from an additional absorption mechanism. High energy electrons can interact with low–energy positron fields and annihilate into two energetic photons:

$$e^+\, e^- \rightarrow \gamma\gamma. \tag{A.8}$$

Seed positrons are found as secondary products of spallation of CRs with matter. Conversely, positrons can interact with cold thermal electrons in ambient gas or plasma. The γ–ray spectrum is steeper than the positron spectrum: $\Gamma_\gamma = \Gamma_p - 1$ at least if the electron are not too much relativistic.

Pion decay

Relativistic protons and nuclei interact with ambient gas through inelastic collisions and produce basically mesons, kaons and hyperions via strong interactions. The larger cross section is for π-mesons (pions) which are produced in equal amounts of positive, negative and neutral charged. The decay of charged pions is accompanied by the emission of neutrinos ν_e, ν_μ whose spectral shape is similar to the accelerated particles shape and, whether observed, could constitute the smoking gun observation of hadronic acceleration. The energy threshold for pions production is $E_{th} = 2m_\pi c^2(1 + m_\pi/4m_p) \simeq 280$ MeV.

Neutral pions almost immediately annihilate into two energetic gammas $\pi^0 \rightarrow \gamma\gamma$. The emission is peaked at $E_\gamma = m_{\pi^0} c^2/2 \sim 67.5$ MeV, independent on the particles velocity distribution or the ambient gas. This is again a clear signature of hadronic acceleration. The spectrum is close to a power–law with spectral index $alpha = -2.5$.

A.3 Interaction with photon fields

During their travel, CR and γ–rays can also interact with dense low–energy photon fields which are widely present in many astrophysical environments.

Compton Scattering

The Compton scattering is the between a photon and an unbound electron:

$$\gamma\ e \rightarrow \gamma\ e. \tag{A.9}$$

The interactions can have very different outcomes depending on the ratio between the rest mass of the electron and the photon energy $alpha = h\nu/m_e c^2$:

i) *Direct Compton.* Or simply Compton scattering. It happens when $alpha \geq 1$. In this process, the photon release some energy to the electron which is consequently accelerated.

ii) *Inverse Compton.* This happens whenever a high–energy electrons scatter off low energy photons, i.e. when $alpha \leq 1$. In this case there is an efficient transmission of momentum from the electron to the photon which is re–emitted at very high energies.

While the former process is responsible for example for the thermalization of plasma or gas, the latter process is far more important for gamma–ray astrophysics as it is one of the main responsible for the acceleration of soft ambient KeV photons to GeV photons or even higher energy γ–rays in galactic objects as pulsar, or extragalactic objects as active galactic nuclei.

The Compton scattering is explained by following the rules of conservation of energy and momentum in the frame of the electron at rest [3]. The energy of the scattered photon can be written as:

$$h\,\nu' = \frac{m_e\,c^2}{1 - \cos\theta + 1/alpha} \tag{A.10}$$

where θ is the angle of the scattered photon. In case $alpha \gg 1$, the energy of the scattered photon is always smaller than the electron rest mass and all the energy goes into the kinetic energy of the scattered electrons.

The cross–sections are calculated in three regimes: in case the $alpha \gg 1$ the Klein–Nishima cross–section is

$$\sigma_{KN} = \pi\, r_0^2\, \{(1/alpha^3)\ln(1+2alpha) + 2(1+alpha)(2alpha^2 - 2alpha - 1)\cdot$$

$$\cdot\,(alpha^2(1+2alpha)^2 + 8alpha^2/3(1+2alpha)^3)^{-1}\}$$

For $alpha \leq 1$, i.e. in the Compton regime, the cross–section reduces to

$$\sigma_C = \frac{8\pi\, r_0^2}{3}\cdot(1 - 3alpha^2 + 9.4alpha^2 + \ldots)$$

which further reduces to $\sigma_T = 8\pi\, r_0^3/3 = 6.65 \times 10^{-25}$ cm^2 in case $alpha \ll 1$ where the so–called Thompson regime applies.

It can be shown that, in case a population of VHE electrons with a power law distribution of $\propto E^{-k_e}$ interacts with a soft photons distribution of density ρ, the spectrum of gamma–rays will have the form $\propto E^{-(k_e+1)/2}$ and a typical characteristic energy of $\gamma_e^n\, h\nu$ where $n = 1, 2$ depending whether the regime is the Klein–Nishina or Thompson one, and γ_e is the electron Lorentz factor.

Self–Compton Scattering (SSC). In radiation–dominated environments (i.e. relativistic jets, pulsar wind nebulae, active star forming regions, etc.), the inverse Compton can act directly onto the diffused seed soft photons produced for example by synchrotron radiation of accelerated electrons. Hence the name *self–Compton* scattering. To a certain extent, the process is always present where are accelerated electrons and is therefore of utmost importance in astrophysical studies.

Interaction of hadrons with photon field. In regions with dense radiation fields, also hadrons could have efficient interactions, sometimes more efficient than with matter fields. For example, hadronic inverse Compton scattering is possible, accompanied by pair production of photon interacting with protons electric field, etc. According to the energies, these processes must be taken into account for detailed modeling of the emission regions.

Pair Production

Pair production is the mechanism through which a high–energy photon annihilates with a low–energy photon and a electron–positron pair is created:

$$\gamma\gamma \rightarrow e^+ + e^-. \tag{A.11}$$

In astrophysics, the pair production can be divided in two families of processes:

i) *Classical Pair Production* A high–energy γ–ray interacts with the electric field of an atomic nucleus or of an electron's one and produce the pair in a process $\gamma(\gamma) \rightarrow e^+e^-$ where the second photon is the virtual photon of the electric field.

ii) *Photon–Photon Pair Production* It is a similar process, but the soft photons are available in the environment as radiation from stars for example. In this case, the process is $\gamma\gamma_{soft} \rightarrow e^+e^-$

The former process prevents high–energy γ–rays to cross the earth atmosphere and protect the life on the earth. The second process is responsible for the absorption of γ–rays in their travel through the interstellar and intergalactic medium. The pair production process starts to be efficient when the γ–rays energy is larger than twice the mass of the electron; the cross section increases with energy (energetic γ–ray are absorbed more) but only up to ~ 2 MeV where it reached a plateau at $\sigma_{PP} = 5.8 \times 10^{-28} \cdot Z^2[28/9 \ln(183/Z^{1/3}) - 2/27]$ cm^{-2} atom^{-1}. In the atmosphere, a gamma–ray can therefore travel undisturbed for only $\lambda_{PP} = 1/\rho_Z \, \sigma_{PP}$, where ρ_Z is the target density, the radiation length being $X_0 = 7/9 \; \lambda_{PP}$.

Interaction with extragalactic background light: the gamma horizon. The photon–photon pair production is an extremely relevant process for the observation of far distant sources. Excluding the galactic plane, the universe is almost isotropically filled with soft photons of the extragalactic background light (EBL). The EBL is composed by a contributions from stellar light summed up at different epochs plus a contribution coming from the dust–scattered light. The former contributions is at the mid–IR wavelengths and the second one is at lower energies in the close UV–band. VHE γ–rays have high cross–section for pair production with the EBL, therefore the universe is not completely transparent to VHE γ–rays, at least beyond 100 GeV. This means that far distant sources cannot be observed, and therefore a *gamma–horizon* is obscuring us what is beyond.

This is particularly relevant for the observation of active galactic nuclei. While they are observed at other wavelengths up to redshift exceeding 5, the farthest AGN was observed by MAGIC at a distance of $z \simeq 0.5$. The effect of the EBL absorption is energy dependent, there original spectra get distorted and the measured spectrum must be deconvoluted.

A.4 Interaction with magnetic field

Synchrotron Radiation

A charged particle spiralizing in a magnetic field emits radiation. The process has two general descriptions according to whether the classical approximation is valid or not. In the former case, the charge particle that spins around the magnetic field lines, emits at the frequency $\omega_L = q \, H/m \, c$, called the Larmor frequency, where H is the magnetic field, q and m are the particle's charge and mass, and c the velocity of light. The radiation has the shape of a dipole radiation with frequency ω_L.

In case of relativist electrons instead, the emission is more complicate: from one hand, it is strongly beamed in the forward direction of motion of the particle, and on the other hand the emission is a broad–band one. The maximum emission is reached for $\omega_C = 1.5 \, \omega_L \gamma^2 \sin\theta$, where γ is the particle Lorentz factor and θ the angle between the velocity and the magnetic field lines. The spectral emission increases as $(\omega/\omega_C)^{1/3}$ before ω_C and later decreases as $\exp(-2\omega/3\omega_C)$, with a Landau–function–like shape.

References

[1] F. Aharonian. *Very High Energy Cosmic Gamma Radiation - A Crucial Window on the Extreme Universe*. World Scientific, Singapore, 2004.

[2] M. G. Baring. Diffusive shock acceleration of high energy cosmic rays. *Nucl. Phys. Proc. Suppl.*, 136:198–207, 2004.

[3] R. Evans. *The Atomic Nucleus*. New York: Mc Graw-Hill, 1955.

[4] M. Kachelriess. Lecture notes on high energy cosmic rays. Prepared for the 17th Jyvasllya Summer School, 2008.

[5] M. A. Malkov and L. O. Drury. Nonlinear theory of diffusive acceleration of particles by shock waves. *Rept. Prog. Phys.*, 64:429–481, 2001.

[6] T. C. Weekes. *Very high energy gamma-ray astronomy*. Very high energy gamma-ray astronomy, by Trevor C. Weekes. IoP Series in astronomy and astrophysics, ISBN 0750306580. Bristol, UK: The Institute of Physics Publishing, 2003, 2003.

B
Atmospheric showers

Very high energy cosmic gamma–rays that impinge on the earth typically interact with atmospheric nuclei and generate an electromagnetic shower. The showers extend over several kilometers in length and few tens to hundreds of meters in width, and their maximum is located around an airmass fraction of $0.2 - 0.3$, or at $8 - 12$ km altitude, in case of vertical incidence. For gammas below ≤ 100 TeV, the shower particles stop high up in the atmosphere, and can not be directly detected at ground. However, a sizeable fraction of the charged secondary shower particles, mostly electrons and positrons in the shower core, move with ultra-relativistic speed and emit Cherenkov light. This radiation is mainly concentrated in the near UV and optical band and therefore passes mostly unattenuated to the ground, with minor losses due to Rayleigh and Mie scattering and Ozone absorption.

B.1 Electromagnetic shower initiated by γ–rays

When a γ–ray impinges the top atmosphere, after interaction with the electric field of atmospheric molecules, it pair–produces an electron–positron couple (see Appendix A):

$$\gamma(\gamma) \rightarrow e^+ e^- \tag{B.1}$$

The reaction has an energy threshold of $h\nu = 2m_e c^2 \simeq 1$ MeV, and therefore normally takes place for γ–rays in the VHE band. The cross section for muon–antimuon pair production is many orders of magnitude smaller due to the its larger mass. Each electron–positron in turn generates new γ–rays via bremsstrahlung:

$$e^{\pm}(\gamma) \rightarrow e^{\pm} \gamma \tag{B.2}$$

where the secondary γ–ray takes away in first approximation half of the energy of the electron. Eventually the secondary γ–ray again pair–produces an electron and a positron and so on, and the shower is initiated. Such a cascade is called electro–magnetic (EM) due to fact that only EM interactions take place. A sketch of a schematic view of the shower development is shown in Figure B.1. A Monte Carlo (MC) simulation of a 100 GeV EM shower is shown in Figure B.3.

The energy of secondary particles produced in the shower decreases as the shower proceeds.

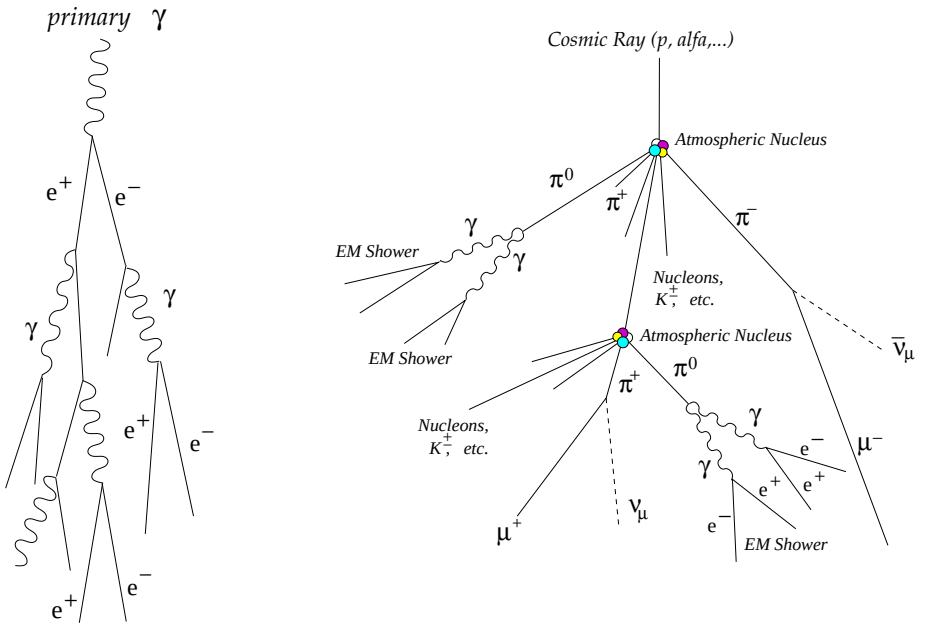

Figure B.1: Scheme of production of an electromagnetic shower (left) and a hadronic shower (right). In the former case, the absence of heavy particle let the shower be tighten, while in the latter case, the heavy particle can have large momenta and spread the shower width.

When the mean energy of $e^{\pm}$ is below a critical energy E_c, which in air is $\simeq 83$ MeV, the dominant energy loss process for electrons becomes ionization, rather than bremsstrahlung. Almost contemporary, when the mean photon energy decreases below few MeV, the cross–section for Compton scattering and photoelectric absorption become dominant over pair–production. Rapidly the showers dies out. In the GeV–TeV regime, the charged particles and γ–rays of the showers cannot cross the atmosphere and are absorbed after few interaction lengths, as shown in Figure B.2. At the altitude of MAGIC telescope, around 2200 m asl (corresponding to circa 22 radiation lengths[1] or 800 g cm^{-2}), one could detect charged particles only for shower exceeding 10^{15} eV, which are very rare.

While the main engine of shower development is the interplay between pair–production and bremsstrahlung radiation, there are internal Coulomb scattering processes on electrons and positrons that make the shower development more complicate. While a precise analytical description is complicate, Heitler showed already in the '40s that the main characteristics of the showers are maintained if the two following simplifications are used [4]:

- the energy of a charged particle after bremsstrahlung interaction is equally distributed between the electron and the γ–ray,
- the radiation length and the interaction length are equal.

Under this simplicist assumptions, the shower has the following properties (n is the $n-th$ radiation/absorption length, E_0 is the primary particle energy):

i) the number of electron, positrons and photons grows with 2^n,

ii) their energy decreases with $E_0/2^n$,

[1]The radiation length in air is $X_0 = 36.7$ g cm^{-2}

iii) the shower maximum is reached when the electrons and positrons are at the critical energy $E_c \simeq 83$ MeV, this happens after n_{max} radiation lengths when $n_{max} = \ln(E_0/E_c)/\ln 2$. Therefore for $E_0 = 10^2, 10^3, 10^4$ GeV the shower develops for $\simeq 3, 6, 10$ radiation lengths respectively.

iv) the position of the shower maximum is determined by $X_{max} = X_0 \ln E_0/E_C$. A sketch of the position of the shower maximum is shown in Figure B.2.

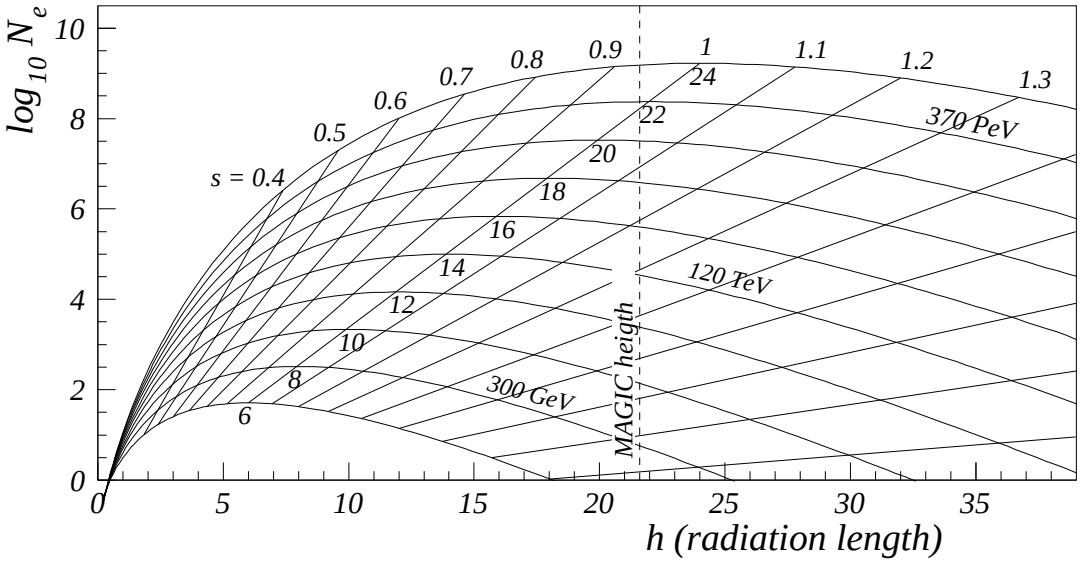

Figure B.2: Maximum development of an electromagnetic shower in the atmosphere. The position of the MAGIC telescope is drawn.

A more refined modelization was proposed by Rossi and Greisen [5]. They calculated the number of $e^{\pm}$ above the critical energy in function of the atmospheric depth (also called the longitudinal development of the shower) in term of the parameter, called shower depth, $t = x/X_0$:

$$N_{e^{\pm}}(t) = \frac{0.31}{\sqrt{\ln(E_0/E_c)}}\, e^{\,t\,(1-1.5\ln s)} \quad \text{where} \quad s = \frac{3t}{t + 2\ln(E_0/E_c)} \tag{B.3}$$

The parameter s is also called the *shower age*, as it indicates the development of the shower: It goes from 0 at the first interaction, through 1 at the shower maximum, and reaches 2 at the point where the shower dies out. Therefore, at the shower maximum, the number of electrons–positrons is:

$$N_{e^{\pm}}(max) = \frac{0.31}{\sqrt{\ln(E_0/E_c)}}\,\frac{E_0}{E_c} \tag{B.4}$$

For a shower of $10^2, 10^3, 10^4$ GeV, the number of electrons at the maximum shower development ($s = 1$) is $140, 1200, 10^4$ respectively. The shower age, the number of electrons and the altitude of development for different energies or primary γ–rays is shown in Figure B.2.

An EM shower is strongly collimated along the incident direction because of the relativistic velocities of its particles, even though multiple scattering and, in second order the Earth magnetic field, broaden the shower transversely. The lateral distribution is explained by

Moliere theory which takes into account only multiple scattering and describes it as a Gaussian for small deflection angles with a long tail. A sketch of the development of gamma shower is shown in Figure B.3.

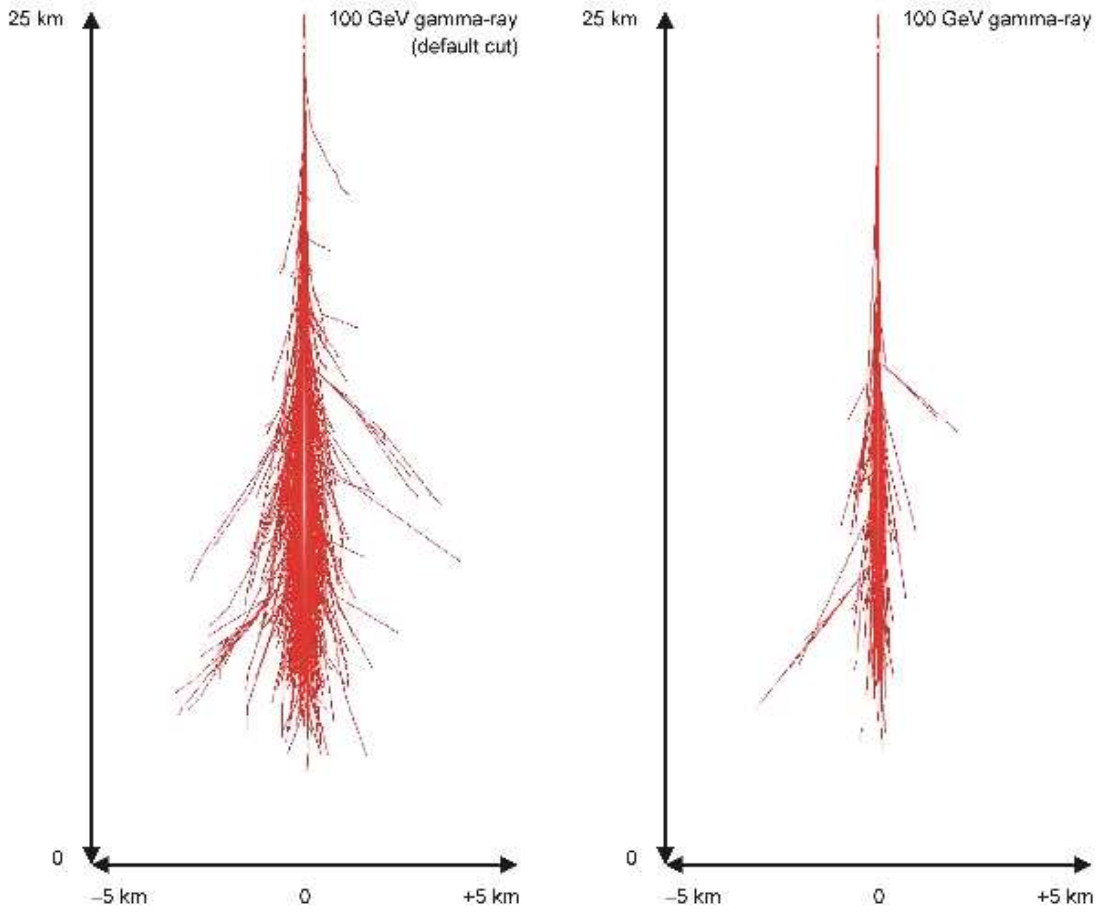

(a) 100 GeV gamma

(b) 100 GeV gamma (only Cherenkov)

Figure B.3: (a) MC simulation of a 100 GeV gamma shower. Red are electron tracks, green are muons tracks. (b) The same shower with only those tracks that produce Cherenkov light.. Courtesy of D. Hrupec. From [2].

When a charged particle crosses a medium made of heavier elements, it is scattered randomly by the interactions with atomic nuclei. If at each interaction the incident particle (suppose an electron) is scattered of an angle θ, after the incident particle has crossed a distance d in the medium and therefore after many interactions, the distribution of the angles θ is a Gaussian centered at zero, with square root standard deviation equal to (in case of electrons)

$$\sigma_0 \simeq \frac{14.1 \text{ MeV}}{E_e}\sqrt{\frac{d}{X_0}}$$

In particular, the incident particle is randomly deviated and after a distance d it statistically situated at a distance $y_0 = 1/\sqrt{(3)}\, d\, \sigma_0$ from the original trajectory. For example, in air ($X_0 = 30420$ cm), an electron of energy 1 GeV, in 10 m is deviated of 0.13°. The effect of the Coulomb scattering increase with decreasing incident particle energy.

B.2 Hadronic showers

The hadronic showers are initiated by hadrons, mainly protons, with small amount of helium and heavier elements. They interact strongly with atmospheric nuclei creating pions, kaons and nucleons. The secondary particles keep on multiplying in successive generations until the mean energy per particle drops below the pion production threshold at around 1 GeV. At that point, ionization becomes the dominant process and the shower starts to die out. Hadron–induced showers have basically three components:

i) a hadronic core built up from high energy nucleons and mesons. Charged pions and kaons can also decay into muons and neutrinos through the channels:

$$\begin{aligned} \pi^{\pm} &\rightarrow \mu^{\pm} + \nu_{\mu}(\bar{\nu_{\mu}}) \\ K^{\pm} &\rightarrow \mu^{\pm} + \nu_{\mu}(\bar{\nu_{\mu}}) \\ K^{\pm} &\rightarrow \pi^{\pm} + \pi^{0} \end{aligned} \tag{B.5}$$

ii) a muonic component which consists of muons produced by meson decays. The basically lose energy via ionization, even if they can also decay in electrons:

$$\mu^{\pm} \rightarrow e^{\pm} + \nu_{e}(\bar{\nu_{e}}) \tag{B.6}$$

Only a small fraction of their energy is released into the electromagnetic component. Due to their large lifetime, muons can travel relevant portion of the atmosphere and carry far from the initial hadron track a substantial part of its energy. As a result, the hadronic shower is way broader compared to EM shower. As shown in Figure B.4.

iii) an electromagnetic component mainly due to the neutral pion decay $\pi^0 \rightarrow \gamma\gamma$. About one third of the produced $\pi-$mesons are neutral, so about one third of the energy in hadronic interactions is transferred to electromagnetic showers. The γ–rays in turn produce EM sub–showers which constitute the main background of ground–based γ–ray astronomy as they are practically indistinguishable by gamma–initiated showers.

The simplest model for the development of hadronic shower model is the so–called Superposition Model described by Gaisser [3]. Assuming that a nucleus with atomic mass A and energy E_0 is equivalent to A independent protons with energy E_0/A, the position of the shower maximum can be described by:

$$X_{max} \simeq \ln\left(\frac{E_0}{A\,E_c}\right)\,\xi_n \tag{B.7}$$

where ξ_n is the nuclear interaction length in air. The equation shows that heavier nuclei are less penetrating than lighter ones, and therefore create showers with larger development. It is important to note that the nuclear interaction lengths ($\simeq 100$ g cm^{-2}) for hadrons are larger than the radiation length ($\simeq 37$ g cm^{-2}) which implies that X_{max} of a hadronic shower has a larger transversal spread than that of an electromagnetic shower of the same energy.

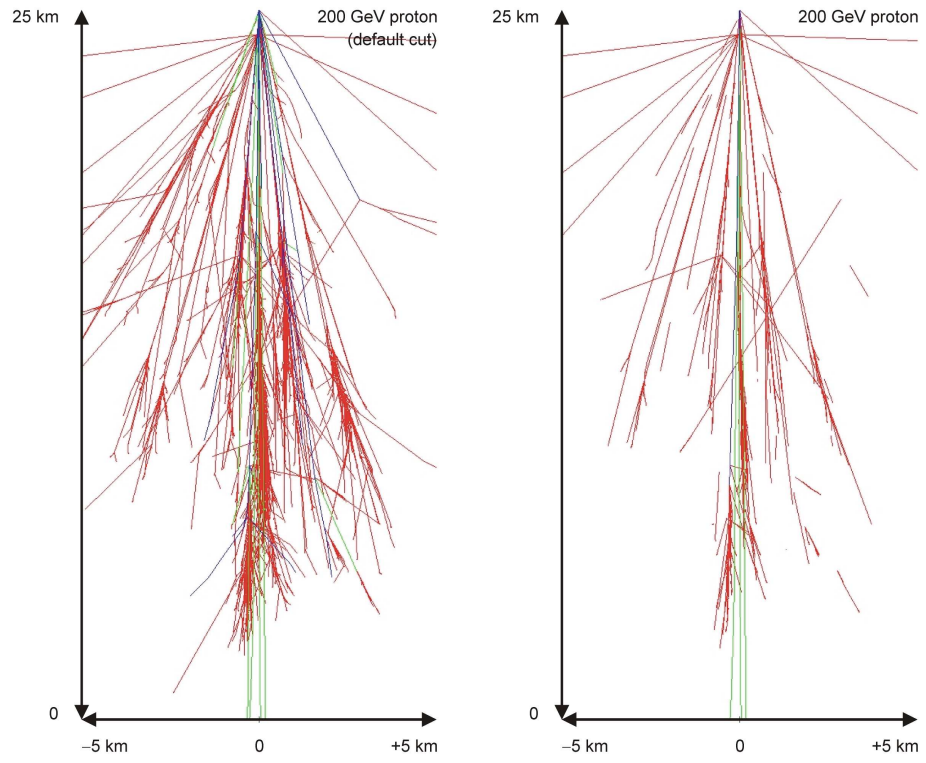

(a) 200 GeV proton (b) 200 GeV proton (only Cherenkov)

Figure B.4: (a) MC simulation of a 200 GeV proton shower. Red are electron tracks, green are muons tracks. (b) The same shower with only those tracks that produce Cherenkov light.. Courtesy of D. Hrupec. From [2].

B.3 Cherenkov emission

When a particle moves in a dielectric medium with refractive index n at a velocity which exceeds the speed of light in the medium (c/n), it produces Cherenkov light. The radiation is due to the in–phase reorientation of the electric dipoles induced by the charged particle in the medium. If the velocity of the particle is smaller than the velocity of light $v < c/n$, there are no in–phase effects. If $v > c/n$, a polarization of the medium occurs along the particle trajectory because the particle is moving faster than the electromagnetic wave which induces the polarization itself. In this case a coherent wave front appears at an angle θ. The emission angle, which defines the so-called Cherenkov cone of light, can be inferred by simple geometrical arguments: $\cos\theta = 1/\beta n$. The maximum emission angle occurs when $\beta = 1$: $\theta_{max} = \arccos(1/n)$. The minimum speed for Cherenkov light emission is $\beta_{min} = 1/n$, which implies an energy threshold for charged particles to emit Cherenkov light:

$$E_{th} = \frac{m_e c^2}{\sqrt{1-\beta_{min}^2}} = \frac{m_e c^2}{\sqrt{1-1/n^2}} \tag{B.8}$$

The refractive index of the isothermal atmosphere is slightly changing with the altitude:

$$n = 1 + \eta_h \simeq 1 + \eta_0 e^{-h/h_0} = 1 + 2.9 \times 10^4 e^{-h/h_0} \tag{B.9}$$

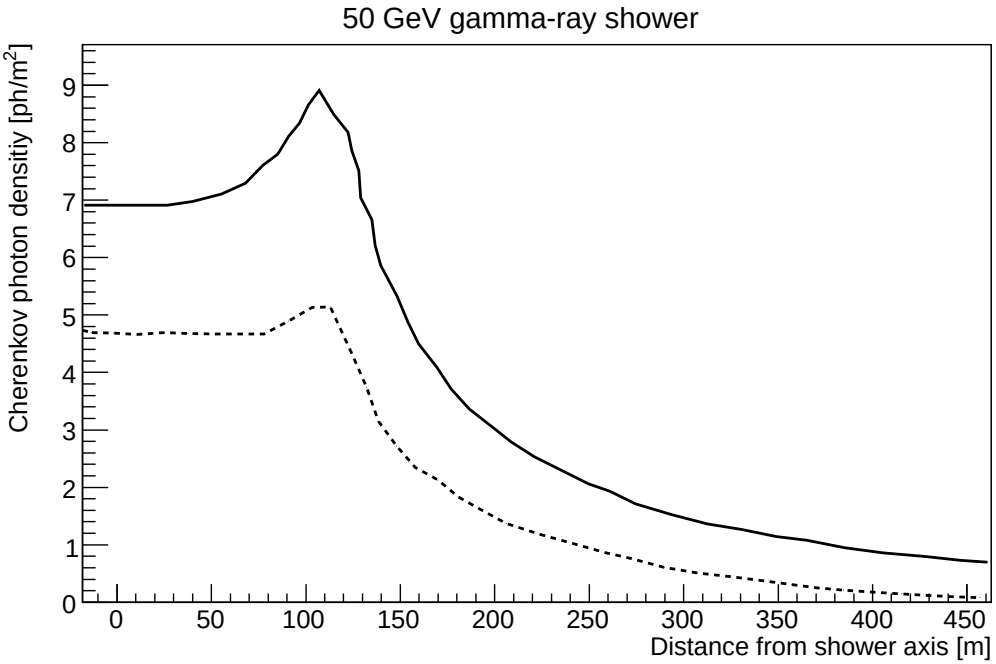

Figure B.5: Radial profile of the Cherenkov light pool initiated by a 50 GeV gamma–ray initiated electromagnetic shower (solid line). The dashed line is including earth magnetic field, telescope finite field of view and atmospheric absorption.

where h_0 is the scale–height, defined as $h_0 = 7.1$ km. The refractive index changes only about 2.5% in the visible range at ground and the dependence can therefore be neglected [1]. At sea level, the refractive index of air is $n \simeq 1.00029$. This implies that the maximum emission angle for Cherenkov emission is $\theta \simeq 1.3^\circ$. The energy threshold for electrons at ground is 21 MeV which is large compared to the electron rest mass, therefore $\beta \sim 1$ for all shower electrons and $\theta = \theta_{max}$.

The light emitted at an height h illuminates a circle on the earth's surface at an altitude h_{obs} of radius $r = h - h_{obs} \tan\theta$. This means that a shower maximum located at 10 km height illuminates a circle which has about 120 m radius and 10^5 m^2 area. A sketch of the Cherenkov light pool is shown in Figure B.5.

The figure shows that the peak of the emission (the so–called *hump*) is concentrated at 120 m distance from the shower axis and decrease exponentially towards the center, following the Cherenkov radiation rules. On the other hand, there would not be photons outside the peak if were not for the effect of Coulomb scattering that moves away electrons and positrons from the shower axis. The figure is taken from MC simulation of Ref. [6]. One can see that the effect of the finite telescope aperture, the magnetic field and the atmospheric absorption (see below) reduce the number of photons and smooth their distribution.

B.3.1 The Cherenkov light spectrum

The spectrum of Cherenkov light gets attenuated in the atmosphere because of absorption, due to interaction of the Cherenkov photons with atmospheric molecules through:

i) *Rayleigh scattering.* This process involves air molecules with diameters around the nm. The cross–section is proportional to λ^{-4}, therefore shorter wavelengths

are rapidly absorbed. In the range $2 - 15$ km above sea level, this process is responsible for most of the Cherenkov light attenuation.

ii) *Mie scattering.* This process is due to aerosol particles, i.e. particles with a diameter about the mm such as dust, pollution, clouds and high humidity. There is no strong dependence on the wavelength of the light. The Mie scattering is difficult to model because the presence of aerosol particles is subject to continuous variations on a hour scale.

The number of emitted Cherenkov photons in the wavelengths interval (λ_1,λ_2) as a function of the path length x is:

$$\frac{dN}{dx} = 2\,\pi\; alpha\; \left(\frac{1}{\lambda_1} - \frac{1}{\lambda_2}\right)\; \left(1 - \frac{1}{\beta^2\, n^2}\right) \tag{B.10}$$

where *alpha* is the fine structure constant. Cherenkov radiation emitted by a shower and traveling through the atmosphere, reaches the ground spanning a wavelength range from about 290 nm to about 600 nm, where the lower limit is due to the ozone cut-off, and the upper one to other absorption mechanisms. Considering this wavelength range and the refractive index of air, the number of Cherenkov photons produced by an ultra-relativistic electron can be approximated by:

$$\frac{dN}{dx} \simeq 44\; e^{-h/h_0}\ \text{photons/m} \tag{B.11}$$

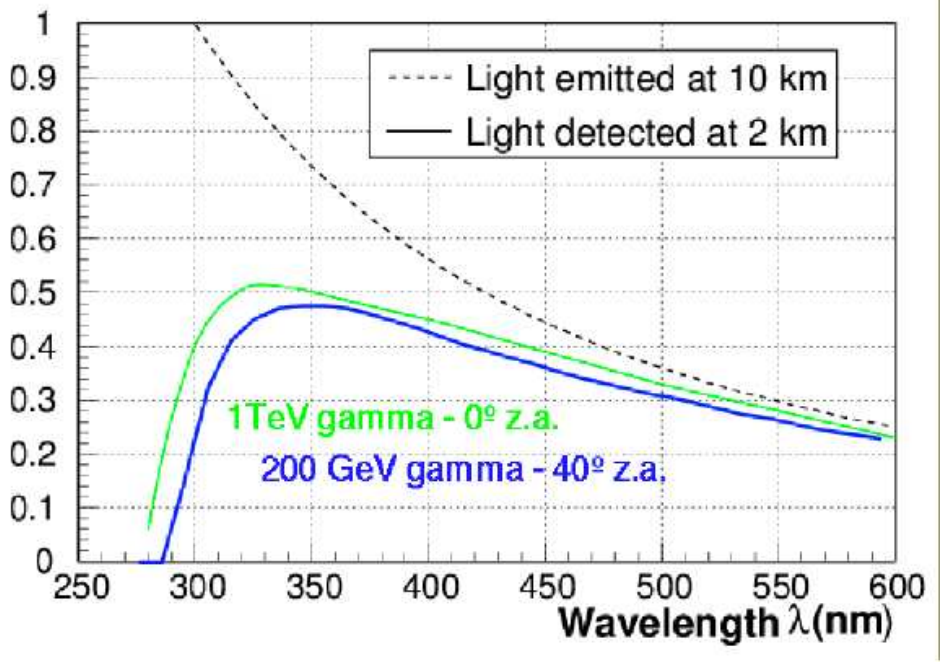

Figure B.6: Effect of the atmospheric absorption in the spectrum of Cherenkov light detected at 2.2 km altitude. The upper green line shows the case were a shower was initiated by 1 TeV photon of vertical incidence; in blue by a 200 GeV photon at 40° of zenith angle.

References

[1] F. I. Boley. Atmospheric Čerenkov Radiation from Cosmic-Ray Air Showers. *Reviews of Modern Physics*, 36:792–808, July 1964.

[2] M. Doro et al. The Reflectors of the Imaging Atmospheric Cherenkov Telscopes MAGIC I and MAGIC II. Under publication in Journal of Instrumentation.

[3] T. K. Gaisser. *Cosmic rays and particle physics*. Cambridge and New York, Cambridge University Press, 1990, 292 p., 1990.

[4] M. S. Longair. *High energy astrophysics. Vol.1: Particles, photons and their detection*. High Energy Astrophysics, by Malcolm S. Longair, pp. 436. ISBN 0521387736. Cambridge, UK: Cambridge University Press, March 1992., Mar. 1992.

[5] B. Rossi and K. Greisen. Cosmic-Ray Theory. *Reviews of Modern Physics*, 13:240–309, Oct. 1941.

[6] D. Sobczynska. Limits to the energy resolution of a single Air Cherenkov Telescope at low energies. 2009.

C
Aberrations

In this appendix we briefly introduce the theory of aberrations limited to the case of a spherical and parabolic reflector of a telescope. This discussion is based on Ref. [1].

In appendix B we discussed the basic characteristics of an atmospheric shower and the Cherenkov emission associated with. We know that the Cherenkov emission is mostly located in a region at $12 - 8$ km asl and is concentrated in a light cone of around $0.7 - 1.3^\circ$ aperture. For example, an atmospheric shower having maximum development at 10 km altitude, the angle of emission is 0.8°. For statistical reason, most of the Cherenkov emission therefore comes at a tilted angle with respect to the telescope axis. In other words, the shower is most probably observed at a certain impact parameter h, which is the distance from the telescope axis.

The image of a point at distance S from the reflector vertex is focussed at a distance S' following the relation:

$$\frac{1}{S} + \frac{1}{S'} = \frac{1}{2R} = \frac{1}{f} \tag{C.1}$$

where f is the reflector focal length and R the vertex radius of curvature, see Figure C.1. In addition, the magnification M introduced by the reflector is defined as:

$$M = \frac{h'}{h} = -\frac{S'}{S} \tag{C.2}$$

therefore it is easy to extrapolate that for MAGIC, with a focal length of 17 m, the magnification $M \simeq 1.7 \times 10^{-3}$. An impact parameter of $h = 130$ m corresponds to a position in the camera of $h' = h \cdot M \simeq 22$ cm (for the centroid of the image).

Seen from the ground, the Cherenkov shower has the shape of an ellipse (it is the intersection of the Cherenkov tilted cone with a horizontal plane). The image at the camera will therefore be ellipse–like too. How much this ellipse differs from the original shape distribution is related to the optical aberrations introduced by the reflector[1].

[1] It must be underlined that an intrinsic blurring of the Cherenkov photons is due to the Coulomb scattering effect on the shower electrons.

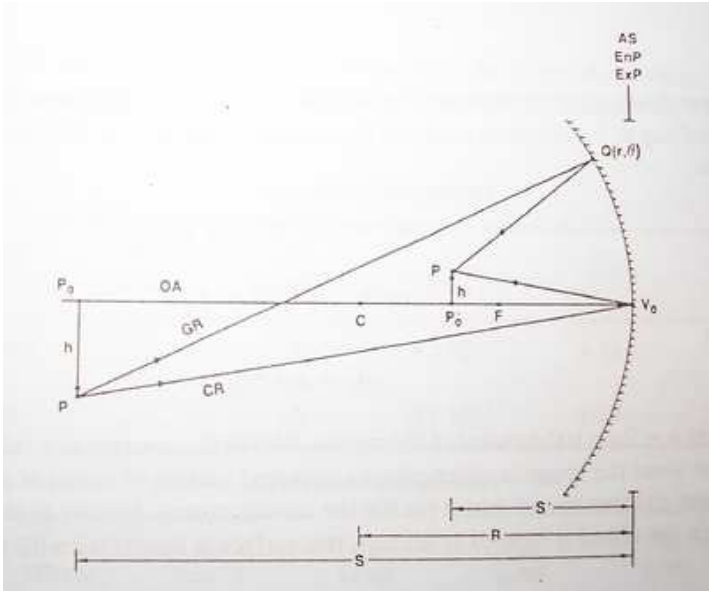

Figure C.1: Imaging by a spherical mirror of radius of curvature R. The line joining the center of vertex of the reflector V_0 and the center of curvature C is the telescope optical axis. The chief–ray CR from the point P in the shower passes through the center of the aperture stop, i.e. the reflector. Figure from [1].

To characterize the aberrations, it is common to define the *chief–ray* as the light–ray which crosses the optical system as the center of the *aperture stop*, which in the case of Cherenkov telescope is the reflector itself, see Figure C.1.

An aberration occur whenever a light–ray is reflected at a position different than that of the chief–ray in the focal plane. For optical systems symmetrical around an optical axis, the aberrations can be defined through a function $W(r, \theta, h')$ which depends on the coordinates r, θ of where the reflector is illuminated and the distance $h' = \beta f$ of the reflected light in the focal plane, where β is the off–axis angle of the light from the shower and f is the focal length of the reflector. The aberrations can be qualified according to their dependence on r:

$$W(r,\theta,h') = \underbrace{a_s\, r^4}_{spherical} + \underbrace{a_c\, h' r^3 \cos\theta}_{coma} + \underbrace{a_a\, h'^2 r^2 \cos^2\theta}_{astigmatism} + \underbrace{a_f\, h'^2 r^2}_{field} + \underbrace{a_d\, h'^3 r \cos\theta}_{distortion} \tag{C.3}$$

These are called the *wave aberrations* which corresponds to the geometrical deviation from the unaberrated light–ray times the refractive index of the medium. The geometrical deviation in the focal plane with respect to the chief–ray (also called transverse ray aberration) can be calculated with the following formula:

$$(\Delta_x, \Delta_y) = \frac{R}{n}\left(\frac{\partial W}{\partial x}, \frac{\partial W}{\partial y}\right) \tag{C.4}$$

The aberrations introduced above are also called *Seidel aberrations* or *primary aberrations* and are fourth–order wave aberrations, which corresponds to third–order ray aberrations.

They have the following properties:

– the **spherical aberration** depends only on the position where the light–ray hits the mirror (r^4) and does not depend on whether the light is tilted or not. Light–rays that hit the reflector in the outermost part suffer from this aberration which grows at the fourth–power. The reflected light is focussed beyond the focal plane, and the whole image is therefore blurred. How the aberration works is shown in Figure C.2(a)

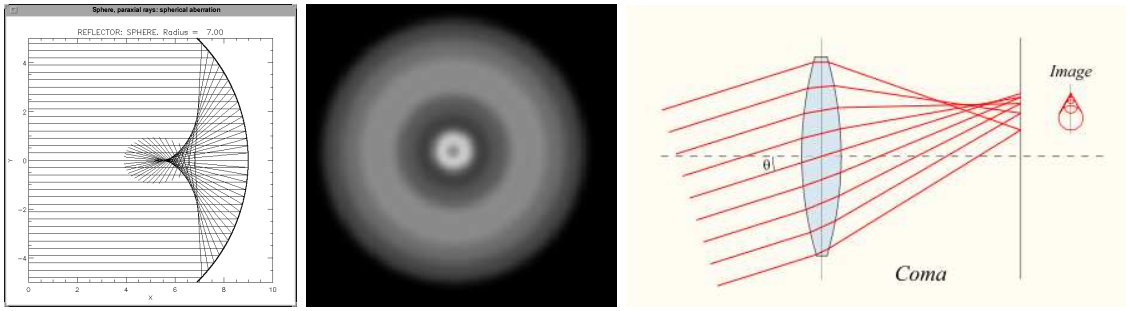

(a) Spherical aberration (b) Coma aberration

Figure C.2: Sketch of the spherical (a) and coma aberration (b). In the coma aberration, for tilted incidence, light rays hitting the lens at different positions are reflected in different positions in the focal plane, with the creation of a comet–like shape of the global reflected image.

- the **coma aberration** has also a strong dependence from the distance of the optical axis. In addition, the coma aberration increases with the angle of incidence β and has an preferential direction in the focal plane $\cos\theta$. The light hitting the mirror at a distance from the center is reflected off the optic axis and after the focal plane, as shown in Figure C.2(b).
- the **astigmatism** is much like coma but the $\cos^2$ dependence make it stretch or expand the optical image on two orthogonal axis.
- the **field curvature aberration** acts much like a defocus (which depends only on d^2. It blurs homogeneously the image at the focal plane.
- the **distortion aberration** is also similar to coma, and is like observing the image at a tilted angle.

For an optical system with conical mirror and aperture stop located at the reflector (as is the case for a telescope) the aberrations function of Eq. C.3 can be written in term of few parameters (see Figure C.1):

$$a_s = \frac{1}{4R}\left(\frac{1}{R}+\frac{1}{S'}\right)^2, \qquad a_c = -\frac{R+S'}{R^2S'^2}, \qquad a_a = \frac{1}{RS'^2}, \qquad a_f = a_d = 0 \tag{C.5}$$

where S' is the distance of the focal plane from the conic vertex and R is the radius of curvature at the vertex of the reflector. It is important to note that for a conical mirror and aperture stop at the mirror, the field curvature and distortion aberrations are null.

C.1 Aberrations of a spherical mirror

In the case of a spherical mirror, we consider the case of light coming from infinity. Therefore $S' = -R/2 = f$ and $d = -2$) and at a tilted angle β (then $h' \simeq \beta f$). The aberration equation can be therefore written:

$$W_{spherical}(r,\theta,\beta) = -\frac{1}{32f^3}r^4 + \frac{1}{4f^2}\beta r^3\cos\theta - \frac{1}{2f}\beta^2 r^2\cos^2\theta \tag{C.6}$$

It is clear from Eq. C.6 that the aberrations increase with the size of the reflector and decreases with an increased focal length. It is easy to see that, if terms of the $f-$number,

the aberrations decrease almost linearly with this value. We also underline that in case the telescope is focussed at 10 km instead of infinity, the focal plane is shifted only by a small amount, of the order of few cm. Formula C.6 therefore remains valid.

Figure C.3 shows the vertical and tilted incidence of light on a spherical telescope.

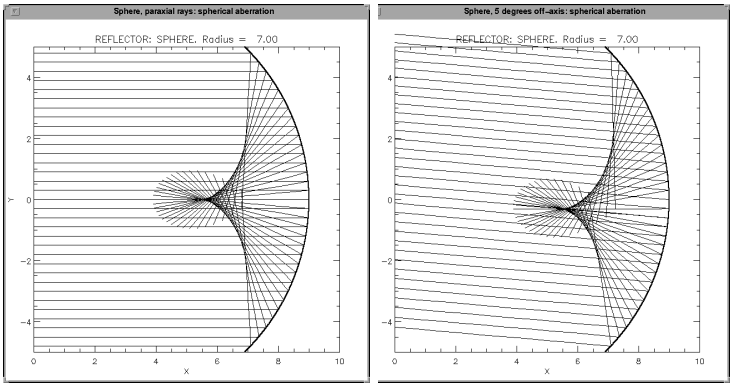

Figure C.3: Imaging of a spherical surface for paraxial and 5 deg incidence light. Figures taken from [2]

C.2 Parabolic mirror

In the case of a parabolic mirror, it can be demonstrated that the spherical aberration vanishes, while the coma and astigmatism aberrations take the same form as described above. The resulting equation for a parabolic reflector aberration simplifies into:

$$W_{parabolic}(r,\theta,\beta) = \frac{1}{4f^2}\beta r^3 \cos\theta - \frac{1}{2f}\beta^2 r^2 \cos^2\theta \tag{C.7}$$

The parabolic surface is therefore the best surface that focus the light coming from infinity at vertical incidence. Also in this case, the effect of having the telescope focussed at 10 km is not particularly relevant for the sake of the aberrations. In the case of MAGIC, with a focal length of 17 m, the shift of the camera would be only 2.9 cm farther from the reflector. For the parabolic profile, in particular, the argument in favor of having large $f-$number remains valid to reduce aberrations.

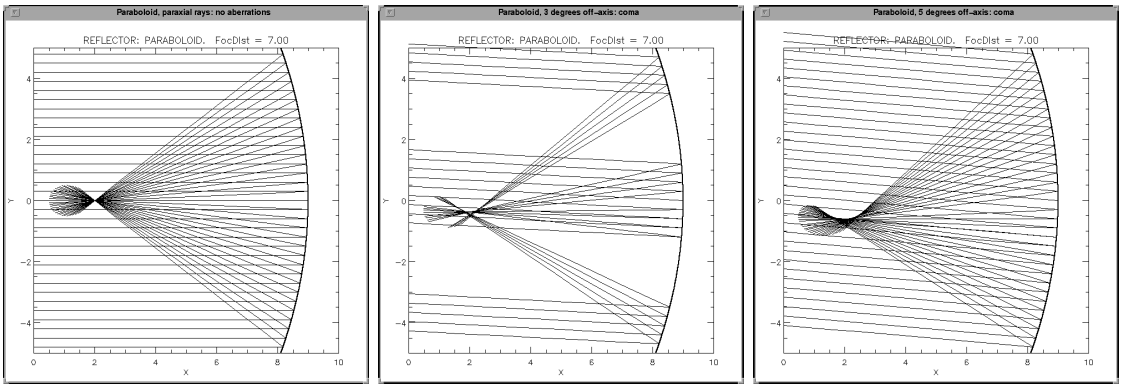

Figure C.4: Imaging of a parabolic surface for paraxial, 3 deg and 5 deg incidence light. Figures taken from [2]

References

[1] V. N. Mahajan. *Aberration Theory Made Simple*. SPIE Optical Engineering Press, 1991.

[2] R. W. O'Connell. Astronomy 511 lecture materials. Available at: http://www.astro.virginia.edu/class/oconnell/astr511/lectureindex.html, 2003.

D

Calculation of flux upper limits for a general spectrum.

In the following we define how to calculate the upper limit in flux from the number of excess events N_{exc} in the hypothesis that the gamma-ray spectrum is a general function $S(E)$ of the energy. This appendix was written with D. Nieto.

If we define the differential flux as the number of gammas per unit time, unit area and unit energy, as:

$$\phi(E) = \frac{dN_\gamma}{dE\, dA\, dt} \qquad [\text{ph cm}^{-2}\ \text{s}^{-1}\ \text{GeV}^{-1}] \tag{D.1}$$

The integral flux coming from one point in the sky above an energy threshold E_0 can be defined as:

$$\Phi(> E_0) = \int_{E_0}^{\infty} \phi(E)\, dE \qquad [\text{ph cm}^{-2}\ \text{s}^{-1}] \tag{D.2}$$

In our case, we assume the spectrum of emission of gamma-ray from a target $S(E)$ (ph cm^{-2} s^{-1}) and we can express the corresponding differential flux with:

$$\phi(E) = K_0\ S(E) \tag{D.3}$$

where K_0 is a normalization constant.

Suppose now that you have observed the target for an effective time of t_{eff} seconds, you have perfomed the analysis and defined a best set of *cuts* in the Hillas parameters and in the estimated energy E_{est} after the Random Forest. At the end you come up with a number of excess events $N_{exc}(cuts)$ (with a significance well below the 5σ), and you want to estimate the upper limit on the flux corresponding to the observational data. The first thing is to apply the Rolke method and estimate the corresponding number of $N^{ul}_{exc}(cuts)$. As the number of excess events is calculated after the cuts, you want to understand the efficiency of these cuts to reconstruct the original number of gammas. This number cannot be known directly from the data, and is only extracted by performing the analysis on a MC sample so that after the

cuts you can define the gamma-efficiency:

$$\epsilon_\gamma(E, cuts) = \frac{N_\gamma^{cuts}(E)}{N_\gamma^{mc}(E)} \tag{D.4}$$

so that if you observe N events, the original number of events is N/ϵ_γ. The ϵ_γ is embedded into the concept of the *effective area*. While the MC gammas are simulated on a geometrical simulation area of a circle of 300 m radius, the effective area is the product of the simulation area times the gamma efficiency [1]:

$$A_{eff}(E, cuts) = A^{mc} \cdot \epsilon_\gamma(E, cuts) \tag{D.5}$$

In the hypothesis the light curve is constant, i.e. that $dN_\gamma/dt = const$ and considering the fact that by definition the effective area is now function of the energy $A_{eff} = A_{eff}(E)$, the following procedure can be used to compute the normalization factor K_0 (given a certain $S(E)$) corresponding to $N_{exc}^{ul}(cuts)$. You compute Eq. D.2 and use definition Eq. D.1 and D.3 and then you come up with:

$$K_0 = \frac{dN_\gamma}{S(E)dE\, dA\, dt} \tag{D.6}$$

now, as we want an integral flux, we have to integrate over the observation time and over the energy. The integral of the numerator of Eq. D.6 gives $N_{exc}^{ul}(cuts)$ and it is integrated in the estimated energy range [$E_{rec,1}$,$E_{rec,2}$]. In the denominator, there is no dependece on time and therefore $\int dt = t_{eff}$ is the effective duration of the ON observation. So we come up with:

$$\begin{aligned} K_0^{ul} &= \frac{N_{exc}^{ul}(cuts)}{\int_{E_{rec,1}}^{E_{rec,2}} S(E) \cdot A_{eff}(cuts, E) \cdot t_{eff}\, dE} && \text{(D.7)} \\ &= \frac{N_{exc}^{ul}(cuts)}{t_{eff}} \cdot \frac{1}{\int_{E_{rec,1}}^{E_{rec,2}} S(E) \cdot A_{eff}(cuts, E)\, dE} && \text{(D.8)} \\ &= \frac{N_{exc}^{ul}(cuts)}{t_{eff}} \cdot \frac{1}{\sum_{E_{rec,1}<k<E_{rec,2}} S(E) \cdot A_{eff}(cuts, E)\Delta E} && \text{(D.9)} \end{aligned}$$

where in the last step we have simply replaced the integral with a sum over the k-th bins in estimated energy. Now, Eq. D.9 lead to a slightly wrong result, because:

1. The cuts in the analysis are all done in *estimated energy*, which is the results of the recontruction of the size parameter of the shower using MC. Due to the finite energy resolution of MAGIC, the reconstruction is not deterministic, so that if you make a cut in estimated energy [$E_{rec,1}$,$E_{rec,2}$], you can either have events with real energy outside this range that are reconstructed inside [$E_{rec,1}$,$E_{rec,2}$] and events with real energy inside this range that are reconstructed outside. The effect is shown in Figure D.1.

   For this reason, regardless the fact that the cut is made on the estimated energy, the integral of the denominator in the Eq. D.9 should be over all the range in true energy to take into account the lost events, see Eq. D.11.

2. The effective area is defined as the product of a geometrical area for the gamma efficiency. It is natural to ask if the gamma efficiency depends on the spectrum of the source. As it is computed in bin, this corresponds to ask whether the efficiency per

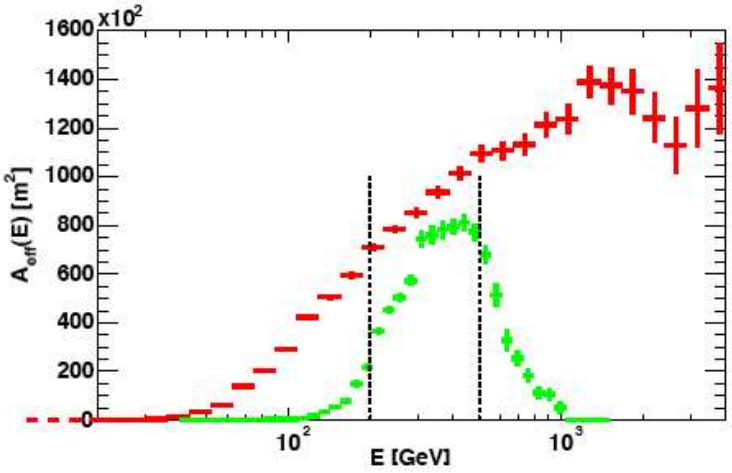

Figure D.1: Distributions of effective areas for a telescope pointing zenith angle around 40° and typical analysis cuts. The red crosses show the effective area without cuts in reconstructed energy, while the green crosses have cuts in $200 < E_{est} < 500$ GeV applied. X axis represents *true* MC energy and dotted vertical lines represents the cuts in *estimated* MC energy. From [1]

bin depends on the number of gammas in that bin. The standard effective area for the telescope is calculated with a crab-like spectrum (is this true?). We do not exactly know how strong is dependence of the computation of the effective area for one bin in function of the number of entries, but we should try to recompute it for our spectrum. It must be said that in the operation of Eq. D.9 the effective area is effectively rescaled for the source spectrum $S(E)$ so that the difference should be small.

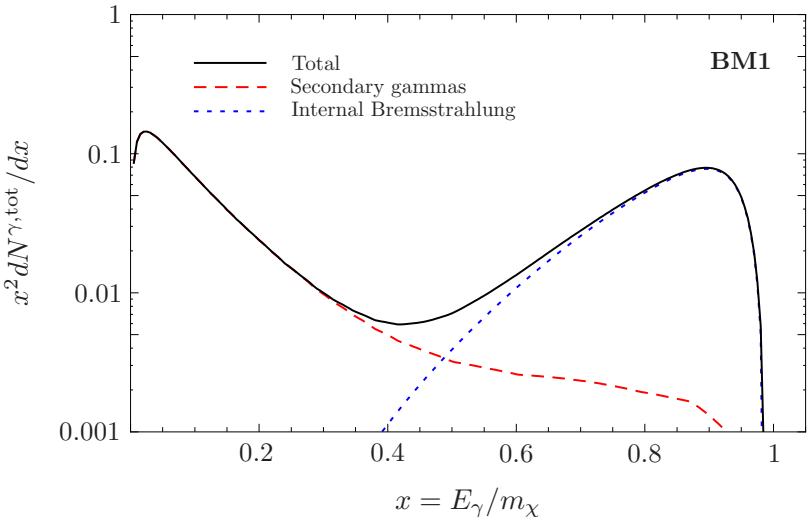

Figure D.2: Example of spectrum for DM annihilation including internal bremmstrahlung. This is model I' described in the text.

3. The spectrum S(E) is defined in function of the real energy, but indeed due to the energy resolution MAGIC *sees* the spectrum as smeared with the energy resolution. A cut in estimate energy also for the spectrum does not correspond to a cut in real energy. To overcome this effect one should already smear the energy spectrum with the energy resolution of the telescope"

$$S^{res}(E') = \int S(E) * res(E - E')dE' \tag{D.10}$$

where $res(E) \simeq 0.3$–$0.2\ E$. In Figure D.2 an example of S(E) is shown (smearing to be done yet)

Therefore, taking into account the above consideration, we have to re-write Eq. D.9 with:

$$K_0^{ul} = \frac{N_{exc}^{ul}(cuts)}{t_{eff}} \cdot \frac{1}{\sum_{0<k<\infty} S^{res}(E) \cdot A_{eff}(E, cuts, S^{res}(E))\Delta E} \tag{D.11}$$

Following Eq. D.3,the final value of integral flux upper limit above a certain energy E_0 is:

$$\Phi^{ul}(E_0, c.l.) = K_0^{ul} \int_{E_0}^{\infty} S(E) dE \tag{D.12}$$

References

[1] M. Gaug. Calibration of the magic telescope and observation of gamma ray bursts. Master's thesis, Institut de Física des Altes Energies, Barcelona, Spain, 2006. Available at http://wwwmagic.mppmu.mpg.de/publications/theses.

List of Figures

List of Tables